A

Actively and Semi-actively Controlled Structures Under Seismic Actions: Modeling and Analysis

Nikos Pnevmatikos[1] and Charis J. Gantes[2]
[1]Department of Civil Engineering, Surveying and Geoinformatics, Technological Educational Institute of Athens, Egaleo-Athens, Greece
[2]Institute of Steel Structures, School of Civil Engineering, National Technical University of Athens, Zografou Campus, Athens, Greece

Synonyms

Active control; Control algorithms; Hybrid control; Semi-active control; Structural control

Introduction

Structural control of seismically excited buildings and other civil structures has attracted considerable attention in recent years. The objective of this entry is to present how seismic design of structures can benefit from the structural control concepts and applications. For this purpose, control theory as applied in other engineering disciplines is adjusted and appropriately modified, where needed, in order to propose integrated control procedures suitable for civil structures subjected to earthquake excitation.

Two approaches can be taken to help buildings withstand seismic excitations. The first involves designing the structure with sufficient strength, stiffness, and inelastic deformation capacity to withstand an earthquake. The choice of material used in construction and the soil beneath the structure are important factors that influence structural vibration and the amount of damage. Because this approach relies on the inherent strength of the structure to dissipate the seismic energy, a certain level of inelastic deformation and associated damage has to be accepted. The second approach relies on using control devices in order to reduce the forces acting on the structure, aiming at reducing all quantities of structural response, that is, floor accelerations, velocities, and displacements. Control systems are categorized according to their energy requirements as passive, active, semi-active, and hybrid. In order to apply a control approach, appropriate control devices are needed. These devices are capable of altering the dynamic characteristics of a structure in real time or applying direct or indirect control forces to the structure, in order to reduce its response. These devices operate as instructed by suitably designed control algorithms.

Several available control algorithms are applied to control structures, many of which were developed by researchers in other fields like electrical or mechanical engineering. However, electrical and mechanical devices are

M. Beer et al. (eds.), *Encyclopedia of Earthquake Engineering*,
DOI 10.1007/978-3-642-35344-4

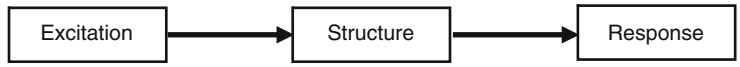

Actively and Semi-actively Controlled Structures Under Seismic Actions: Modeling and Analysis, Fig. 1 Conventional structure and the response under the seismic excitation

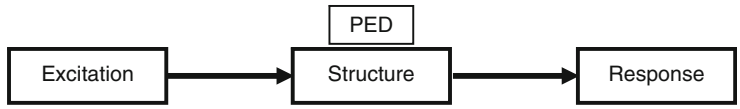

Actively and Semi-actively Controlled Structures Under Seismic Actions: Modeling and Analysis, Fig. 2 Structure with passive energy dissipation devices (PED)

Actively and Semi-actively Controlled Structures Under Seismic Actions: Modeling and Analysis, Fig. 3 Structure with active control devices

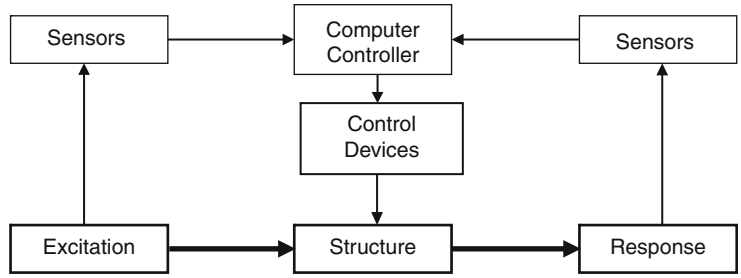

Actively and Semi-actively Controlled Structures Under Seismic Actions: Modeling and Analysis, Fig. 4 Structure with semi-active control devices

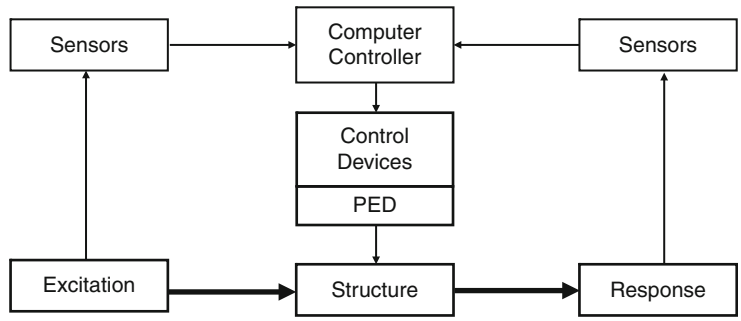

different from buildings as far as their structural behavior is concerned. The former, in most cases, are mechanisms, while the latter are constructions with a high degree of redundancy. Moreover, in the control of electromechanical devices, the loading is known a priori and is usually harmonic, while for buildings the earthquake loading is unknown and contains a multitude of frequencies. Thus, there is a need of selecting among existing algorithms those that are suitable for the control of buildings and then modifying them accordingly. Along these lines, a common feature of all control strategies that are presented here is that they are applied to structures excited at their base by incoming earthquake waves.

Structural Control (Passive, Active, Semi-active, Hybrid), Corresponding Control Devices, and Practical Applications

Structural control systems fall into four basic categories: passive, active, semi-active, and hybrid control (Soong 1990; Soong and Spencer 2002). These structural control systems are presented in Figs. 1, 2, 3, 4, and 5 below.

Passive Control

Passive control devices are devices that do not require power to operate. Examples of passive devices are base isolation, tuned mass dampers (TMD), tuned liquid dampers (TLD), metallic yield dampers, viscous fluid dampers, and

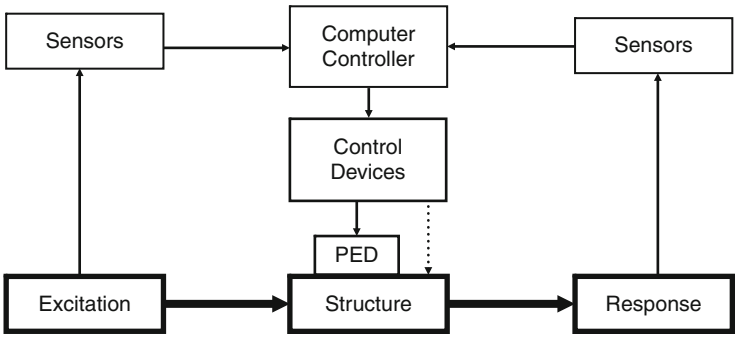

Actively and Semi-actively Controlled Structures Under Seismic Actions: Modeling and Analysis, Fig. 5 Structure with hybrid control devices

friction dampers. They dissipate energy using the motion of the structure to produce relative movement within the control device or to alter the dynamic properties of the structure (damping, natural frequencies), so that the earthquake action will be minimized. Since they do not inject energy into the system, they are stable devices. Another advantage of such devices is their low maintenance requirements and the fact that they are unaffected by potential interruptions in power supply. These systems are well understood and well accepted by the engineering community as a means for mitigating the effects of dynamic loadings, such as strong earthquakes and high winds. However, such passive devices have the limitation of not being able to adapt to structural changes and to different earthquake excitations. Active, semi-active, and hybrid control systems aim at addressing these shortcomings.

Active Control

Active control strategies have been developed in the 1990s, (Soong 1990; Housner et al. 1997); they operate by using external energy supplied by actuators to impart forces on the structure. The appropriate control action is determined based on measurements of the structural response. Active control devices include the active tendon system (Abdel-Rohman and Leipholz 1983), the active bracing system (Reinhorn et al. 1989), and the active tuned mass damper (Abdel-Rohman and Leipholz 1983).

The most famous active control device is the active mass damper (AMD), which uses a mass–spring–damper system combined with an actuator that moves the mass as needed to increase the amount of damping and the operational frequency range of the device. The first implementation of this control method, and of active control in general, was performed in 1989 in the Kyobashi Seiwa building, Tokyo, Japan, by Kajima Corporation (Kobori et al. 1991). Other applications of such devices include the Applause Tower (Hankyu Chayamachi building) in Osaka, Japan; the Riverside Sumida Central Tower, in Tokyo, Japan; the Nanjing Communication Tower, in Nanjing, China; and the Shin-Jei building in Taipei, Taiwan (Spencer and Nagarajaiah 2003).

Active control devices require considerable amount of external power to operate actuators that supply a control force to the structure. Such power may not always be available during seismic events. Another drawback is that due to their capacity to add energy to the system, they may destabilize it. Cost and maintenance of such systems is also significantly higher than that of passive devices. On the other hand, they are more effective than passive devices because of their ability to adapt to different loading conditions and to control different modes of vibration. Housner et al. (1997) point out the importance of system integration in the design and development of active control systems. Not only is it necessary to consider the individual components of a control system, but the system as a whole must be understood, including the structure, control devices, sensors, and computer control system. Błachowski (2007) uses model-based predictive control to reduce the vibration for guyed mast.

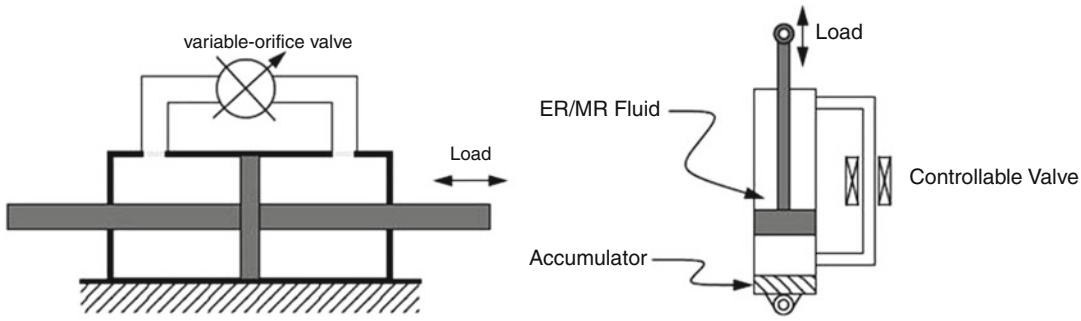

Actively and Semi-actively Controlled Structures Under Seismic Actions: Modeling and Analysis, Fig. 6 Variable-orifice damper and controllable fluid damper

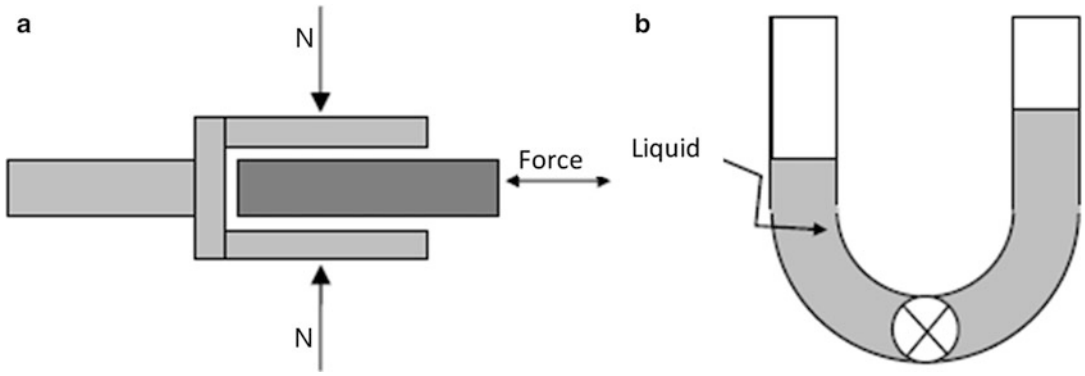

Actively and Semi-actively Controlled Structures Under Seismic Actions: Modeling and Analysis, Fig. 7 Friction semi-active device (**a**) and semi-active tuned liquid column damper (**b**)

Semi-active Control

Semi-active control devices offer the adaptability of active ones without requiring such high power, since external power is only used to change the device's properties, such as damping or stiffness, and not to generate a control force (Symans et al. 1994) In fact, many semi-active devices can operate on battery power, which is critical during seismic events, when the main power source to the structure may fail.

A semi-active control device cannot inject energy into the controlled system (structure and device) but has properties that can be varied in real time in order to reduce the response of a structural system (Housner et al. 1997). Changes in mechanical properties of the device are based on feedback from measured response and/or ground excitation. Therefore, in contrast to active control devices, semi-active ones do not destabilize the structural system. They offer stability and reliability, since they function as passive devices in case of power failure (Soong and Spencer 2002). A lot of studies indicate that appropriately designed semi-active systems perform significantly better than passive ones. Moreover, they perform better than active systems for a variety of dynamic loading conditions.

Examples of such devices include variable orifice fluid dampers, controllable friction devices, variable stiffness devices, controllable liquid dampers, and controllable fluid dampers (Figs. 6 and 7). A variable orifice fluid damper uses an electromechanically variable orifice to alter the resistance to flow of a conventional hydraulic fluid (Feng and Shinozuka 1992; Constantinou et al. 1993).

A semi-active controllable fluid device is a combination of dampers with fluids that have the ability to reversibly change their viscosity. The two controllable fluids used in structural

control devices are electrorheological (ER) and magnetorheological (MR) fluids. They consist of dielectric polarizable (electrorheological, ER fluids) or magnetically polarized (magnetorheological, MR fluids) particles suspended in an oil medium. They have the ability to reversibly change from viscous fluids to semi-solids with controllable yield strength in milliseconds, with the application of an electrical or magnetic field, respectively. This property makes them ideal for use in controllable dampers. The advantage of controllable fluid devices is that they contain no moving parts other than the piston, which makes them very reliable and very easy to maintain. Moreover, they require low power to operate.

The discovery of both ER and MR fluids dates back to the late 1940s (Winslow 1947). ER fluid dampers have been developed, modeled, and tested for civil engineering applications (Erhrogott and Marsi 1992, 1993; Makris et al. 1995). Work on MR devices have been done by Spencer et al. (1997), Soong and Spencer (2002), Spencer and Nagarajaiah (2003), Carlson et al. (1995), and Dyke et al. (1996c–f).

Other semi-active devices use the force generated by surface friction to dissipate energy in a structural system.

Other types of semi-active control devices use the dynamic motion of a sloshing fluid or a column of fluid to reduce the response of a structure. These liquid dampers are the evolution of passive tuned sloshing dampers (TSD) and tuned liquid column dampers (TLCD). The TSD uses the liquid in a sloshing tank to add damping to the structural system. Similarly, in a TLCD the moving mass is a column of liquid, which is driven by the vibrations of the structure. These passive systems are not very effective for varying loading conditions. To improve their effectiveness, a semi-active device based on the passive TSD has been proposed, in which the length of the sloshing tank, thus also the properties of the device, and therefore its natural frequency can be changed. Similarly, in semi-active devices based on a TLCD, a variable orifice within the liquid column is used, or the cross section of the sloshing tank is changed.

Semi-active tuned mass dampers are similar to TMDs, but with the capability of varying their level of damping. They are mainly used for wind vibration reduction. Another type of semi-active TMD is the semi-active variable stiffness tuned mass damper (SAIVS-TMD), where the stiffness is also controllable. Their performance is similar to that of AMDs but with less power consumption.

Variable stiffness control devices have the ability to modify the structure's stiffness and therefore its natural frequency to avoid resonant conditions. These systems have been studied by Kobori et al. (1993). They are installed in bracing systems, and with opening or closing a valve, they allow the connection between the brace and beam, thus changing the building stiffness and therefore its frequency, to avoid resonance with the incoming earthquake. Their energy operation is very low, and they are designed so that in the case of power failure, the connection is automatically closed and the structure's stiffness is increased.

The first full-scale application of semi-active control was the installation of variable stiffness devices on both sides of the Kajima Technical Research Institute.

Hybrid Control

Hybrid control refers either to a combination of passive and active systems or, more commonly, to a combination of passive with semi-active systems, aiming at lowering the forces required by active or semi-active systems, respectively. One such device is the hybrid mass damper (HMD), which combines tuned mass dampers with active actuators. The actuator force is only used to increase efficiency and robustness to changes in structural dynamic characteristics. Also in the category of hybrid mass dampers is the active–passive composite tuned mass damper (APTMD) developed by Ohrui et al. (1994) and named DUOX. This device is composed of an active mass damper mounted on a tuned mass damper, Fig. 8. During structural motion, the mass of the AMD is driven in the opposite direction of the TMD, therefore magnifying the motion of the passive device. When the building

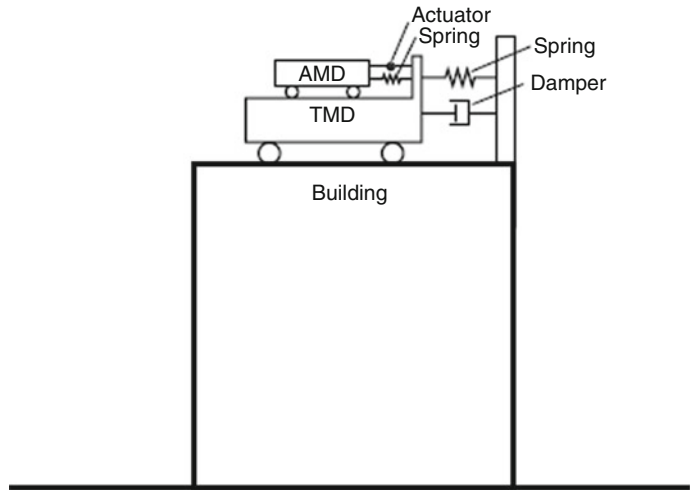

Actively and Semi-actively Controlled Structures Under Seismic Actions: Modeling and Analysis, Fig. 8 Simplified diagram of DUOX control system

deformation stops, the AMD is used to suppress useless motion of the TMD.

Base isolation systems are passive systems, and they do not have the ability to adapt and change their properties in different external excitation (e.g., near- or far-fault excitation). With the addition of an active or semi-active control device to a base-isolated structure, a higher level of performance can be achieved without a substantial increase in the cost. This thought has led to another type of hybrid control system, referred to as hybrid seismic isolation, consisting of active or semi-active devices introduced in base-isolated structures (see Fig. 9). Although base isolation has the ability to reduce interstory drifts and structural accelerations, it increases base displacement, hence the need for an active or semi-active device. In addition, a semi-active friction-controllable fluid bearing has been employed in parallel with a seismic isolation system (Feng and Shinozuka 1992; Sriram et al. 2003).

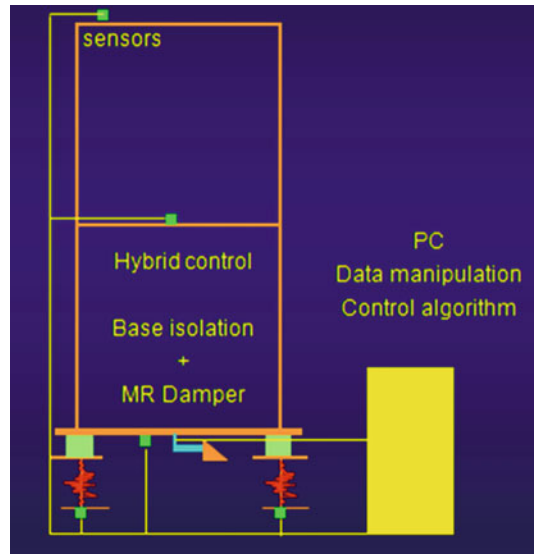

Actively and Semi-actively Controlled Structures Under Seismic Actions: Modeling and Analysis, Fig. 9 Hybrid control system

Hybrid control strategy, HMD, was first implemented in 1993, in the Ando Nishikicho Building in Tokyo, Japan. During strong winds or moderate earthquakes, when the structure's first mode of vibration can be considered dominant, the control system will simply act as a passive device. However, in the case of a stronger earthquake, where the ground excitation is spread over a wider frequency band and the first mode of vibration may no longer be dominant, the actuator is activated to compensate the response due to higher modes.

A combination of passive and active control systems has been applied to USC University Hospital and includes five of the six buildings of the medical center. Both linear and high damping rubber bearings were chosen for the base isolation, to provide lateral stiffness,

which controls natural vibration period and hysteretic damping. Active control is accomplished by the placement of viscous damping devices at the base of the structure to provide velocity-dependent damping, which controls the overall building displacements.

Structures equipped with hybrid mass dampers are the Kansai International Airport in Osaka, Japan; the Mitsubishi Heavy Industry in Yokohama, Japan; and the RIHGA Royal Hotel in Hiroshima, Japan. An interesting device can be found in the Shinjuku Park Tower consisting of a V-shaped HMD developed by the Ishikawajima-Harima Heavy Industries. This device has an easily adjustable fundamental period.

An application of hybrid control carried out by Lin et al. (2007) included a series of large-scale experimental tests conducted on a mass equipped with a hybrid controlled base isolation system, consisting of a rolling pendulum system (RPS) and a 20-KN magnetorheological (MR) damper. The 12-t mass and its hybrid isolation system were subjected to various intensities of near-fault and far-fault earthquakes on a large shake table. The results showed that a combination of rolling pendulum system and an adjustable MR damper can provide robust vibration control for large civil engineering structures that need protection from a wide range of seismic events.

A benchmark smart base-isolated eight-story building structure has been presented by Narasimhan et al. (2003), similar to existing buildings in Los Angeles, California. The base isolation system includes both linear and nonlinear bearings and control devices. Design and implementation of active semi-active and hybrid systems can also be found in the work of (Chu et al. 2005; Yi et al. 2001).

Modeling

Continuous and Discrete Control

The equation of motion of a controlled structural system with n degrees of freedom u_i, subjected to an earthquake excitation a_g, is given by Eq. 1:

$$\mathbf{M}\ddot{\mathbf{U}}(t) + \mathbf{C}\dot{\mathbf{U}}(t) + \mathbf{K}\mathbf{U}(t) = -\mathbf{M}\mathbf{E}a_g(t) + \mathbf{E}_f\mathbf{F}(t) \tag{1}$$

where **M**, **C**, **K** denote the mass, damping, and stiffness matrixes of the structure, respectively, **E**, $\mathbf{E}_f$ are the location matrix for the earthquake and the control forces on the structure, and **F**(t) is the control force matrix which is applied to the structure.

In the state space approach, Eq. 1 can be written as follows:

$$\begin{aligned}\dot{\mathbf{X}}(t) &= \mathbf{A}\mathbf{X}(t) + \mathbf{B}_g a_g(t) + \mathbf{B}_f\mathbf{F}(t)\\ \mathbf{Y}(t) &= \mathbf{C}\mathbf{X}(t) + \mathbf{D}\mathbf{F}(t) + \mathbf{v}\end{aligned} \tag{2}$$

The matrixes **X**, **A**, $\mathbf{B}_g$, $\mathbf{B}_f$ are given by

$$\mathbf{X} = \begin{bmatrix}\mathbf{U}\\ \dot{\mathbf{U}}\end{bmatrix}_{2n\times 1}, \mathbf{A} = \begin{bmatrix}\mathbf{O} & \mathbf{I}\\ -\mathbf{M}^{-1}\mathbf{K} & -\mathbf{M}^{-1}\mathbf{C}\end{bmatrix}_{2n\times 2n},$$
$$\mathbf{B}_g = \begin{bmatrix}\mathbf{O}\\ -\mathbf{E}\end{bmatrix}_{2n\times 1}, \mathbf{B}_f = \begin{bmatrix}\mathbf{O}\\ \mathbf{M}^{-1}\mathbf{E}_f\end{bmatrix}_{2n\times 1} \tag{3}$$

The matrixes **Y**, **C**, **D**, and **v** are the output states, the output matrix, the feed forward control force matrix, and the noise matrix, respectively. In the case where the output variables are the same with the states of the system and there is no application of the control forces to the output variables, the matrixes **C**, **D** are the identity and zero matrix, respectively. The noise matrix depends on the sensor that is used to measure the response of the system. The above equation can be solved by any numerical technique for differential equations, like an explicit Runge–Kutta formula, the Dormand–Prince pair, Bogacki–Shampine, and Adams–Bashforth–Moulton PECE solver.

The continuous solution of Eq. 3 is

$$\mathbf{x}(t) = \mathbf{e}^{\mathbf{A}(t-t_O)}\mathbf{x}_O + \int_{t_o}^{t} \mathbf{e}^{\mathbf{A}(t-\tau)}\left(\mathbf{B}_F\mathbf{F}(\tau) + \mathbf{B}_g a_g(\tau) + \mathbf{B}_p\mathbf{p}(\tau)\right)\mathbf{d}\tau \tag{4}$$

Equation 4 is applied assuming that the displacement or velocity and control force are continuous

functions of time. This does not apply to a real control situation, where the control force is calculated by observed values of displacement, velocity, or acceleration at discrete time intervals. For discrete description, the total time is divided into small intervals t_0-t_1, t_1-t_2, ... t_n-t_f, with time interval Δt.

An approximate solution of Eq. 3 between two points of time t_j and $t_{j+1} = t_j + \Delta t$ is obtained making the following substitutions in the above continuous solution Eq. 4 and editing the exponential integral:

$$\begin{aligned} &t = t_{j+1} \;\; t_o = t_j \\ &\mathbf{X}(t_j) = \mathbf{X}_j \;\; \mathbf{F}(\tau) = \mathbf{F}(t_j) = \mathbf{F}_j \\ &p(\tau) = p(t_j) = p_j \;\; a_g(\tau) = a_g(t_j) = a_{g_j} \end{aligned} \tag{5}$$

$$\mathbf{X}_{j+1} = e^{\mathbf{A}\Delta t}\mathbf{X}_j + \mathbf{A}^{-1}\left(e^{\mathbf{A}\Delta t} - \mathbf{I}\right)\left[\mathbf{B}_F\mathbf{F}_j + \mathbf{B}_g\mathbf{a}_{g,j} + \mathbf{B}_p\mathbf{p}_j\right] \tag{6}$$

The above equation provides an estimate of the response at time t_{j+1} based on values of the response at previous time t_j. The first term in the right-hand side represents the free oscillation response (transient state), while the other terms provide the response to load during time Δt (steady state). The above approach can be applied to adaptive systems (term in civil structures: material nonlinearity), wherein the stiffness and damping constants vary with time, while the mass is maintained constant. In that case matrix $\mathbf{A}$ is altered over time but remains constant during the interval Δt. In this case Eq. 6 becomes

$$\mathbf{X}_{j+1} = e^{\mathbf{A}_j\Delta t}\mathbf{X}_j + \mathbf{A}_j^{-1}\left(e^{\mathbf{A}_j\Delta t} - \mathbf{I}\right)\left[\mathbf{B}_F\mathbf{F}_j + \mathbf{B}_g\mathbf{a}_{g,j} + \mathbf{B}_p\mathbf{p}_j\right] \tag{7}$$

where

$$k(t) = k(t_j) = k_j \;\; \mathbf{A}(t) = \mathbf{A}(t_j) = \mathbf{A}_j \;\; c(t) = c(t_j) = c_j \tag{8}$$

The feedback control force in discrete form is

$$\begin{aligned} \mathbf{F}_j &= -\mathbf{K}_{f,j}\mathbf{X}_j,\ t_j \le t \le t_{j+1} \\ \mathbf{K}_{f,j} &= \left[k_d(t_j)\, k_v(t_j)\right] \end{aligned} \tag{9}$$

Replacing into Eq. 7 yields

$$\begin{aligned} \mathbf{X}_{j+1} = &\left(e^{\mathbf{A}_j\Delta t} - \mathbf{A}_j^{-1}\left(e^{\mathbf{A}_j\Delta t} - \mathbf{I}\right)\mathbf{B}_F\mathbf{K}_f\right)\mathbf{X}_j \\ &+ \mathbf{A}_j^{-1}\left(e^{\mathbf{A}_j\Delta t} - \mathbf{I}\right)\left[\mathbf{B}_g a_{g,j} + \mathbf{B}_p p_j\right] \end{aligned} \tag{10}$$

The output response is obtained by starting from time t_o, when the response is known, and calculating subsequent time points. The critical issue here is the determination of time Δt and the distribution of stiffness and feedback parameters k_v and k_d.

Linear and Nonlinear Control

In Eq. 1, the change of the material properties change during loading leads to changes in the stiffness matrix. Then, the differential equations become nonlinear:

$$\mathbf{M}\ddot{\mathbf{U}}(t) + \mathbf{C}\dot{\mathbf{U}}(t) + \mathbf{F}_s(\mathbf{U}(t)) = -\mathbf{M}\mathbf{E}a_g(t) + \mathbf{E}_f \mathrm{satF}(t - t_d) \tag{11}$$

In this case the nonlinearity originates from the structure and is described as material nonlinearity.

When the equation of motion is formulated in the deformed configuration to account for the structure's flexibility and associated large displacements, then equation of motion (1) also becomes nonlinear; the nonlinearity also originates from the structure, but now it is described as geometric nonlinearity.

When the control force, $\mathbf{F}$, is a linear function of the response of the structure, then the above equations of motion (1) are linear differential equations, and the control is said to be linear. When the control force is not a linear function, then Eq. 1 are nonlinear differential equations, and the nonlinearity originates from the control force.

Thus, the source of nonlinearity could be either from the structure or from the control force. In Table 1 below, the possible cases are presented.

Practical Considerations

Over the past few decades, various control algorithms and control devices have been developed, modified, and investigated by various groups of researchers. Several well-established algorithms

Actively and Semi-actively Controlled Structures Under Seismic Actions: Modeling and Analysis, Table 1 Linear and nonlinear cases of analysis

	Structure		
Control force	Linear	Nonlinear	
		Material	Geometric
Linear	Linear structure, linear control	Nonlinear structure, linear control	Nonlinear structure, linear control
Nonlinear	Linear structure, nonlinear control	Nonlinear structure, nonlinear control	Nonlinear structure, nonlinear control

in control engineering have been introduced to control structures. While many of these structural control strategies have been successfully applied, technological problems and challenges relating to time delay, saturation capacity effects, cost, reliance on external power, and mechanical complexity and reliability during the life of the structure have delayed their widespread use, and relatively few actual structures are equipped with control systems.

Another practical issue that influences the effectiveness and the reliability of the proposed control algorithms is the effect of the position of control forces. The selection of locations of control forces influences the location matrix, $\mathbf{B}_f$ of the control force in the differential equation of motion of controlled structure. Thus, this effect can be investigated numerically by parametric variation of the location matrix.

Other practical effects include control–structure interaction, actuator dynamics, and digital control implementation. The reliability of applied semi-active structural control systems and practical applications and verification for active and semi-active vibration control of buildings in Japan have been studied by Ikeda (2009).

Time Delay–Saturation Capacity

Two practical issues that influence the effectiveness and the reliability of the proposed control algorithms are time delay and saturation of the control force. Those parameters come into consideration by solving the differential equation of motion as a delay differential equation with saturation effects. The expected negative influence of those parameters should be considered in the design process. Thus, there is a need to take them into account in the numerical simulations before the installation of the control system on the real building.

The equation of motion (1) of a controlled structural system considering time delay and saturation becomes

$$\mathbf{M}\ddot{\mathbf{U}}(t)+\mathbf{C}\dot{\mathbf{U}}(t)+\mathbf{K}\mathbf{U}(t)=-\mathbf{M}\mathbf{E}a_g(t)+\mathbf{E}_f sat\mathbf{F}(t-t_d) \tag{12}$$

$sat\mathbf{F}$ is the saturated control force matrix which is applied to the structure with time delay t_d and is given as

$$sat\mathbf{F}(t-t_d)=\begin{cases}\mathbf{F}(t-t_d) & \mathbf{F}(t-t_d)<\mathbf{F}_{allowable}\\ \mathbf{F}_{allowable} & \mathbf{F}(t-t_d)>\mathbf{F}_{allowable}\end{cases} \tag{13}$$

$\mathbf{F}_{allowable}$ is the maximum capacity of the control device. In the state space approach, Eq. 12 can be written as follows:

$$\begin{aligned}\dot{\mathbf{X}}(t)&=\mathbf{A}\mathbf{X}(t)+\mathbf{B}_g a_g(t)+\mathbf{B}_f satF(t_d-t)\\ \mathbf{Y}(t)&=\mathbf{C}\mathbf{X}(t)+\mathbf{D}\mathbf{F}(t_d-t)+\mathbf{v}\end{aligned} \tag{14}$$

This equation can be solved by the technique of delay differential equation, or one can use the following transformation

$$\mathbf{Z}(t)=\mathbf{X}(t)+\int e^{-\mathbf{A}(\eta+t_d)}\mathbf{B}_f\mathbf{F}(t+\eta)d\eta \tag{15}$$

Then:

$$\begin{aligned}\dot{\mathbf{Z}}(t)&=\mathbf{A}\mathbf{Z}(t)+\mathbf{B}_g a_g(t)+\mathbf{B}(\mathbf{A})\mathbf{F}(t)\\ \mathbf{B}(\mathbf{A})&=e^{-\mathbf{A}t_d}\mathbf{B}_f\end{aligned} \tag{16}$$

Since the entire control process involves measuring response data, computing control forces through an appropriate algorithm, transmitting data and signals to actuators, and activating the actuators to a specified level of force, time delays

arise and cannot be avoided. The problem of time delay in the active control of structural systems has been investigated from many scientists and engineers. The stability of the structure could be lost due to time delay, and two ways of time-delay compensation can be followed. In the first the gain matrix is redesigned considering the presence of time delay, while in the second low-pass filters are used to filter the velocity measurements from the frequency components of the high-order modes. In the first case, the structure could remain unstable when using control moments as control actions, while in the second a number of vibration modes can be controlled and compensated for time delay, but the higher-order modes remain uncontrolled. Time delay can be compensated with Pade approximations. The allowable time delay is related with natural period and feedback gain. The maximum allowable time delay is decreased with decrease in natural period of the structure, as well as with increase in active damping. Under earthquake excitations, simulation results for the response of multi-degree of freedom structures indicated that the degradation of the control performance due to fixed time delay is significant when time delay is close to a critical value. The time-delay problem is more serious for structures with closely spaced vibration modes.

In optimal control of linear systems, time delay is considered at the very beginning of the control design, and no approximations and estimations are made in the control system. Thus, the system performance and stability can be guaranteed. Instability in the response might occur only if a system with time delay is controlled by an optimal controller that was designed with no consideration of time delay.

For pole assignment algorithm, through varied location of the controlled poles, the control system shows variable performance. However, the locations of the controlled pole pairs should be carefully specified and checked according to the characteristics of the system. Analytical expressions of limiting values of time delay for single degree of freedom systems were derived by Connor (2003); however, such expressions were very difficult to obtain for multi-degree of freedom systems. Casciati et al. (2006) have taken into consideration the time-delay effect solving numerically delayed differential equations. All of these studies demonstrate how important the issue of time delay is in structural control and how it may result in a degradation of the control performance and may even drive the controlled structure to become unstable. Most studies show that time delays influence negatively the control system; therefore, they should be kept small compared to the fundamental period of vibration of the system and should, if possible, be eliminated.

The second important practical problem is the saturation of the control force. Actuator saturation occurs when the force which is given by the control algorithm is larger than its designed peak capacity. Failure to account for this nonlinear effect can decrease the efficiency of the control system and possibly drive the structure to become unstable. Most control algorithms are linear, assuming that there is no limit in the magnitude of the control force. However, maximum capacity of the control devices is limited. Therefore, designing controllers to account for the bounded nature of the devices is desirable.

The two issues of time delay and saturation of the control device are, in most cases, considered and studied separately. However, in the application of real control systems, these two issues act simultaneously. Pnevmatikos and Gantes (2011) investigated a combined effect of the nonlinear phenomena of bounded capacity of the actuators and time delay of the system, acting simultaneously during the control process, on the systems response. They proposed limits for pair of time delay and saturation capacity that can be used in the design process of controlled structures.

Spillover Effect

With the discretization of a continuous system to a finite degree of freedom system, some information is lost since a real physical system has infinite natural mode shapes and frequencies, while the discrete systems contain some of them. Those frequencies that are not included in the discrete model are called remaining frequencies or

residual modes. If flexible structure is modeled, there is a danger that the control based on a reduced model is destabilized due to the high remaining modes which are not included in the model. Balas (1978) defined and studied the above phenomenon, which is called spillover effect. Meirovich (1990) investigated observation spillover (measurements at some points, without having the total picture of the response) and stated that this can be really dangerous for the controlled structures.

Controllability: Observability

Controllability of system deals with the number of control positions and degrees of freedom of the structure. When the number of control positions is equal to the number of degrees of freedom of the structure, then full control of the system is achieved. In that case, the building performs a rigid body motion, following the imposed ground motion, without relative displacements between the floors. It was also shown that with reduced number of control forces, positioned at appropriate locations, which is a more realistic choice for real buildings, the response can be reduced to a satisfactory level. Observability is associated with measurement positions in the structure to degrees of freedom of the structure. When the measurement positions are equal to the number of degrees of freedom of the structure, then full-state feedback is achieved. Otherwise, feedback with an observer is performed.

Collocated and Not Collocated Control/ Centralized and Decentralized Control

A definition of collocation and centralization is given by Casciati et al. (2006). A control system is collocated when the force generated by an actuator at a point of the structure is measured by a force sensor at the same location, in other words when the actuator and sensor are connected exactly at the same location. Otherwise, control is non-collocated.

A control system is centralized if it is managed by a unique computer that receives the inputs from all sensors and gives the command output to all actuators. The system is decentralized (noncentralized) if the control system is managed by several computers that take the input from some specific sensors and give the command output to some actuators. It is thus possible that a noncentralized system could be collocated or that a centralized system could be non-collocated.

Analysis

Control Strategies and Algorithms

Several well-established algorithms in control engineering have been introduced to control structures, such as optimal control, LQR or LQG, pole assignment, sliding mode control, H_2 and H_∞, fuzzy control, and many others. The most suitable algorithms for structural application and the practical considerations that should be taken into account are described by Soong (1990) and Casciati et al. (2006).

Optimal Control, LQR, or LQG

Research in structural control has focused on a variety of control algorithms based on different control design criteria. Some algorithms originate from direct applications of optimal control theory. Some others, however, are specifically proposed for civil engineering structural control applications.

The control force, $\mathbf{F}$, can be applied directly or indirectly to the structure. The way in which the control force is calculated is determined from the control algorithm that is used. If the control force is calculated by linear state feedback:

$$\mathbf{F} = -\mathbf{G}_1\mathbf{U} - \mathbf{G}_2\dot{\mathbf{U}} = -[\mathbf{G}_1\,\mathbf{G}_2]\begin{bmatrix}\mathbf{U}\\ \dot{\mathbf{U}}\end{bmatrix} = -\mathbf{G}\mathbf{X} \tag{17}$$

$\mathbf{G}$ is the gain matrix, which is calculated according to the desired poles of the controlled system. Replacing the force $\mathbf{F}$ into Eq. 1 or 2, the controlled system can be described by

$$\begin{aligned}\mathbf{M}\ddot{\mathbf{U}}(t) + (\mathbf{E}_f\mathbf{G}_2 + \mathbf{C})\dot{\mathbf{U}}(t)\\ + (\mathbf{E}_f\mathbf{G}_1 + \mathbf{K})\mathbf{U}(t) = -\mathbf{M}\mathbf{E}a_g(t)\end{aligned} \tag{18}$$

$$\dot{\mathbf{X}} = (\mathbf{A} - \mathbf{B}_f\mathbf{G})\mathbf{X} + \mathbf{B}_g a_g \tag{19}$$

$$\mathbf{X}(t_o) = \mathbf{X}(0) = \mathbf{X}_o$$

From the above equation, it is seen that control of structures can be achieved by changing the stiffness or damping and consequently the dynamic characteristics of the building in a direct or indirect way, depending on the device that is used. The question is how to estimate the control force or the matrix **G** in such a way that the desired dynamic characteristics for the controlled building are achieved.

The feedback matrix can be calculated based on optimal control theory like linear quadratic regulator, LQG. Optimal control methods are based on the concept of minimizing a cost criterion. The criterion of cost, represented by J, has a common format:

$$J = \lim_{T->\infty} \frac{1}{T}\int_{t_0}^{t_f} e^T(t)e(t)dt \tag{20}$$

where

$$\mathbf{e}(t) = \mathbf{X}(t) - \mathbf{X}^*(t) \tag{21}$$

e(t) is the error between the desired behavior, $\mathbf{X}^*$, and the actual behavior, **X**, of the system.

The scope of the problem of optimal control is to determine a control force, **F**(t), such that it determines the behavior of the control system to minimize some cost criterion while satisfying some physical constraints of the system. The cost criterion is usually formulated so as to express a quantity to have physical significance, e.g., displacement and energy. A specialized form of cost criterion of Eq. 20 is as follows:

$$J = \theta[\mathbf{X}(t), t]|_{t=t_o}^{t=t_f} + \int_{t_o}^{t_f} \phi[\mathbf{X}(t),\ \mathbf{F}(t)]dt \tag{22}$$

The first term refers to the cost to the ends of the interval or to the boundary condition, while the second term refers to the cost to the entire space. Depending on the requirements of the problem, functions $\theta(X(t), t)$, $f(X(t), F(t))$ are taking specific forms. One of the most common forms of criterion J, which minimizes the energy of the system, is

$$J = \mathbf{X}(t_f)^T\mathbf{S}\mathbf{X}(t_f) + \int_{t_o}^{t_f}\Big[\mathbf{X}(t_f)^T\mathbf{Q}(t)\mathbf{X}(t) + \mathbf{F}^T(t)\mathbf{R}(t)\mathbf{F}(t)\Big]dt \tag{23}$$

The weighted matrixes **S**, **Q**(t), and **R**(t) are selected according to the importance one wants to give to the error vector, **e**(t), or to the excitation vector **F**(t). The selection of suitable **S**, **Q**(t), and **R**(t) for a particular problem is usually a difficult issue that requires experience and engineering insight.

The minimization of the cost criterion can be accomplished using the maximum principle introduced by Pontryagin and the principle of optimality introduced by Bellman. The procedure results in a system of differential equations as follows:

$$\begin{aligned}&\dot{\mathbf{P}}(t) + \mathbf{P}(t)\mathbf{A}(t) + \mathbf{A}^T(t)\mathbf{P}(t) - \mathbf{P}(t)\mathbf{B}(t)\mathbf{R}^{-1}(t)\mathbf{B}^T(t)\\ &\mathbf{P}(t) = -\mathbf{C}^T(t)\mathbf{Q}(t)\mathbf{C}(t)\\ &\mathbf{P}(t_f) = -\mathbf{C}^T(t_f)\mathbf{Q}(t_f)\mathbf{C}(t_f)\end{aligned} \tag{24}$$

$$\begin{aligned}&\dot{\boldsymbol{\mu}}(t) + \big[\mathbf{A}(t) - \mathbf{B}(t)\mathbf{R}^{-1}(t)\mathbf{B}^T(t)\mathbf{P}(t)\big]^T\\ &\boldsymbol{\mu}(t) = -\mathbf{C}^T(t)\mathbf{Q}(t)\mathbf{X}^*(t)\\ &\boldsymbol{\mu}(t_f) = -\mathbf{C}(t_f)\mathbf{Q}(t)\mathbf{X}^*(t_f)\end{aligned} \tag{25}$$

Solving the above differential equations, **P**(t) and **μ**(t) are computed, and then from Eq. 26, the feedback matrix **K**(t) and the control force **F**(t) are calculated. Equation 24 is called Riccati equation:

$$\begin{aligned}&\mathbf{f}(t) = \mathbf{K}(t)\mathbf{X}(t) + \boldsymbol{\rho}(t)\\ &\mathbf{K}(t) = -\ddot{\mathbf{R}}^{-1}(t)\mathbf{B}^T(t)\mathbf{P}(t),\ \boldsymbol{\rho}(t) = \ddot{\mathbf{R}}^{-1}(t)\mathbf{B}^T(t)\boldsymbol{\mu}(t)\end{aligned} \tag{26}$$

The above control law is under the assumption that all states are available and measurable.

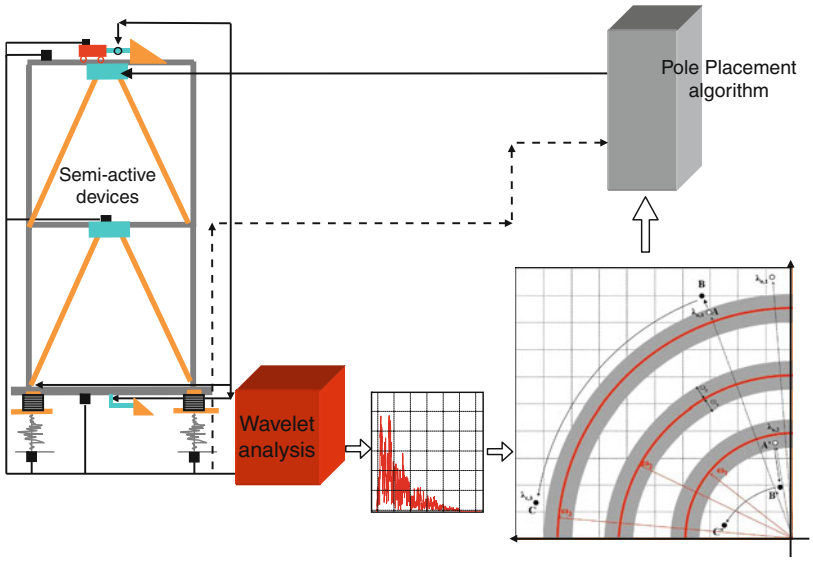

Actively and Semi-actively Controlled Structures Under Seismic Actions: Modeling and Analysis, Fig. 10 The general flowchart of the pole placement control strategy

In civil structures it is unrealistic to expect that the state vector can be fully measured. The case that a few degrees of freedom are measured and used for the calculation of the control force is called output control, in contrast to the full-state control where all degrees of freedom of the system are measured. Suitable control design techniques, like observers with linear quadratic Gaussian (LQG) control, have been developed for output feedback and random disturbances. Many researchers have studied and applied optimal control in civil structures (Abdel-Rohman and Leipholz 1983; Chang and Soong 1980; Yang 1975). An evolutionary control of damaged systems using a rehabilitative, modified LQR algorithm has been proposed by Attard and Dansby (2008).

Pole Placement Algorithm

It should be note that, if the external excitation is ignored or set to zero in the derivation of the Riccati equation, the provided control law is not optimal. In order to include the excitation in the Riccati equation, a priori knowledge of the loading history is required. This is generally not possible for excitations such as earthquakes, wind, or waves, which are common in structural engineering applications.

A control algorithm which addresses this difficulty is pole assignment (pole placement) algorithm. Pole placement algorithms have been studied extensively in the general control literature, while its applications in structural control have been investigated by Martin and soong (1976), Leonard (1990), Soong (1990), Utku (1998), and Preumont (2002).

A procedure of on-line selection of poles in such a way that first resonance is avoided and secondly sufficient equivalent damping is added, based on the specific characteristics of the incoming dynamic earthquake excitation, have been proposed by Pnevmatikos and Gantes (2010a). This procedure drives the poles to their optimum location and does not need the poles to be predefined and constant during the application of dynamic loading. Numerical simulations show that sufficient reduction of the response, in terms of both displacement and acceleration, can be achieved for all examined earthquakes with reasonable amount of required equivalent control force. The procedure is shown schematically in Fig. 10. The effectiveness to the response of the structure of the control strategy is shown in Fig. 11. It is shown that both the displacement and the acceleration are reduced one order of magnitude.

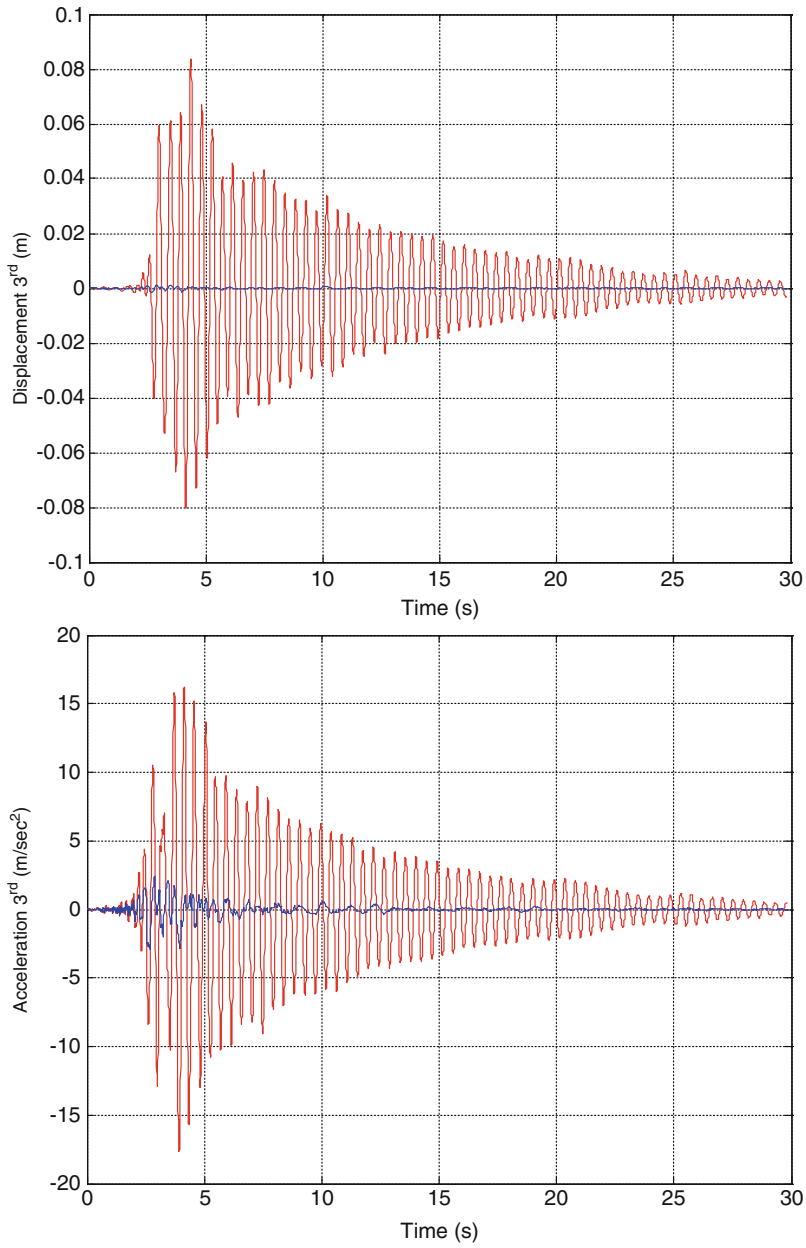

Actively and Semi-actively Controlled Structures Under Seismic Actions: Modeling and Analysis, Fig. 11 Displacement and acceleration of the controlled (*blue line*) and uncontrolled (*red line*) system for the third floor of the three-story building subjected to earthquake

H_2/H_∞ Control Algorithm

The objective of the $\mathbf{H}_2$ or $\mathbf{H}_\infty$ control algorithms is to design a controller $\mathbf{K}$ that minimizes the $\mathbf{H}_2$ or $\mathbf{H}_\infty$ norm of the closed-loop transfer function matrix, $\mathbf{H}$, from the disturbance to the output vector. By definition, the $\mathbf{H}_2$ norm of a stable transfer function matrix is

$$||\boldsymbol{H}||_2 = \sqrt{trace\left\{\frac{1}{2\pi}\int_{-\infty}^{\infty}\mathbf{H}(j\omega)\mathbf{H}^*(j\omega)d\omega\right\}} \quad (27)$$

More details regarding the use of control H_2 and LQR methods for civil engineering applications can be found in Zacharenakis et al. (2001).

Sliding Mode Control

Sliding mode control or variable structure strategies were developed specifically for robust control of uncertain nonlinear systems. The fundamental idea of SMC is to design a controller to drive the state trajectory on the sliding surface (or switching surface), whereas the motion on the sliding surface is stable, remains there all the subsequent time, and moves toward the equilibrium position. The first step in SMC is to design the sliding surface on which the response is stable, while the second step is the determination of the control demand which will drive the response trajectory into the sliding surface and force it to stay there all the subsequent time. In most studies the sliding surface, **s**, is defined as a linear combination of the state vector:

$$\mathbf{s} = \dot{\overline{\mathbf{U}}} + \boldsymbol{\lambda}\overline{\mathbf{U}} = [\boldsymbol{\lambda}\ \mathbf{I}]\begin{bmatrix}\overline{\mathbf{U}} \\ \dot{\overline{\mathbf{U}}}\end{bmatrix} = \mathbf{PX} \tag{28}$$

In the work of Slotin and Li (1991), a more general approach is proposed. The sliding surface can be obtained using optimal control theory. In the work of Pnevmatikos and Gantes (2009), the sliding surface, **s**, is defined by pole assignment method, where the selection of the poles of the controlled system is based on the frequency content of the incoming earthquake signal.

Following the design of the sliding surface, the control force which will drive the response trajectory into this surface and force it to stay there is calculated using Lyapunov stability theory. To achieve this goal, first, a Lyapunov function is chosen, and then, under the condition that the derivative of the function **V** is negative, the control force is obtained. The control forces F are given by

$$\mathbf{F} = \mathbf{G} - \boldsymbol{\delta} \times \boldsymbol{\lambda}^{\mathsf{T}}, \mathbf{G} = -(\mathbf{PB}_{\mathrm{f}})^{-1}\mathrm{P}\left(\mathbf{AX} + \mathbf{B}_{\mathrm{g}}\mathbf{a}_{\mathrm{g}}\right),$$
$$\boldsymbol{\lambda} = \mathbf{s}^{\mathsf{T}}\mathbf{PB}_{\mathrm{f}} \tag{29}$$

Matrix **G** includes the restoring, damping, inertial, and seismic forces. The magnitude of **G** is very large for controlling conventional civil engineering structures. Thus, the control force should be restricted to a certain level, and a saturated controller should be considered in the design of SMC. In this case, full compensation of the response cannot be achieved. If the maximum control force is bounded by $\pm\ \mathbf{f}_{\max}$, the control force is estimated as follows:

$$\mathbf{F} = \begin{cases} \mathbf{G} - \boldsymbol{\delta} \times \boldsymbol{\lambda}^{\mathsf{T}}, \text{ if } \left|\mathbf{G} - \boldsymbol{\delta} \times \boldsymbol{\lambda}^{\mathsf{T}}\right| \le \mathbf{f}_{\max} \\ \mathbf{f}_{\max} sign\left(\mathbf{G} - \boldsymbol{\delta} \times \boldsymbol{\lambda}^{\mathsf{T}}\right), \text{otherwise} \end{cases} \tag{30}$$

The force $\mathbf{f}_{\max}$ is specified by the device capacity.

Active Variable Stiffness Control Algorithm

Variable stiffness control has been developed by Kobori and verified experimentally at Kajima Research Institute in Japan, in 1993. The control algorithm is based on the nonresonant state under seismic excitation by altering the stiffness and thus natural frequencies, of a building, based on the nature of the earthquake. Nagarajaiah et al. (1998) developed a semi-active instantaneously variable stiffness (SAIVS) system which varies the structural stiffness continuously and smoothly so as to maintain a nonresonant state. Yang et al. (2000) have developed a resetting semi-active stiffness device (RSASD) and suitable algorithm to regulate RSASD at appropriate time instants.

In Pnevmatikos et al. (2004, 2010a), a control algorithm based on the frequency content of the incoming earthquake is described, suitable for application in active variable stiffness systems installed in buildings designed against seismic actions. The control strategy consists of two stages: (i) the design stage, where the bracing system is designed based on the frequency content of a range of earthquakes, and (ii) the operation phase, where the control algorithm uses the dynamic characteristics of the measured on-line excitation signal, in order to take an appropriate decision regarding the function of the variable stiffness device. Based on the frequency content

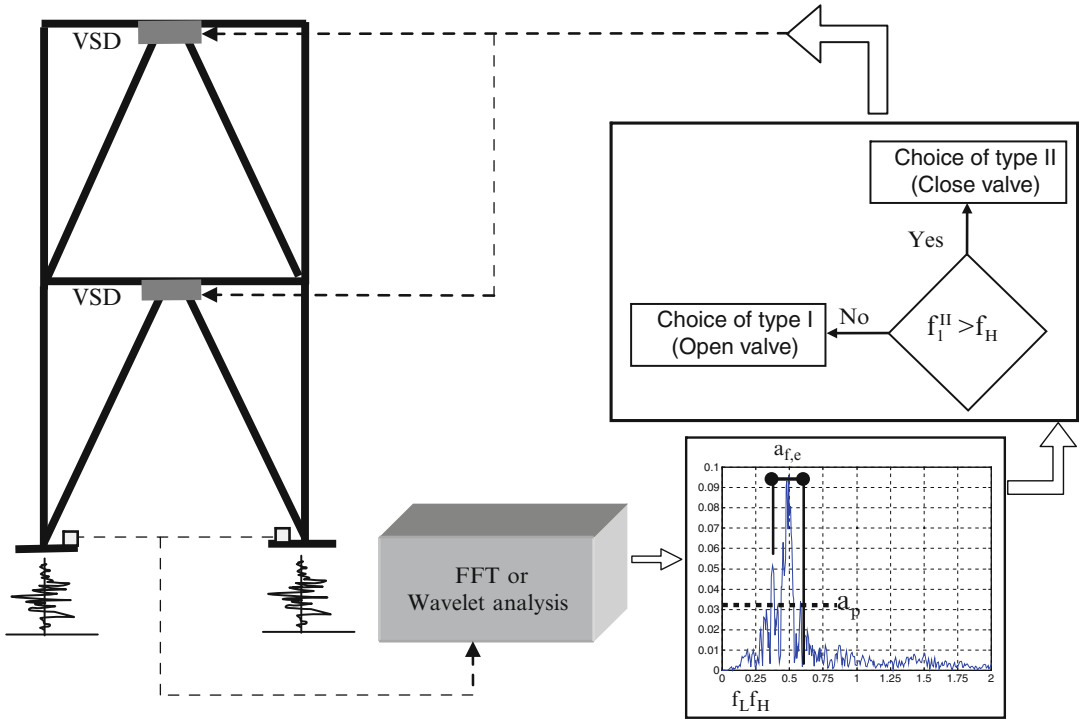

Actively and Semi-actively Controlled Structures Under Seismic Actions: Modeling and Analysis, Fig. 12 The integrated control strategy for buildings equipped with active variable stiffness systems and subjected to earthquake actions

of the incoming signal, the variable stiffness device, by connecting or disconnecting the bracing system, alters the stiffness of the structure and consequently changes its dynamic characteristics in real time, avoiding resonance between the controlled structure and the applied signal. Thus, the structural safety and serviceability against extreme dynamic excitation are enhanced. The general scheme of the proposed algorithm is shown in Fig. 12.

Fuzzy Logic Control

A very useful application of fuzzy logic in civil engineering is fuzzy control. Fuzzy logic, introduced by Zadeh (1965), has to do with the way that the human brain deals with concepts such as uncertainty, vagueness, and imprecision. Boolean logic determines whether an argument definitely belongs or not to some set, while fuzzy logic considers the idea of partial truths, and determines the degree of membership of an argument to a fuzzy set.

Fuzzy control defines fuzzy rules to determine actions to be taken, based on the measured structure's responses. The advantages of fuzzy controller are simple algorithms, suitable for real-time control, no need for information on structural and vibration characteristics, and a robust system in terms of performance and implementation.

Fuzzy control uses experience instead of differential equations to determine desirable control actions. Fuzzy control consists of implementation of rules, in the format of IF...THEN statements, which relate the input variables to the control action. The process begins by first defining membership functions to classify the inputs and outputs using linguistic terms. In structural control applications, the inputs are usually a combination of structural responses: displacement, velocity, and acceleration. The input values are then converted to fuzzy values, using the membership functions. This step is referred to as fuzzification. The next step is

named decision making and consists of using predetermined rules to correlate the fuzzy inputs values to fuzzy outputs. Finally, in the last step, the fuzzy output values are defuzzified, that is, they are converted to values that can be used as control actions.

The rules and the membership functions are important to the effectiveness of the fuzzy controller. Several methods are available for the creation of such rules, including logical reasoning, experiments and simulations, and learning from examples. Fuzzy control rules can be created based on data obtained by an LQG controller. Genetic algorithms can be tuned to the membership functions in order to improve the results. Genetic algorithms can also be used to simultaneously determine the optimal rules and membership functions.

Fuzzy theory can be applied to determine the desired control force to be applied by the actuator. Neural network performance function selection can be used in structural control (Casciati et al. 1993).

Fuzzy logic has been used to vary the mechanical properties of the control device. It has been applied for the reduction of longitudinal bridge displacement due to earthquake or traffic loading with variable dampers or control of structural vibrations with hybrid systems composed of base isolation and semi-active dampers. Fuzzy control is also used to regulate a structure with an MR damper system (Choi Kang-Min et al. 2004, Zhou et al. 2003).

Clip Optimal Control

The clip optimal control has two parts: the first part consists of designing a control law assuming that an ideal device is installed to the building. In the second part, a controller is designed allowing the semi-active damper to develop the force that the control law calculated. In the first part, any control law can be chosen.

Clipped-optimal control strategy has been proposed by Dyke et al. (1996) to control a single MR damper. The control algorithm was extended to control multiple MR devices, and the performance of this algorithm has been experimentally verified.

In the clipped-optimal control algorithm, the control forces f_c is given by the following expression:

$$f_c = L^{-1}\left\{-K_c(s)L\left\{\begin{matrix} y_m \\ f_m \end{matrix}\right\}\right\} \tag{31}$$

where L{} is the Laplace transform, $K_c(s)$ is a linear optimal controller obtained from H_2 or LQG strategies because of the stochastic nature of earthquake ground motions (any other control law can also be chosen), y_m is the measured structural response vector, and f_m is the measured control force vector.

Because the force generated in the semi-active device is dependent on the local responses of the structural system, the desired optimal control force, f_c, cannot always be produced by the control device. Only the control voltage, v_i, can be directly controlled to increase or decrease the force produced by the device. Thus, a force feedback loop is incorporated to induce the semi-active device to generate approximately the desired optimal control force f_c. To clip the active control law to the semi-active one and to generate approximately the desired optimal control force, the command signal is selected as follows.

When the semi-active device is providing the desired optimal force $f_i = f_c$, the voltage applied to the damper should remain at the present level. If the magnitude of the force produced by the device f_i is smaller than the magnitude of the required target force f_c and the two forces have the same sign, the voltage applied to the current driver is increased to the maximum level so as to increase the force produced by the device to match the desired control force. Otherwise, the commanded voltage is set to zero.

The above procedure that regulates the applied voltage has the following mathematical expression:

$$v_i = V_{max}H((f_{ci} - f_i)f_i) \tag{32}$$

where V_{max} is the maximum voltage to the current driver and H( ) is the Heaviside step function

which is a discontinuous function whose value is zero for negative argument and one for positive argument.

In clipped-optimal control algorithm, the command voltage takes two values, either zero or the maximum value. In some situations when the dominant frequencies of the system under control are low, large changes in the forces applied to the structure may result in high local acceleration values. This behavior is dependent on the time lag in the generation of the control voltage. In Yoshida (2003), a modification to the original clipped-optimal control algorithm is proposed to reduce this effect. In the modified version of the control algorithm, the control voltage can be any value between 0 and V_{max}. The control voltage, v_{ci}, is determined using a linear relationship between the applied voltage and the maximum force of MR damper. The modified clipped-optimal control algorithm is given as

$$v_i = V_{ci} H((f_{ci} - f_i) f_i) \tag{33}$$

where

$$V_{ci} = \begin{cases} \mu f_{ci} & \text{for } f_{ci} \le f_{max} \\ V_{max} & \text{for } f_{ci} \le f_{max} \end{cases} \tag{34}$$

Skyhook/Ground Hook Control

On skyhook control, the damper is controlled by two damping values. The choice between high or low state is made using the following law: based on the product of the relative velocity u_{rel} across the damper and the absolute velocity of the system body mass attached to that damper, a damping value is chosen as follows:

$$\begin{aligned} \dot{z}_b \times v_{rel} \ge 0 \quad & c = \text{high state} \\ \dot{z}_b \times v_{rel} \le 0 \quad & c = \text{low state} \end{aligned} \tag{35}$$

The skyhook control is an on–off strategy. When the relative velocity of the damper is positive, the force of the damper acts to pull on the system body mass, while when the relative velocity of the damper is negative, the force of the damper pushes the body mass.

Since the damping values now are not limited to this state alone and can take any value within this state, a continuous version of skyhook control can be achieved. The choice of damping is now given as follows:

$$\begin{aligned} \dot{z}_b \times v_{rel} \ge 0 \quad & c = a \\ \dot{z}_b \times v_{rel} < 0 \quad & c = \text{low state} \end{aligned} \tag{36}$$

where

$$a = \max\{\textit{low state}, \min(g \times \dot{z}_b, \textit{high state})\} \tag{37}$$

In the case of ground hook control, the damper is adjusted to its high or low state depending on the product of the relative velocity across the damper and the absolute velocity of lower mass attached to that damper. Contrary to skyhook control, this control law is driving the lower vibration mass to a reduced vibration.

The mathematical expression of the ground hook control is as follows:

$$\begin{aligned} \dot{z}_t \times v_{rel} \le 0 \, c = \text{high state} \\ \dot{z}_t \times v_{rel} > 0 \, c = \text{low state} \end{aligned} \tag{38}$$

The continuous ground hook control strategy is similar to the sky hook control.

Summary

Representative control devices and their applications have been presented. Then, mathematical formulations and simulation of controlled structures have been illustrated. Control algorithms suitable for civil structure inspired by the classical control theory were presented. Optimal control, LQR, pole assignment, sliding mode control, H_2, fuzzy control, clipped-optimal control, and skyhook/ground hook control algorithms were briefly described. It was shown that with the help of modern technology, it is possible to control civil structures in order to protect them from earthquake excitations.

Cross-References

- ▶ Buildings and Bridges Equipped with Passive Dampers Under Seismic Actions: Modeling and Analysis
- ▶ Early Earthquake Warning (EEW) System: Overview
- ▶ Model Class Selection for Prediction Error Estimation
- ▶ Parametric Nonstationary Random Vibration Modeling with SHM Applications
- ▶ Passive Control Techniques for Retrofitting of Existing Structures
- ▶ Rubber Shock Absorbers as a Mitigation Technique for Earthquake-Induced Pounding
- ▶ Seismic Resilience
- ▶ Tuned Mass Dampers for Passive Control of Structures Under Earthquake Excitations

References

Abdel-Rohman M, Leipholz HH (1983) Active control of tall buildings. J Struct Div ASCE 109:628–645

Attard TL, Dansby RE (2008) Evolutionary control of damaged systems using a rehabilitative algorithm. In: Proceedings of tenth pan American congress of applied mechanics PACAM X. Grand Oasis Resort Cancun, Mexico, pp 166–169

Balas MJ (1978) Feedback control of flexible strucutres. IEEE Trans Autom Control AC-23 673–679

Błachowski BD (2007) Model based predictive control for guyed mast vibration. J Theoret Appl Mech 45(2):405–423

Carlson JD, Catanzarite DM, St Clair KA (1995) Commercial magneto-rheological fluid devices. In: Proceedings of the 5th international conference on ER fluids, MR fluids and associated technology. University of Sheffield, Sheffield

Casciati F, Faravelli L, Venini P (1993) A neural-network performance-function selection in active structural control. In: Proceedings of the international workshop on structural control. University of Southern California, Los Angeles

Casciati F, Magonette G, Marazzi F (2006) Technology of semiactive devices and applications in vibration mitigation. Wiley, Chichester. ISBN 978-0-470-02289-4

Chang J, Soong TT (1980) Structural control using active tuned mass dampers. J Eng Mech Div ASCE 106 (6):1091–1098

Choi KM, Cho SW, Jung HJ, Lee IW (2004). Semiactive fuzzy control for seismic response reduction using magnetorheological dampers. Earthq Eng Struct Dyn 33:723–736

Choi Kang-Min, Cho Sang-Won, Jung Hyung-Jo, Lee In-Won (2004) Semi-active fuzzy control for seismic response reduction using magnetorheological dampers. Earthquake Eng Struct Dyn 33:723–736

Chu SY, Soong TT, Reinhorn AM (2005) Active, hybrid, and semi-active structural control a design and implementation handbook. Wiley, United Kingdom

Connor JJ (2003) Introduction to structural motion control. In: Mit-prentice hall series on civil, environmental, and system. Prentice Hall, USA

Constantinou MC, Symans MD, Tsopelas P, Taylor DP (1993) Fluid viscous dampers in applications for seismic energy dissipation and seismic isolation. In: NIST workshop 1995. Proceedings of the ATC-17-1 seminar on seismic isolation, passive energy dissipation, and active control, San Francisco, 2 Mar 1993, pp 581–592

Constantinou MC, Symans MD, Tsopelas P, Taylor DP (1993) Fluid viscous dampers in application of seismic energy dissipation and seismic isolation. In: Proceedings of ATC-17-1 seminar of seismic isolation, passive energy dissipation, and active control, San Francisco, March 2, pp. 581–592

Dyke SJ, Spencer BF, Sain MK, Carlson JD (1996) Modeling and control of magnetorheological dampers for seismic response reduction. Smart Mater Struct 5:565–75

Ehrgott RC, Masri SF (1992) Modelling the oscillatory dynamic behavior of electrorheological materials in shear. Smart Mater Struct 1(4):275–285

Erhrogott RC, Marsi SF (1993) Structural control applications of an electrorheological device. In: Proceedings of the international workshop on structural control, Honolulu, pp 115–129

Feng MQ, Shinozuka M (1992) Experimental and analytical study of a hybrid isolation system using friction controllable sliding bearings. Report no 92-0009, National center for earthquake engineering Research, Buffalo

Housner G, Bergman L, Caughey T, Chassiakos A, Claus R, Masri S, Skelton R, Soong T, Spencer B, Yao J (1997) Structural control: past, present, and future. J Eng Mech 123(9):897–971

Ikeda Y (2009) Active and semi-active vibration control of buildings in Japan – practical applications and verification. Struct Control Health Monit 16(7–8):703–723

Kobori T, Koshika N, Yamada K, Ikeda Y (1991) Seismic -response-controlled structure with active mass driver system. Part 1: design. Earthquake Eng Struct Dyn 20:133–149

Kobori T, Takahashi M, Nasu T, Niwa N, Ogasawara K (1993) Seismic response controlled structure with active variable stiffness system. Earthquake Eng Struct Dyn 22:925–941

Leonard M (1990) Dynamics and control of structures. Wiley, USA

Lin C, Chen L, Chen C (2007) RCMAC Hybrid control for MIMO uncertain non linear system using sliding mode technology. IEEE Trans Neural Netw 18(3):708–720

Makris N, Hill D, Burton S, Jordan M (1995) Electrorheological fluid damper for seismic protection of structures. In: Proceedings of the smart structures and materials, San Diego, pp 184–194
Martin RC, Soong TT (1976) Modal control of multistory structures. ASCE J Eng Mech 102:613–623
Nagarajaiah S, Mate D (1998). Semi-active control of continuously variable stiffness system. In: Proceedings of the 2nd world conference on structural control, Kyoto, vol 1, pp 397–405
Narasimhan S, Nagarajaiah S, Johnson E, Gavin H (2003) Smart base isolated building benchmark problem. In: 16th ASCE engineering mechanics conference, 16–18 July 2003. University of Washington, Seattle
Ohrui S, Kobori T, Sakamoto M, Koshika N, Nishimura I, Sasaki K, Kondo A, Fukushima I (1994) Development of active-passive composite tuned mass damper and an application to the high rise building. In: Proceedings of the first world conference on structural control, Pasadena, California, pp 100–109
Pnevmatikos N, Gantes C (2009) Sliding mode control for structures based on the frequency content of the earthquake loading. Smart Struct Syst 5(3):209–221
Pnevmatikos N, Gantes C (2010a) Control strategy for mitigating the response of structures subjected to earthquake actions. Eng Struct 32:3616–3628
Pnevmatikos NG, Gantes JC (2010b) Design and control algorithm for structures equipped with active variable stiffness devices. J Struct Control Health Monit 17(6):591–613
Pnevmatikos N, Gantes C (2011) Influence of time delay and saturation capacity to the response of controlled structures under earthquake excitations. Smart Struct Syst Int J 8(5):449–470
Pnevmatikos NG, Kallivokas LF, Gantes CJ (2004) Feedforward control of active variable stiffness systems for mitigating seismic hazard in structures. Eng Struct 26:471–483
Preumont A (2002) Vibration control of active structures, an introduction, 2nd edn. Kluwer, The Netherlands
Reinhorn AM, Soong TT, Lin RC, Wang YP, Fukao Y, Abe H, Nakai M (1989) 1:4 scale model studies of active tendon systems and active mass dampers for aseismic protection, technical report NCEER-89-0026
Slotin JJ, Li W (1991) Applied non linear control. Prentice Hall, New Jersey, USA
Soong TT (1990) Active structural control: theory and practice. Longman Scientific and Technical/Wiley, London/New York
Soong TT, Spencer BF Jr (2002) Supplemental energy dissipation: state-of-the-art and state-of-the practice. Eng Struct 24:243–259
Spencer BF Jr, Nagarajaiah S (2003) State of the art of structural control. J Struct Eng 129(7):845–856
Spencer BF, Dyke SJ, Sain MK, Carlson JD (1997) Phenomenological model for magnetorheological dampers. J Eng Mech 123(3):230–38
Sriram N, Satish N, Erik J, Henri G (2003) Smart base isolated building benchmark problem. In: 16th ASCE engineering mechanics conference. University of Washington, Seattle
Symans MD, Constantinou MC, Taylor DP, Garnujost KD (1994) Semi-active fluid viscous dampers for seismic response control. In: Proceedings of first world conference on structural control, Los Angeles, FA4 pp 3–12
Utku S (1998) Theory of adaptive structures: incorporative intelligent into engineering products. CRC Press, London
Winslow WM (1947) Methods and means for translatinfg electrical impulses into mechanical forces. US patent 2,417,850
Yang JN (1975) Application of optimal control theory to civil engineering structures. J Eng Mech Div ASCE 819–838
Yang JN, Kim J-H, Agrawal AK (2000) A resetting semiactive stiffness damper for seismic response control. J Struct Eng 126:1427–1433
Yi F, Dyke SJ, Caicedo JM, Carlson JD (2001) Experimental verification of multi-input seismic control strategies for smart dampers. J Eng Mech ASCE 127(11):1152–1164
Yoshida O (2003) Torsionally coupled response control of earthquake excited asymmetric buildings: development and application of effective control systems using smart dampers. PhD thesis, Washington University, Sever Institute of Technology, Department of Civil Engineering (supervised: Dyke SJ)
Zacharenakis EC, Arvanitis KG, Soldatos AG, Stavroulakis GE (2001) LQR and H_∞ optimal structural control in aseismic design. In: Proceedings of national mechanics congress, Thessaloniki, pp 240–245
Zadeh LA (1965) Fuzzy sets. Info Control 8:338–353
Zhou L, Chang C, Wang L (2003) Adaptive fuzzy control for nonlinear building-magnetorheological damper system. J Struct Eng 129(7):905–913

Advances in Online Structural Identification

Ka-Veng Yuen
Faculty of Science and Technology, University of Macau, Macau, China

Synonyms

Bayesian inference; Extended Kalman filter; Model class selection; Model updating; Nonparametric identification; Online updating; Outlier, structural health monitoring; System identification

Introduction

Structural health monitoring using dynamic response measurement has received a tremendous attention over the last decades. A number of methods have been developed, including the novelty measure technique (Worden 1997), the GA-based substructural identification methods (Koh and Shankar 2003), and the evolutionary strategy (Franco et al. 2004). On the other hand, the Bayesian inference (Beck and Katafygiotis 1998; Beck 2010; Yuen 2010a) using probability logic provides a rigorous solution to parametric identification and uncertainty quantification for different problems in structural and geotechnical engineering, such as modal identification using nonstationary noisy response measurements (Yuen and Katafygiotis 2005; Yuen et al. 2006a), ambient vibration survey (Yuen and Katafygiotis 2006; Yuen et al. 2006b; Yuen and Kuok 2010a), particulate matters (Hoi et al. 2009), fatigue problem (Papadimitriou et al. 2011), and model class selection (Worden and Hensman 2012). A detailed review of Bayesian methods for structural dynamics and civil engineering can be found in Yuen and Kuok (2011). In particular, the well-known Kalman filter (KF) is one of the most widely applied recursive Bayesian state estimation techniques for trajectory estimation of linear dynamical systems (Kalman and Bucy 1961). Based on the concept of the KF, the extended Kalman filter (EKF) was developed for nonlinear systems (Jazwinski 1970). By introducing an augmented state vector, the EKF can be applied to parametric identification problems, and it has become a standard technique for state tracking, system identification, and control design for dynamical systems.

In the KF or EKF, the covariance matrices of the process noise and measurement noise are required. The conventional way is to tune these noise covariance matrices in a trial-and-error manner. However, ad hoc selection may lead to biased estimation, misleading uncertainty estimation, and even divergence problems (Zhou and Luecke 1994). Insights have been given into the convergence mechanisms, asymptotic behavior, and estimation performance of the KF and EKF. It was emphasized that discrepancy between the actual and prescribed noise covariance matrices degrades substantially the performance of the filters and induces divergence problems. Existing methodologies for the estimation of these noise covariance matrices can be classified into three categories: covariance matching techniques (Myers and Tapley 1976), correlation techniques (Mehra 1970), and Bayesian techniques (Zhou and Luecke 1994). However, the majority of the literature focused on stationary situation which is not satisfied for general applications.

In this chapter, a computationally efficient Bayesian approach is presented for online estimation of the noise parameters. On the filter performance, it prevents the possible divergence problem and ensures the accuracy of the estimates and the estimated uncertainty. On the adaptability, it takes into explicit consideration the non-stationarity of the excitation, response, and measurement noise. These features of the presented approach enhance the applicability and reliability for the practical usage of the KF and EKF for online structural identification.

Next, the treatment of outliers in dynamic response data for online updating is addressed. In practice, it often occurs that some data points deviate drastically from the model output. The presence of outliers indicates irregularities of the data and/or deficiency of the model or theory. On one hand, outliers may occur due to extraordinarily large measurement error, e.g., human error, sensor noise, sensor failures, unknown environmental disturbances, etc. On the other hand, outliers may also occur due to imperfection of theory, i.e., existence of unmodeled mechanisms.

Since the performance of KF and EKF is severely deteriorated in the presence of outliers, a number of methods have been developed to enhance the robustness to outliers for KF and EKF. The first class of methods uses a non-Gaussian likelihood model for the measurement noise distribution and/or process noise distribution since the Gaussian likelihood model is sensitive to outliers, e.g., the Gaussian sum

approximation (Sorenson and Alspach 1971). However, this class of methods is often computationally very demanding, especially for online updating. Furthermore, the conditional mean of the state vector is not available in some cases. Another class of methods attempts to assign different weights, which are some heuristic function of the data, to different data points (Durovic and Kovacevic 1999). Methods of this class require tuning of the threshold parameters. However, performance is deteriorated with improper choice of the weights due to the difficulty in the choice of the thresholds. Therefore, this class of methods should be utilized with special attention.

In this chapter, an outlier-resistant extended Kalman filter (OR-EKF) is presented for robust online structural parametric identification using dynamic response data, contaminated with outliers in addition to Gaussian noise. In this algorithm, a novel outlier detection algorithm is embedded into the EKF. It is capable for robust online estimation of structural parameters using outlier-contaminated dynamic response data. Instead of definite judgment on the outlierness of a data point, the OR-EKF provides its outlier probability, which is the extension of the concept in Yuen and Mu (2012). Data points with outlier probability over 0.5 will be regarded as suspicious data points, and they will be discarded for the identification purpose. In contrast to other existing outlier detection criteria that require some subjective threshold (e.g., normalized residual larger than 2.5), the outlier probability threshold of 0.5 is intuitive in the presented approach.

The third issue to be introduced is on the online model class selection. The usual approach in system identification is to find the best/optimal model in a prescribed class of models, e.g., class of shear building models with uncertain inter-story stiffnesses. This problem is commonly referred to as parametric identification. The more general problem of model class selection has not been explored as intensively as parametric identification. It is well known that a more complicated model class often fits the data better than one which has fewer adjustable parameters. However, an over-fitted model leads to poor predictions because the model parameters depend too much on the detail of the data, and consequently the measurement noise and the modeling error play an important role in the data fitting. Therefore, in order to select a suitable model class for identification purposes, it is necessary to penalize a complicated model albeit the quantification of this penalty is a nontrivial task. This was first recognized by H. Jeffreys who did pioneering work on the application of Bayesian methods (Jeffreys 1961). In the present context, the selected class of models should agree closely with the observed behavior of the system but otherwise be as simple as possible. In recent years, the Bayesian approach to model class selection has been further developed by showing that the evidence for each model class provided byte data automatically enforces a quantitative expression of principle of model parsimony or of Ockham's razor (Gull 1988). As a result, no ad hoc penalty is needed as in some of the earlier work on model class selection. Applications in civil engineering include the damage detection (Lam et al. 2006), selection of nonlinear hysteretic models (Muto and Beck 2008), soil compressibility (Yan et al. 2009), ambient effects to structural modal parameters (Yuen and Kuok 2010b), and seismic attenuation relationships (Yuen and Mu 2011). In this chapter, a recently developed recursive algorithm is introduced for Bayesian online model class selection.

In section "Structural Parametric Identification by Extended Kalman Filter," online structural parametric identification using the EKF will be briefly reviewed. In section "Online Identification of Noise Parameters," an online identification algorithm for the noise parameters in the EKF is introduced. Then, in section "Outlier-Resistant Extended Kalman Filter," an online outlier detection algorithm is presented, and it is embedded into the EKF. This algorithm allows for robust structural identification in the presence of possible outliers. In section "Online Bayesian Model Class Selection," a recursive Bayesian model class section method is presented for non-parametric identification problems.

Structural Parametric Identification by Extended Kalman Filter

Formulation

Consider a linear dynamical system with N_d degrees of freedom (DOFs):

$$\mathbf{M}\ddot{\mathbf{x}} + \mathbf{r}(\mathbf{x}, \dot{\mathbf{x}}; \boldsymbol{\varphi}) = \mathbf{T}\mathbf{f}\ (t) \tag{1}$$

where $\mathbf{M} \in \mathbb{R}^{N_d \times N_d}$ is the mass matrix of the system; $\mathbf{r}(\mathbf{x}, \dot{\mathbf{x}}; \boldsymbol{\varphi})$ is the restoring force that is governed by the unknown structural parameter vector $\boldsymbol{\varphi} \in \mathbb{R}^{N_\varphi}$ to be identified; $\mathbf{f}$ is the zero-mean Gaussian excitation; and $\mathbf{T} \in \mathbb{R}^{N_d \times N_f}$ is the force distribution matrix. The mass matrix $\mathbf{M}$ is assumed known.

Then, the augmented state vector $\mathbf{y}(t) \in \mathbb{R}^{2N_d + N_\varphi}$ is introduced to include the displacement, velocity, and the unknown structural parameters:

$$\mathbf{y}(t) = \left[\mathbf{x}^T, \dot{\mathbf{x}}^T, \boldsymbol{\varphi}^T\right]^T \tag{2}$$

where the superscript T denotes the transpose a vector/matrix. As a result, Eq.1 can be converted to the state-space form:

$$\frac{\mathrm{d}}{\mathrm{d}t}\mathbf{y}(t) = \begin{bmatrix} \dot{\mathbf{x}} \\ -\mathbf{M}^{-1}\mathrm{r}\left(\mathbf{x}, \dot{\mathbf{x}}; \boldsymbol{\varphi}\right) \\ \mathbf{0}_{N_\varphi \times 1} \end{bmatrix} + \begin{bmatrix} 0_{N_d} \times 1 \\ \mathbf{M}^{-1}\mathbf{T} \\ 0_{N_\varphi \times 1} \end{bmatrix} \mathbf{f}(t) \tag{3}$$

To simplify the notation, the rate vector and input distribution matrix are defined as follows:

$$\mathbf{s} \equiv \begin{bmatrix} \dot{\mathbf{x}} \\ -\mathbf{M}^{-1}\mathrm{r}\left(\mathbf{x}, \dot{\mathbf{x}}; \boldsymbol{\varphi}\right) \\ \mathbf{0}_{N_\varphi \times 1} \end{bmatrix};\ \mathbf{B} \equiv \begin{bmatrix} 0_{N_d \times N_f} \\ \mathbf{M}^{-1}\mathbf{T} \\ 0_{N_\varphi \times N_f} \end{bmatrix} \tag{4}$$

where $\mathbf{0}_{\alpha \times \beta}$ denotes the $\alpha \times \beta$ zero matrix.

The structural response is sampled at N_o DOFs with time step Δt, and the measurement at the kth time step can be represented by the observation vector:

$$\mathbf{z}_k = \mathbf{C}_\mathrm{d}\mathbf{y}_k + \mathbf{n}_k \tag{5}$$

Where $\mathbf{y}_k \equiv \mathbf{y}(k\Delta \mathrm{t})$, $\mathbf{C}_\mathrm{d} \in \mathbb{R}^{N_o \times \left(2N_d + N_\varphi\right)}$ is the observation matrix, and the measurement noise $\mathbf{n}_k$ is assumed to be Gaussian with zero-mean and covariance matrix $\sum_{\mathbf{n},k} \in \mathbb{R}^{N_o \times N_o}$. Note that the measurement noise $\mathbf{n}$ is assumed to be i.i.d. (independent and identically distributed) and statistically independent to the excitation $\mathbf{f}$.

In order to obtain a discrete state-space equation for computation, the functions in Eq. 4 is linearized for each time step $t \in [k\Delta t, (k+1)\Delta t)$ as follows:

$$\frac{\mathrm{d}}{\mathrm{d}t}\mathbf{y}(t) = \mathbf{s}\Big|_{\mathbf{y}(t)=\mathbf{y}_k} + \left.\frac{\partial \mathbf{s}}{\partial \mathbf{y}}\right|_{\mathbf{y}(t)=\mathbf{y}_k} (\mathbf{y}(t) - \mathbf{y}_k) + \mathbf{B}\mathbf{f}(t) \tag{6}$$

And it can be rearranged as follows:

$$\dot{\mathbf{y}}(t) = \mathbf{A}_k\mathbf{y}(t) + \mathbf{B}\mathbf{f}(t) + \mathbf{h}_k,\ t \in [k\Delta \mathrm{t},\ (k+1)\Delta t] \tag{7}$$

where the system matrix $\mathbf{A}_k$ is given by

$$\begin{aligned} \mathbf{A}_k &= \left.\frac{\partial \mathbf{s}}{\partial \mathbf{y}}\right|_{\mathbf{y}(t)=\mathbf{y}_k} \\ &= \left[\begin{array}{c|c|c} 0_{N_d \times N_d} & \mathbf{I}_{N_d} & 0_{N_d \times N_\varphi} \\ -\mathbf{M}^{-1}\dfrac{\partial \mathbf{r}}{\partial \mathbf{x}} & -\mathbf{M}^{-1}\dfrac{\partial \mathbf{r}}{\partial \dot{\mathbf{x}}} & -\mathbf{M}^{-1}\dfrac{\partial \mathbf{r}}{\partial \boldsymbol{\varphi}} \\ 0_{N_\varphi \times N_d} & 0_{N_\varphi} \times N_d & -\delta \mathbf{I}_{N_\varphi} \end{array}\right] \end{aligned} \tag{8}$$

and the vector $\mathbf{h}_k$ is given by

$$\mathbf{h}_k = \mathbf{r}|_{\mathrm{y}(t)=\mathrm{y}_k} - \mathbf{A}_k\mathbf{y}_k \tag{9}$$

The variable δ in $\mathbf{A}_k$ in Eq. 8 is chosen as a small positive number to prevent singularity of the matrix $\mathbf{A}_k$;$\mathbf{I}_\alpha$, and $\mathbf{0}_{\alpha \times \beta}$ denote the $\alpha \times \alpha$ identity matrix and the $\alpha \times \beta$ zero matrix, respectively.

State Estimation and Parametric Identification by Kalman Filter

The augmented state vector $\mathbf{y}$ can be updated by the Kalman filter. First, the linearized state-space

equation in Eq. 7 can be discretized to a difference equation:

$$\mathbf{y}_{k+1} = \mathbf{A}_{\mathrm{d},k}\mathbf{y}_k + \mathbf{B}_{\mathrm{d},k}\mathbf{f}_k + \mathbf{h}_{\mathrm{d},k} \tag{10}$$

where $\mathbf{y}_{k+1} = \mathbf{y}((k+1)\Delta t)$, $\mathbf{A}_{\mathrm{d},k} = \exp(\mathbf{A}_k\,\Delta t)$, $\mathbf{B}_{\mathrm{d},k} = \mathbf{A}_k^{-1}\left(\mathbf{A}_{\mathrm{d},k} - \mathbf{I}_{2N_d+N_\varphi}\right)\mathbf{B}$, $\mathbf{f}_k = \mathbf{f}(k\Delta t)$, and $\mathbf{h}_{\mathrm{d},k} = \mathbf{A}_k^{-1}\left(\mathbf{A}_{\mathrm{d},k} - \mathbf{I}_{2N_d+N_\varphi}\right)\mathbf{h}_k$.

With the measurement $D_k \equiv \{\mathbf{z}_1, \mathbf{z}_2, \ldots, \mathbf{z}_k\}$ defined in Eq. 5, the predicted state at the $(k+1)^{\text{th}}$ time step ($\mathbf{y}_{k+1|k} \equiv \mathrm{E}[\mathbf{y}_{k+1}|\mathbf{z}_1, \mathbf{z}_2, \ldots, \mathbf{z}_k]$) can be estimated by taking the conditional expected value of Eq. 10:

$$\mathbf{y}_{k+1|k} = \mathbf{A}_{\mathrm{d},k}\mathbf{y}_{k|k} + \mathbf{h}_{\mathrm{d},k} \tag{11}$$

where $\mathbf{y}_{k|k}$ is the updated state at the kth time step. In addition, the covariance matrix of $\mathrm{y}_{k+1|k}$ is

$$\boldsymbol{\Sigma}_{\mathbf{y},k+1|k} = \mathbf{A}_{\mathrm{d},k}\boldsymbol{\Sigma}_{\mathbf{y},k|k}\mathbf{A}_{\mathrm{d},k}^T + \mathbf{B}_{\mathrm{d},k}\boldsymbol{\Sigma}_{\mathrm{f},k}\mathbf{B}_{\mathrm{d},k}^T \tag{12}$$

where $\boldsymbol{\Sigma}_{\mathbf{f},k}$ is the covariance matrix of the excitation at the kth time step.

With a new data point $\mathbf{z}_{k+1}$, the updated state $\mathbf{y}_{k+1|k+1}$ and its covariance matrix $\boldsymbol{\Sigma}_{\mathbf{y},k+1|k+1}$ can be obtained by using the following Kalman filter recursive formulae (Kalman and Bucy 1961):

$$\mathbf{y}_{k+1|k+1} = \mathbf{y}_{k+1|k} + \mathbf{G}_{k+1}\left(\mathbf{z}_{k+1} - \mathbf{C}_{\mathrm{d}}\mathbf{y}_{k+1|k}\right) \tag{13}$$

$$\boldsymbol{\Sigma}_{\mathbf{y},k+1|k+1} = \left(\mathbf{I}_{2N_d+N\varphi} - \mathbf{G}_{k+1}\mathbf{C}_{\mathrm{d}}\right)\boldsymbol{\Sigma}_{\mathbf{y},k+1|k} \tag{14}$$

where $\mathbf{G}_{k+1}$ is called the Kalman filter gain (Kalman and Bucy 1961)

$$\mathbf{G}_{k+1} = \boldsymbol{\Sigma}_{\mathbf{y},k+1|k}\mathbf{C}_{\mathrm{d}}^T\left(\mathbf{C}_{\mathrm{d}}\boldsymbol{\Sigma}_{\mathbf{y},k+1|k}\mathbf{C}_{\mathrm{d}}^T + \Sigma_{\mathbf{n},k}\right)^{-1} \tag{15}$$

Fading Memory

Fading memory filtering was developed to compensate the modeling error in the identification process (Sorensen and Sacks 1971). Here, it is employed to track the time-varying structural and noise parameters. The underlying concept of fading memory filtering is to discount the contribution of the past data gradually for adaptive identification of the time-varying parameters. This can be accomplished by assigning an appropriate weighting, which is called the fading factor $\mu(>1)$, to enlarge the estimated covariance matrix at every time step so that the information from the past data will fade out gradually. In particular, the covariance matrix of the filtered augmented state in Eq. 14 is modified as follows:

$$\boldsymbol{\Sigma}_{\mathbf{y},k+1|k+1} = \mu\left(\mathbf{I}_{2N_d+N\varphi} - \mathbf{G}_{k+1}\mathbf{C}_{\mathrm{d}}\right)\boldsymbol{\Sigma}_{\mathbf{y},k+1|k} \tag{16}$$

where μ is the widely adopted exponential fading factor (Sorensen and Sacks 1971)

$$\mu = \exp\left(\frac{\ln\mu_\sigma^2}{N_\mu}\right) \tag{17}$$

where $\mu \geq 1$. The effect of this exponential fading factor is to dilute the information of a data point with a factor of μ_σ^2, in terms of the contribution to the posterior variance, after every $N\mu$ time steps.

Online Identification of Noise Parameters

In this section, a Bayesian probabilistic approach is presented for online estimation of the noise parameters of the process noise and measurement noise. Section "Parameterization and Bayesian Formulation" introduces the parameterization of the noise covariance matrices and the Bayesian formulation. Thereafter, the online identification algorithm is presented in section "Online Estimation of Noise Parameters."

Parameterization and Bayesian Formulation

First, the covariance matrices of the process noise and measurement noise are parameterized

as $\boldsymbol{\Sigma}_{\mathbf{f},k} = \boldsymbol{\Sigma}_{\mathbf{f},k}(\boldsymbol{\theta}_{\mathbf{f},k})$ and $\boldsymbol{\Sigma}_{\mathbf{n},k+1} = \boldsymbol{\Sigma}_{\mathbf{n},k+1}(\boldsymbol{\theta}_{\mathbf{n},k+1})$, respectively. In other words, both matrices are time varying in order to allow online tracking. The uncertain noise parameter vector is given by

$$\boldsymbol{\theta}_{k+1} = \left[\boldsymbol{\theta}_{\mathbf{f},k}^T, \boldsymbol{\theta}_{\mathbf{n},k+1}^T\right]^T \in \mathbb{R}^{N_\theta} \tag{18}$$

This parameterization allows for the tracking problem for general nonstationary situations. In the following, a concurrent procedure is introduced to estimate the noise parameter vector. As a result, not only the optimal estimation can be obtained but also the associated uncertainty can be quantified.

When a new measurement $\mathbf{z}_{k+1}$ is available, the noise parameters can be updated. Using the Bayes' theorem, the posterior probability density function (PDF) of the noise parameter vector given the measurement data set D_{k+1} is given by (Yuen 2010a)

$$p(\boldsymbol{\theta}_{k+1}|D_{k+1}) = \frac{p(\boldsymbol{\theta}_{k+1}|D_k)p(\mathbf{z}_{k+1}|\boldsymbol{\theta}_{k+1}, D_k)}{p(\mathbf{z}_{k+1}|D_k)} \tag{19}$$

where $p(\boldsymbol{\theta}_{k+1}|D_k)$ is the prior PDF of $\boldsymbol{\theta}_{k+1}$; $p(\mathbf{z}_{k+1}|\boldsymbol{\theta}_{k+1},D_k)$ is the likelihood function; and $p(\mathbf{z}_{k+1}|D_k)$ is a normalizing constant such that the integral of the posterior PDF over the entire parameter space is unity. The prior PDF is approximated as a Gaussian distribution:

$$p(\boldsymbol{\theta}_{k+1}|D_k) = (2\pi)^{-N_\theta/2}|\boldsymbol{\Sigma}_{\boldsymbol{\theta},k+1|k}|^{-1/2} \exp\left[-\frac{1}{2}\left(\boldsymbol{\theta}_{k+1} - \boldsymbol{\theta}_{k+1|k}\right)^T \boldsymbol{\Sigma}_{\boldsymbol{\theta},k+1|k}^{-1}\left(\boldsymbol{\theta}_{k+1} - \boldsymbol{\theta}_{k|k}\right)\right] \tag{20}$$

Given the measurement D_k, the one-step ahead predictor for the noise parameters is taken as the updated noise parameters of the previous time step:

$$\boldsymbol{\theta}_{k+1|k} = \boldsymbol{\theta}_{k|k} \tag{21}$$

On the other hand, the associated covariance matrix is assumed to be the following:

$$\boldsymbol{\Sigma}_{\boldsymbol{\theta},k+1|k} = \mu\boldsymbol{\Sigma}_{\boldsymbol{\theta},k|k} \tag{22}$$

where the fading factor μ is defined in Eq. 17. Here, it is assumed that the noise covariances are time slowly varying so the ensemble mean can be approximately estimated by the temporal average with certain time delay.

On the other hand, the likelihood function is given by

$$p(\mathbf{z}_{k+1}|\boldsymbol{\theta}_{k+1}, D_k) = (2\pi)^{-N_o/2}|\boldsymbol{\Sigma}_{\mathbf{z},k+1|k}|^{-1/2} \exp\left[-\frac{1}{2}\left(\mathbf{z}_{k+1} - \mathbf{z}_{k+1|k}\right)^T \boldsymbol{\Sigma}_{\mathbf{z},k+1|k}^{-1}\left(\mathbf{z}_{k+1} - \mathbf{z}_{k+1|k}\right)\right] \tag{23}$$

where $\mathbf{z}_{k+1|k}$ and $\boldsymbol{\Sigma}_{\mathbf{z},k+1|k}$ are readily obtained from Eqs. 11 and 12 given the measurement data set D_k:

$$\mathbf{z}_{k+1|k} = \mathbf{C}_\mathrm{d}\mathbf{A}_{\mathrm{d},k}\mathbf{y}_{k|k} + \mathbf{C}_\mathrm{d}\mathbf{h}_{\mathrm{d},k} \tag{24}$$

$$\boldsymbol{\Sigma}_{\mathbf{z},k+1|k} = \mathbf{C}_\mathrm{d}\mathbf{A}_{\mathrm{d},k}\boldsymbol{\Sigma}_{\mathbf{y},k|k}\mathbf{A}_{\mathrm{d},k}^T\mathbf{C}_\mathrm{d}^T + \mathbf{C}_\mathrm{d}\mathbf{B}_{\mathrm{d},k}\boldsymbol{\Sigma}_{\mathbf{f},k|k}\mathbf{B}_{\mathrm{d},k}^T\mathbf{C}_\mathrm{d}^T + \boldsymbol{\Sigma}_{\mathbf{n},k+1|k} \tag{25}$$

By substituting Eq. 20–Eq. 23 to Eq. 19, the posterior PDF becomes

$$p(\boldsymbol{\theta}_{k+1}|D_{k+1}) = \frac{(2\pi)^{-(N_\theta+N_o)/2}}{p(\mathbf{z}_{k+1}|D_k)|\mu\boldsymbol{\Sigma}_{\boldsymbol{\theta},k|k}|^{1/2}}|\boldsymbol{\Sigma}_{\mathbf{z},k+1|k}|^{-1/2}\exp\left[-\frac{1}{2\mu}\left(\boldsymbol{\theta}_{k+1} - \boldsymbol{\theta}_{k|k}\right)^T\boldsymbol{\Sigma}_{\boldsymbol{\theta},k|k}^{-1}\left(\boldsymbol{\theta}_{k+1} - \boldsymbol{\theta}_{k|k}\right) - \frac{1}{2}\left(\mathbf{z}_{k+1} - \mathbf{z}_{k+1|k}\right)^T\boldsymbol{\Sigma}_{\mathbf{z},k+1|k}^{-1}\left(\mathbf{z}_{k+1} - \mathbf{z}_{k+1|k}\right)\right] \tag{26}$$

where $\mathbf{z}_{k+1|k}$ and $\boldsymbol{\Sigma}_{\mathbf{z},k+1|k}$ are given by Eqs. 24 and 25, respectively. The objective function $J(\boldsymbol{\theta}_{k+1})$ is defined as the negative logarithm of the posterior PDF without taking the terms that do not depend on the noise parameters:

$$\begin{aligned} J(\boldsymbol{\theta}_{k+1}) &= \frac{1}{2}\ln|\boldsymbol{\Sigma}_{\mathbf{z},k+1|k}| + \frac{1}{2\mu}\left(\boldsymbol{\theta}_{k+1}-\boldsymbol{\theta}_{k|k}\right)^T\boldsymbol{\Sigma}^{-1}_{\boldsymbol{\theta},k|k}\left(\boldsymbol{\theta}_{k+1}-\boldsymbol{\theta}_{k|k}\right) \\ &\quad + \frac{1}{2}\left(\mathbf{z}_{k+1}-\mathbf{z}_{k+1|k}\right)^T\boldsymbol{\Sigma}^{-1}_{\mathbf{z},k+1|k}\left(\mathbf{z}_{k+1}-\mathbf{z}_{k+1|k}\right) \end{aligned} \tag{27}$$

The updated noise parameter vector $\boldsymbol{\theta}_{k+1|k+1}$ can be obtained by maximizing the posterior PDF $p(\boldsymbol{\theta}_{k+1}|D_{k+1})$ in Eq. 26, and it is equivalent to minimizing the objective function $J(\boldsymbol{\theta}_{k+1})$ in Eq. 27:

$$\boldsymbol{\theta}_{k+1|k+1} = \arg\min_{\boldsymbol{\theta}_{k+1}} J(\boldsymbol{\theta}_{k+1}) \tag{28}$$

Furthermore, the uncertainty of the updated noise parameter vector $\boldsymbol{\theta}_{k+1|k+1}$ can be represented by its covariance matrix $\boldsymbol{\Sigma}_{\boldsymbol{\theta},k+1|k+1}$ which is equal to the inverse of the Hessian matrix of the objective function calculated at $\boldsymbol{\theta}_{k+1} = \boldsymbol{\theta}_{k+1|k+1}$:

$$\boldsymbol{\Sigma}_{\boldsymbol{\theta},k+1|k+1} = \left[\mathbf{H}_J\left(\boldsymbol{\theta}_{k+1|k+1}\right)\right]^{-1} \tag{29}$$

where the Hessian matrix is given by $\mathbf{H}_J\left(\boldsymbol{\theta}_{k+1|k+1}\right) = \left[\nabla J(\boldsymbol{\theta}_{k+1})\nabla^T\right]|_{\boldsymbol{\theta}_{k+1}=\boldsymbol{\theta}_{k+1|k+1}}$, and it can be computed using the finite difference method.

Online Estimation of Noise Parameters

In this subsection, a computationally efficient algorithm is presented for online updating of the noise parameter vector $\boldsymbol{\theta}_{k+1|k+1}$ and the associated covariance matrix $\boldsymbol{\Sigma}_{\boldsymbol{\theta},k+1|k+1}$. Starting with an arbitrary initial condition $\boldsymbol{\theta}_{0|0}$ and arbitrarily positive definite matrix $\boldsymbol{\Sigma}_{\boldsymbol{\theta},0|0}$, the noise parameter vector and its associated covariance matrix can be updated based on Eqs. 28 and 29. As aforementioned, the noise parameter vector can be updated by solving the optimization problem in Eq. 28. However, due to the large prior uncertainty and numerical considerations, a training process is necessary for a preliminary solution before solving directly this optimization problem. In this training process, a heuristic local search method is utilized. Thereafter, a modified Newton's method is used for the operating stage. Details of this estimation scheme are presented as follows.

Training Stage

At the beginning of the identification process, the Gaussian approximation is inaccurate due to the large prior uncertainty, i.e., large difference between the prior mean and the actual values, and large prior variances. Therefore, solving directly the optimization problem in Eq. 28 may result in computational problems. Herein, a training process is introduced to obtain a preliminary solution before the long-term operating stage. During the training process, a heuristic local search method is applied to the optimization problem. This method provides a generic tool for complicated optimization problems. The basic principle is to conduct the optimization within a prescribed parameter set. By exhaustive search from this finite set, the optimal (suboptimal) solution is the one that gives the smallest objective function value. Specifically, the candidate parameter set of the $(k+1)$th time step is defined as

$$\begin{aligned} \boldsymbol{\Theta}_{k+1} \equiv \Big\{ &\boldsymbol{\theta}_{k+1} \in \mathbb{R}^{N_\theta} : \theta^{(l)}_{k+1} = v\theta^{(l)}_{k|k}, l = 1, \ldots, \\ &N_\theta, v \in \{1/2, 1, 2\} \Big\} \end{aligned} \tag{30}$$

where $\theta^{(l)}_{k+1}$ and $\theta^{(l)}_{k|k}$ are the lth component of the noise parameter vector $\boldsymbol{\theta}_{k+1}$ and the lth

component of the updated noise parameter vector $\boldsymbol{\theta}_{k/k}$, respectively. By considering all the combinations of the N_θ noise parameters, there are 3^{N_θ} candidate solutions in the candidate parameter set $\boldsymbol{\Theta}_{k+1}$. The objective function $J(\boldsymbol{\theta}_{k+1})$ is evaluated for all candidate solutions. Then, the noise parameter vector is updated under the optimization criterion given by

$$\boldsymbol{\theta}_{k+1|k+1} = \arg\min_{\boldsymbol{\theta}_{k+1}} J(\boldsymbol{\theta}_{k+1}) \text{ where } \boldsymbol{\theta}_{k+1} \in \boldsymbol{\Theta}_{k+1} \tag{31}$$

This heuristic local search method is the online version of the half-or-double optimization method in Yuen et al. (2007). If the updated noise parameter vectors of ten consecutive time steps remain unchanged, the training process will be terminated. However, this training process is enforced to be not shorter than one fundamental period of the underlying dynamical system (or its equivalent linear system). This one-period requirement ensures that sufficient information can be gained from the data for the preliminary estimation of the augmented state vector.

Operating Stage

After the training process, the updated noise parameter vector is obtained using a modified Newton's method in the operating stage. Instead of an iterative procedure in the Newton's method, it is necessary to take only one step because the updated parameter vector of the previous time step is very close to the solution. Specifically, the updated noise parameter vector can be obtained as follows:

$$\boldsymbol{\theta}_{k+1|k+1} = \boldsymbol{\theta}_{k|k} - \boldsymbol{\Sigma}_{\boldsymbol{\theta},k|k}\left(\nabla J(\boldsymbol{\theta}_k)|_{\boldsymbol{\theta}_k=\boldsymbol{\theta}_{k|k}}\right) \tag{32}$$

where the gradient $\nabla J(\boldsymbol{\theta}_k)|_{\boldsymbol{\theta}_k=\boldsymbol{\theta}_{k|k}}$ can be computed using the finite difference method. Since the information carried by one data point is limited, the updated noise parameter vector of the previous time step provides an accurate initial estimation of the current time step. Therefore, Eq. 32 is sufficient without iteration.

Outlier-Resistant Extended Kalman Filter

In this section, the outlier-resistant extended Kalman filter (OR-EKF) is introduced for online outlier detection and robust structural parametric identification using dynamic response data. In this algorithm, an online outlier detection algorithm is embedded into the EKF. Section "Online Outlier Detection by Outlier Probability" introduces the concept of outlier probability, and it will be utilized for online outlier detection. This outlier detection algorithm is embedded in the EKF for online structural identification. Section "Procedure of the Outlier-Resistant Extended Kalman Filter" summarizes the procedure of the OR-EKF algorithm.

Online Outlier Detection by Outlier Probability

In this section, the concept of outlier probability and an online outlier detection algorithm are introduced. Instead of definite judgment on the "outlierness" of a data point being an outlier, this algorithm provides the outlier probability, which is the extension of the concept in Yuen and Mu (2012) for linear regression problems, for the measurement in each time step. The outlier probability is a function of the normalized residual, which is defined as the difference between the measured value and the corresponding one-step-ahead predictor, normalized by its standard deviation. Data points with outlier probability over 0.5 are regarded as suspicious data points, and they will be discarded for the identification purpose.

Outlier Probability

Recall that the predicted state $\mathbf{y}_{k+1|k}$ can be calculated using Eq. 11. Therefore, the one-step-ahead predictor of the measurements is readily obtained:

$$\mathbf{z}_{k+1|k} = \mathbf{C}_\mathrm{d}\mathbf{y}_{k+1|k} \tag{33}$$

Use $z_{k+1}^{(s)}$ to denote the sth component of the observation vector $\mathbf{z}_{k+1}$ and $z_{k+1|k}^{(s)}$, $s = 1,2,\ldots,N_o$, to denote the sth component of its

one-step-ahead predictor $\mathbf{z}_{k+1|k}$. Hereafter, the superscript (s) is used to denote the sth component of a vector. Then, the normalized residual (prediction error) for $z_{k+1}^{(s)}$ can be defined (Myers and Tapley 1976):

$$\varepsilon_{k+1}^{(s)} = \left(z_{k+1}^{(s)} - z_{k+1|k}^{(s)}\right)/\sigma_{\varepsilon,k+1}^{(s)} \tag{34}$$

where $\sigma_{\varepsilon,k+1}^{(s)}$ is the standard deviation for the sth measured channel of the difference between the measurement and the corresponding one-step-ahead predictor. Since the probability model for the measurement noise is Gaussian, the probability of a data point falling outside the interval $(-|\varepsilon_{k+1}^{(s)}|, |\varepsilon_{k+1}^{(s)}|)$ is

$$Q_{k+1} = 2\Phi\left(-\left|\varepsilon_{k+1}^{(s)}\right|\right) \tag{35}$$

where $\Phi(\cdot)$ is the cumulative distribution function (CDF) of the standard Gaussian random variable. Then, a moving time window is introduced to include not more than N_w previous regular data points, and the set $\mathrm{R}_k^{(s)}$ is introduced to include the absolute normalized residuals of the regular data points in this time window:

$$\begin{aligned}\mathrm{R}_k^{(s)} = \Big\{ &\left|\varepsilon_l^{(s)}\right| : z_l^{(s)} \text{is a regular data point,} \\ &l = \max(1, k - N_\mathrm{W}), \ldots, k \Big\}\end{aligned} \tag{36}$$

where $n(\mathrm{R}_k^{(s)})$ is used to denote the number of elements in the set $\mathrm{R}_k^{(s)}$. Define η_{k+1} as the number of elements, among the set $\mathrm{R}_k^{(s)}$, with absolute normalized residuals larger than $|\varepsilon_{k+1}^{(s)}|$. In other words, η_{k+1} is the number of previous regular data points, within the aforementioned moving time window, that has larger absolute normalized residual than the current one. This is equivalent to counting the numbers of the normalized residuals of the previous regular points falling outside the interval $(-|\varepsilon_{k+1}^{(s)}|, |\varepsilon_{k+1}^{(s)}|)$ in the moving time window.

In order to determine the outlierness of a data point $z_{k+1}^{(s)}$, the probability that τ points, out of $n(\mathrm{R}_k^{(s)}) + 1$ data points, falling outside the interval $(-|\varepsilon_{k+1}^{(s)}|, |\varepsilon_{k+1}^{(s)}|)$ is considered. Note that τ is a random variable, and it follows the binomial distribution with probability Q_{k+1}. Then, the outlier probability for $z_{k+1}^{(s)}$ can be defined as the probability that no more than η_{k+1} samples drawn from the normalized residuals among the $(\mathrm{R}_k^{(s)})$ previous regular data points fall outside the interval $(-|\varepsilon_{k+1}^{(s)}|, |\varepsilon_{k+1}^{(s)}|)$. This probability can be obtained by considering the total probability:

$$\begin{aligned}P_o\left(z_{k+1}^{(s)}\right) = &\sum\nolimits_{\tau=0}^{\eta_{k+1}} C\left(n\left(\mathrm{R}_k^{(s)}\right), \tau\right) \\ &Q_{k+1}^{\tau}\left(1 - Q_{k+1}\right)^{n\left(\mathrm{R}_k^{(s)}\right)-\tau}\end{aligned} \tag{37}$$

where $C\left(n\left(\mathrm{R}_k^{(s)}\right), \tau\right) = \frac{n\left(\mathrm{R}_k^{(s)}\right)!}{\left(n\left(\mathrm{R}_k^{(s)}\right)-\tau\right)!\tau!}$ is the binomial coefficient. Note that introduction of this moving window is to release the memory and computational burden in considering the entire history. On the other hand, due to possible condition changes of the excitation and the underlying structure, it is suitable to consider only the past data points in a reasonable neighborhood of the current time step. It is suggested to use a value for N_w that corresponds to approximately 100 fundamental periods of the structure.

Efficient Screening Criteria

In order to enhance the computational efficiency, an efficient screening rule is introduced. First, a data point is classified as a regular point when $|\varepsilon_{k+1}^{(s)}| \leq \xi_\mathrm{L}$, a conservatively small bound (e.g., $\xi_\mathrm{L} = 2$). On the other hand, a data point is classified as an outlier when $|\varepsilon_{k+1}^{(s)}| \geq \xi_\mathrm{U}$. This bound can be obtained by solving $[1 - 2\Phi(-\xi_\mathrm{U})]^{N_W+1} = 0.5$. As a result, it is given by

$$\xi_\mathrm{U} = -\Phi^{-1}\left[\left(\frac{1}{2} - 2^{-1-\frac{1}{N_\mathrm{W}+1}}\right)\right] \tag{38}$$

where Φ^{-1} is the quantile function which is the inverse function of the CDF of the standard Gaussian random variable. For example, $\xi_\mathrm{U} = 3.9787$ for $N_w = 10{,}000$. It can be easily shown that the outlier probability of the data points with absolute normalized residuals larger than ξ_U is larger than 0.5. Therefore, computation of the outlier probability is necessary only when

the absolute value of the normalized residual of the measurement lies within (ξ_L, ξ_U). This helps to determine efficiently the outlierness for a large portion of data points without computing the outlier probability.

Procedure of the Outlier-Resistant Extended Kalman Filter

The procedure of the OR-EKF is summarized as follows.

Training Process

The initial value of $\sigma_{\varepsilon,1}^{(s)}$ can be estimated as follows:

(i) Implement the EKF for roughly ten fundamental periods of the underlying system.
(ii) Calculate the residuals $|z_k^{(s)} - z_{k|k-1}^{(s)}|$ for these data points (ignoring the first one period of data points), and sort them in the ascending order. Then, the standard deviation $\sigma_{\varepsilon,1}^{(s)}$ can be estimated as the value of the 68-percentile point. This is a robust estimator of the standard deviation for possible presence of outliers.

Operating Process

Compute the ξ_U using Eq. 38 and initialize $R_0^{(s)} = \phi$, an empty set for $s = 1, \ldots, N_o$.

1. Calculate the one-step-ahead predictor $\mathbf{z}_{k+1|k}$ by Eq. 33, the sth element of the normalized residual $|\varepsilon_{k+1}^{(s)}|$ by Eq. 34.
2.
   (a) If $|\varepsilon_{k+1}^{(s)}| \le \xi_L$ (=2), $z_{k+1}^{(s)}$ will be classified as a regular data point.
   (b) If $|\varepsilon_{k+1}^{(s)}| \ge \xi_U$, $z_{k+1}^{(s)}$ will be classified as an outlier.
   (c) When $\xi_L < |\varepsilon_{k+1}^{(s)}| < \xi_U$, calculate Q_{k+1} using Eq. 35 and count η_{k+1} from $R_k^{(s)}$. Then, compute the outlier probability $P_o(z_{k+1}^{(s)})$ using Eq. 37. If $P_o(z_{k+1}^{(s)}) < 0.5$, $z_{k+1}^{(s)}$ will be classified as a regular point. Otherwise, it will be concluded as a suspicious data point, and it will be discarded for identification purpose.
3. According to the outlier detection result in step (2), update the sets $R_{k+1}^{(s)}$, s = 1, …, N_o. If $z_{k+1}^{(s)}$ is an outlier, $R_{k+1}^{(s)} = R_k^{(s)}$.

   If $z_{k+1}^{(s)}$ is a regular point, $R_{k+1}^{(s)} = R_k^{(s)} \cup \{|\varepsilon_{k+1}^{(s)}|\}$ if $n(R_k^{(s)}) < N_W$. Otherwise, $R_{k+1}^{(s)} = R_k^{(s)} \cup \{|\varepsilon_{k+1}^{(s)}|\} - \{|\varepsilon_{old}^{(s)}|\}$, where $|\varepsilon_{old}^{(s)}|$ is the oldest element in the set $R_k^{(s)}$.
4. Update $\sigma_{\varepsilon,k+1}^{(s)}$ with the elements in $R_{k+1}^{(s)}$. This can be done by using recursive formula.
5. Remove the outliers from $\mathbf{z}_{k+1}$ Note that the observation matrix $\mathbf{C}_d$ and the noise covariance matrix $\boldsymbol{\Sigma}_{\mathbf{n},k+1}$ have to be modified accordingly.
6. Update the state vector and the associated covariance matrix using the measurement obtained from step (5) using Eq. 13 to Eq. 15. If all N_0 elements of the (k+1)th data points are suspicious measurements, $\mathbf{y}_{k+1|k+1} = \mathbf{y}_{k+1|k}$ and $\boldsymbol{\Sigma}_{\mathbf{y},k+1|k+1} = \boldsymbol{\Sigma}_{\mathbf{y},k+1|k}$.
7. Continue for the next time step.

One can refer to Mu and Yuen (2014) for numerical examples.

Online Bayesian Model Class Selection

Bayesian model class selection is utilized for selecting the most plausible model class from a set of N_C dynamic model class candidates $C_1, C_2, \ldots, C_{N_C}$ by considering their plausibility $P(C_j|D)$ conditional on the available set of dynamic measurement D (Beck and Yuen 2004; Yuen 2010b):

$$P(C_j|D) = \frac{P(C_j)p(D|C_j)}{p(D)} \tag{39}$$

where the denominator $p(D)$ is the normalizing constant; $P(C_j)$ is the prior plausibility of model class C_j. In general, a noninformative prior can be used, i.e., $P(C_j) = 1/N_C$, where $j = 1,\ldots,N_C$, and $p(D/C_j)$ is the evidence given by

$$p(D|C_j) = \int_{\Theta_j} p(D|\boldsymbol{\theta}; C_j)p(\boldsymbol{\theta}|C_j)d\boldsymbol{\theta} \tag{40}$$

where Θ_j denotes the parameter space of model class C_j. However, direct numerical computation of this integral is in general computationally

prohibitive unless the number of uncertain parameters is very small (say 3 or less). To overcome this computational obstacle, an asymptotic expansion was developed for the globally identifiable cases (Beck and Yuen 2004):

$$p(D|C_j) \approx (2\pi)^{N_j/2} p\left(D|\hat{\boldsymbol{\theta}};C_j\right) p\left(\hat{\boldsymbol{\theta}}|C_j\right) \left|\mathbf{H}_j\left(\hat{\boldsymbol{\theta}}\right)\right|^{-1/2} \tag{41}$$

where N_j is the number of uncertain parameters of model class C_j and $\hat{\boldsymbol{\theta}}$ is the parameter vector that maximizes the posterior PDF, which is proportional to the integrand on the right-hand side of Eq. 40.

In the locally identifiable cases (Katafygiotis and Beck 1998), the product of the likelihood function and the prior PDF can be approximately by weighted Gaussian distributions:

$$p\left(D|\boldsymbol{\theta};C_j\right)p\left(\boldsymbol{\theta}|C_j\right) \approx (2\pi)^{N_j/2} \Sigma_{i=1}^{N_i} p\left(D|\hat{\boldsymbol{\theta}}_i;C_j\right) p\left(\hat{\boldsymbol{\theta}}_i|C_j\right) \left|\mathbf{H}_j\left(\hat{\boldsymbol{\theta}}_i\right)\right|^{-\frac{1}{2}} G\left(\boldsymbol{\theta};\hat{\boldsymbol{\theta}},\mathbf{H}_j\left(\hat{\boldsymbol{\theta}}_i\right)^{-1}\right) \tag{42}$$

where $\hat{\boldsymbol{\theta}}_i$ is the ith local optimal point, $i = 1, \ldots, N_i$, and $G\left(\boldsymbol{\theta};\hat{\boldsymbol{\theta}}_i,\mathbf{H}_j\left(\hat{\boldsymbol{\theta}}_i\right)^{-1}\right)$ denotes the multivariate Gaussian distribution for the random vector $\boldsymbol{\theta}$ with mean $\hat{\boldsymbol{\theta}}_i$ and covariance matrix $\mathbf{H}_j\left(\hat{\boldsymbol{\theta}}_i\right)^{-1}$. Then, the evidence is given as

$$p(D|C_j) \approx (2\pi)^{N_j/2} \Sigma_{i=1}^{N_i} p\left(D|\hat{\boldsymbol{\theta}}_i;C_j\right) p\left(\hat{\boldsymbol{\theta}}_i|C_j\right) \left|\mathbf{H}_j\left(\hat{\boldsymbol{\theta}}_i\right)\right|^{-1/2} \tag{43}$$

For general unidentifiable cases, the evidence integral in Eq. 40 can be computed using the transitional Markov chain Monte Carlo (TMCMC) method (Ching and Chen 2007).

Next, an online Bayesian model class selection algorithm is introduced. It was first developed to model the transportation system of particulate matters (Hoi et al. 2011). The plausibility of model class C_j conditional on the measured data up to the $(k+1)th$ time step $D_{k+1} = \{\mathbf{z}_1, \ldots, \mathbf{z}_{k+1}\}$ can be rewritten into the following form using the Bayes' theorem:

$$P\left(C_j|D_{k+1}\right) = \frac{p\left(\mathbf{z}_{k+1}|D_k;C_j\right)P\left(C_j|D_k\right)}{p(\mathbf{z}_{k+1}|D_k)} \tag{44}$$

where $p(\mathbf{z}_{k+1}|D_k;C_j)$ denotes the evidence of model class C_j conditional on the data of the previous k time steps. The denominator $p(\mathbf{z}_{k+1}|D_k)$ is a normalizing constant that does not depend on the model class. Note that the plausibility $P(C_j|D_0)$ is deduced to the prior plausibility of the model class $P(C_j)$. By using the theorem of total probability, the conditional evidence $p(\mathbf{z}_{k+1}|D_k;C_j)$ can be expressed as

$$p\left(\mathbf{z}_{k+1}|D_k;C_j\right) = \int_{\Theta_j} p\left(\mathbf{z}_{k+1}|\boldsymbol{\theta}_k;D_k;C_j\right)p\left(\boldsymbol{\theta}_k|D_k;C_j\right)\mathrm{d}\boldsymbol{\theta}_k \tag{45}$$

where $\boldsymbol{\theta}_k$ denotes the parameter vector containing all the uncertain parameters of model class C_j at the kth time step and Θ_j denotes the parameter space for model class C_j. The factor $p(\mathbf{z}_{k+1}|\ \boldsymbol{\theta}_k;\ D_k;\ C_j)$ in the integrand is the conditional likelihood function of model class C_j at the $(k+1)th$ time step. It represents the level of data fitting of the model with a given parameter vector $\boldsymbol{\theta}_k$. The second factor in the integrand is the posterior PDF of the parameter vector $\boldsymbol{\theta}_k$ conditional on the previous data points $\mathbf{z}_1, \mathbf{z}_2, \ldots, \mathbf{z}_k$. For globally identifiable cases, an asymptotic expansion of this integral can be obtained in a similar fashion as Eq. 41:

$$p\left(\mathbf{z}_{k+1}|D_k;C_j\right) \approx (2\pi)^{N_j/2} p\left(\mathbf{z}_{k+1}|\boldsymbol{\theta}_k^*|D_k;C_j\right) p\left(\boldsymbol{\theta}_k^*|D_k;C_j\right)\left|\mathbf{H}_j\left(\boldsymbol{\theta}_k^*\right)\right|^{-1/2} \tag{46}$$

where N_j denotes the number of uncertain parameters in model class C_j and $\boldsymbol{\theta}_k^* = \boldsymbol{\theta}_{k|k+1}$ is the parameter vector that maximizes the integrand of Eq. 45 but it will be approximated by $\boldsymbol{\theta}_k^* \approx \boldsymbol{\theta}_{k|k}$. The maximum conditional likelihood of model class C_j evaluated at $\theta_{k|k}$ is given by

$$\begin{aligned} p\left(\mathbf{z}_{k+1}|\boldsymbol{\theta}_k^*; D_k; C_j\right) \\ \approx (2\pi)^{-N_o/2}\left|\mathbf{C}_\mathrm{d}\boldsymbol{\Sigma}_{\mathbf{y},k+1|k}\mathbf{C}_\mathrm{d}^T + \boldsymbol{\Sigma}_{\mathbf{n},k+1}\right|^{-1/2} \\ \times \exp\left[-\frac{1}{2}\left(\mathbf{z}_{k+1} - \mathbf{C}_\mathrm{d}\mathbf{y}_{k+1|k}\right)^T\left(\mathbf{C}_\mathrm{d}\boldsymbol{\Sigma}_{\mathbf{y},k+1|k}\mathbf{C}_\mathrm{d}^T + \boldsymbol{\Sigma}_{\mathrm{n},k+1}\right)^{-1}\left(\mathbf{z}_{k+1} - \mathbf{C}_\mathrm{d}\mathbf{y}_{k+1|k}\right)\right] \end{aligned} \tag{47}$$

The maximum posterior probability density of $\boldsymbol{\theta}_k^*$ conditional on D_k for model class C_j is given by

$$p\left(\boldsymbol{\theta}_k^*|D_k; C_j\right) \approx (2\pi)^{-N_j/2}\left|\boldsymbol{\Sigma}_{\boldsymbol{\theta},k|k}\right|^{-1/2} \tag{48}$$

where $\boldsymbol{\Sigma}_{\boldsymbol{\theta},k|k}$ denotes the covariance matrix of the updated parameters. The matrix $\mathbf{H}_j(\boldsymbol{\theta}_k^*)$ denotes the Hessian matrix of the negative natural logarithm of the integrand in Eq. 45 with respect to the parameter vector, evaluated at $\boldsymbol{\theta}_k^*$:

$$\begin{aligned} \mathbf{H}_j\left(\boldsymbol{\theta}_k^*\right) = -\left[\nabla \ln p\left(\mathbf{z}_{k+1}|\boldsymbol{\theta}_k; D_k; C_j\right)\nabla^\mathrm{T}\right]|_{\boldsymbol{\theta}_k=\boldsymbol{\theta}_{k|k}} \\ + \sum\nolimits_{\theta,\mathrm{k|k}}^{-1} \end{aligned} \tag{49}$$

where ∇ denotes the gradient operator with respect to the parameter vector $\boldsymbol{\theta}_k$. The term $\left[\nabla \ln p\left(\mathbf{Z}_{k+1}\middle|\boldsymbol{\theta}_k; D_k; C_j\right)\nabla^T\right]\Big|_{\boldsymbol{\theta}_k=\boldsymbol{\theta}_{k|k}}$ can be calculated using the finite difference method. Therefore, the conditional evidence in Eq. 46 can be calculated using Eq. 47–49.

Summary

This chapter presented several recent advances in online structural identification using the extended Kalman filter (EKF). First, a Bayesian approach was introduced for online identification of the noise parameters. This approach resolves the divergence problem possibly encountered in the conventional EKF due to improper selection of the noise covariance matrices. Furthermore, the presented approach ensures reliable estimation of the state vector, the structural parameters and their associated uncertainty. This approach allows for the tracking of nonstationary process noise and measurement noise. It estimates the noise parameters recursively for every time step. Then, the outlier-resistant extended Kalman filter (OR-EKF) was presented for robust online outlier detection and structural parametric identification. This method embeds an online outlier detection algorithm into the EKF. It is capable for robust estimation of structural parameters using outlier-contaminated dynamic response data in an online manner. In contrast to other existing robust KF/EKF algorithms, the OR-EKF requires no prior information of the outlier distribution model. Finally, the Bayesian model class selection approach allows for nonparametric online structural identification. This recursive algorithm allows for online model class selection to maintain the optimal balance between the data fitting capability and the robustness to modeling error and measurement noise. Through these recent developments, it is expected that reliable online structural identification using EKF can be achieved.

Cross-References

- ▶ Blind Identification of Output-Only Systems and Structural Damage via Sparse Representations
- ▶ Model Class Selection for Prediction Error Estimation
- ▶ Nonlinear System Identification: Particle-Based Methods
- ▶ Stochastic Structural Identification from Vibrational and Environmental Data

References

Beck JL (2010) Bayesian system identification based on probability logic. Struct Control Health Monit 17(7):825–847

Beck JL, Katafygiotis LS (1998) Updating models and their uncertainties. I: Bayesian statistical framework. J Eng Mech (ASCE) 124(4):455–461

Beck JL, Yuen KV (2004) Model selection using response measurements: Bayesian probabilistic approach. J Eng Mech (ASCE) 130(2):192–203

Ching J, Chen YC (2007) Transitional Markov chain Monte Carlo method for Bayesian model updating, model class selection and model averaging. J Eng Mech (ASCE) 133(7):816–832

Durovic ZM, Kovacevic BD (1999) Robust estimation with unknown noise statistics. IEEE Trans Automat Control 44(6):1292–1296

Franco G, Betti R, Luş H (2004) Identification of structural systems using an evolutionary strategy. J Eng Mech (ASCE) 130(10):1125–1139

Gull SF (1988) Bayesian inductive inference and maximum entropy. In: Skilling J (ed) Maximum entropy and Bayesian methods. Kluwer, Boston, pp 53–74

Hoi KI, Yuen KV, Mok KM (2009) Prediction of daily averaged PM10 concentrations by statistical time-varying model. Atmos Environ 43(16): 2579–2581

Hoi KI, Yuen KV, Mok KM (2011) Iterative probabilistic approach for selection of time-varying model classes. Procedia Eng 14:2585–2592. doi:10.1016/j.proeng.2011.07.325

Jazwinski AH (1970) Stochastic processes and filtering theory. Academic, New York

Jeffreys H (1961) Theory of probability, 3rd edn. Clarendon, Oxford

Kalman RE, Bucy R (1961) New results in linear filtering and prediction theory. J Basic Eng 83:95–108

Katafygiotis LS, Beck JL (1998) Updating models and their uncertainties. II: model identifiability. J Eng Mech (ASCE) 124(4):463–467

Koh CG, Shankar K (2003) Substructural identification method without interface measurement. J Eng Mech (ASCE) 129(7):769–776

Lam HF, Yuen KV, Beck JL (2006) Structural health monitoring via measured Ritz vectors utilizing artificial neural networks. Comput-Aided Civil Infrastruct Eng 21(4):232–241

Mehra R (1970) On the identification of variances and adaptive Kalman filtering. IEEE Trans Automat Control 15:175–184

Mu HQ, Yuen KV (2014) Novel outlier-resistant extended Kalman filter for robust online structural identification. J Eng Mech (ASCE). doi:10.1061/(ASCE)EM.1943-7889.0000810

Muto M, Beck JL (2008) Bayesian updating and model class selection for hysteretic structural models using stochastic simulation. J Vib Control 14(1–2):7–34

Myers K, Tapley B (1976) Adaptive sequential estimation with unknown noise statistics. IEEE Trans Automat Control 21(4):520–523

Papadimitriou C, Fritzen C-P, Kraemer P, Ntotsios E (2011) Fatigue predictions in entire body of metallic structures from a limited number of vibration sensors using Kalman filtering. Struct Control Health Monit 18(5):554–573

Sorensen SW, Sacks JE (1971) Recursive fading memory filters. Inform Sci 3:101–119

Sorenson HW, Alspach DL (1971) Recursive Bayesian estimation using Gaussian sums. Automatica 7(4):465–479

Worden K (1997) Structural fault detection using a novelty measure. J Sound Vib 201(1):85–101

Worden K, Hensman JJ (2012) Parameter estimation and model selection for a class of hysteretic systems using Bayesian inference. Mech Systems Signal Process 32:153–169

Yan WM, Yuen KV, Yoon GL (2009) Bayesian probabilistic approach for the correlations of compressibility index for marine clays. J Geotech Geoenviron Eng (ASCE) 135(12):1932–1940

Yuen KV (2010a) Bayesian methods for structural dynamics and civil engineering. Wiley, New York

Yuen KV (2010b) Recent developments of Bayesian model class selection and applications in civil engineering. Struct Safety 32:338–346

Yuen KV, Katafygiotis LS (2005) Model updating using response measurements without knowledge of the input spectrum. Earthq Eng Struct Dyn 34(2):167–187

Yuen KV, Katafygiotis LS (2006) Substructure identification and health monitoring using noisy response measurements only. Comput-Aided Civil Infrastruct Eng 21(4):280–291

Yuen KV, Kuok SC (2010a) Ambient interference in long-term monitoring of buildings. Eng Struct 32(8):2379–2386

Yuen KV, Kuok SC (2010b) Modeling of environmental influence in structural health monitoring assessment for reinforced concrete buildings. Earthq Eng Eng Vib 9(2):295–306

Yuen KV, Kuok SC (2011) Bayesian methods for updating dynamic models. Appl Mech Rev (ASME) 64(1):010802–1–010802–18

Yuen KV, Mu HQ (2011) Peak ground acceleration estimation by linear and nonlinear models with reduced order Monte Carlo simulation. Comput-Aided Civil Infrastruct Eng 26(1):30–47

Yuen KV, Mu HQ (2012) A novel probabilistic method for robust parametric identification and outlier detection. Probab Eng Mech 30:48–59

Yuen KV, Beck JL, Katafygiotis LS (2006a) Efficient model updating and monitoring methodology using incomplete modal data without mode matching. Struct Control Health Monitor 13(1):91–107

Yuen KV, Beck JL, Katafygiotis LS (2006b) Unified probabilistic approach for model updating and damage detection. J Appl Mech (ASME) 73(4):555–564

Yuen KV, Hoi KI, Mok KM (2007) Selection of noise parameters for Kalman filter. Earthq Eng Eng Vib 6:49–56

Zhou J, Luecke RH (1994) Estimation of the covariances of the process noise and measurement noise for a linear discrete dynamic system. Comput Chem Eng 19(2):187–195

Ambient Vibration Testing of Cultural Heritage Structures

Carmelo Gentile and Antonella Saisi
Department ABC, Politecnico di Milano, Milan, Italy

Synonyms

Operational modal analysis; Operational modal testing

Introduction

Ambient vibration testing (AVT), long-term dynamic monitoring, and operational modal analysis (OMA, i.e., the identification of modal parameters from ambient vibration data) of Cultural Heritage structures are a rather recent topic, and only a limited number of complete investigations are reported in the literature (Jaishi et al. 2003; Bennati et al. 2005; Ivorra and Pallares 2006; Gentile and Saisi 2007, 2013; Pau and Vestroni 2008; Casarin and Modena 2008; Peña et al. 2010; Ramos et al. 2010; Aras et al. 2011; Oliveira et al. 2012). On the other hand, there is a growing interest on this topic since the preservation of Cultural Heritage is of primary concern in many countries all over the world.

AVT and OMA are especially suitable to historic structures for several reasons: (a) the easy and fully nondestructive way of testing, performed by measuring only the structural response under ambient excitation; (b) the sustainability of testing, which does not interfere with the normal use of the structure and does not induce additional loads rather than those due to normal conditions (dead loads, wind, microtremors); and (c) the multiple-input nature of ambient excitation, ensuring that the response includes the contribution of a certain number of modes. It is indeed true that the response of a historic building to ambient excitation is generally low, but this cannot be considered a prohibitive issue as currently highly sensitive and relatively inexpensive accelerometers are available on the market.

In addition, the popularity of operational modal testing and analysis of civil engineering structures has been favored also by the technological advances (i.e., the availability of data acquisition and storage systems, which are fully computer based) and by the large number of output-only modal identification techniques available in the literature (see, e.g., Magalhães and Cunha 2011).

Furthermore, AVT and OMA seem ideal tools to methodologically complement the investigations currently carried out to assess the structural safety of Cultural Heritage structures. Although general rules, which can be applied to all historic constructions, are very difficult to define, it is generally agreed (see, e.g., Binda et al. 2000) that the first phase of a correct diagnostic approach (i.e., the evaluation of the current health state or performance of the building) involves the collection of all the essential information on the geometry of the building, its evolution from the origin to the present state, the construction technologies, the characteristics of masonry texture, the mechanical characterization of the materials, and the evaluation of their state of preservation.

The above documentary and experimental information – as it is suggested also in current Italian Guidelines for the seismic risk mitigation of Cultural Heritage (DPCM 2011) – provide a 1st-level diagnosis, highlighting the overall state of preservation, the presence of local defects and vulnerabilities, as well as the need of possible repair interventions, especially when local issues are detected; in this case, the intervention design should be addressed by simplified local models (see, e.g., Giuffrè 1993; DPCM 2011).

In principle, the previously collected knowledge of the building should be synthesized in

a finite element (FE) model of the structure. The FE model, in turn, should provide a 2nd-level diagnosis since it could be used for evaluating the structural safety under service loads, predicting the performance under exceptional loads (such as earthquakes), and simulating the effects of structural modifications or repair interventions.

However, FE modeling of historic structures is characterized by well-known issues:

(a) The correlation between the results of local tests (which indeed provide the mechanical characterization of the materials) and quantitative parameters to build up global structural capacity models is still an open issue (Binda et al. 2000).
(b) The structural model of a historic structure, even when all the collected information is accurately represented, continues to involve significant uncertainties, e.g., in the material properties (and their distribution) as well as in the boundary conditions. This aspect is especially critical for complex historic buildings evolved in different phases.
(c) FE models are often used, even in refined nonlinear analyses, without experimental validation, and only occasionally the model validation is roughly performed by using few available local data (such as the stress level evaluated in few points through flat-jack tests).

Within this context, one possible key role of AVT and OMA is to provide effective and accurate validation of the FE model prior to its use in numerical analysis, as demonstrated in different studies on temples and monuments (Jaishi et al. 2003; Pau and Vestroni 2008), churches (Casarin and Modena 2008; Ramos et al. 2010; Gattulli et al. 2013), ancient palaces (Aras et al. 2011), towers, and minarets (Bennati et al. 2005; Ivorra and Pallares 2006; Gentile and Saisi 2007, 2013; Peña et al. 2010; Ramos et al. 2010; Oliveira et al. 2012).

In some cases, AVT can possibly help also to limit the number of on-site and laboratory tests, which are time-consuming and cost-ineffective. Other possible applications of ambient vibration-based modal analysis in the field of historic structures include periodic or continuous monitoring in order to evaluate the effects of repair interventions or to perform dynamics-based damage assessment (Ramos et al. 2010).

The present entry, after a review of some output-only modal identification techniques, presents the application of ambient vibration-based modal and structural identification to a historic masonry tower. Subsequently, the role of AVT and OMA in the preservation of Cultural Heritage structures is exemplified in a further application (i.e., the long-term dynamic monitoring of a tower) aimed at (1) evaluating the effects of structural modifications, (2) assessing the influence of environmental effects on natural frequencies, (3) identifying the evolution of damage mechanisms.

Modal Identification from Ambient Vibration Data

As previously pointed out, a large number of output-only modal identification techniques are available in the literature, ranging from the simple *peak picking* technique (PP, Bendat and Piersol 1993) to the more advanced *frequency domain decomposition* (FDD, Brincker et al. 2000) and *stochastic subspace identification* (SSI, van Overschee and De Moor 1996). In this section, the PP, FDD, and SSI techniques are briefly described.

Peak Picking and Frequency Domain Decomposition

The PP and FDD techniques work in frequency domain and are based on the evaluation of the spectral matrix $\mathbf{G}_{yy}(f)$ of the recorded responses:

$$\mathbf{G}_{yy}(f) = \mathrm{E}\left[\boldsymbol{Y}(f)\,\boldsymbol{Y}^{\mathrm{H}}(f)\right] \tag{1}$$

where the vector $\boldsymbol{Y}(f)$ collects the responses in the frequency domain, the superscript $^{\mathrm{H}}$ denotes the Hermitian transpose operation (i.e., complex conjugate matrix transpose), and E denotes expected value. The diagonal terms of the matrix $\mathbf{G}_{yy}(f)$ are the (real valued) auto-spectral

densities (ASD), while the other terms are the (complex) cross-spectral densities (CSD). The spectral matrix $\mathbf{G}_{yy}(f)$ is generally computed by using the modified periodogram method (Welch 1967). According to this approach, an average is made over each recorded signal, divided into M frames of $2n$ samples, where windowing and overlapping are applied.

The principle of the two techniques is easiest illustrated by recalling that any response vector $\boldsymbol{y}(t)$ can be expressed in modal coordinates $\boldsymbol{q}(t)$ as

$$y(t) = \boldsymbol{\phi}_1 q_1(t) + \boldsymbol{\phi}_2 q_2(t) + \ \ldots = \boldsymbol{\Phi}\boldsymbol{q}(t) \quad (2)$$

where $\boldsymbol{\phi}_i$ represents the i-th mode shape vector and $\boldsymbol{\Phi}$ is the mode shape matrix. Hence, the correlation matrix $\mathbf{C}_{yy}(\tau)$ (see, e.g., Bendat and Piersol 1993) of the responses

$$\mathbf{C}_{yy}(\tau) = \mathrm{E}\left[\boldsymbol{y}(t+\tau)\boldsymbol{y}^{\mathrm{T}}(t)\right] \quad (3)$$

becomes

$$\mathbf{C}_{yy}(\tau) = \boldsymbol{\Phi}\mathrm{E}\left[\boldsymbol{q}(t+\tau)\boldsymbol{q}^{\mathrm{T}}(t)\right]\boldsymbol{\Phi}^{\mathrm{T}} = \boldsymbol{\Phi}\mathbf{C}_{qq}(\tau)\boldsymbol{\Phi}^{\mathrm{T}} \quad (4)$$

On the other hand, the spectral matrix may be defined as the Fourier transform of the correlation matrix:

$$\mathbf{G}_{yy}(f) = \mathfrak{I}\left[\mathbf{C}_{yy}(\tau)\right] = \boldsymbol{\Phi}\mathbf{G}_{qq}(f)\boldsymbol{\Phi}^{\mathrm{H}} \quad (5)$$

where $\mathbf{G}_{qq}(f)$ is the spectral matrix of the modal coordinates. It is worth underlining that since the modal coordinates are uncorrelated, the matrix $\mathbf{G}_{qq}(f)$ is diagonal.

The more traditional approach to estimate the modal parameters of a structure is often called *peak picking* method after its key step: the identification of the resonant frequencies as the peaks of ASDs and CSDs. In fact, for a lightly damped structure subjected to a white-noise random excitation, both ASDs and CSDs reach a local maximum at the frequencies corresponding to the system normal modes (Bendat and Piersol 1993); furthermore, if the assumption is introduced of modes having well-separated frequencies, it can be shown (see, e.g., Peeters 2000) that the spectral matrix can be approximated, in the neighborhood of a resonant frequency f_k, as

$$\mathbf{G}_{yy}(f_k) \approx a_k \boldsymbol{\phi}_k \boldsymbol{\phi}_k{}^{\mathrm{H}} \quad (6)$$

where α_k depends on the damping ratio, the natural frequency, the modal participation factor, and the excitation spectra. Equation 6 highlights that (a) each row or column of the spectral matrix at a natural frequency f_k can be considered as an estimate of the mode shape $\boldsymbol{\phi}_k$ at that frequency and (b) the square root of the diagonal terms of the spectral matrix at a natural frequency f_k can be considered as an estimate of the mode shape $\boldsymbol{\phi}_k$ at that frequency.

The PP technique leads to reliable results provided that the basic assumptions of low damping and well-separated modes are satisfied; drawbacks of the method are related to the difficulties in identifying closely spaced modes and damping ratios.

Some refinements or variants of the classic PP technique have been proposed in the literature. For example, Felber (1993) suggested obtaining a "global picture" of the eigenfrequencies by evaluating an appropriate function, called averaged normalized power spectral density (ANPSD). More specifically, only the diagonal elements of the spectral matrix $\mathbf{G}_{yy}(f)$ are considered, normalized, and averaged so that a unique function is obtained, summarizing the information on the "modal" peaks contained in all the ASDs.

The FDD technique (Brincker et al. 2000) involves the singular value decomposition (SVD) of the spectral matrix at each frequency and the inspection of the curves representing the singular values, in order to identify the resonant frequencies and to estimate the corresponding mode shape using the information contained in the singular vectors of the SVD.

The SVD of the spectral matrix at each frequency is given by

$$\mathbf{G}_{yy}(f) = \mathbf{U}(f)\boldsymbol{\Sigma}(f)\mathbf{U}^{\mathrm{H}}(f) \quad (7)$$

where the diagonal matrix $\boldsymbol{\Sigma}$ collects the real positive singular values in descending order and $\mathbf{U}$ is a complex matrix containing the singular

vectors as columns. The SVD is used for estimating the rank of $\mathbf{G}_{yy}$ at each frequency with the number of nonzero singular values being equal to the rank; if only one mode is important at a given frequency f_k, as it has to be expected for well-separated modes, the spectral matrix can be approximated by a rank-one matrix:

$$\mathbf{G}_{yy}(f) \approx \boldsymbol{u}_1(f)\sigma_1(f)\boldsymbol{u}_1{}^{H}(f) \tag{8}$$

By comparing Eq. 5 with Eq. 7, it is evident that (if the mode shapes are orthogonal) Eq. 5 is an SVD of the spectral matrix. Furthermore, the comparison of Eqs. 6 and 8 clearly reveals that the first singular vector $\boldsymbol{u}_1(f)$ is an estimate of the mode shape. Since the first singular value $\sigma_1(f)$ at each frequency represents the strength of the dominating vibration mode at that frequency, the first singular function can be suitably used as a modal indication function (yielding the resonant frequencies as local maxima). In addition, the successive singular values contain either noise or modes close to a strong dominating one.

The FDD is a rather simple procedure that represents an improvement of the PP because:

1. The SVD is an effective method for separating signal space from noise space, and the evaluation of mode shapes is automatic and significantly easier than in the PP.
2. The FDD technique is able to detect closely spaced modes. In such instances, more than one singular value will reach a maximum in the neighborhood of a given frequency, and every singular vector corresponding to a nonzero singular value is a mode shape estimate. The latter, however, is valid in the strict sense for orthogonal modes.
3. The damping ratios can be identified through the refinement of the FDD technique, namely, the *enhanced frequency domain decomposition* (EFDD, Brincker et al. 2001). The EFDD technique is based on the fact that the first singular value in the neighborhood of a resonant peak is the ASD of a modal coordinate. Hence, moving the partially identified ASD of the modal coordinate back in the time domain by inverse FFT yields a free decaying time domain function, which represents the autocorrelation function of the modal coordinate. The natural frequency and the related damping ratio are thus simply found by estimating crossing times and employing the logarithmic decrement method.

Stochastic Subspace Identification

The SSI technique lies in the class of time domain methods and is based on the discrete-time stochastic state-space form of the dynamics of a linear time-invariant system under unknown excitation.

The continuous-time state-space equation of motion of a linear time-invariant system can be written as

$$\dot{x}(t) = \mathbf{A}_c x(t) + \mathbf{B}_c f(t) \tag{9}$$

$$\mathbf{A}_c = \begin{bmatrix} \mathbf{0} & \mathbf{I} \\ -\mathbf{M}^{-1}\mathbf{K} & -\mathbf{M}^{-1}\mathbf{C}_1 \end{bmatrix} \quad \mathbf{B}_c = \begin{bmatrix} \mathbf{0} \\ \mathbf{M}^{-1} \end{bmatrix} \tag{10}$$

where

- $x(t) = \begin{bmatrix} \boldsymbol{u}(t)^{T} & \dot{\boldsymbol{u}}(t)^{T} \end{bmatrix} \in \Re^{2N\times 2N}$ is the state vector of the process, containing the displacement $\boldsymbol{u}(t)$ and the velocity $\dot{\boldsymbol{u}}(t)$ vectors.
- $\mathbf{A}_c \in \Re^{2N \times 2N}$ is the continuous-time state matrix, which is related to the matrices of mass $\mathbf{M}$, damping $\mathbf{C}_1$, and stiffness $\mathbf{K}$.
- $\boldsymbol{f}(t) \in \Re^{N}$ is the load vector and $\mathbf{B}_c \in \Re^{2N \times 2N}$ is the system control influence coefficient matrix.
- The subscript c denotes continuous time.

It should be noticed that the eigenvalues $\boldsymbol{\Lambda}_c$ and eigenvectors $\boldsymbol{\Psi}$ of the state-space matrix $\mathbf{A}_c$ (solving the eigenvalue problem $\mathbf{A}_c\boldsymbol{\Psi} = \boldsymbol{\Psi}\boldsymbol{\Lambda}_c$) contain the eigenvalues and the eigenvectors of the original second-order system $\mathbf{M}\ddot{\boldsymbol{u}}(t) + \mathbf{C}_1\dot{\boldsymbol{u}}(t) + \mathbf{K}\boldsymbol{u}(t) = \boldsymbol{f}(t)$.

In dynamic testing, only a subset L of the N responses are measured; hence, the vector of measured outputs $\boldsymbol{y}(t) \in \Re^{L}$ can be expresses as

$$\boldsymbol{y}(t) = \mathbf{C}_a\ddot{\boldsymbol{u}}(t) + \mathbf{C}_v\dot{\boldsymbol{u}}(t) + \mathbf{C}_d\boldsymbol{u}(t) \tag{11}$$

where $\mathbf{C}_a$, $\mathbf{C}_v$, and $\mathbf{C}_d$ are the output location matrices for accelerations, velocity, and displacements, respectively. These matrices contain a lot of zeros and a few unit entries since they are formulated in order to assign the measured degrees of freedom. The vector $\boldsymbol{y}(t)$ can be written as

$$\boldsymbol{y}(t) = \mathbf{C}_c\,\boldsymbol{x}(t) + \mathbf{D}_c\boldsymbol{f}(t) \tag{12}$$

$$\begin{aligned}\mathbf{C}_c &= \left[\mathbf{C}_d - \mathbf{C}_a\mathbf{M}^{-1}\mathbf{K}, \quad \mathbf{C}_v - \mathbf{C}_a\mathbf{M}^{-1}\mathbf{C}_1\right]\\ \mathbf{D}_c &= \mathbf{C}_a\mathbf{M}^{-1}\end{aligned} \tag{13}$$

By combining the state Eq. 9 and the observation Eq. 12, the classical continuous-time state-space model is found:

$$\begin{cases}\dot{\boldsymbol{x}}(t) = \mathbf{A}_c\boldsymbol{x}(t) + \mathbf{B}_c\boldsymbol{f}(t)\\ \boldsymbol{y}(t) = \mathbf{C}_c\boldsymbol{x}(t) + \mathbf{D}_c\boldsymbol{f}(t)\end{cases} \tag{14}$$

Since real measurements are taken at discrete-time instants and in order to fit model Eq. 14 to the measurements, this model needs to be converted into discrete time. Hence, assuming a constant sampling period Δt and that the input is piecewise constant over the sampling period, the continuous-time equations (Eq. 14) are discretized and solved at all discrete-time instants $t_k = k\Delta t$, obtaining the discrete-time state-space model:

$$\begin{cases}\boldsymbol{x}_{k+1} = \mathbf{A}\,\boldsymbol{x}_k + \mathbf{B}\boldsymbol{f}_k\\ \boldsymbol{y}_k \;\;= \mathbf{C}\,\boldsymbol{x}_k + \mathbf{D}\boldsymbol{f}_k\end{cases} \tag{15}$$

where $\boldsymbol{x}_k$ is the discrete-time state vector (containing displacements and velocities describing the state of the system at time instant $t_k = k\Delta t$), $\boldsymbol{f}_k$ and $\boldsymbol{y}_k$ are the sampled input and output vectors, $\mathbf{A}$ is the discrete state matrix (dependent on the mass, stiffness, and damping properties of the structure), $\mathbf{B}$ is the discrete input matrix, $\mathbf{C}$ is the discrete output matrix (which maps the state vector into the measured output), and $\mathbf{D}$ is the direct transmission matrix. The matrices $\mathbf{A}$, $\mathbf{B}$, $\mathbf{C}$, and $\mathbf{D}$ are related to their continuous-time counterparts Eq. 10 and Eq. 13 by the following:

$$\begin{aligned}\mathbf{A} &= e^{\mathbf{A}_c\Delta t} \quad \mathbf{B} \;\; = \;\; (\mathbf{A} - \mathbf{I})\mathbf{A}_c^{-1}\mathbf{B}_c\\ \mathbf{C} &= \mathbf{C}_c \quad \mathbf{E} = \mathbf{E}_c\end{aligned} \tag{16}$$

It is finally observed that the deterministic model (Eq. 15) is not capable of exactly describing real measurement data; consequently, Eq. 15 needs to be modified to account for both the process noise $\boldsymbol{w}_k \in \Re^{2N}$ due to disturbances and modeling inaccuracies and the measurement noise $\boldsymbol{v}_k \in \Re^{L}$ due to sensor inaccuracy:

$$\begin{cases}\boldsymbol{x}_{k+1} \;\; = \;\; \mathbf{A}\,\boldsymbol{x}_k + \mathbf{B}\boldsymbol{f}_k + \boldsymbol{w}_k\\ \boldsymbol{y}_k \;\;\; = \;\; \mathbf{C}\,\boldsymbol{x}_k + \mathbf{D}\boldsymbol{f}_k + \boldsymbol{v}_k\end{cases} \tag{17}$$

Furthermore, both $\boldsymbol{w}_k$ and $\boldsymbol{v}_k$ are unmeasurable vectors, assumed to be zero mean, white, and with covariance matrices:

$$\mathrm{E}\left[\begin{pmatrix}\boldsymbol{w}_p\\ \boldsymbol{v}_p\end{pmatrix}\begin{pmatrix}\boldsymbol{w}_p^T & \boldsymbol{v}_p^T\end{pmatrix}\right] = \begin{bmatrix}\mathbf{Q} & \mathbf{S}\\ \mathbf{S}^T & \mathbf{R}\end{bmatrix}\delta_{pq} \tag{18}$$

It is very important to remark that an AVT provides information only on the vibration responses of a structure excited by unmeasured inputs. Consequently, it is impossible to distinguish the input term $\boldsymbol{f}_k$ from the noise terms $\boldsymbol{w}_k$ and $\boldsymbol{v}_k$ in Eq. 17. This results in the following discrete-time stochastic state-space model:

$$\begin{cases}\boldsymbol{x}_{k+1} = \mathbf{A}\,\boldsymbol{x}_k + \boldsymbol{w}_k\\ \boldsymbol{y}_k \;\;\; = \;\; \mathbf{C}\,\boldsymbol{x}_k + \boldsymbol{v}_k\end{cases} \tag{19}$$

where the input is implicitly modeled by the noise terms and the white noise assumption of these terms turns out to be essential: if the white noise assumption is violated because the input contains some dominant frequency components, these frequency components cannot be distinguished from the eigenfrequencies of the system (of the state matrix $\mathbf{A}$).

The key step of the SSI techniques is the estimation of the state-space matrices $\mathbf{A}$ and $\mathbf{C}$ from the measured output $\boldsymbol{y}_k$. The estimation of $\mathbf{A}$ and $\mathbf{C}$ can be performed by using different algorithms. The well-known data-driven SSI algorithms are based on linear algebra theorems

(van Overschee and De Moor 1996) demonstrating that the state-space matrices can be calculated from the knowledge of the block Hankel matrix of the measurements, defined as

$$\mathbf{H}_i = \left(\begin{array}{cccc} \boldsymbol{y}_0 & \boldsymbol{y}_1 & \cdots & \boldsymbol{y}_{j-1} \\ \boldsymbol{y}_1 & \boldsymbol{y}_2 & \cdots & \boldsymbol{y}_j \\ \vdots & \vdots & \ddots & \vdots \\ \boldsymbol{y}_{i-1} & \boldsymbol{y}_i & \cdots & \boldsymbol{y}_{i+j-2} \\ \hline \boldsymbol{y}_i & \boldsymbol{y}_{i+1} & \cdots & \boldsymbol{y}_{i+j-1} \\ \boldsymbol{y}_{i+1} & \boldsymbol{y}_{i+2} & \cdots & \boldsymbol{y}_{i+j} \\ \vdots & \vdots & \ddots & \vdots \\ \boldsymbol{y}_{2i-1} & \boldsymbol{y}_{2i} & \cdots & \boldsymbol{y}_{2i+j-2} \end{array}\right) = \left(\begin{array}{c} \mathbf{Y}_p \\ \hline \mathbf{Y}_f \end{array}\right) \tag{20}$$

where 2i and j are user-defined quantities, representing the number of output block rows and the number of columns of matrix $\mathbf{H}_i$, respectively.

In Eq. 2, the block Hankel matrix of the measurements is subdivided into two sub-matrices, named as $\mathbf{Y}_p$ and $\mathbf{Y}_f$, which are usually referred to as past and future output block matrices. The orthogonal projection of the row space of $\mathbf{Y}_f$ onto the row space of $\mathbf{Y}_p$ can be directly calculated yielding to matrix $\mathbf{P}_i$, which is known as projection matrix. The observability matrix $\mathbf{O}_i$ of the system – which, in turn, allows to compute $\mathbf{A}$ and $\mathbf{C}$ – can be estimated from the SVD of matrix $\mathbf{W}_1\mathbf{P}_i\mathbf{W}_2$, where $\mathbf{W}_1$ and $\mathbf{W}_2$ are convenient weight matrices. The available SSI-data algorithms essentially differ for the expressions of the weight matrices (van Overschee and De Moor 1996).

After estimating the model matrices, the modal parameters f_i, ζ_i, and $\boldsymbol{\phi}_i$ of the structural system are calculated from

$$\mathbf{A} = \boldsymbol{\Psi}\boldsymbol{\Lambda}\boldsymbol{\Psi}^{-1} \tag{21a}$$

$$\boldsymbol{\Lambda} = \operatorname{diag}(\lambda_i) \quad \lambda_i^c = \frac{\ln\lambda_i}{\Delta t} \tag{21b}$$

$$f_i = \frac{\left|\lambda_i^c\right|}{2\pi} \quad \varsigma_i = \frac{\operatorname{real}\left(\lambda_i^c\right)}{\left|\lambda_i^c\right|} \tag{21c}$$

$$\boldsymbol{\Phi} = [\boldsymbol{\phi}_1, \boldsymbol{\phi}_2, \ldots, \boldsymbol{\phi}_i, \ \ldots] = \mathbf{C}\,\boldsymbol{\Psi} \tag{21d}$$

It is further noticed that the order 2N of the model should equal, in principle, twice the number of modes that are needed to accurately describe the structural response. However, with the purpose of detecting weakly excited modes, it is often necessary to consider more than 2 N values, which are what would be physically sufficient. On the other hand, over-modeling leads to the appearance of spurious modes associated with the noise content of the measurements. A common practice for identifying the physical modes is based on the creation of the stabilization diagrams, where the modal parameters obtained for increasing model orders are collectively represented. A physical mode is conceivably identified when consistent frequencies, damping, and mode shapes (classified as stable poles) are obtained for models of increasing order.

Ambient Vibration Testing and Structural Identification of a Historic Masonry Tower

Description of the Tower

The first investigated historic building is a bell tower (Fig. 1), about 37.0 m high and built in stonework masonry (Gentile and Saisi 2013). The tower – located in the small town of Arcisate (northern Italy) – has a square cross section, with sides of 5.8 m, and is connected to the church *Chiesa Collegiata* on the East side and partly on the South side. The church, dedicated to St. Vittore, dates back to the fifteenth century and replaced a more ancient church, built in the fourth century and modified in the eleventh century. Probably the tower foundation dates back to the late Roman age, as well.

The first historic document concerning the tower goes back to the sixteenth century and reports St. Carlo Borromeo's request of access modification. Seven orders of floors are present, with five of them being defined by masonry offsets at the corners and by corresponding sequences of small hanging arches marking the floor levels; the last two orders were probably added in the eighteenth century to host the bell trusses. The wall thickness decreases

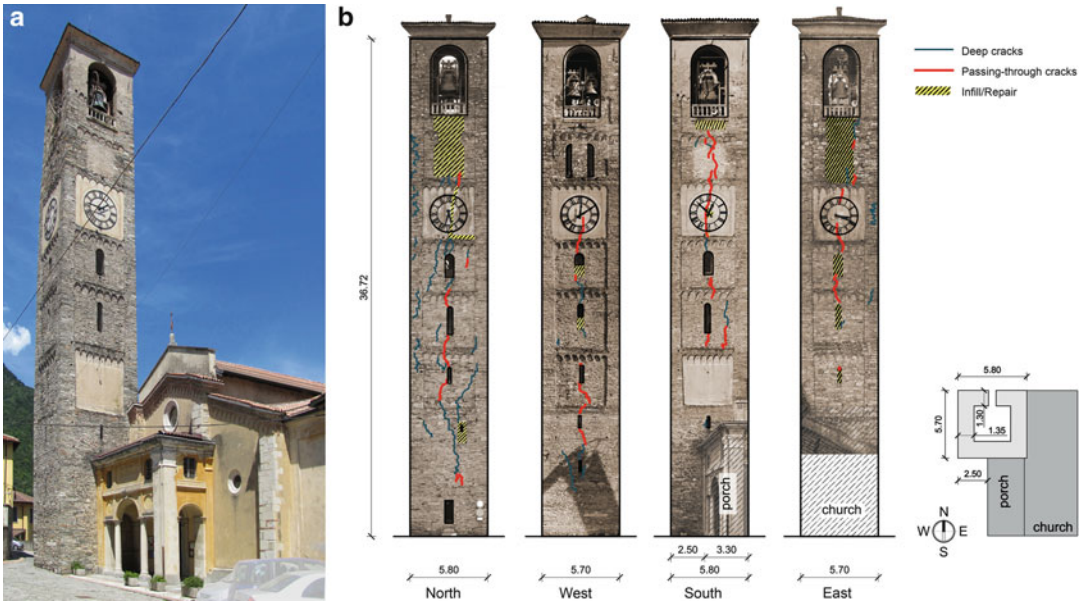

Ambient Vibration Testing of Cultural Heritage Structures, Fig. 1 (**a**) View of the bell tower of *Chiesa Collegiata* (Arcisate, Varese); (**b**) crack patterns on the fronts of the tower (dimensions in m)

progressively along the height, from 135 cm at the ground level up to 65 cm at the top level.

Although extensive visual inspections and few sonic tests generally indicate that the stone masonry is relatively compact and of fairly good execution, the masonry texture appears locally often highly disordered and characterized by the local presence of vertical joints.

The crack pattern (Fig. 1b) has been accurately surveyed also by using an aerial platform. The tower exhibits long vertical cracks on every side, most of them cutting the entire wall thickness and passing through the keystones of the arch window openings. These cracks are mainly distributed between the second/third order of the tower. Many superficial cracks are also diffused, particularly on the North and West fronts, which are not adjacent to the church.

The visual inspection highlighted that the upper part of the tower, beneath the belfry level, could be probably considered the most vulnerable, due to the widespread mortar erosion and the infilled openings (Fig. 1b), mainly on the East and North fronts; in addition, the infillings are often not properly linked to the surrounding load-bearing masonry.

Ambient Vibration Testing Procedures and Modal Identification

The dynamic tests were carried out in June 2007, using a 16-channel data acquisition system and WR 731A piezoelectric accelerometers (10 V/g sensitivity and 0.5 g peak acceleration). Each accelerometer was connected with a short cable (1 m) to a WR P31 power unit/amplifier, providing the constant current needed to power the accelerometer's internal amplifier, signal amplification, and selective filtering.

The response of the tower was measured in 15 selected points, belonging to 5 different cross sections along the height of the building, according to the sensor layout illustrated in Fig. 2a. Figure 2b shows the mounting of accelerometers in the instrumented cross section at level +22.78 m.

The acceleration time histories induced by ambient excitation were recorded for 3,600 s at a sampling frequency of 200 Hz. A sample of the acceleration time histories recorded during the test in the upper part of the tower is shown in Fig. 3: it should be noticed that very low level of ambient excitation was present during the tests, with the maximum recorded acceleration being always lower than 0.4 cm/s^2.

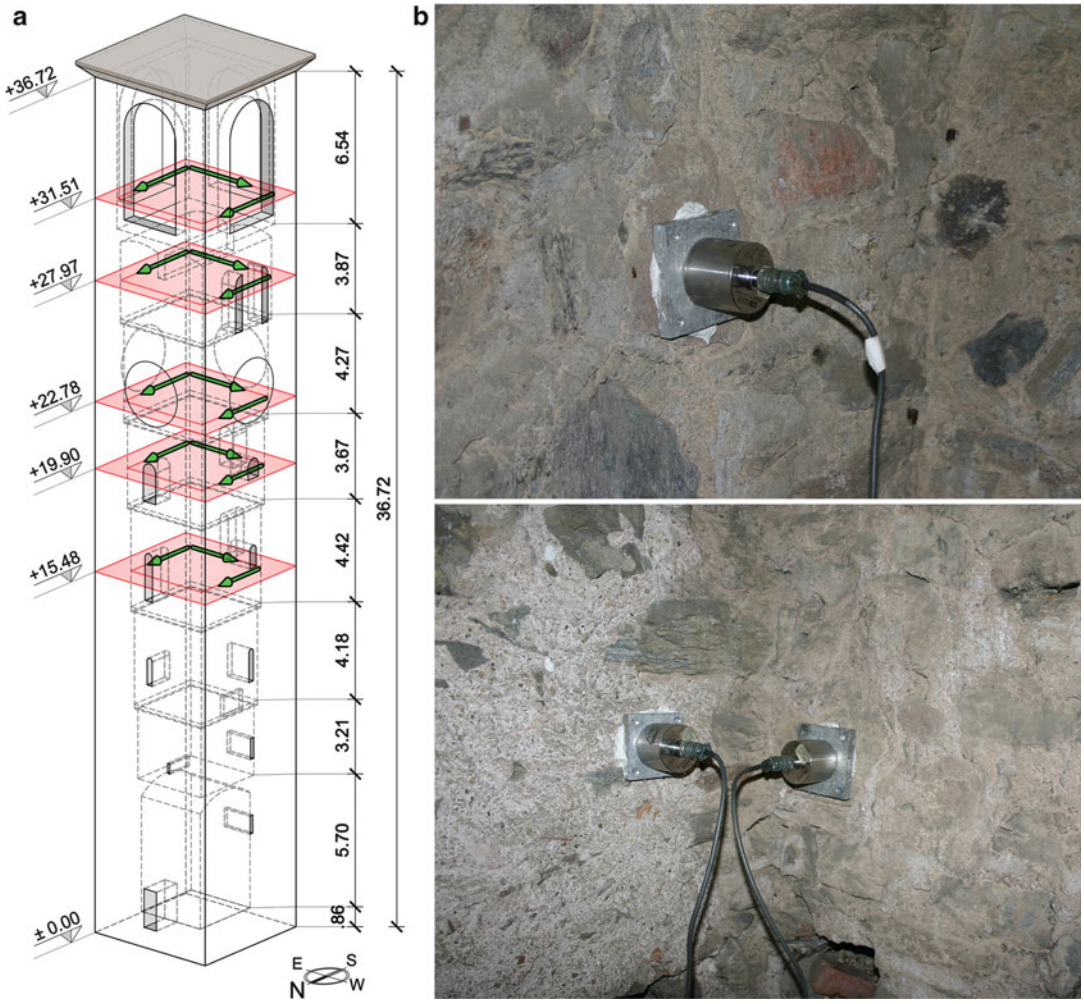

Ambient Vibration Testing of Cultural Heritage Structures, Fig. 2 (**a**) Sensor layout adopted in the dynamic tests (dimensions in m), (**b**) mounting of the accelerometers at level +22.78 m

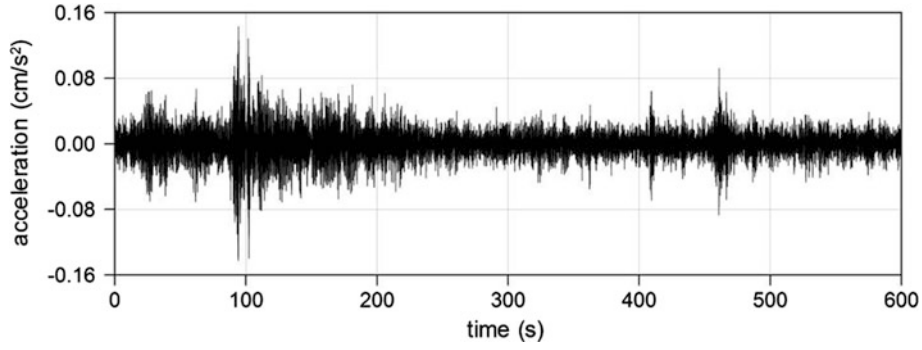

Ambient Vibration Testing of Cultural Heritage Structures, Fig. 3 Typical acceleration time series measured at the upper instrumented level

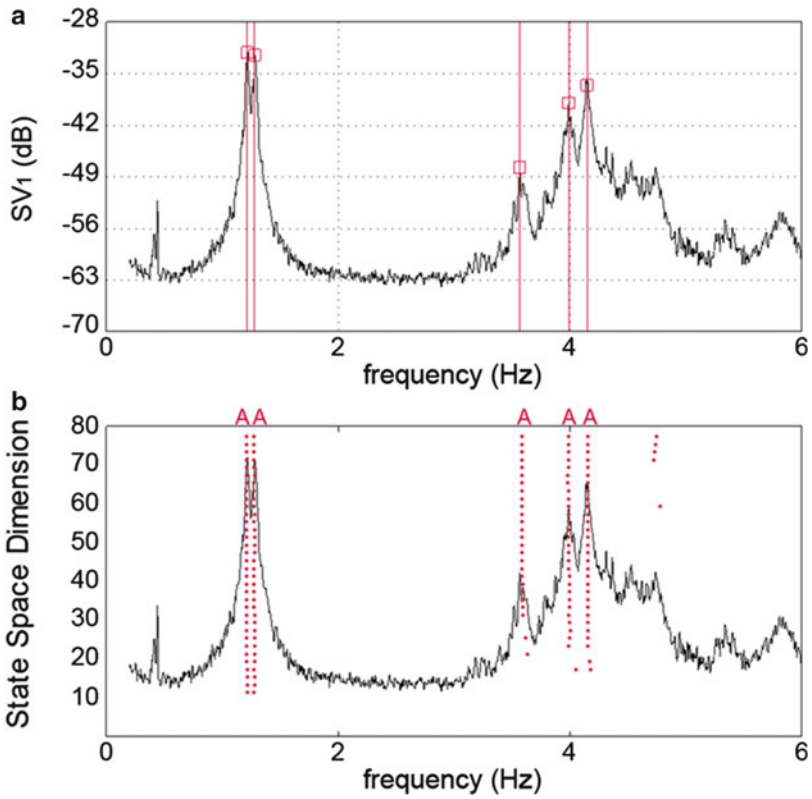

Ambient Vibration Testing of Cultural Heritage Structures, Fig. 4 (**a**) First singular value (*SV*) curve and identification of natural frequencies (*FDD*), (**b**) stabilization diagram and automatic (*A*) identification of natural frequencies (*SSI*)

The modal identification was performed using time windows of 3,600 s, in order to comply with the widely agreed recommendation of using an appropriate duration of the acquired time window (ranging between 1,000 and 2,000 times the fundamental period of the structure; see, e.g., Cantieni 2005) to obtain accurate estimates of the modal parameters from OMA techniques. In fact, as already pointed out in section "Modal Identification from Ambient Vibration Data," OMA methods assume that the excitation input is a zero mean Gaussian white noise, and this assumption is as closely verified as the length of the acquired time window is longer.

The extraction of modal parameters from ambient vibration data was carried out using the FDD and the data-driven SSI techniques available in the commercial software ARTeMIS (SVS 2012). Notwithstanding the very low level of ambient response (Fig. 3) that existed during the tests, the application of both techniques allowed to identify five vibration modes in the frequency range of 0–6 Hz.

The results of OMA in terms of natural frequencies can be summarized through the plots of Fig. 4a, b, showing the first singular value (SV) of the spectral matrix and the stabilization diagrams obtained by applying the FDD and the SSI technique, respectively. The inspection of Fig. 4a highlights that the FDD technique provides a clear indication of the tower modes through well-defined local maxima in the first SV; similarly, Fig. 4b shows that the alignments of the stable poles in the stabilization diagram of the SSI method provide a clear indication of these modes, as well. Furthermore, Fig. 4a, b shows the correspondence of the natural frequency estimates between the two techniques, with the resonant peaks of Fig. 4a being placed practically at the same frequencies of the alignments of stable poles in Fig. 4b.

As it had to be expected, the identified modes can be classified as bending and torsion. Figure 5 shows the identified mode shapes (SSI technique): dominant bending (B) modes were identified at 1.22 (B1), 1.28 (B2), 4.01 (B3), and

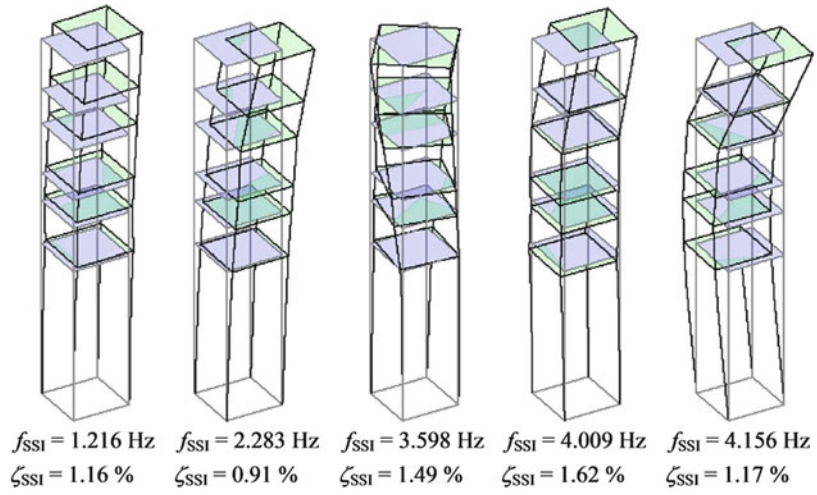

Ambient Vibration Testing of Cultural Heritage Structures, Fig. 5 Vibration modes identified from ambient vibration data (SSI)

4.16 Hz (B4), while only one torsion mode (T1) was identified at 3.60 Hz. It is observed that the dominant bending modes of the tower involve flexure practically along the diagonals.

FE Modeling and Model Tuning

A 3D structural model (Fig. 6) of the tower was developed (using the FE program Straus7), based on the available geometric survey.

The tower was modeled using 8-node brick elements. A relatively large number of finite elements have been used in the model, so that a regular distribution of masses could be obtained, and all the geometric variations and openings in the load-bearing walls could be reasonably represented. The model consists of 3,475 solid elements with 17,052 active degrees of freedom.

Since the geometry of the tower was surveyed on site and accurately described in the model, the main uncertainties are related to the characteristics of the material and boundary conditions. In order to reduce the number of uncertainties in the model calibration, the following initial assumptions were introduced: (a) homogeneous distribution of the masonry elastic properties; (b) the weight per unit volume of the masonry and Poisson's ratio of the masonry were assumed as 17.0 kN/m^3 and 0.15, respectively; and (c) the tower footing was considered as fixed since the soil-structure interaction is hardly

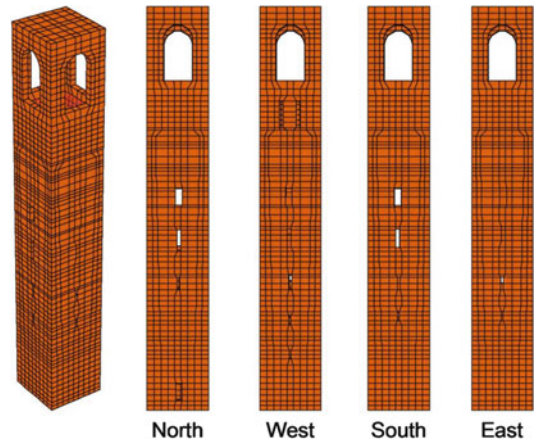

Ambient Vibration Testing of Cultural Heritage Structures, Fig. 6 Finite element model of the tower

involved at the low level of ambient vibrations that existed during the tests.

Under the above assumptions, a sensitivity analysis (see, e.g., Maia and Silva 1997) pointed out that sensitive parameters were (1) the average Young's modulus E of stone masonry, since all natural frequencies are very sensitive to its variation; (2) the ratio $\alpha = G/E$, implying the assumption of orthotropic material and significantly affecting the natural frequency of the torsion mode; (3) the connection between the tower and the neighboring building (represented by linear nodal springs), which highly affects the bending mode shapes.

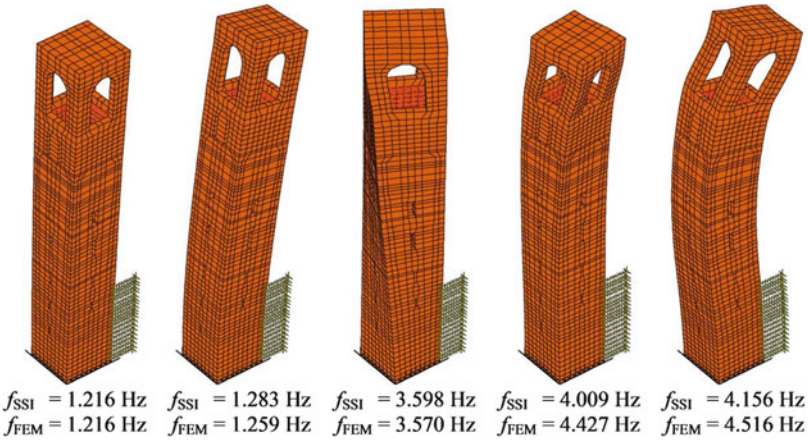

Ambient Vibration Testing of Cultural Heritage Structures, Fig. 7 Vibration modes of the initial model

Hence, three steps of manual tuning were carried out to establish a base FE model. In the base model, the following assumptions were adopted:

1. An orthotropic elastic behavior was assumed for the stone masonry, with the average characteristics of the material being $E = 3.00$ GPa and $G_{13} = G_{23} = 0.45$ GPa (corresponding to $\alpha = G_{13}/E = G_{23}/E = 0.15$). It is worth noting that the assumed Young's modulus was in good agreement with the results of the tests performed to characterize the masonry and reported in (Binda et al. 2012): more specifically, the average sonic velocity (P waves) varied between 1,620 and 2,240 m/s^2, and the values measured by double flat-jack tests at the base of the tower were slightly larger than 3.00 GPa.
2. The effects of the connection between the tower and the church were accounted for through a series of linear (nodal) springs of constant k. After tuning the parameter k in a preselected interval (1×10^4 kN/m $\leq k \leq 10 \times 10^4$ kN/m), the value $k = 4 \times 10^4$ kN/m was assumed since it tends to minimize the average difference between the measured and predicted modal frequencies.

Figure 7 illustrates the dynamic characteristics of the base model and highlights that the mode shapes are fully consistent with the experimental results (Fig. 5). Furthermore, the correspondence with the identified frequencies is fairly good for the first three modes. The discrepancy is conceivably related to the simplified distribution of the model elastic properties.

As suggested by the mode shapes, the higher bending modes depend on the elastic characteristics of the masonry in the upper part of the tower. In addition, as pointed out in section "Description of the Tower,", the upper region is characterized by a more evident mortar joint erosion and changes of the masonry texture including wide infilled openings on the East and North fronts, beneath the belfry level.

Hence, the distribution of Young's modulus was updated, and the tower was divided in two regions, with the masonry Young's modulus being assumed as constant within each zone. The two regions, denoted as I and II, correspond to the lower five levels of the building (E_I, h $\leq$ 26.0 m, including a large number of passing-through cracks) and the upper part (E_{II}, h $>$ 26.0 m, including infilled/repaired areas and the belfry), respectively. The possible set of updating parameters includes E_I, E_{II}, α, and k. It should be noticed that assuming only one parameter α means that the ratio between the shear moduli in the two regions of the tower equals to the ratio between Young's moduli.

Subsequently, the optimal values of the updating structural parameters were determined. Among the different classes of procedures available in the literature (see, e.g., Friswell and Mottershead 1995), it was decided to evaluate the updating parameters by minimizing the

Ambient Vibration Testing of Cultural Heritage Structures, Table 1 Structural parameters for FE model identification

Structural parameter	Base value	Upper value	Base value	Optimal value
E_{I} (height $\leq$ 26 m) (GPa)	2.0	4.0	3.0	2.97
E_{II} (height $>$ 26 m) (GPa)	1.0	3.0	2.0	1.60
α	0.110	0.190	0.150	0.172
k (kN/m)	1.0×10^4	10.0×10^4	4.0×10^4	8.30×10^4

difference between theoretical and experimental natural frequencies, through the simple procedure proposed in (Douglas and Reid 1982). According to this approach, the dependence of the natural frequencies of the model on the unknown structural parameters X_k ($k = 1, 2, \ldots, N$) is approximated around the current values of X_k, by the following:

$$f_i^*(X_1, X_2, \ldots, X_N) = \sum_{k=1}^{N} \left[A_{i,k} X_k + B_{i,k} X_k^2\right] + C_i \tag{22}$$

where f_i^* represents the approximation of the i-th frequency of the FE model. Once the set of approximating functions Eq. 22 has been established, the structural parameters of the model are evaluated by a least-square minimization of the difference between each f_i^* and its experimental counterpart $f_{\mathrm{i}}^{\mathrm{EXP}}$:

$$J = \sum_{i=1}^{M} w_i \varepsilon_i^2 \tag{23a}$$

$$\varepsilon_i = f_i^{\mathrm{EXP}} - f_i^*(X_1, X_2, \ldots, X_{\mathrm{N}}) \tag{23b}$$

where w_i is a weight constant. However, Eq. 22 represents a reasonable approximation in a range, around the "base" value of the structural parameters $X_k{}^B$, limited by lower $X_k{}^L$ and upper values $X_k{}^U$ ($k = 1, 2, \ldots, N$); thus, the coefficients A_{ik}, B_{ik}, C_i are dependent on both the base value of the structural parameters and the range in which these parameters can vary. The coefficients A_{ik}, B_{ik}, C_i are readily evaluated from ($2N + 1$) finite element analyses (Douglas and Reid 1982), each with a different choice of the parameters: the first choice of the parameters corresponds to the base values; then each parameter is varied, one at time, from the base value to upper and lower limit, respectively.

It is further noticed that, in principle, the quadratic approximation Eq. 22 is as better as the base values are closer to the solution; hence, the accuracy and stability of the optimal estimates should be carefully checked either by the complete correlation with the experimental data or by repeating the procedure with new base values.

Table 1 summarizes the optimal estimates of the structural parameters, the base values, and the assumed lower and upper limits. By examining the optimal values in Table 1, the following comments can be made: (a) the optimal values of the elastic parameters in the lower region ($E_{\mathrm{I}} = 2.97$ GPa, $G^{\mathrm{I}}{}_{13} = G^{\mathrm{I}}{}_{23} = \alpha \times E_{\mathrm{I}} = 0.172 \times 2.97 \cong 0.51$ GPa) are very similar to those of the base model; (b) the optimal estimates of the elastic parameters in the upper region ($E_{\mathrm{II}} = 1.60$ GPa, $G^{\mathrm{II}}{}_{13} = G^{\mathrm{II}}{}_{23} = \alpha \times E_{\mathrm{II}} = 0.172 \times 1.60 \cong 0.28$ GPa) turned out to be lower than the ones in the lower part, reflecting the observed state of preservation in that region; and (c) the stiffness of the springs becomes larger than in the base model to better fit the ratio between the natural frequencies of the first two modes.

Figure 8 shows the mode shapes of the updated model, corresponding to the experimental ones (Fig. 5), and the correlation with the measured modal behavior. It should be noticed that the updated model represents an excellent approximation of the real structure, with the maximum relative error between predicted and measured modal frequencies being larger than 1 % only for mode B3.

Furthermore, also the correlation between mode shapes – estimated via the MAC (Allemang and Brown 1983) – is very good for

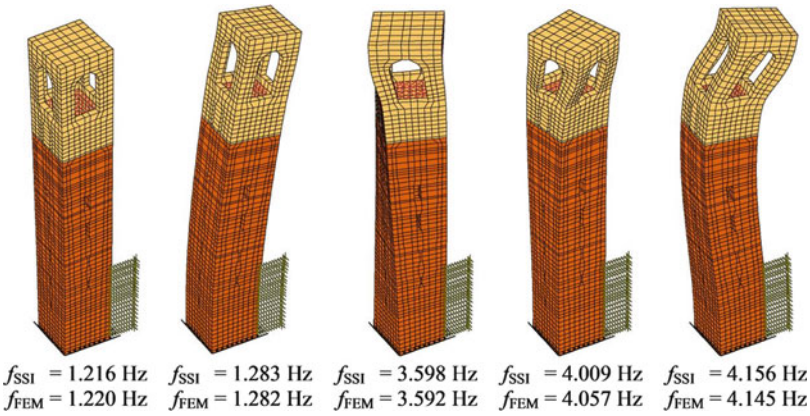

Ambient Vibration Testing of Cultural Heritage Structures, Fig. 8 Vibration modes of the optimal (updated) model

Ambient Vibration Testing of Cultural Heritage Structures, Fig. 9 Views of the *Gabbia Tower* (Mantua, Italy) from South and East

the first two modes (with the MAC being larger than 0.96); for the higher modes, the MAC is in the range 0.711–0.845 so that appreciable average differences are detected and again related to the simplified distribution of the model elastic properties, which were held constant for large regions of the tower.

Ambient Vibration Testing and Dynamic Monitoring of a Historic Masonry Tower

After the Italian earthquakes of May 2012, an extensive research program has been performed to assess the state of preservation of the tallest historic tower in Mantua, Italy. The investigated tower (Fig. 9), about 54.0 m high and dating back to the twelfth century, is known as the *Gabbia Tower*.

Visual inspection of all main-bearing walls (Saisi et al. 2013) clearly indicated that the upper part of the tower is characterized by the presence of several discontinuities due to the historic evolution of the building, local lack of connection, and extensive masonry decay. The poor state of preservation of the same region was confirmed by the observed dynamic characteristics (Saisi et al. 2013), and one local mode involving the upper part of the tower was clearly identified by applying different output-only techniques to the response data collected for more than 24 h on the historic building.

These results clearly highlighted the critical situation of the upper part of the tower, pointing out the need for structural interventions to be carried out. With this motivation, and in order to allow for better indoor inspection of the tower-bearing walls, a metal scaffolding and a light

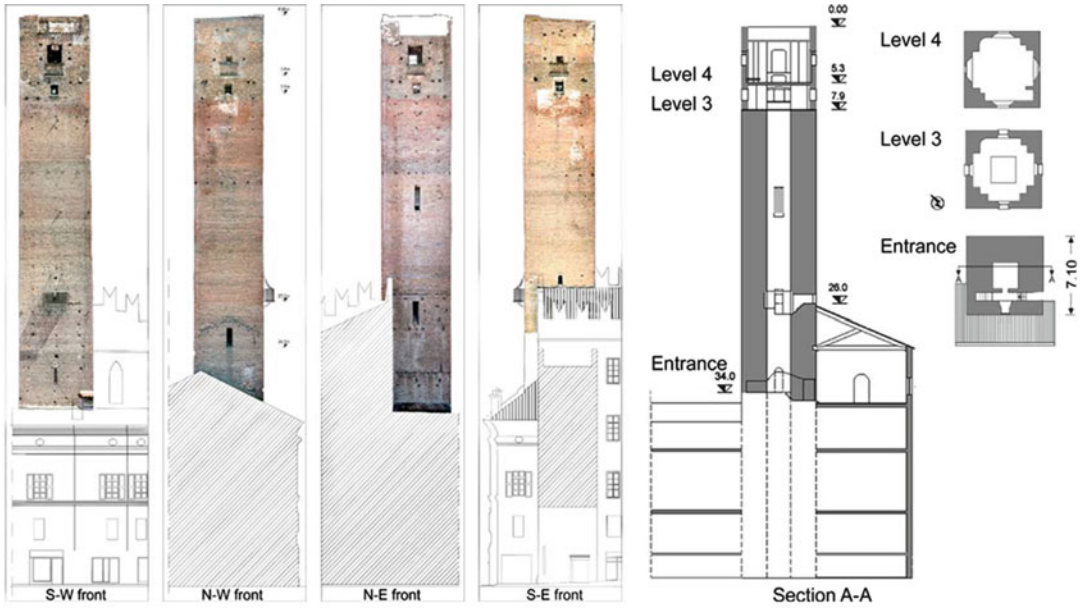

Ambient Vibration Testing of Cultural Heritage Structures, Fig. 10 Fronts and section of the *Gabbia Tower* (dimensions in m)

wooden roof have been installed inside the tower. Hence, a second dynamic test was performed – aimed at checking the possible effects of scaffolding and wooden roof on the modal characteristics of the structure – and a simple permanent dynamic monitoring system (including three highly sensitive accelerometers and one temperature sensor) was installed in the tower, with structural health monitoring and seismic early warning purposes.

Description of the Tower and On-Site Inspections

The *Gabbia Tower*, about 54.0 m high, is built in solid masonry bricks and has an almost square base; the load-bearing walls are about 2.4 m thick up to the upper levels (Fig. 10) where the thickness of the masonry cross section decreases to about 0.7 m. The top part of the building has a two-level lodge, which hosted in the nineteenth century the observation and telegraph post. A wooden staircase reached the lodge, but it is no more practicable since several years due to the lack of maintenance. The inner access to the tower was reestablished recently (October 2012) through provisional scaffoldings.

The original layout of the surrounding structures is unknown. At present, the tower is part of an important palace, evolved since the thirteenth century, complicating the geometry of the structure and the mutual links.

Few historic documents are available on the past interventions on the tower, but the observation of the masonry texture reveals passing-through discontinuities in the upper region, which are conceivably related to the tower evolution. Traces of past structures are visible on all fronts, and the presence of merlon-shaped discontinuities suggests modifications and further adding at the top of the tower. Moreover, at about 8.0 m from the top, a clear change of the brick surface workmanship (the bricks of the lower part are superficially scratched) could reveal a first addition; in the same region concentrated changes of the masonry texture reveal local repair.

An accurate on-site survey of all fronts of the tower was firstly performed using a mobile platform. The visual inspection, omitting the upper part of the tower (i.e., a portion about 8.0 m high), did not reveal evident structural damage but only superficial decay of the materials (mainly mortar

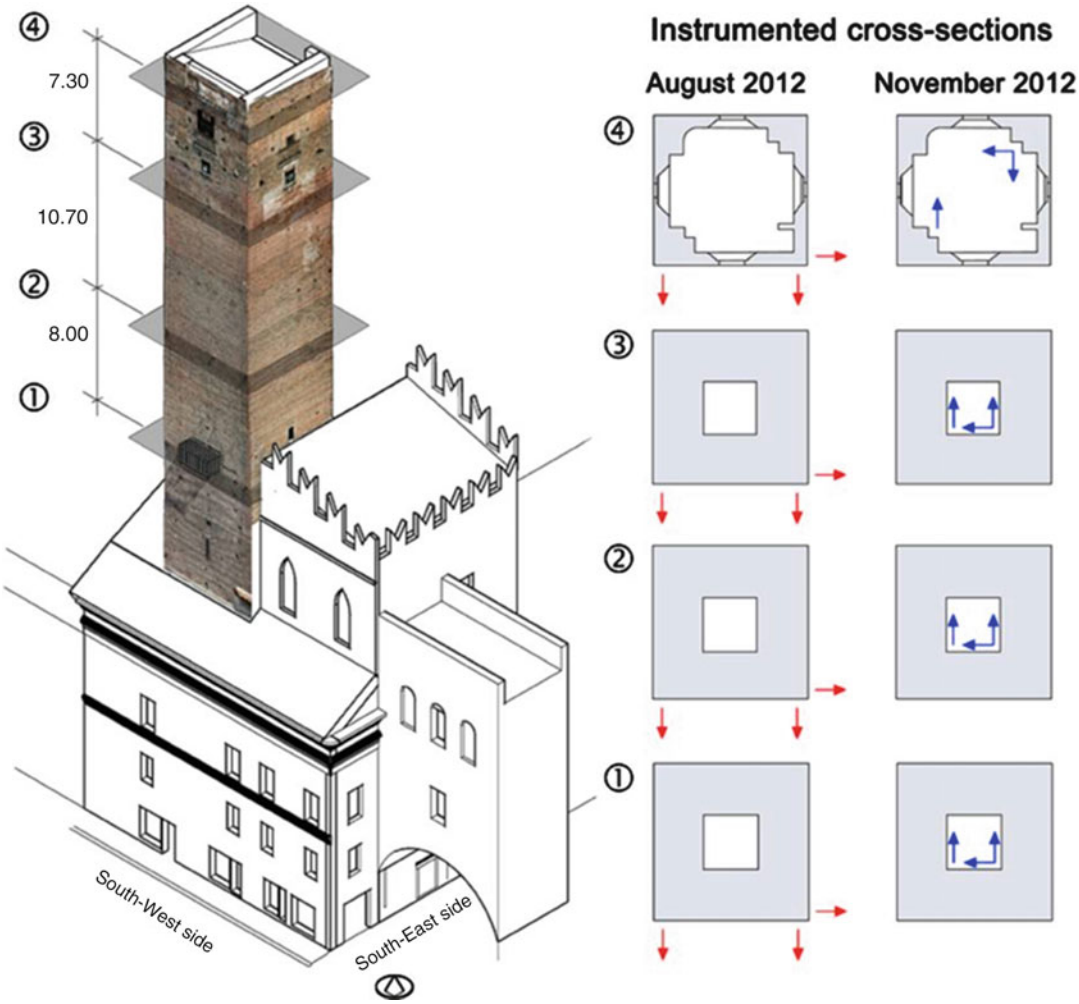

Ambient Vibration Testing of Cultural Heritage Structures, Fig. 11 Instrumented cross sections and sensors layout during the dynamic tests performed on August and November 2012 (dimensions in m)

joint erosion, due to the natural aging and the lack of maintenance). Subsequent pulse sonic tests, double flat jacks, and laboratory tests on sampled mortars and bricks confirm the soundness and the compactness of the masonry until the height of about 46.0 m. On the contrary, significant damages were observed in the upper 8.0 m of the tower; those damages are related to the abovementioned detachment of the several construction phases and worsened by the natural decay. More specifically, critical areas are the infillings between the merlons, supported only by few courses of thin masonry due to the unusual layout of the scaffolding holes.

Ambient Vibration Testing Procedures and Modal Identification

Two AVTs were conducted on the tower: between 31/07/2012 and 02/08/2012 and on 27/11/2012. It is worth recalling that the second test was performed after the installation of a metallic scaffolding and a wooden roof inside the tower in order to check the possible effects of those additions on the dynamic characteristics of the structure.

The response of the tower was measured in 12 selected points, belonging to 4 different cross sections along the height of the building, according to the sensor layout shown in Fig. 11.

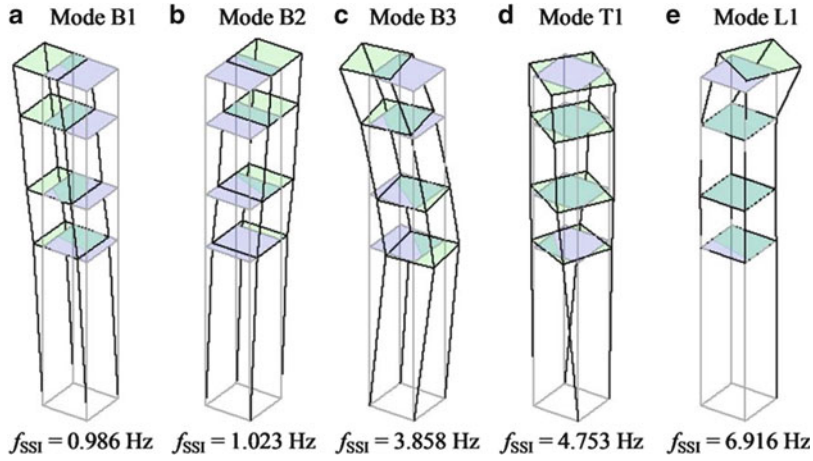

Ambient Vibration Testing of Cultural Heritage Structures, Fig. 12 Vibration modes generally identified during the first AVT (SSI, 31/07/2012, 21:00–22:00)

It is worth noting that the same cross sections were instrumented in the two tests, but in the second survey the accelerometers were installed on the inner side of load-bearing walls.

In both tests, the excitation was provided only by wind and micro-tremors. In the first test, acceleration data were acquired for 28 h (between 16:00 and 23:00 of 31/07/2012 and from 9:00 of 01/08/2012 to 6:00 of 02/08/2012), and a second acquisition system was used to measure the temperature in three different points of the tower: on the S-W front both indoor and outdoor temperature were measured, whereas only the outdoor temperature was measured on the S-E front. It is worth mentioning that the changes of outdoor temperature were very significant, ranging between 25 °C and 55 °C, whereas slight variations were measured by the indoor sensor (29–30 °C), due to the high thermal inertia of the load-bearing walls.

The modal identification was performed using 3,600 s long time windows and applying the data-driven SSI algorithm available in the Artemis software (SVS 2012).

Figure 12 shows typical results of the first AVT, in terms of natural frequencies and mode shapes. It should be noticed that (a) two closely spaced modes were identified around 1.0 Hz and these modes (Fig. 12a, b) are dominant bending (B) and involve flexure in the two main planes of the tower, respectively; (b) the third mode (Fig. 12c) involves dominant bending in the N-E/S-W plane with slight components also in the orthogonal N-W/S-E plane; (c) just one torsion mode (T) was identified (Fig. 12d); and (d) the last identified mode is local (L) and only involves deflections of the upper portion of the tower (Fig. 12e).

The presence of a local vibration mode provides further evidence of the structural effect of the change in the masonry quality and morphology observed on top of the tower during the visual inspection. On the other hand, both visual inspection and operational modal analysis confirm the concerns about the seismic vulnerability of the building and explain the fall of small masonry pieces from the upper part of the tower, reported during the earthquake of May 29, 2012.

Statistics of the modal frequencies identified between 31/07/2012 and 02/08/2012 are summarized in columns (2)–(5) of Table 2 through the mean value, the standard deviation, and the extreme values of each modal frequency. It should be noticed that the natural frequencies of all modes exhibit slight but clear variation, with the standard deviation ranging between 0.011 Hz (mode B2) and 0.037 Hz (mode L1). The correlation analysis performed to investigate the possible relationships between natural frequencies and temperature (Saisi et al. 2013) clearly indicated that the natural frequencies of the global modes B1–B3 and T1 increase with increased temperature. This behavior, observed also in previous measurements on masonry structures

Ambient Vibration Testing of Cultural Heritage Structures, Table 2 Natural frequencies identified (SSI) in the ambient vibration tests of *Gabbia Tower*

	31/07/2012 – 02/08/2012				27/11/2012
Mode	f_{ave} (Hz)	σ_f (Hz)	f_{min} (Hz)	f_{max} (Hz)	f (Hz)
(1)	(2)	(3)	(4)	(5)	(6)
1 (B1)	0.981	0.018	0.957	1.014	0.918
2 (B2)	1.026	0.011	1.006	1.052	0.986
3 (B3)	3.891	0.025	3.857	3.936	3.887
4 (T1)	4.763	0.022	4.714	4.802	4.648
5 (L1)	6.925	0.037	6.849	6.987	–
6 (L1′)	–	–	–	–	9.893

B bending mode, *T* torsion mode, *L* local mode

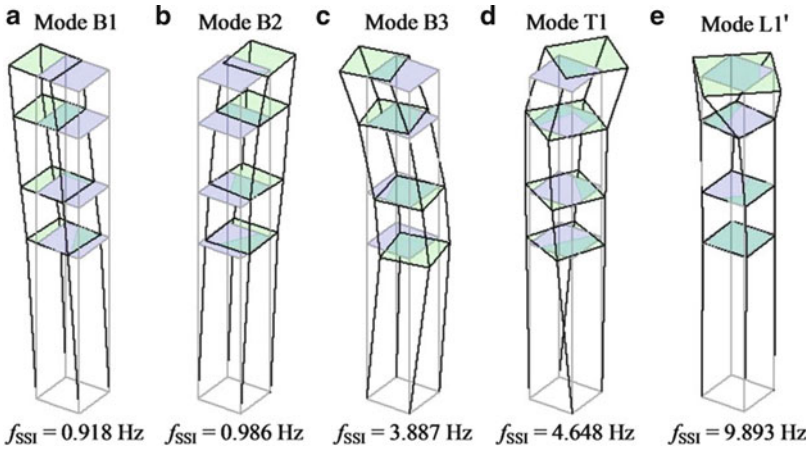

Ambient Vibration Testing of Cultural Heritage Structures, Fig. 13 Vibration modes identified during the second AVT (SSI, 27/11/2012)

(Ramos et al. 2010; Gentile et al. 2012), can be explained through the closure of superficial cracks, minor masonry discontinuities, or mortar gaps induced by the thermal expansion of materials. Hence, the temporary "compacting" of the materials induces a temporary increase of stiffness and modal frequencies, as well.

As previously stated, the possible effects of scaffolding and wooden roof on the dynamic characteristics of the tower were investigated in the second AVT, performed on November 27, 2012 with the outdoor temperature being almost constant (10–11 °C). The results of this investigation in terms of identified natural frequencies' main and mode shapes are shown in Fig. 13 and can be summarized as follows:

1. Beyond the difference in terms of natural frequency (that are conceivably related to the temperature effects), the mode shapes of bending modes B1–B3 did not exhibit significant changes (see Figs. 12a–c and 13a–c). Hence, the metallic scaffolding and the wooden roof practically do not affect those modes.
2. On the contrary, the mode shape T1 (Fig. 13d) now involves both torsion and bending. The identified frequency did not change appreciably with respect to the first dynamic survey, but the mode shape looks significantly different. The torsion component is still dominant in the lower portion of the structure, while the upper part is characterized by dominant bending with significant components along the two main planes of the tower. In other words, after the installation of the wooden roof, mode shape T1 becomes mixture of previous modes T1 (Fig. 12d, lower part of the structure) and L1 (Fig. 12e, upper part of the structure). Furthermore, the previous mode L1 was no more detected.

3. The previous local mode L1 (Fig. 12e) has been "replaced" by another local mode, with higher frequency of 9.89 Hz, involving torsion of the upper part of the tower (Fig. 13e).

As a further comment, it seems that especially the wooden roof, even if very light, affects the dynamic characteristics of the upper part of the building: the roof acts as a mass directly connected to a highly inhomogeneous and weaker portion of the building, so that a possible decrease of the natural frequency of the previous local mode is generated.

Long-Term Dynamic Monitoring and Typical Results

Few weeks after the execution of the second AVT, a simple dynamic monitoring system was installed in the tower. The system is composed by a 4-channel data acquisition system (24-bit resolution, 102 dB dynamic range, and anti-aliasing filters) with three piezoelectric accelerometers (WR model 731A, 10 V/g sensitivity, and ±0.50 g peak). The response of the tower is measured in three points, belonging to the cross section at the crowning level of the tower. Furthermore, a temperature sensor is installed on the S-W front, measuring the outdoor temperature.

The digitized data are transmitted to an industrial PC on site. A binary file, containing three acceleration time series (sampled at 200 Hz) and the temperature data, is created every hour, stored on the local PC, and transmitted to Politecnico di Milano for subsequent data processing.

The continuous dynamic monitoring system has been active since December 2012. The data files received from the monitoring system are managed by a software developed in LabVIEW and including the following tasks: (a) creation of a database with the original data (in compact format) for later developments; (b) preliminary preprocessing (i.e., de-trending, automatic recognition and extraction of possible seismic events, creation of one dataset per hour); (c) statistical analysis of data, including the evaluation of averaged acceleration amplitudes and temperature trends; (d) low-pass filtering and decimation of the each dataset; and (e) creation of a second database, with essential data records, to be used in the modal identification phase. The results of modal identification herein presented were obtained applying the SSI technique.

Figure 14a presents the evolution of the outdoor temperature on the S-W front during the period from 07/01/2013 to 06/04/2013 and shows that the temperature changed between −2 °C and 25 °C with significant daily variations in sunny days.

The identification of the modal frequencies from the datasets collected during the same period provided the frequency tracking shown in Fig. 14b. The inspection of Fig. 14b firstly suggests that the slight fluctuation of the natural frequencies of global modes follows the temperature variation. In order to better explore the temperature effect on the modal frequencies, Fig. 15 presents the first four natural frequencies of the tower plotted with respect to temperature, along with linear best fit lines. The plots in Fig. 15 confirm what already observed in the first dynamic survey: the natural frequencies of the global modes tend to increase with increased temperature almost linearly, as a consequence of the temporary increase of the local stiffness due to the thermal expansion of materials.

The time evolution of the natural frequency of the upper mode, i.e., the local mode L1′ (Fig. 13e), deserves some concern because the trend of this modal frequency is very different from the others (Fig. 14b). More specifically, the modal frequency exhibits more significant fluctuations and clearly decreases in time, from an initial value of about 10.0 Hz (07/01/2013) to a final value of about 9.0 Hz at the end of the analyzed period (06/04/2013).

A better inspection of Fig. 14b reveals that two clear drops of the modal frequency took place: (a) between 03/02/2013 and 04/02/2013 and (b) between 14/03/2013 and 15/03/2013. These drops divide the analyzed time period in three parts that are also easily identified by plotting the modal frequency versus the measured outdoor temperature, as shown in Fig. 16. The temperature-frequency plot of Fig. 16 highlights that the clouds of temperature-frequency points corresponding to each of the three different periods are characterized by similar slope of the best fit

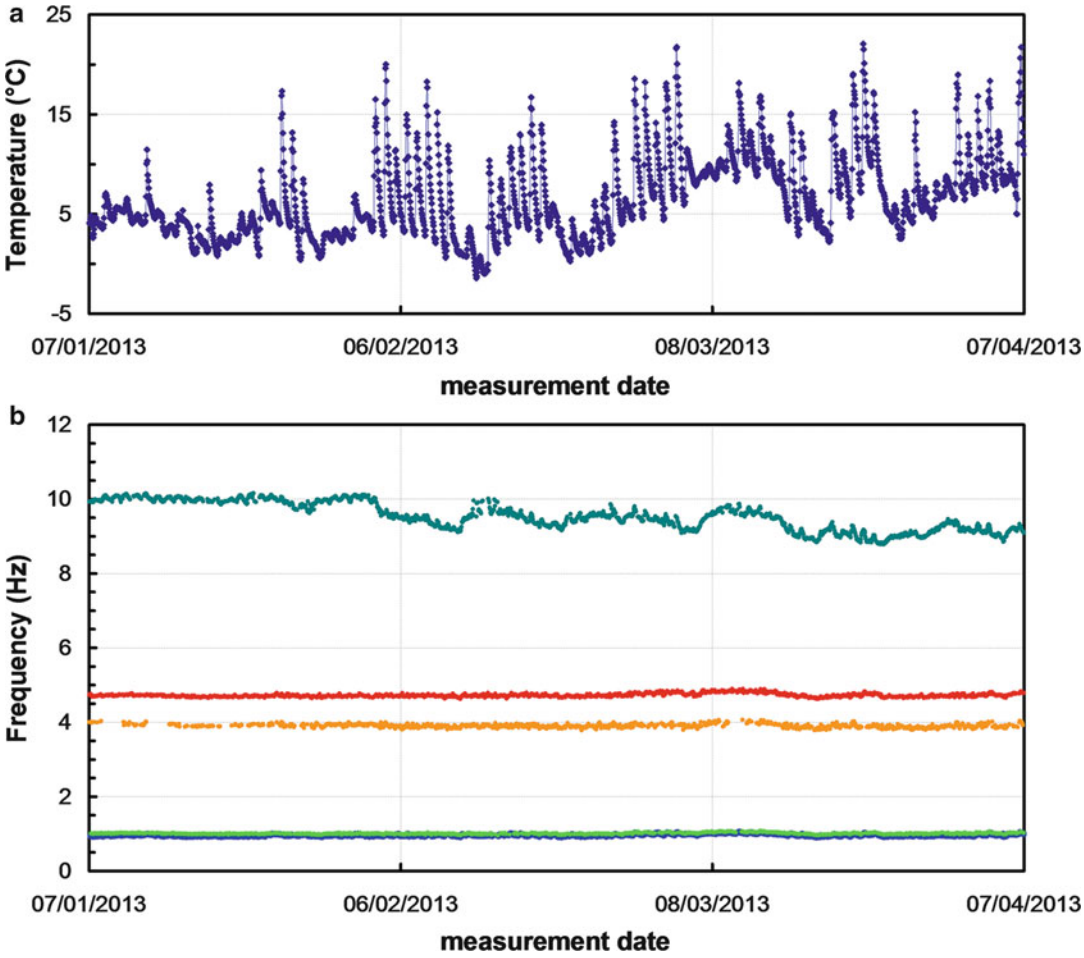

Ambient Vibration Testing of Cultural Heritage Structures, Fig. 14 Time evolution of (**a**) the outdoor temperature measured on the S-W front, (**b**) the natural frequencies identified with the SSI technique

line, whereas the average frequency value significantly decreases. This behavior suggests the quick progress of a damage mechanism, conceivably related to the worsening of the connection between the wooden roof and the masonry walls, and confirms – once more – the poor structural condition and the high seismic vulnerability of the upper part of the tower, highlighting the urgent need for preservation actions to be performed.

Summary

This entry focuses on the application of ambient vibration testing (AVT) and operational modal analysis (OMA, i.e., the identification of natural frequencies, mode shapes, and damping ratios from ambient vibration data) to Cultural Heritage structures. Although the topic is rather recent, it is emerging as a subject of great importance in the modern approach to preservation of historic structures.

AVT is a fully nondestructive test, especially suitable to historic structures because it is performed by just measuring the response in operational conditions. In turn, the knowledge of global parameters of the building, such as the modal parameters, provides essential information to validate the numerical models currently used to quantitatively estimate the structural safety of Cultural Heritage structures or to design repair interventions.

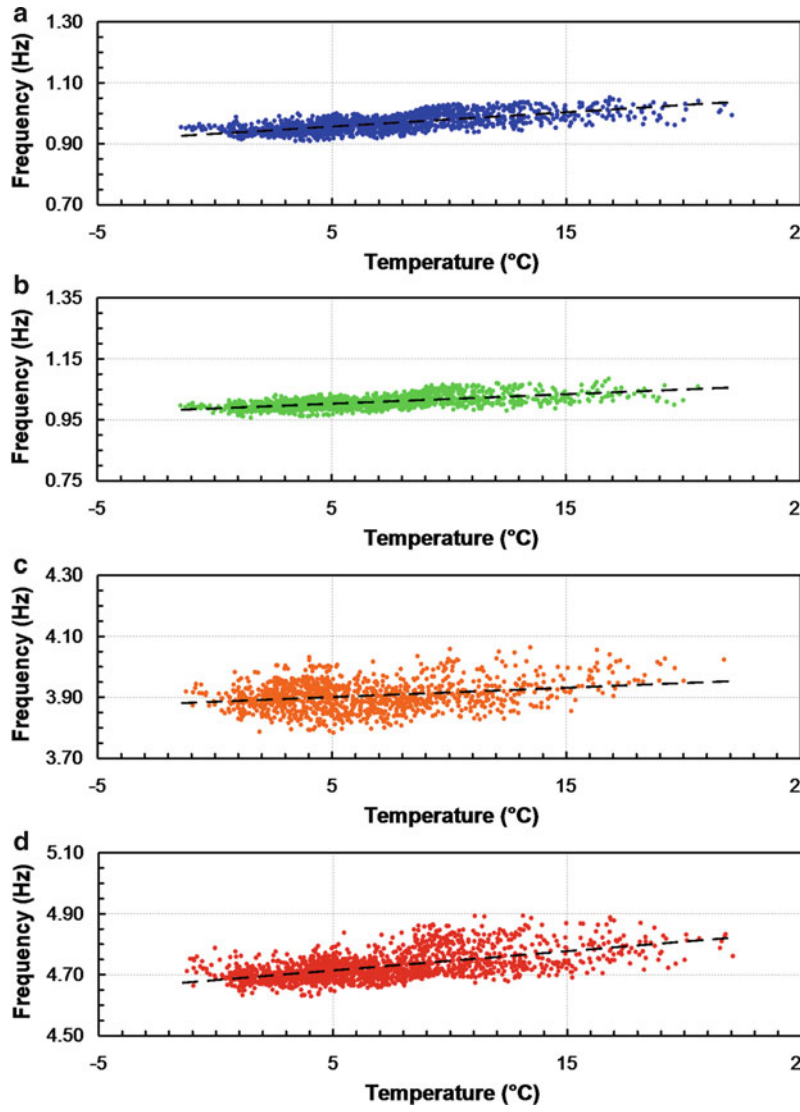

Ambient Vibration Testing of Cultural Heritage Structures, Fig. 15 Correlation between the identified modal frequencies and the outdoor temperature (S-W front): (**a**) mode B1, (**b**) mode B2, (**c**) mode B3, (**d**) mode T1

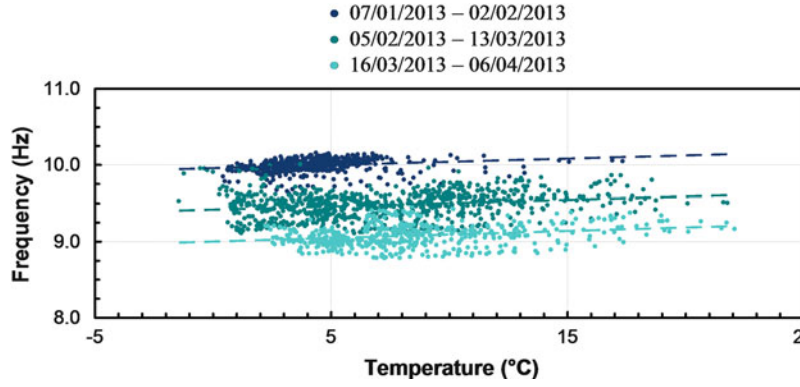

Ambient Vibration Testing of Cultural Heritage Structures, Fig. 16 Natural frequency of local mode L1' plotted with respect to the outdoor temperature

Furthermore, in some cases, AVT can possibly help also to limit the number of on-site and laboratory tests of materials, which are time-consuming and cost-ineffective. Other possible applications of ambient vibration-based modal analysis in the field of historic structures are for evaluation of the effects of repair interventions or in order to perform dynamics-based damage assessment.

In the first part of this entry, some robust techniques to perform OMA are reviewed, namely, the classical *peak picking* method and the more recent *frequency domain decomposition* and data-driven *stochastic subspace identification*.

Subsequently, the application of these techniques is exemplified with reference to two historic towers. In both cases, notwithstanding the very low level of ambient vibrations that existed during the tests, AVT and OMA have proved to be effective tools for identifying the dynamic characteristics of key vibration modes, provided that appropriate and very sensitive acquisition chain (capable of capturing the "interesting" dynamics embedded in the noise) is used in the tests.

In the first case study (the bell tower of the church *Chiesa Collegiata* in Arcisate, Varese), a rational vibration-based methodology, developed for the calibration of the numerical model, has been discussed as well. The presented methodology – involving systematic manual tuning, sensitivity analysis, and a simple system identification algorithm – provided a linear elastic model of the tower, representing an excellent approximation of the structure in its present condition (i.e., the calibrated model summarizes all the collected documentary and geometric and experimental information and exhibits very good agreement between predicted and measured modal parameters).

In the second case study, typical results from long-term monitoring of the ambient vibration data collected on the *Gabbia Tower* in Mantua, Italy (twelfth century), are summarized. The results clearly demonstrate that the modal identification is capable of highlighting (a) the effects of slight structural modifications; (b) the impact of temperature on the natural frequencies (i.e., the modal frequencies increase with increased temperature); and (c) the quick progress of a damage mechanism, involving the upper part of the tower, which is clearly identified through the remarkable fluctuations and the significant decrease (about 10 % in 3 months) of the natural frequency corresponding to a local mode.

Cross-References

- ▶ Bayesian Operational Modal Analysis
- ▶ Masonry Structures: Overview
- ▶ Operational Modal Analysis in Civil Engineering: An Overview
- ▶ Seismic Analysis of Masonry Buildings: Numerical Modeling
- ▶ Seismic Vulnerability Assessment: Masonry Structures
- ▶ Stochastic Structural Identification from Vibrational and Environmental Data

References

Allemang RJ, Brown DL (1983) Correlation coefficient for modal vector analysis. In: Proceedings of the 1st international modal analysis conference (IMAC-I), Orlando, FL, USA

Aras F, Krstevska L, Altay G, Tashkov L (2011) Experimental and numerical modal analyses of a historical masonry palace. Constr Build Mater 25(1):81–91

Bendat JS, Piersol AG (1993) Engineering applications of correlation and spectral analysis. Wiley Interscience, New York

Bennati S, Nardini L, Salvatore W (2005) Dynamic behavior of a medieval masonry bell tower. II: measurement and modeling of the tower motion. J Struct Eng ASCE 131(11):1656–1664

Binda L, Saisi A, Tiraboschi C (2000) Investigation procedures for the diagnosis of historic masonries. Constr Build Mater 14(4):199–233

Binda L, Condoleo P, Tiraboschi C, Rigamonti P (2012) On-site investigation and crack monitoring of an ancient bell-tower. In: Proceedings of the 14th international conference on structural faults & repair (SF&R-2012), Edinburgh, Scotland

Brincker R, Zhang LM, Andersen P (2000) Modal identification from ambient responses using frequency domain decomposition. In: Proceedings of the 18th international modal analysis conference (IMAC-XVIII), San Antonio, TX, USA

Brincker R, Ventura CE, Andersen P (2001) Damping estimation by frequency domain decomposition. In: Proceedings of the 19th international modal analysis conference (IMAC-XIX), Orlando, FL, USA
Cantieni R (2005) Experimental methods used in system identification of civil engineering structures. In: Proceedings of the 1st international operational modal analysis conference (IOMAC-2005), Copenaghen, Denmark
Casarin F, Modena C (2008) Seismic assessment of complex historical buildings: application to Reggio Emilia Cathedral, Italy. Int J Archit Herit 2(3):304–327
Douglas BM, Reid WH (1982) Dynamic tests and system identification of bridges. J Struct Div ASCE 108(10):295–312
DPCM (2011) Valutazione e riduzione del rischio sismico del patrimonio culturale con riferimento alle NTC 14 gennaio 2008. G.U.R.I, Rome
Felber AJ (1993) Development of a hybrid bridge evaluation system. PhD thesis, University of British Columbia
Friswell M, Mottershead JE (1995) Finite element model updating in structural dynamics. Kluwer, Boston/London/Dordrecht
Gattulli V, Antonacci E, Vestroni F (2013) Field observations and failure analysis of the Basilica S. Maria di Collemaggio after the 2009 L'Aquila earthquake. Eng Fail Anal 34(X):715–734
Gentile C, Saisi A (2007) Ambient vibration testing of historic masonry towers for structural identification and damage assessment. Constr Build Mater 21(6): 1311–1321
Gentile C, Saisi A (2013) Operational modal testing of historic structures at different levels of excitation. Constr Build Mater 48:1273–1285
Gentile C, Saisi A, Cabboi A (2012) Dynamic monitoring of a masonry tower. In: Proceedings of the 8th international conference on structural analysis of historical constructions (SAHC-2012), Wroclaw, Poland
Giuffrè A (1993) Sicurezza e conservazione di centri storici in area sismica: il caso Ortigia. Laterza, Bari
Ivorra S, Pallares FJ (2006) Dynamic investigation on a masonry bell tower. Eng Struct 25(5):660–667
Jaishi B, Ren WX, Zong ZH, Maskey PN (2003) Dynamic and seismic performance of old multi-tiered temples in Nepal. Eng Struct 25(14):1827–1839
Magalhães F, Cunha A (2011) Explaining operational modal analysis with data from an arch bridge. Mech Syst Signal Process 25(5):1431–1450
Maia NMM, Silva JMM (1997) Theoretical and experimental modal analysis. Research Studies Press, Baldock, Hertfordshire, England
Oliveira CS, Çakti E, Stengel D, Branco M (2012) Minaret behavior under earthquake loading: the case of historical Istanbul. Earthq Eng Struct Dyn 41:19–39
Pau A, Vestroni F (2008) Vibration analysis and dynamic characterization of the Colosseum. Struct Control Health Monit 15(8):1105–1121
Peeters B (2000) System identification and damage detection in civil engineering structures. PhD thesis, Katholieke Universiteit Leuven
Peña F, Lourenço PB, Mendes N, Oliveira DV (2010) Numerical models for the seismic assessment of an old masonry tower. Eng Struct 32(5):1466–1478
Ramos LF, Marques L, Lourenço PB, De Roeck G, Campos-Costa A, Roque J (2010) Monitoring historical masonry structures with operational modal analysis: two case studies. Mech Syst Signal Process 24(5):1291–1305
Saisi A, Gentile C, Cantini L (2013) Post-earthquake assessment of a masonry tower by on-site inspection and operational modal testing. In: Proceedings COMPDYN 2013, Kos, Greece
SVS (2012) ARTeMIS extractor 2012. http://www.svibs.com
van Overschee P, De Moor B (1996) Subspace identification for linear systems: theory, implementation, applications. Kluwer, Boston/London/Dordrecht
Welch PD (1967) The use of fast Fourier transform for the estimation of power spectra: a method based on time averaging over short modified periodograms. IEEE Trans Audio Electro-Acoust 15(2):70–73

Analysis and Design Issues of Geotechnical Systems: Flexible Walls

Amir M. Halabian
Department of Civil Engineering, Isfahan University of Technology, Isfahan, Iran

Synonyms

Non-yielding walls; Retaining flexible walls; Soil thrust

Introduction

The effect of ground motion on rigid retaining walls is examined using the method proposed by Mononobe and Okabe, which is based on the Coulomb's theory of static soil pressure. The analysis and design issues for these walls are covered in a separate companion article. M-O method requires that the retaining walls can move freely (slide or rotate) so that active or passive earth pressures develop behind the wall. Nevertheless, there are many cases (such as basement walls) where the free movement of the wall is fully or

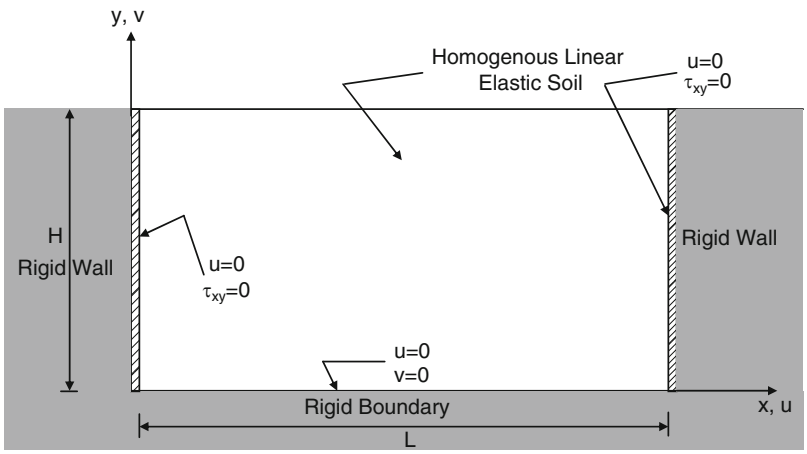

Analysis and Design Issues of Geotechnical Systems: Flexible Walls, Fig. 1 Walls geometry taken in Wood (1973) analysis of pressures on non-yielding walls

partially restrained, referred as non-yielding walls; furthermore, in situ retaining wall systems made from sequential excavation process provide stability and minimize movements of the adjacent ground throughout their flexible facing. In the last decades, a great deal of research work both in the analytical and in experimental areas has been performed to evaluate the adequacy of the M-O method or to extend the method for specific applications such as non-yielding walls or flexible retaining structures. Discussion of the existing approaches to evaluate the seismic soil pressure on non-yielding walls and practical design methods based on limit equilibrium concept and numerical algorithms are described below.

Non-Yielding Walls

Although there are reports of damage and failure on retaining walls due to earthquakes around the world, the distress has been attributed to some form of soil or foundation failure, such as slope instability or soil liquefaction (Al Atik and Sitar 2010). There have been a few reports of damage to building basement walls as a result of seismic earth pressures in recent earthquakes including damages to basements in two recent earthquakes in Turkey. Gur et al. (2009) reported that basement damage occurred in a half-buried basement of a school building during 1999 Düzce earthquake; the half-buried basement was surrounded by partial height earth-retaining concrete walls and there were windows between the top of the earth-retaining walls and the beams at the top of the basement.

Wood's Method

M-O method requires that the retaining walls can move freely (slide or rotate) so that active or passive earth pressures develop behind the wall. Nevertheless, there are many cases where the free movement of the wall is fully or partially restrained (such as basement walls, massive gravity walls embedded in rock-like formations, and braced walls). Wood (1973) analyzed the response of a homogenous linear elastic soil trapped between two rigid walls connected to rigid base (Fig. 1). In this figure, u, v, and τ_{xy} are referred to the in-plane deformations and shear stresses, respectively.

If both walls are spaced far apart, the pressures on one wall are not influenced by the presence of the other. For low-frequency input motions with frequency less than half the fundamental frequency of the unrestrained backfill, V_s/4H (V_s is the soil shear wave velocity), the pseudo static conditions are governed (i.e., the dynamic amplification is negligible). For this range of frequencies, wall pressures with plane strain assumption can be obtained from elastic solution for the case of a uniform, constant horizontal acceleration applied throughout the soil. The dynamic earth pressures obtained from this method must be

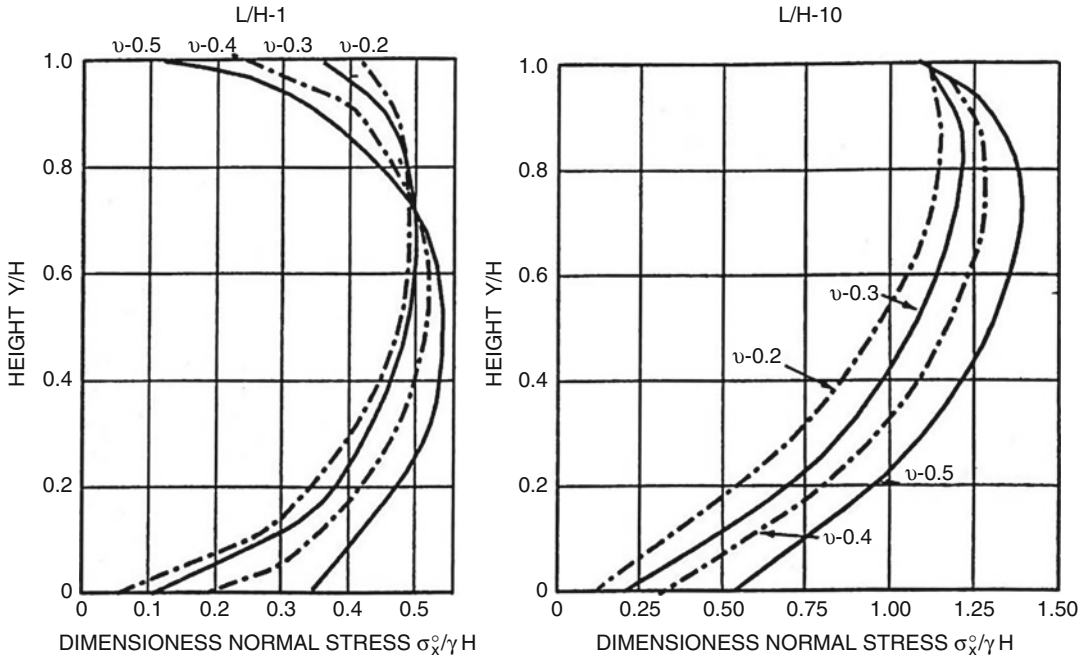

Analysis and Design Issues of Geotechnical Systems: Flexible Walls, Fig. 2 Normal wall stresses from Wood's Solution (From Ebeling et al. 1992)

added to the static earth pressures to obtain the total earth pressures during an earthquake. Figure 2 presents two examples of the variation in the values for normalized horizontal stresses with normalized elevations above the base of a wall, based on Wood's solution (Wood 1973). An L/H value of 1 (where L = the width of backfill and H = the wall height) where value of 1 corresponds to a narrow backfill placed within rigid containment, and an L/H value of 10 represents a backfill of great width. The horizontal stresses ($\sigma_x{}^O$) at any vertical location Y, along the wall, are normalized by the product of γH in Fig. 2, where γ is the soil unit weight.

With the assumption of smooth rigid walls, the dynamic thrust and dynamic overturning moment about the base of the wall are expressed as:

$$\Delta F_{\text{eq}} = \gamma H^2 \frac{a_h}{g} F_p \tag{1}$$

$$\Delta M_{\text{eq}} = \gamma H^3 \frac{a_h}{g} F_m \tag{2}$$

where a_h is the amplitude of the harmonic base acceleration, and F_p and F_m are the dimensionless dynamic thrust and moment factors which can be obtained from Fig. 3. The point of application the dynamic thrust will be located at a height

$$h_{\text{eq}} = \frac{\Delta M_{\text{eq}}}{\Delta F_{\text{eq}}} \tag{3}$$

Ostadan-White Approach

The solution by Wood (1973) commonly used for critical facilities are, in fact, based on static "1g" loading of the soil-wall system and does not include the wave propagation and amplification of motion. On the other hand, Wood's solution is mathematically complicated to apply in engineering practice and is limited to harmonic input motions. Employing the finite element technique, in a simplified method proposed by Ostadan and White (1997) and Ostadan (2004) which incorporates the main parameters affecting the seismic soil pressure for buildings, the lateral seismic soil pressure on these structures

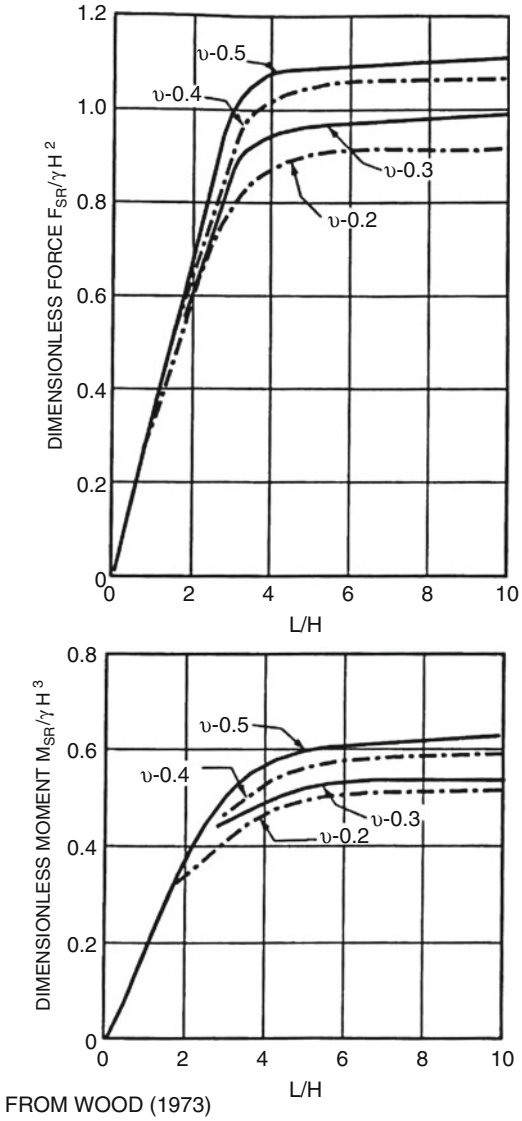

Analysis and Design Issues of Geotechnical Systems: Flexible Walls, Fig. 3 Dimensionless thrust and moment factors in Wood's Solution (From Ebeling et al. 1992), ν is the soil Poisson's ratio

can be predicted. The studies showed that seismic soil pressure is affected by the long period part of ground motion and amplified near the resonant frequency of the backfill. The method is focused on the building walls rather than soil-retaining walls and specifically considers the dynamic soil nonlinear properties, relative motion between soil, and the structure and frequency content of the design motion in its formulation. The method is focused on the building walls rather than soil-retaining walls where the movement of the walls is limited due to the presence of the floor diaphragms representing non-yielding walls. To reach a simplified approach for estimating the lateral seismic pressures on non-yielding walls, Ostadan (2004) performed a series of seismic soil-structure interaction analyses. A typical numerical model of a building basement wall is shown in Fig. 4. The base of the wall is resting on the rock or a firm soil layer.

Having the model shown in Fig. 4 subjected to 1g harmonic acceleration, the frequency contents of the pressure response were evaluated using the pressure transfer functions (TF) amplitude which is the ratio of the amplitude of the seismic soil pressure to the amplitude of the input motion. The pressure transfer functions were evaluated using Poisson's ratio of 1/3 for a wide range of frequencies (Fig. 5a).

If the transfer functions are expressed in terms of normalized frequencies using the soil column frequency which is

$$f_s = V_s/4H \tag{4}$$

it was shown that the maximum amplifications take place at the frequency corresponding to the soil column frequency (Fig. 5b). V_s is the soil column shear velocity. Comparing the dynamic characteristics of the normalized pressure amplitudes (Fig. 5b), one can conclude that such characteristics are similar to a single degree of freedom (SDOF) system.

For the parametric studies conducted by Ostadan (2004), the results showed that low-frequency pressure profiles depict the same pressure distribution along the height of the wall. In Fig. 6, the soil pressure distribution obtained from such a nonlinear numerical method is compared with the normalized solutions from Wood (1973) and M-O methods. Using the soil pressure distributions obtained from a parametric study, a polynomial relationship has been developed to fit the normalized pressure curves. This relationship is expressed in terms of the

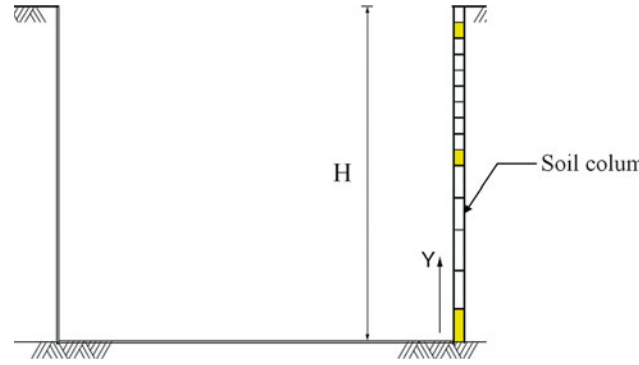

Analysis and Design Issues of Geotechnical Systems: Flexible Walls, Fig. 4 A typical numerical model of a building basement wall

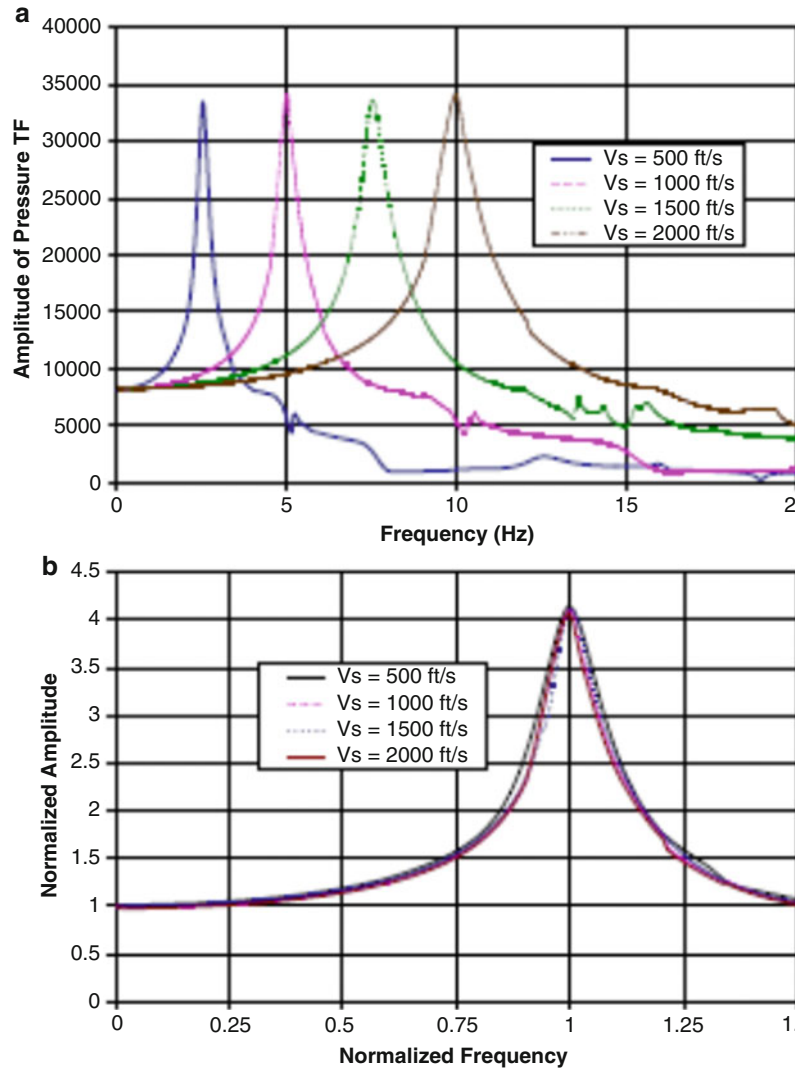

Analysis and Design Issues of Geotechnical Systems: Flexible Walls, Fig. 5 Pressure transfer functions (Ostadan (2004)) (**a**) A typical pressure transfer functions versus frequency (**b**) Normalized transfer functions versus normalized frequency

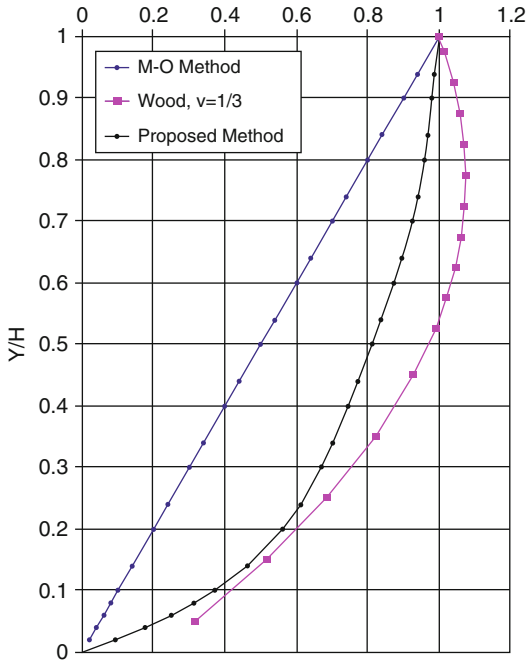

Analysis and Design Issues of Geotechnical Systems: Flexible Walls, Fig. 6 Normalized pressure distributions (Ostadan (2004))

normalized height, $y = Y/H$ (Y coordinate defined in Fig. 4), as:

$$p(y) = -0.0015 + 5.05y + 15.84y^2 + 28.25y^3 + 24.59y^4 + 8.14y^5 \quad (5)$$

The total thrust applied to the wall is corresponding to the area under the normalized pressure profile curve which can be obtained from the integration of the pressure distribution over the height of the wall. The total area is 0.744H for a wall with height H. Keeping in mind that the normalized shape of the pressure distribution is similar to the response of SDOF systems, the amplitudes of the seismic pressure can be obtained from the response spectrum analysis of SDOF systems. Accordingly, the total thrust applied to the wall is subsequently obtained from the product of the total mass in the equivalent SDOF system times the acceleration spectral value at the respective frequency of the system. Having the total thrust, the frequency of the system and the input motion to the SDOF system, the relationship in the form proposed by Veletsos and Younan (1994) can be used to compute the total mass and the damping of the SDOF system. Therefore, the total mass is obtained from

$$m = 0.5\rho H^2 \Psi_v \quad (6)$$

in which ρ is the soil density and Ψ_v is a factor to take into account the Poisson's ratio effect. Since the original study performed for Poisson's ratio equals 1/3 (Ostadan (2004)), the pressure distribution should be adjusted for different Poisson's ratios using a factor recommended by Veletsos et al., Ψ_v, defined as

$$\Psi_v = \frac{2}{[(2-v)(1-v)]^{0.5}} \quad (7)$$

Study of the soil pressure transfer functions and the free-field response motions for wall with height of 50 ft showed that spectral values at the soil column frequency and at 30 % damping have the best correlation with the forces computed directly from the SSI analysis (Ostadan (2004)).

The computational steps of the proposed method by Ostadan (2004) to evaluate the lateral seismic soil pressures applied to the basement walls as a type of the non-yielding wall can be summarized as follows:

- Perform seismic free-field soil column analysis and obtain the acceleration response spectrum at the base of the wall using a free-field analysis code such as SHAKE91 (Schnabel et al. 1972) taking into account soil nonlinearities with input motion specified at the ground surface or at the depth of foundation base mat, $S_{a(\text{free})}$.
- Obtain total mass in the representative SDOF using Eq. 6.
- Obtain the total seismic lateral force by multiplying the mass of the representative SDOF by the spectral amplitude of the free-field response at the soil column frequency.

$$F = m\, S_{a(\text{free})} \tag{8}$$

- The maximum lateral earth pressure at the ground surface is calculated by dividing the total seismic lateral force by the area under normal soil pressure curve (0.744H).
- The lateral soil pressure distribution along the height of the wall is obtained by multiplying Eq. 5 by the maximum lateral earth pressure at the ground surface.

Soil-Reinforced Walls

Limit Equilibrium Methods

The fundamental stability concept of soil-nailed walls is based on reinforcing soil mass with reinforcement elements such as steel rebars so that the soil mass could behave as a unit mass. Therefore, during an earthquake, in addition to static forces, a reinforced soil wall is subjected to a dynamic soil thrust at the back of the reinforced zone and to internal forces within the reinforced zone. Accordingly, the wall should be designed to have global (external) stability such as avoiding sliding or overturning failure of the reinforced zone as well as local (internal) stability such as avoiding pullout failure of the reinforcement. Stability analyses based on limit-force equilibrium methods have been developed to assess the global static stability of soil-nailed walls along with local stability of reinforced soil mass by taking into account different factors influencing the wall performance, i.e., shearing, tension, and pullout resistance of the inclusions. Therefore, the reinforced wall is treated much like a gravity wall. The reinforced zone recommended by several researchers, shown in Fig. 7, is assumed to be acted on by its own weight, W, and the earthquake loading from unreinforced soil mass represented pseudostatically by dynamic soil thrust, F_D, and the inertial force on the reinforced zone, F_i. The normalized width of the reinforced soil mass, the inertial force on the reinforced zone, and the dynamic soil thrust suggested by Seed and Mitchell (1981), Dhouib (1987) and Segrestin and Bastick (1988) are given in Table 1.

Seed and Mitchell (1981) in their recommendation to FHWA suggested that the reinforced soil area should be taken equal to 0.5H independent of the ground horizontal acceleration, a_h. On the other hand, developing a nonlinear finite element code, Dhouib (1987) showed that the incremental dynamic force is proportional to the distribution of static forces, and the geometry of the active failure zone should be expressed in terms of the system's relative stiffness and the ground acceleration.

Segrestin and Bastick (1988) also conducted finite element analyses to understand seismic response of soil-reinforced structures. In their studies, the elastoplastic behavior of the soil was simulated by varying the modulus of elasticity as a function of observed deformations. The results of the study indicated that the distribution of dynamic tensile forces along the strips is fairly uniform and does not give significant change in the position of points of maximum tension. Unlike the FHWA recommendation, Segrestin and Bastick (1988) suggested that the active failure zone is not affected that much by the earthquake loading, and therefore the width of this area should be limited to 0.3 H. In their studies, the elastoplastic behavior of the soil was simulated by varying the modulus of elasticity as a function of observed deformations. The results of their study indicated that the distribution of dynamic tensile forces along the strips is fairly uniform and does not give significant change in the position of points of maximum tension.

In Table 1, m is the horizontal ground acceleration coefficient calculated at the centroid of the reinforced zone using

$$m = \left(1.45 - \frac{a_h}{g}\right)\frac{a_h}{g} \tag{9}$$

recommended by FHWA.

Pseudostatic Approaches

While limit equilibrium methods fail to give any information regarding developed tensile and shear forces along nails and they cannot evaluate local stability of structure, numerically derived pseudostatic approaches have been developed to investigate behavior of soil-nailed walls under

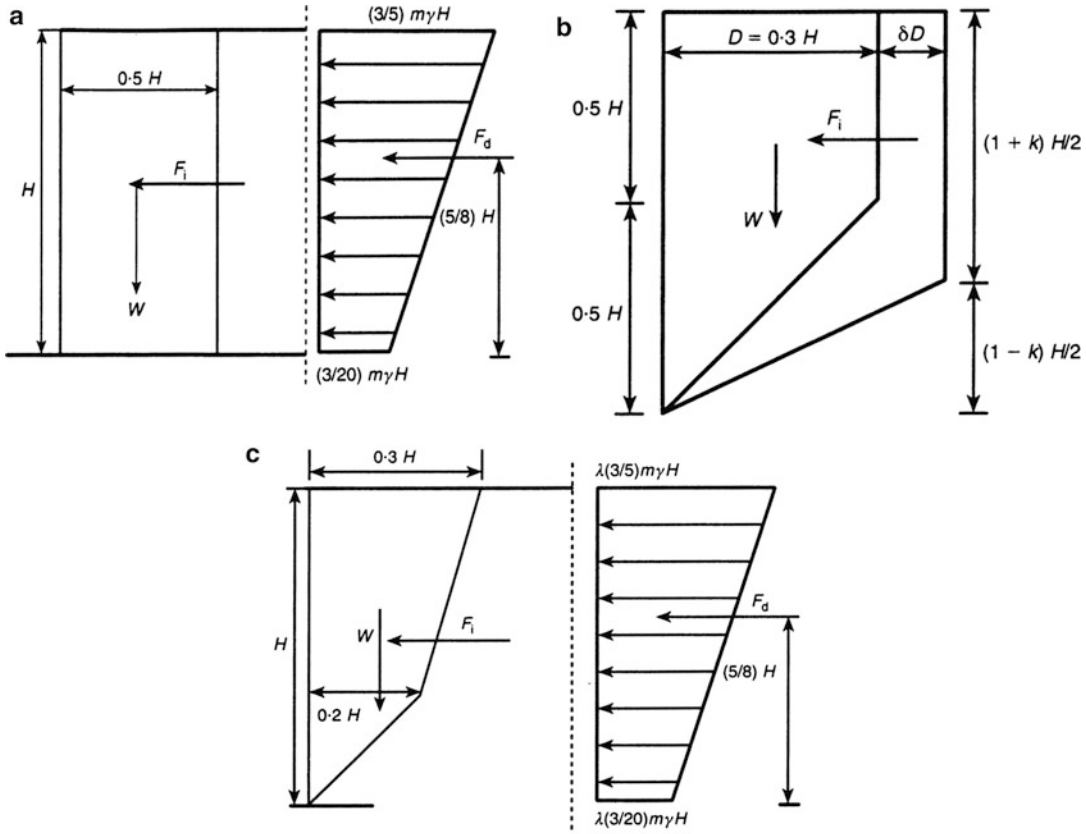

Analysis and Design Issues of Geotechnical Systems: Flexible Walls, Fig. 7 Dynamic soil thrust acting on soil-reinforced walls' evaluation using different pseudostatic approaches (the symbols are defined in Table 1)

Analysis and Design Issues of Geotechnical Systems: Flexible Walls, Table 1 Inertia and dynamic forces applied to the reinforced soil mass

Design method	S/H	Inertial force F_i	Dynamic force F_D
Seed and Mitchell (1981)	0.50	$0.5\ m\gamma H^2$	$(3/8)\ m\gamma H^2$
Dhouib (1987)	$0.30 + m/2$	$\frac{(0.30+m/2)m\gamma H^2}{4(2K+3)}$	–
Se grestin and Bastick (1988)	0.30	$0.20\ m\gamma H^2$	$\lambda(3/8)$ $m\gamma H^2$

$K = 2.5\ m$, $\lambda = 0.6$

dynamic-loading conditions. On the other hand, unlike common gravity retaining structures, soil-nailed walls have also shown remarkably well performance during many ground motions, which could be attributed to the intrinsic flexibility of soil-nailed wall system and possibly some level of conservatism in current design procedures (Choukeir et al. (1997)). Accordingly, as an extension of static limit equilibrium methods, pseudostatic approaches in which dynamic earth pressure is computed based on conventional Mononobe-Okabe approach were developed. Choukeir et al. (1997) presented a new pseudostatic method to analyze soil-nailed slopes. Their proposed approach is derived as an extension of the kinematical working-stress design method developed by Juran et al. (1990) for static loading of soil-nailed structures. The applicability of this working-stress design method under static loading has been described in details by Juran and Elias (1991) and is incorporated in several design codes (FHWA 2003).

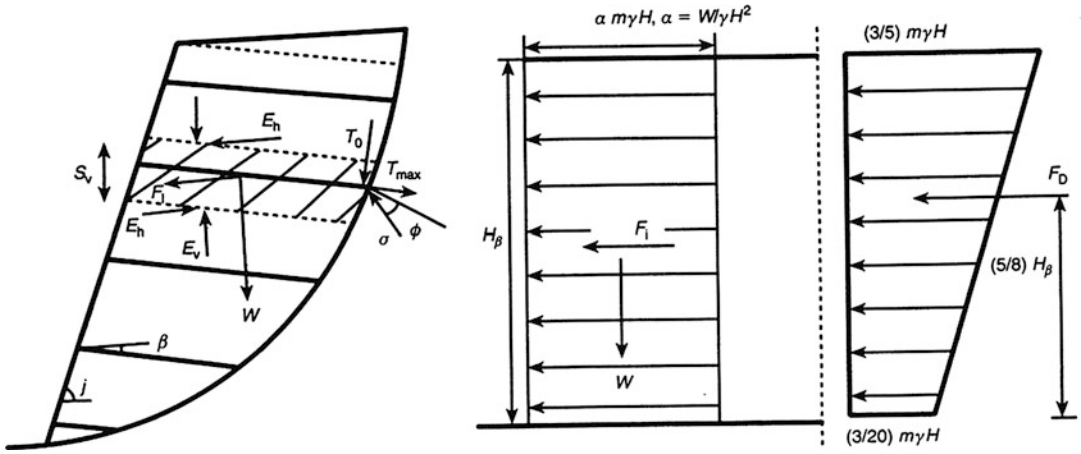

Analysis and Design Issues of Geotechnical Systems: Flexible Walls, Fig. 8 Pseudostatic method suggested by Choukeir et al. (1997), H_β = the projected height of the inclined wall

The main design assumptions of the kinematical analysis are as follows:

- Failure occurs by a quasi-rigid body rotation of the active zone, which is limited by a log-spiral failure surface.
- The locus of the maximum tension and shear forces at failure coincides with the failure surface developed in the soil mass.
- The shearing resistance of the soil, defined by Coulomb's failure criterion, is entirely mobilized along the sliding surface.
- The shearing resistance of stiff inclusions, defined by Tresca's failure criterion, is mobilized in the direction of the sliding surface in the soil.
- The horizontal components of the inter-slice forces, E_h (see Fig. 8), are equal.
- The effect of a slope (or horizontal surcharge), at the upper surface of the nailed soil mass, on the tension forces in the nails is linearly decreasing along the failure surface.

The extension of the kinematical design method for pseudostatic stability analysis involves the following assumptions:

- The failure-reinforced wedge is subjected to horizontal pseudostatic forces specified as the mass of the wedge multiplied by the pseudostatic horizontal acceleration $a_h = mg$.
- Shear modulus of the soil is constant along the depth.
- Shear strength parameters of the soil are constant during earthquake loading.
- The soil is not saturated, and thus no effect of pore water pressure is present.
- The failure-reinforced wedge is assumed to be subjected by its own weight, W, and the earthquake loading from unreinforced soil mass represented pseudostatically by dynamic soil thrust, F_D, and its own inertial force, F_i (Fig. 8)

$$K_h = n.m\cdots,\cdots,\cdots n = \frac{a_{ps}}{a_m} = \left[\frac{0.5}{1-r^2}\right]^{\frac{1}{2}}\cdots,\cdots r = \frac{\omega}{\omega_n} \qquad (10)$$

Do check that all symbols in Eq. 10 have been defined somewhere else.

Nonlinear Dynamic Analysis Method

As it was presented, there are several pseudostatic methods by which the magnitude of dynamic forces along reinforcements for a soil-nailed structure under dynamic loading conditions could be determined. To get better

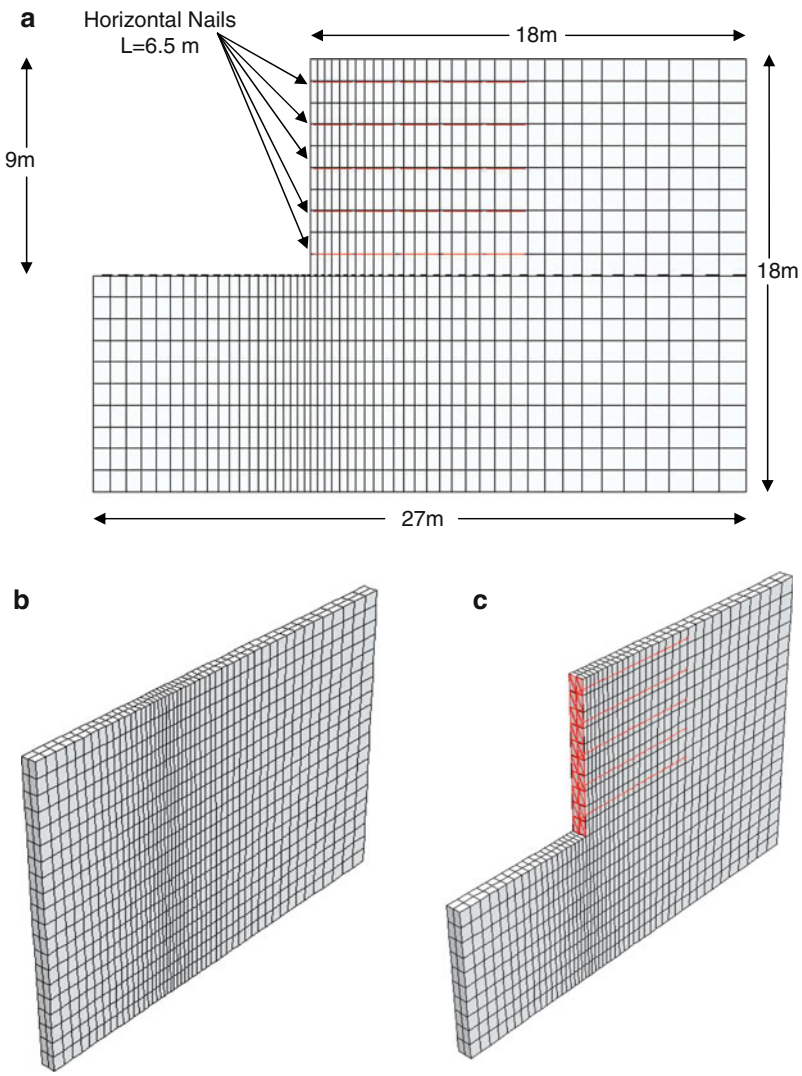

Analysis and Design Issues of Geotechnical Systems: Flexible Walls, Fig. 9 (**a**) Model geometry (**b**) Numerical mesh used for analyses (**c**) Soil-nailed wall after final stage of excavation (Halabian et al. 2010)

understanding of dynamic response of soil-nailed wall systems under earthquake excitations, a numerical model like what is shown in Fig. 9 for a typical reinforced wall, rather than empirical formulations could be employed to evaluate the wall performance.

To gain better perception of dynamic soil-nailed structures behavior, the numerical model should take into account the wall construction stages which include nail installation and application of shotcrete facing. It should be noted that the model dimensions have to be determined wide enough so that the effects of boundary conditions on the response of structure would be negligible. Due to repetitive arrangement of nails along the length of the excavation, only a slice of the soil can be modeled (Fig. 9b and c). To have more reliable results of analyses, a somewhat finer mesh should be utilized for those areas near the excavation face. It should be noted that initial state of equilibrium has to be established before any stage proceeds. Afterward as each excavation ends, the equilibrium conditions (according to maximum unbalanced force) will be examined in order to ensure whether or not that model meets the equilibrium conditions to resume the next stage. An appropriate soil constitutive law should be used to simulate the stress

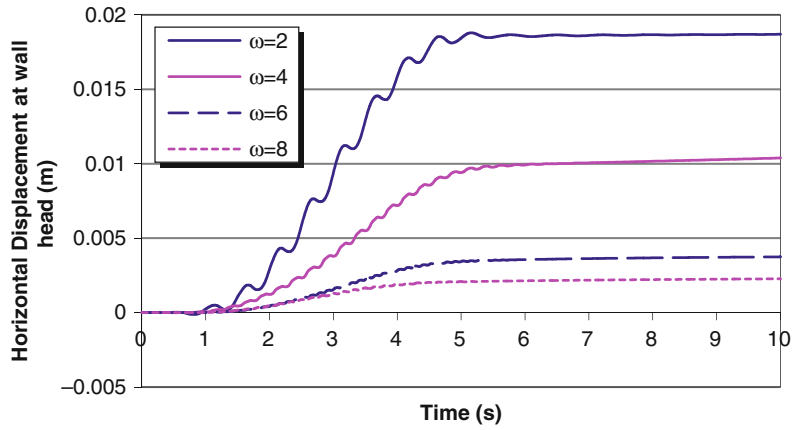

Analysis and Design Issues of Geotechnical Systems: Flexible Walls, Fig. 10 Horizontal displacement response time history at the wall head during the harmonic base excitation (Halabian et al. 2010)

path induced to soil mass during the earthquake loading. After static equilibrium is achieved, the full width of soil subgrade should be subjected to dynamic excitations.

Harmonic Ground Excitation

Despite having a single-frequency content and short duration of the excitation, Halabian et al. (2010) used a variable-amplitude harmonic ground motion to understand the effects of crucial parameters on the performance of soil-nailed structure under actual earthquake acceleration records. The accelerogram follows a trend which has both increasing and decaying peak acceleration parts expressed as:

$$\ddot{U}(\mathrm{t}) = \frac{1}{2}\left(1 - \cos\left(\frac{2\pi}{T}t\right)\right)\sin\left(2\pi f t\right) \quad (11)$$

in which T and f are the duration of net harmonic excitation and the frequency of excitation.

Influence of Harmonic Excitation Frequency The effect of the excitation frequency on the horizontal displacement time histories at the crest of the wall is presented in Fig. 10. The displacement time histories indicate that the horizontal displacement at the crest of the wall was influenced by the excitation frequency and increases monotonically with the time during the harmonic base excitation. However, it can be concluded that as the excitation frequency increases, the horizontal displacement at the wall crest decreases. Figure 11a indicates that while the input frequency motion increases, the peak outward horizontal displacement of the wall decreases. Conversely, as illustrated by Fig. 11b, the peak horizontal acceleration response along the wall facing is increased by an ascending trend of input motion frequency. From the other results shown in Fig. 12, it is worth noting that increasing input motion frequency made tensile forces to less mobilize along nail bars due to the fact that the critical state becomes more inaccessible since the input motion frequency gets higher than fundamental frequency of the system.

Influence of Angle of Nail Inclination The influence of nail inclination angle on dynamic response of the structure is shown in Fig. 13a. The peak outward horizontal displacement of walls shows decreasing in value by increasing nails inclination angle while it varies in the range of 0–15°. Afterwards, increasing nail inclination angle results in slight increase of wall deformations, especially when it ranges in 25–30°. As a result, it is shown that the increase in nail inclination angle would have destabilizing effect on the performance of structure during harmonic base excitations.

When it comes to the peak horizontal acceleration, as it is demonstrated in Fig. 13b, it can be concluded that increasing nail inclination angle would result in increase of peak horizontal acceleration response of the wall. Figure 14 shows distribution of maximum tensile forces along nail bars.

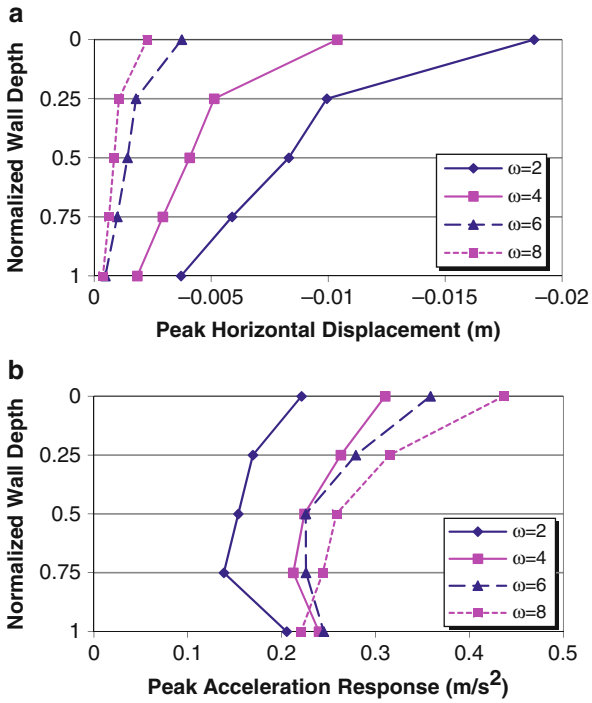

Analysis and Design Issues of Geotechnical Systems: Flexible Walls, Fig. 11 Normalized peak horizontal deformations distribution along height of wall facing (Halabian et al. 2010) (**a**) Normalized peak horizontal displacement (**b**) Normalized peak horizontal displacement

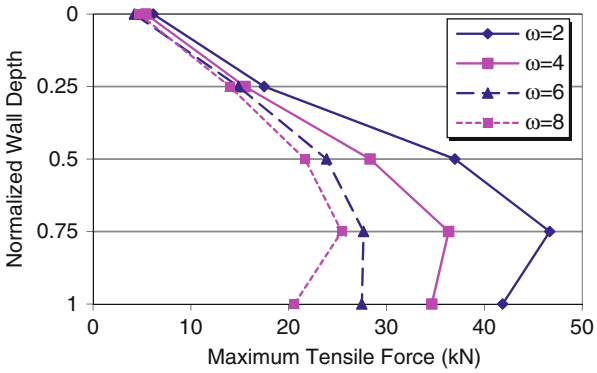

Analysis and Design Issues of Geotechnical Systems: Flexible Walls, Fig. 12 Maximum tensile forces distribution along height of wall facing (Halabian et al. 2010)

It is of interest to note that tensile forces along nail bars increase for the upper nail bars as their inclination angle increases.

Influence of Nail Length The effect of nail length on the peak outward horizontal displacement of the wall is shown in Fig. 15a. It can be noted that the peak outward horizontal displacement of the wall decreases as the nails length increases; while, the peak horizontal acceleration along the wall facing has been greater for longer nail bars (Fig. 15b). However, the major influence of nail length on increasing the peak horizontal acceleration response of the wall would be in the range of 7.5–10 m. Therefore, there would be no considerable influence as the nail length increases beyond the value of 12 m. The results of the maximum nails tensile forces (Fig. 16) indicate that there would be no significant differences in the mobilized maximum tensile forces along nail bars (excluding the third nail) as the nails length increases.

Influence of Soil Strength Properties The soil strength properties, soil friction angle, ϕ, and soil cohesion, c, can also influence on the

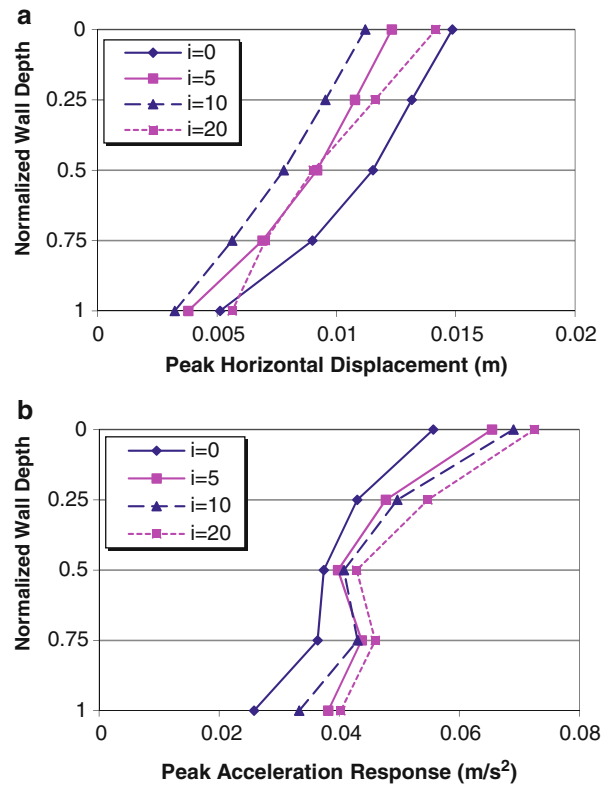

Analysis and Design Issues of Geotechnical Systems: Flexible Walls, Fig. 13 Normalized peak horizontal deformations distribution along height of wall facing (Halabian et al. 2010) (**a**) Normalized peak horizontal displacement (**b**) Normalized peak horizontal acceleration

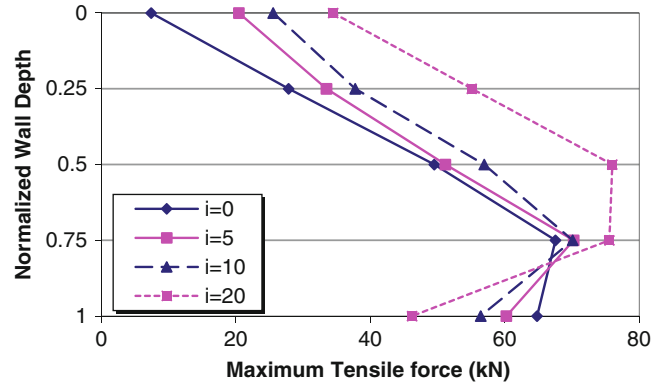

Analysis and Design Issues of Geotechnical Systems: Flexible Walls, Fig. 14 Maximum tensile forces distribution along height of wall facing (Halabian et al. 2010)

wall performance such as horizontal deflections along the wall facing and the maximum mobilized tensile forces along the nail bars during an earthquake. Global performances of soil-nailed walls during earthquakes have shown that increasing in soil strength properties would improve soil shear strength so that soil-nailed wall would better resist against dynamic loads due to harmonic base excitations. As illustrated in Fig. 17a and b, peak horizontal displacements along wall facing decrease as the soil cohesion and internal friction angle increase. Figure 17c and d show that increasing soil strength properties would result in reduction of maximum tensile forces along nail bars.

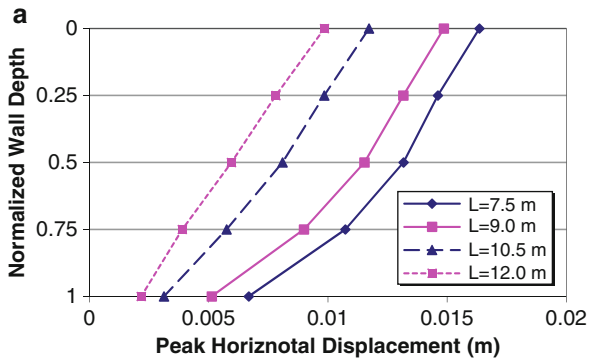

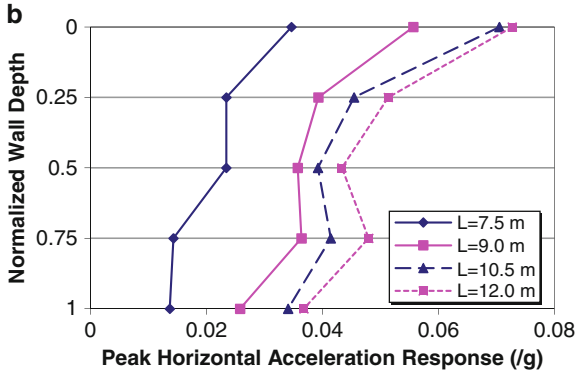

Analysis and Design Issues of Geotechnical Systems: Flexible Walls, Fig. 15 Normalized peak horizontal deformations distribution along height of wall facing (Halabian et al. 2010) (**a**) Normalized peak horizontal displacement (**b**) Normalized peak horizontal acceleration

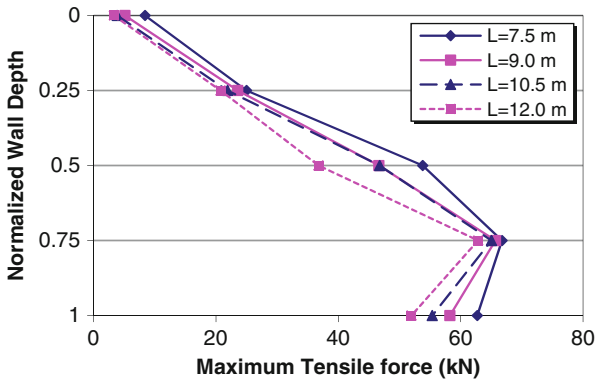

Analysis and Design Issues of Geotechnical Systems: Flexible Walls, Fig. 16 Maximum tensile forces distribution along height of wall facing (Halabian et al. 2010)

Seismic Base Excitations

Similar to the harmonic base excitations, numerous parameters including nails inclination, nails lengths, soil mechanical properties, and nail spacing can contribute to the performance of soil-nailed walls during seismic excitations. In addition to these parameters, the earthquake motions depending on their frequency content and peak amplitude have also substantial influences on deformations of soil-nailed walls. In a study conducted by Halabian et al. (2010) for a soil-nailed wall example, the effects of three different base excitation records (El Centro, Kobe, and Northridge earthquakes) were examined. It is noteworthy that the ground motion with the frequency content close to the soil-nailed system and higher peak amplitude induced considerable lateral displacements along the wall facing compared to the other ground motions (Fig. 18a).

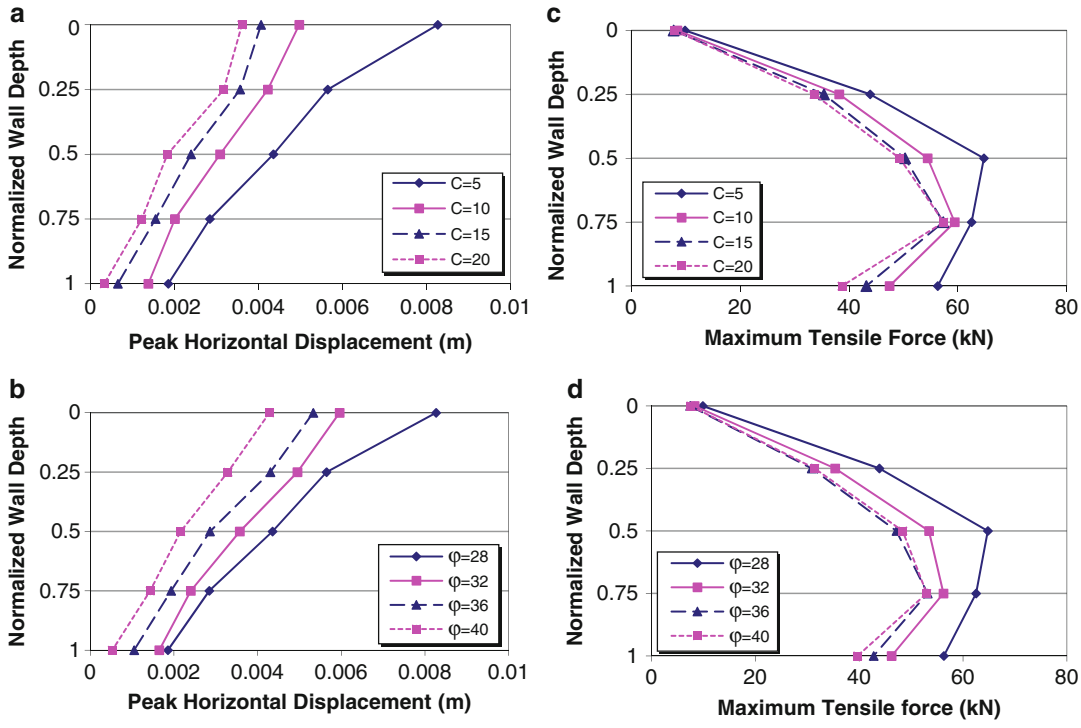

Analysis and Design Issues of Geotechnical Systems: Flexible Walls, Fig. 17 Normalized peak horizontal displacement and maximum tensile forces distribution along height of wall facing (Halabian et al. 2010) (**a**) Normalized peak horizontal displacement (**b**) Normalized peak horizontal displacement (**c**) Maximum tensile forces distribution along height of wall facing (**d**) Maximum tensile forces distribution

Analysis and Design Issues of Geotechnical Systems: Flexible Walls, Fig. 18 The peak response distributions along the height of wall facing (Halabian et al. 2010) (**a**) Normalized peak horizontal displacement distribution (**b**) Maximum tensile forces distribution

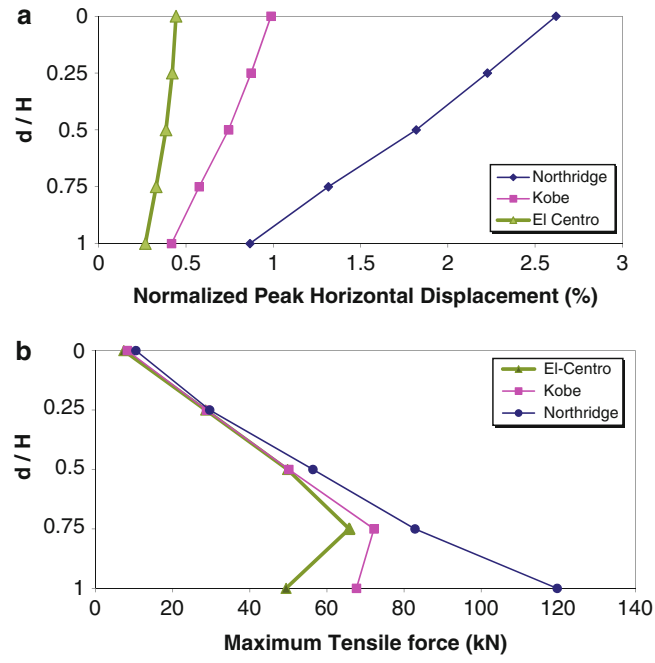

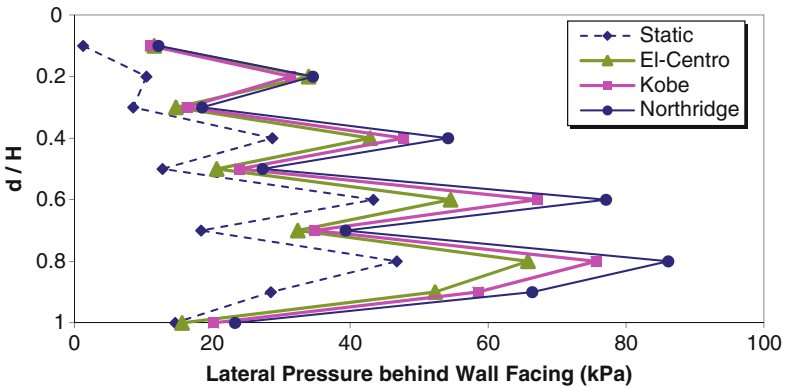

Analysis and Design Issues of Geotechnical Systems: Flexible Walls, Fig. 19 Lateral earth pressure distribution behind wall facing along height of wall (Halabian et al. 2010)

Besides, as illustrated in Fig. 18b, earthquake motions with high peak amplitude of base acceleration would cause higher nail forces along nails. There is considerable difference between the values of nail forces in the fifth row of nails. Furthermore, the earth lateral pressure distribution behind the wall facing for different earthquake motions is depicted in Fig. 19, and it can be concluded that earth pressure will increase as the base excitation peak amplitude rises. The observed pattern in earth lateral distribution could be interpreted due to stage construction of soil-nailed structures.

Summary

Several methods to evaluate the maximum seismic soil pressures for some cases (such as basement walls) where the free movement of the wall is fully or partially restrained, referred as non-yielding walls, are presented. Furthermore, based on a comprehensive parametric study, the influence of crucial parameters on performance of soil-nailed walls after being subjected to harmonic and seismic base excitations were also given.

Cross-References

- Bridge Foundations
- Seismic Analysis of Masonry Buildings: Numerical Modeling
- Seismic Design of Earth-Retaining Structures

References

Al Atik L, Sitar N (2010) Seismic earth pressures on cantilevered retaining structures. J Geotech Geoenviron ASCE Eng 136:1324–1333

Choukeir M, Juran I, Hanna S (1997) Seismic design of reinforced-earth and soil-nailed structures. Ground Improv 1:223–238

Dhouib A (1987) Contribution a L'etude du comportement des sols renforces sous sollicitations statiques et dynamiques. These de Docteur-Ingeniuer, Universite des Sciences et Techniques de Lille Flandres Artois, France

Ebeling RM, Morrison EE, Whitman RV, Liam Finn WD (1992) A manual for seismic design of waterfront retaining structures. US Army Corps of Engineers, Technical Report ITL-92-11

Federal Highway Administration (FHWA), Lazarte CA, Elias V, Espinoza RD, Sabatini PJ (2003) Geotechnical engineering circular no. 7, Soil nailed walls, report no. FHWA0-IF-03-017. Washington, DC

Gur T, Pay AC, Ramirez JA, Sozen MA, Johnson AM, Irfanoglu A, Bobet A (2009) Performance of school buildings in Turkey during the 1999 Düzce and the 2003 Bingöl Earthquakes. Earthq Spectra 25(2):239–256

Halabian AM, Sheikhbahaei AM, Hashemolhosseini SH (2010) Analysis of nailed walls under seismic excitation using finite difference method. In: 9th US national and 10th Canadian conference on earthquake engineering, Toronto

Juran I, Baudrand G, Farrag, K, Elias V (1990) Kinematical limit analysis for design of soil nailed structures. J Geotech Eng 116(1):54–72

Juran I, Elias V (1991) Ground anchors and soil nails in retaining structures. Foundation Engineering Handbook, 2nd edn, Hasai-Yang Fang, Chapter 26

Ostadan F (2004) Seismic soil pressure for building walls-an updated approach. In: 11th international conference on soil dynamics and earthquake engineering (11th ICSDEE) and the 3rd international conference on earthquake geotechnical engineering (3rd ICEGE), University of California, Berkeley

Ostadan F, White WH (1997) Lateral seismic soil pressure-an updated approach. Bechtel Technical Grant Report, Bechtel Corporation, San Francisco
Schnabel PB, Lysmer J, Seed HB (1972) SHAKE – a computer program for earthquake response analysis of horizontally layered sites. Earthquake Engineering Research Center, University of California, Berkeley, Report no. EERC 72–12, Dec
Seed HB, Mitchell JK (1981) Earthquake resistant design of reinforced earth walls. International study for the reinforced earth company, Progress report, Berkeley
Segrestin P, Bastick MJ (1988) Seismic design of reinforced earth retaining walls. In: Proceedings of the international geotechnical symposium on theory and practice of earth reinforcement, Fukuok Kyushu, pp 577–582
Veletsos A, Younan AH (1994) Dynamic soil pressure on rigid vertical walls. Earthq Eng Soil Dyn 23:275–301
Wood J (1973) Earthquake-induced soil pressures on structures. Report EERL 73–05, California Institute of Technology, Pasadena

Analysis and Design Issues of Geotechnical Systems: Rigid Walls

Amir M. Halabian
Department of Civil Engineering, Isfahan University of Technology, Isfahan, Iran

Synonyms

Pseudo-dynamic method; Rigid retaining walls; Yielding walls

Introduction

Earthquakes have caused transient and permanent deformations of retaining structures in past severe earthquakes followed by collapse of walls in some cases. Therefore, knowledge of seismic active earth pressure behind retaining walls is very important in the design of these structures in seismically active regions. This article discusses commonly used pseudo-static approaches such as the Mononobe-Okabe method, which gives the linear distribution of seismic earth pressure on rigid retaining walls in an approximate way. A general pseudo-dynamic method is also presented to compute the distribution of seismic active earth pressure on a rigid retaining walls supporting cohesionless backfill in more realistic manner by considering time and phase difference within the backfill.

Types of Retaining Walls

Earth retaining structures are structures that can be used to support backfill along a slope or to support an excavation as illustrated in Fig. 1.

Various types of retaining structures are adopted for different applications. Over the time, the classical gravity rigid retaining walls evolved into reinforced concrete cantilever walls (e.g., sheet piles), with or without buttresses and counter forts (Fig. 2). These were then followed by a variety of crib- and bin-type walls. All these walls are externally stabilized walls or conventional gravity retaining walls.

In order to stabilize the deep excavation projects in metropolitan areas or even slopes where sequential construction in comparison with other common retaining walls is beneficial, the flexible retaining structures could be considered. During the sequential excavation, an in situ flexible retaining wall system is constructed to provide stability and to minimize movements of the adjacent ground. Soldier piles with shotcrete lagging are being used extensively as an excavation support system, particularly in stiff soil conditions and where ground water ingress into the excavated area is not problematic (Tomlinson 1995). Furthermore, since the soldier piles are not contiguous, much fewer soldier piles often need to be driven in comparison with sheet piles, thereby yielding significant savings in time and cost of installation and thus allowing excavation to commence with a minimum of lead time. These systems are usually being constrained against certain types of movements by the presence of external bracing elements such as struts (Figs. 3 and 4). In the case of basement walls or bridge abutments, lateral movements at the top of the retaining structure are restrained by the presence of the structure they support.

Soil reinforcement in various constructions is also used to provide the stability for excavations

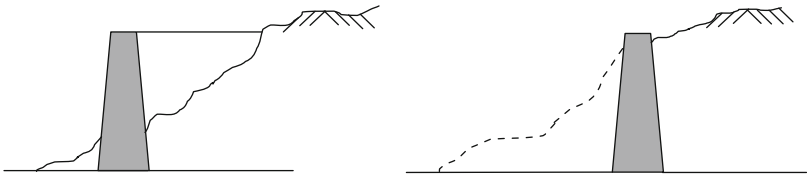

Analysis and Design Issues of Geotechnical Systems: Rigid Walls, Fig. 1 Gravity retaining structures

and is proven to be effective and under practice from the last two decades. Among the reinforced soil retaining structures, geosynthetic reinforced soil retaining walls with modular block facing are functioned well during the past seismic events compared to the other flexible retaining walls. The reinforced layers of soil in the mechanically stabilized earth mass made with this technique allow the modular construction, which was clearly recognized as being advantageous in most practical situations (Fig. 5).

Soil nailing is another in situ reinforcing technique of the soil while it is excavated from the top down. Using soil-nailed walls which consist of passive reinforcement to the existing ground by installing closely spaced steel bars or cables encased in grout has gained a lot of popularity in recent years (Fig. 6). This method is typically used in order to stabilize slopes and excavations where sequential construction is beneficial in comparison with other common retaining walls. The mass of reinforced soil made by an array of soil nails functions to retain the less stable material behind it. In the right soil conditions, soil nailing is a rapid and economical means of constructing excavation support systems and retaining walls. The process of construction of soil-nailed walls commonly involves three important stages: excavation, nail installation, and face stabilization. The fundamental stability concept of soil-nailed walls is based on reinforcing soil mass with reinforcement elements such as steel rebars so that the soil mass could behave as a unit mass.

Due to significant flexibility of soil-nailed walls which is attributed to particular construction procedure of these systems, soil-nailed walls can experience more deflections comparing with other common gravity walls. After the 1989 Loma Prieta, 1995 Kobe, and 2001 Nisqually earthquakes, it was reportedly observed that soil-nailed walls have shown no sign of being

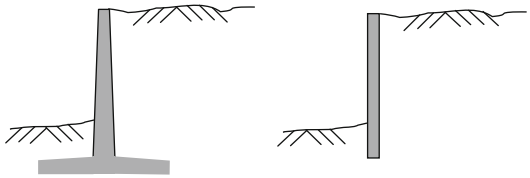

Analysis and Design Issues of Geotechnical Systems: Rigid Walls, Fig. 2 Cantilever retaining structures

distressed or significant permanent deflection, despite having experienced, in some cases, ground accelerations as high as 0.7 g. The observations from post-earthquake investigations imply that soil-nailed walls appear to have an inherent satisfactory seismic response. This has been attributed to the intrinsic flexibility of soil-nailed wall system and possibly some level of conservatism in current design procedures (Choukeir et al. (1997)).

Although soil nailing is now recognized as a viable technique in retaining structures, tiebacks have been used and continue to be employed as a temporarily supporting system for excavations. Permanent tieback walls have been used in cuts, bridge abutments, underpinning of structures, and stabilization of sliding slopes. Essentially, there are two types of tieback walls: the slurry wall that is also called diaphragm wall and the soldier pile wall. The main advantage of using soldier piles is their relatively low cost and ease of installation, compared to other forms of supporting systems such as diaphragm walls and bored piles.

Furthermore, since the soldier piles are not contiguous, much fewer soldier piles often need to be driven in comparison to sheet piles. The soldier pile walls are built by driving piles (usually H-piles) in a line with spacing of the order of 2–3 m. Soldier piles are driven to a depth slightly below the final excavation. Sometimes bored piles are used by drilling a hole, lowering an H-pile in the center and filling the annulus with low strength concrete.

Analysis and Design Issues of Geotechnical Systems: Rigid Walls, Fig. 3 Braced excavation

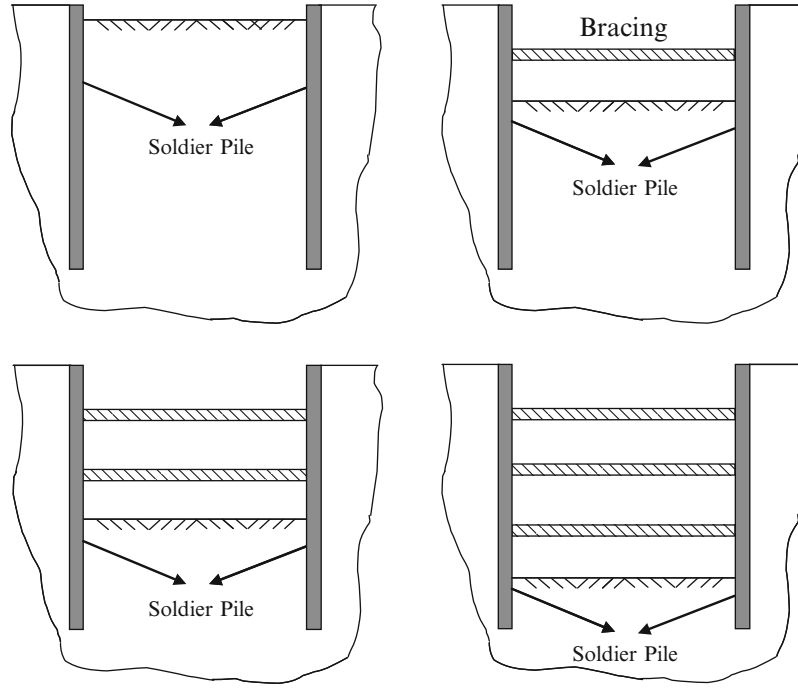

Analysis and Design Issues of Geotechnical Systems: Rigid Walls, Fig. 4 Braced excavation steps

As excavation proceeds, wood lagging or sheeting (concrete shotcrete) is placed to retain the soil between the piles. Then, the anchors are installed at regular intervals and grouted in a zone beyond the failure zone. The anchors are stressed up to a chosen load when the grout has sufficiently cured. The process continues until the final excavation level is reached. Tiebacks eliminate

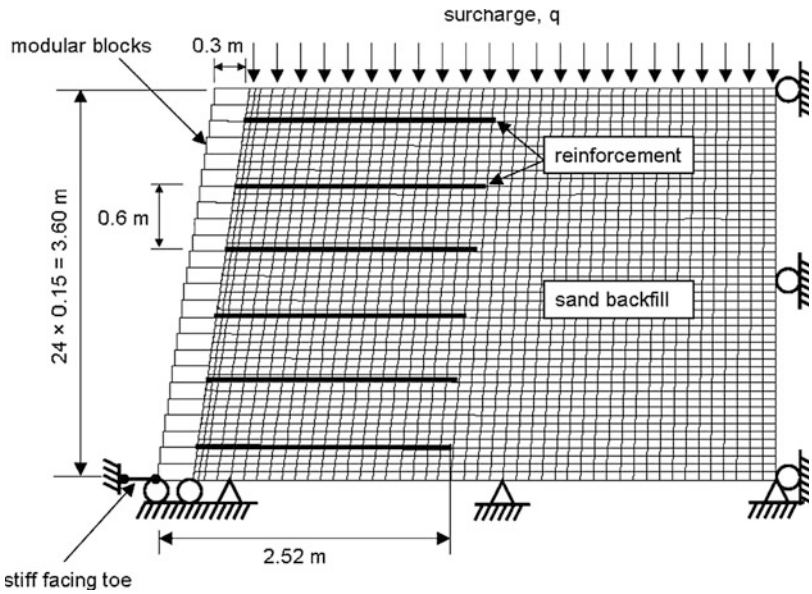

Analysis and Design Issues of Geotechnical Systems: Rigid Walls, Fig. 5 Geosynthetic reinforced soil retaining wall with modular block facing

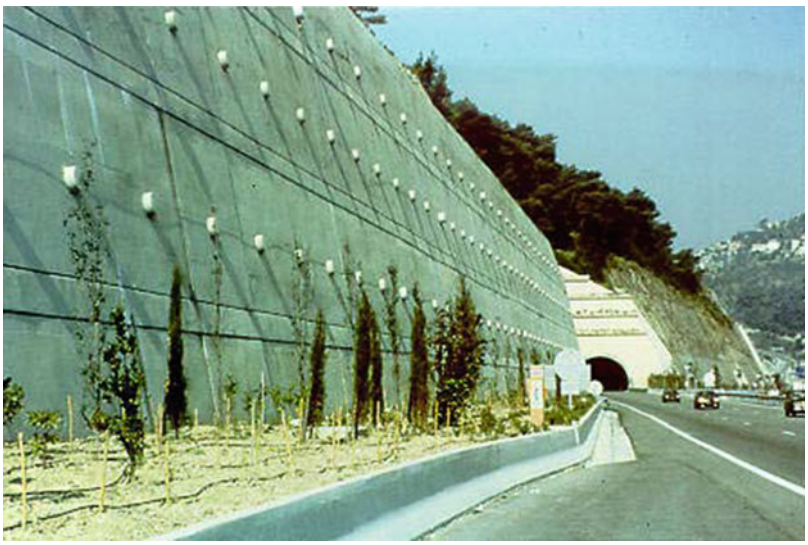

Analysis and Design Issues of Geotechnical Systems: Rigid Walls, Fig. 6 Soil-nailed walls

obstructions in the excavation inherent in struts. The total structural system acts in tension and receives its support in earth and, therefore, consists of the earth mass, which provides the ultimate support for the system, tension members which transfers the load from the soil-retention system to the earth mass. A stressing unit, which engages the anchors, permits the tieback element to be stressed and allows the load to be maintained in the tieback. A typical tieback wall is shown in Fig. 7.

Depending on soil-induced deformation values, earth retaining structures are broadly categorized into non-yielding, yielding, and self-yielding walls. Non-yielding walls are inherently incapable of and/or constrained against both deformation and displacement in the horizontal direction under static or dynamic loads. Basement walls of buildings, bridge abutments, and free-standing retaining walls that are restrained against horizontal displacement due to physical restraint or structure geometry can be named as

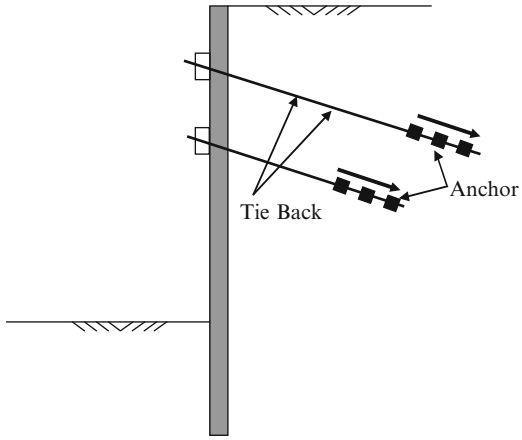

Analysis and Design Issues of Geotechnical Systems: Rigid Walls, Fig. 7 Tieback retaining system

the common examples. In the static loading phases, non-yielding structures can be logically designed assuming the at-rest earth pressure state within the retained soil. However, in the metropolitan areas where one major concern with deep excavations is the potentially large ground deformations in and around the excavation resulting damages to the adjacent buildings and utilities, there are many uncertainties corresponding to the calculation of the lateral earth pressure distribution of braced excavation systems. While active and passive earth pressure theory is applicable in simple cases, multilevel braced excavations tend to experience more complex earth pressures.

Yielding walls define earth retaining systems that can either displace or deform or both in the horizontal direction under design loads. For rigid retaining walls, the deformation mode shapes could be translation, rotation, or both (Fig. 8). These structures are assumed to be capable of developing the active or passive earth pressure states within the retained soil. The third type of earth retaining structures is so-called self-yielding rigid walls whose as a result of thermal changes in their surrounding environment displace horizontally on their own as opposed to displacing (or not) as a reaction from earth loads as in the classic cases of yielding and non-yielding earth retaining walls. Examples include various types of circular water- and wastewater-treatment tanks (Horvath 2005).

Dynamic Earth Pressure on Rigid Retaining Structures

Design of retaining structures to sustain strong earthquakes may further assure the efficient functioning of these structures. Among several aspects to be considered for seismic design of these structures, seismic lateral earth pressure on rigid walls is the important parameter for designing proper reinforcement materials and configuration. Earth pressure theories associated with conventional rigid retaining walls which are based on limit state analysis of yielding walls on the static conditions can be extended to the dynamic states. According to IBC 2006, the natural frequency (in terms of Hz) of a retaining wall with height H can be roughly calculated by

$$f = \frac{20}{H^{0.75}} \tag{1}$$

in which H is the height of the wall in meter. If the natural frequency of wall is considerably larger than the frequency of the input motion applied to the wall, the soil structure system could be assumed to be rigid, and therefore, earth pressure theories, hereafter, are applicable. Methods that are commonly used for design of retaining walls could be classified as force-based methods developed on limit state analysis basis and performance-based approaches.

Force-Based Method

Increasing lateral earth pressures on retaining walls during earthquakes has been one of the major causes of their damage and excessive displacement (Seed and Whitman 1970; Dakoulas and Gazetas 2008). Therefore, correct estimation of the active earth pressure distribution acting on retaining walls during earthquakes is vital for evaluating the safety and designing of the wall. Some simplified approaches have been proposed to calculate the rather complicated dynamic earth pressures on retaining walls during earthquakes (Okabe 1926; Mononobe and Matsuo 1929; Wood 1973;

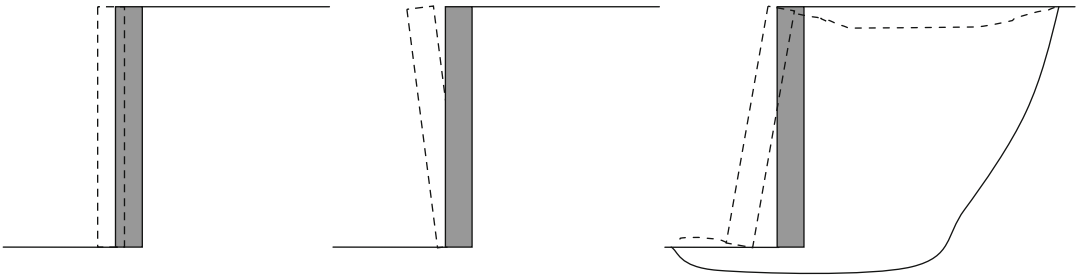

Analysis and Design Issues of Geotechnical Systems: Rigid Walls, Fig. 8 Deformation mode shapes for yielding rigid retaining walls

Steedman and Zeng 1990; Richards et al. 1999; Choudhury and Singh 2006; Ghosh 2008).

Mononobe-Okabe Approach

Okabe (1926) and Mononobe and Matsuo (1929) extended Coulomb's theory and considered seismic forces by applying earthquake loads as pseudo-static inertial forces to the Coulomb active or passive failure wedge. This pseudo-static method (known as the Mononobe-Okabe method) has been widely used in practical applications (Mylonakis et al. 2007) and is recommended by several building codes and guidelines (e.g., EAU 1996; FHWA 1997; CHBDC 1998; ASCE 4–98 2000; FEMA 369 2000; PIANC 2001; EN 1997 2002; AASHTO 2006; IBC 2006) because of its simplicity in practical applications and reasonable predictions of the actual dynamic pressures acting on walls (Seed and Whitman 1970; Whitman 1990; Ebeling et al. 1992; Veletsos and Younan 1994; Dakoulas and Gazetas 2008).

The dynamic lateral earth pressure on rigid retaining structures proposed in the Mononobe-Okabe method is obtained from the equilibrium of the active or passive wedges (Fig. 9a and b). In addition to the forces that exist under static conditions of the failure wedge in a dry, cohesionless backfill, the wedge is also subjected to horizontal and vertical pseudo-static forces specified as the mass of the wedge multiplied by pseudo-static accelerations $a_h = k_h g$ and $a_v = k_v g$. The total active and passive thrusts on a rigid wall retaining a dry, cohesionless backfill can be presented in a form similar to what is developed for the static conditions in the Coulomb's theory:

$$P_{AE} = \frac{\gamma_b H^2}{2}(1 - k_v) K_{AE} \tag{2}$$

$$P_{PE} = \frac{\gamma_b H^2}{2}(1 - k_v) K_{PE} \tag{3}$$

in which γ_b is the backfill unit weight, H is the height of the wall, and P_{AE} and P_{PE} are the dynamic active and passive earth pressures. K_{AE} and K_{PE} are the coefficient of dynamic active and passive earth pressures given by:

$$K_{AE} = \frac{\cos^2(\varphi_b - \varphi - \beta)}{\cos\varphi \cos^2\beta \cos(\delta + \varphi + \beta)\left(1 + \sqrt{\frac{\sin(\varphi_b + \delta)\sin(\varphi_b - \varphi - i)}{\cos(\delta + \beta + \varphi)\cos(i + \beta)}}\right)^2} \tag{4}$$

$$K_{PE} = \frac{\cos^2(\varphi_b - \varphi + \beta)}{\cos\varphi \cos^2\beta \cos(\delta + \varphi - \beta)\left(1 - \sqrt{\frac{\sin(\varphi_b + \delta)\sin(\varphi_b - \varphi + i)}{\cos(\delta - \beta + \varphi)\cos(i + \beta)}}\right)^2} \tag{5}$$

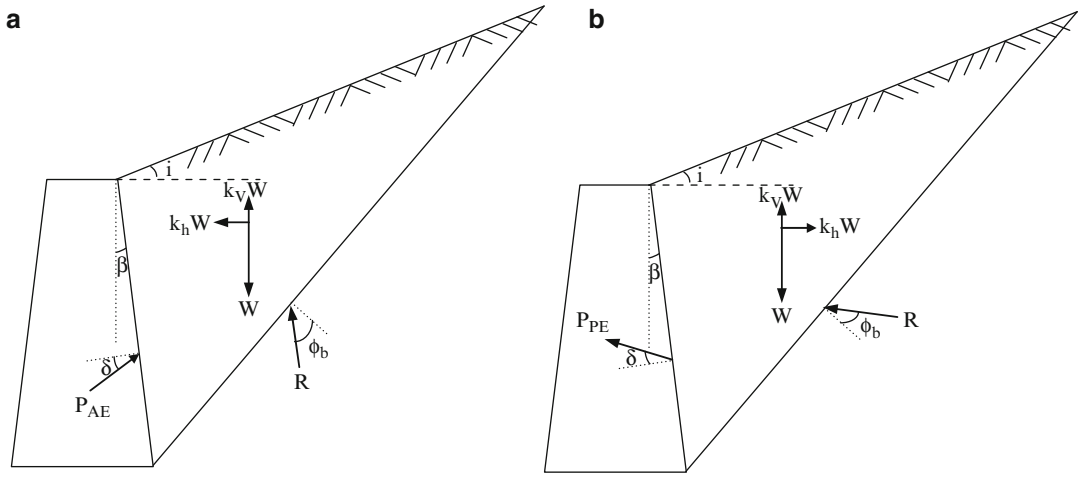

Analysis and Design Issues of Geotechnical Systems: Rigid Walls, Fig. 9 Mononobe-Okabe approach's failure wedges. (**a**) Forces acting on active wedge in Mononobe-Okabe analysis. (**b**) Forces acting on passive wedge in Mononobe-Okabe analysis

φ_b is the internal friction angle of the backfill. i is the slope of the backfill with respect to the horizontal axis. δ is the friction angle between the inner face of the wall and the backfill. β is the angle between the inner face of the wall and the vertical axis. $\varphi = \tan^{-1}\frac{k_h}{1-k_v}$ in which k_h and k_v stand for the horizontal and vertical accelerations of the soil wedge in g unit. The wall is unstable when k_h is higher than $(1-k_v)$ tan φ. During the earthquake, k_h and k_v are time varying and chaos so that the seismic earth pressures in both active and passive cases are not constant. The vertical ground excitation has a great influence on dynamic stability of rigid retaining structures during an earthquake. Despite time-varying nature of ground excitations accelerations, the vertical accelerations of earthquakes usually assumed to be a fraction of their horizontal accelerations.

Although the Mononobe-Okabe method suggests that the total dynamic lateral earth pressure on rigid retaining structures should apply at a point H/3 above the base of the wall of height, H, experimental results demonstrated that it actually occurs at the higher point under dynamic loading conditions (Fig. 10). The total dynamic lateral earth pressure can be divided into the static active or passive component, P_A or P_P, and the dynamic contribution, ΔP_{AE} or ΔP_{PE}:

$$P_{AE} = P_A + \Delta P_{AE},\ P_{PE} = P_P + \Delta P_{PE} \qquad (6)$$

According to the Coulomb theory for linear backfill surfaces with no surcharge loading, the static component acts at a point located H/3 above the height of the wall. On the other hand, the dynamic part can be taken to act at a point approximately 0.6H above the base of the wall (Seed and Whitman 1970). Therefore, the total lateral earth pressure is applied at a height:

$$h = \frac{P_A\,(H/3) + \Delta P_{AE}(0.6H)}{P_{AE}} \qquad (7)$$

above the base of the wall.

Effects of Water on Dynamic Lateral Pressures

Hydrodynamic Pressure

The retaining walls in practice are usually designed with drainage systems to prevent water from building up. In these cases, the dynamic lateral earth pressure can be

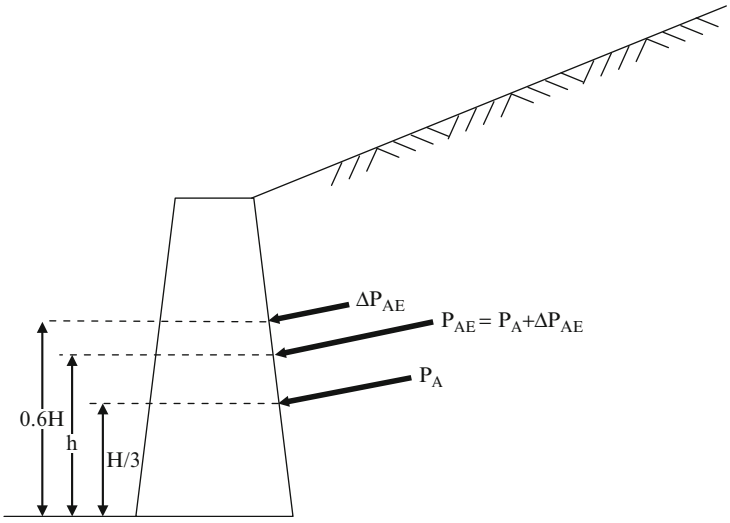

Analysis and Design Issues of Geotechnical Systems: Rigid Walls, Fig. 10 Acting point of the total active thrust

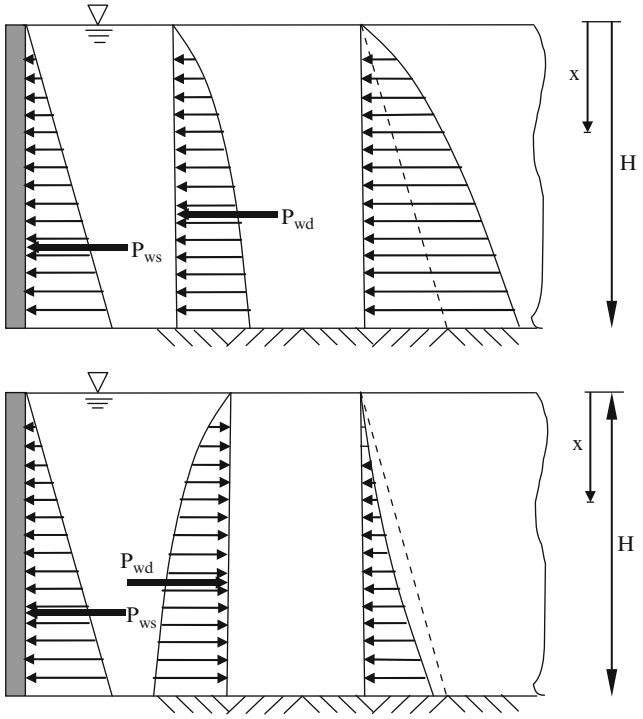

Analysis and Design Issues of Geotechnical Systems: Rigid Walls, Fig. 11 Acting point of the total active thrust

determined based on soil dry unit weight using the Mononobe-Okabe theory. However, the presence of water in retaining walls in waterfront areas and in backfills behind retaining walls can play a significant role in determining seismic loads that act on the wall during and after earthquakes. During any ground excitations, besides the hydrostatic pressure, p_{ws}, water in front of a retaining wall will exert dynamic pressures, p_{wd}, on the face of the wall (Fig. 11). The hydrostatic pressure is calculated by

$$p_{ws}(x) = \gamma_w x \tag{8}$$

in which γ_w is the water unit weight and x is the distance from the reservoir surface. The total hydrostatic thrust is then determined as

$$P_{ws} = \int_0^H p_{ws}(x)\,dx = \frac{1}{2}\gamma_w H^2 \qquad (9)$$

The application point of the hydrostatic thrust is a point H/3 above the base of the wall of height, H.

Hydrodynamic pressure results from the seismic response of the water mass in front of the wall and is usually estimated using Westergaard's theory (Westergaard 1931). Westergaard's theory applies for a vertical rigid wall retaining a very large (theoretically infinite) extent of water basin with no backfill horizontally excited by harmonic motion of its rigid base. The amplitude of hydrodynamic pressure is then determined using Westergaard's theory as

$$p_{wd}(x) = \frac{7}{8} k_h \gamma_w H\sqrt{x/H} \qquad (10)$$

The resultant hydrodynamic force is obtained as

$$P_{wd} = \int_0^H p_{wd}(x)\,dx = \frac{7}{12} k_h \gamma_w H^2 = (1.17\ k_h P_{ws}) \qquad (11)$$

According to Westergaard's theory, the hydrodynamic thrust can be taken to act at a point approximately 0.4H above the base of the wall. The excess hydrodynamic pressures could be applied toward or outward the wall depending on the base excitation direction. Thus, the direction of the excitation should be taken into account in determining the total hydrodynamic pressure acting on the wall.

Effect of Wall Inclination

The hydrodynamic pressure on the walls with facing inclination (Fig. 12) could be estimated taking the wall inclination using Zangar (1953) and Chwang (1978):

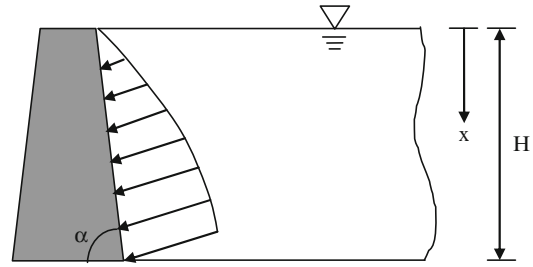

Analysis and Design Issues of Geotechnical Systems: Rigid Walls, Fig. 12 Effect of wall inclination on hydrodynamic pressure

$$p_{wd}(x, \alpha) = C_m(\alpha)\, k_h \gamma_w H\left[\frac{x}{H}\left(2 - \frac{x}{H}\right) + \sqrt{\frac{x}{H}\left(2 - \frac{x}{H}\right)}\right] \qquad (12)$$

or approximately using Westergaard's approach can be estimated by

$$p_{wd}(x, \alpha) = \frac{7}{8} C_m(\alpha)\, k_h \gamma_w H\sqrt{x/H} \qquad (13)$$

in which $C_m(\alpha)$ is the inclination factor given by

$$C_m(\alpha) = 2.0\,\frac{\alpha}{\pi} \qquad (14)$$

The total hydrodynamic thrust considering the wall inclination acts at a point located 0.4H above the base of the wall of height, H with amplitude

$$P_{wd}(\alpha) = \frac{7}{12} C_m(\alpha) k_h \gamma_w H^2 = (1.17\ C_m(\alpha) k_h P_{ws}) \qquad (15)$$

Effect of Water Basin Length

Westergaard's theory was developed based on this assumption that the rigid wall is retaining a semi-infinite reservoir of water. For the case a finite water basin (Fig. 13), the hydrodynamic pressure applied to the wall can be evaluated using Werner and Sundquist's (1943) suggestion by intruding the water basin length modification factor, C_n, as

$$p_{wd}(x) = \frac{7}{8} C_n k_h \gamma_w H\sqrt{x/H} \qquad (16)$$

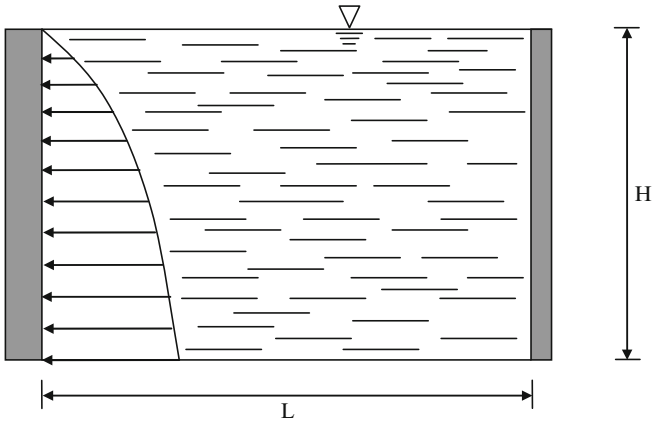

Analysis and Design Issues of Geotechnical Systems: Rigid Walls, Fig. 13 Wall retaining finite water basin

where C_n is defined in terms of ratio of water basin length, L, over the wall height, H, as

$$C_n = \frac{4}{3}\frac{L/H}{1+L/H} \le 1.0 \qquad C_n = 1.0 \quad L/H \ge 2.7 \tag{17}$$

The total hydrodynamic thrust considering the water basin length effect acts at a point located 0.4H above the base of the wall of height, H with amplitude

$$P_{wd} = \frac{7}{12} C_n k_h \gamma_w H^2 = (1.17\ C_n k_h P_{ws}) \tag{18}$$

Dynamic Pressure for Saturated Backfill

Seismic response of rigid walls retaining saturated backfills could be affected by the presence of water changing the inertial forces within the backfill, developing the hydrodynamic pressures with the saturated soil and generating excess pore water pressure resulting in the cyclic deformation of the backfill soil (Matsuo and Ohara 1965). The soil permeability plays an important role in developing hydrodynamic pressures within the backfill soil. For soils with small permeability, the pore water moves within the soil in restrained conditions during the ground shaking; while if the permeability of the backfill is very high, the soil particles move easily through the pore water, and the pore water may remain stationary. Hydrodynamic water pressures resulting from the seismic response of the water in the backfill soils could be estimated by Westergaard's theory modifying the effect of the soil permeability as

$$p_{wd}(x) = \frac{7}{8} C_e k_h \gamma_w H \sqrt{x/H} \tag{19}$$

in which C_e is the correction factor that expresses the portion the pore water which vibrates freely within the soil:

$$C_e = 0.5 - 0.5 \tan h \left[\log \frac{2\pi n \gamma_w H^2}{7 E_w K T}\right] \tag{20}$$

where n is the porosity, H is the water depth, E_w is the bulk modulus of water (2×10^6 kPa), K is the backfill permeability, and T is the predominant period of the excitation (Fig. 14).

The total hydrodynamic thrust considering the water within the backfill acts at a point located 0.4H above the base of the wall of height, H with amplitude

$$P_{wd} = \frac{7}{12} C_e k_h \gamma_w H^2 = (1.17\ C_e k_h P_{ws}) \tag{21}$$

Earth Lateral Pressures on Walls Retaining Saturated Backfills

For walls retaining saturated soils with restrained pore water conditions, to take into account the presence of water within the backfill, the Mononobe-Okabe approach is modified using

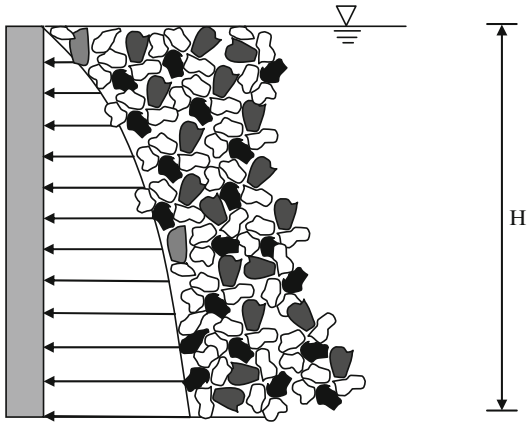

Analysis and Design Issues of Geotechnical Systems: Rigid Walls, Fig. 14 Wall retaining saturated backfill

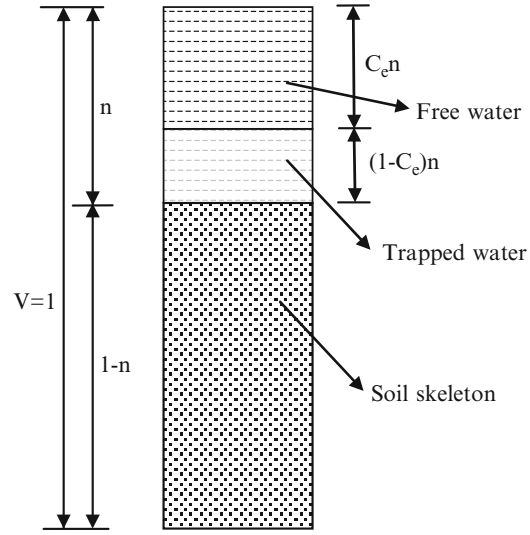

Analysis and Design Issues of Geotechnical Systems: Rigid Walls, Fig. 15 Physical analogy proposed by Matsuzawa et al. (1985)

physical analogy proposed by Matsuzawa et al. (1985). The dynamic lateral pressures act on a yielding wall are coming from the soil skeleton, the trapped water which vibrates together with the soil skeleton and free water which vibrates independently from the soil skeleton (Fig. 15). The total active static soil thrust acts at a point located H/3 above the height of the wall can be evaluated as

$$P_A = \frac{1}{2} k_A (\gamma_{sat} - \gamma_w) H^2 \tag{22}$$

Besides the hydrostatic force exerted on the wall, the hydrodynamic pressures considering the wall facing inclination, the water basin length, and the saturated backfill resulting from the seismic response of the water in the backfill soil could be estimated as

$$p_{wd}(x) = \frac{7}{8} C_n C_m C_e k_h \gamma_w H \sqrt{x/H} \tag{23}$$

and the total hydrodynamic thrust acts at a point located 0.4H above the base of the wall (Fig. 16) and is determined by

$$\begin{aligned} P_{wd} &= \frac{7}{12} C_n C_m C_e k_h \gamma_w \\ H^2 &= (1.17\ C_n C_m C_e k_h P_{ws}) \end{aligned} \tag{24}$$

If the total dynamic earth pressure coefficient, K_{AE}, is written as

$$K_{AE} = K_A + \Delta K_{AE}$$

and using an approximation for ΔK_{AE} equal to $(3/4)k_h$ suggested by Seed and Whitman, therefore, the dynamic lateral force component for a rigid wall retaining dry backfill soil would be

$$\Delta P_{AE} = \frac{1}{2} \gamma H^2 \Delta K_{AE} = \frac{1}{2} \left(\frac{3}{4} k_h \right) \gamma H^2 \tag{25}$$

For saturated backfill soil, the dynamic component of the earth thrust acting on the wall (Fig. 16), employing $\gamma^* = C_e \gamma_{dry} + (1 - C_e) \gamma_{sat}$, should be computed as

$$\Delta P_{AE} = \frac{1}{2} \left(\frac{3}{4} k_h \right) \gamma^* H^2 \tag{26}$$

P_A computation requires $\gamma_{sat} - \gamma_w$, while γ^* should be used in determining ΔP_{AE}. However, sometimes it is necessary to compute

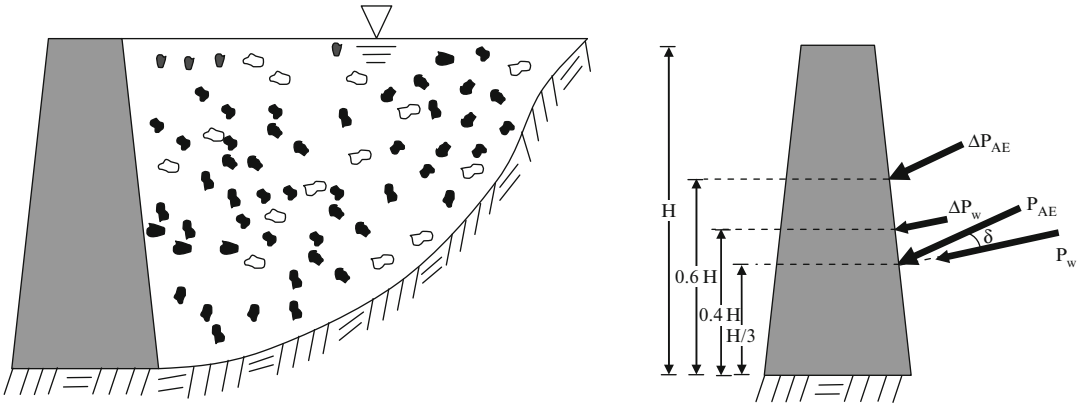

Analysis and Design Issues of Geotechnical Systems: Rigid Walls, Fig. 16 Different components of acting thrust on the wall

P_A and ΔP_{AE} with a common unit weight (e.g., EAK 2002). In this case, the buoyant unit weight, $\gamma_{sat} - \gamma_w$, and a modified seismic coefficient as

$$k^* = k\frac{\gamma^*}{\gamma_{sat} - \gamma_w} \tag{27}$$

For impermeable soils such as clayey sand, clayey silts, and clayey gravels, $C_e = 0$, and therefore, should be used $\gamma^* = \gamma_{sat}$ resulting $P_{wd} = 0$ and

$$\Delta P_{AE} = \frac{1}{2}\left(\frac{3}{4}k_h\right)\gamma_{sat}H^2 \tag{28}$$

or

$$\Delta P_{AE} = \frac{3}{8}\left(k_h\frac{\gamma_{sat}}{\gamma_{sat} - \gamma_w}\right)(\gamma_{sat} - \gamma_w)H^2 \tag{29}$$

On the other hand, for permeable soils such as sands, gravels, and cobbles, $C_e = 1$, and therefore, $\gamma^* = \gamma_{dry}$ resulting

$$P_w = \frac{1}{2}\gamma_W H^2,\ P_{wd} \neq 0$$

$$\Delta P_{AE} = \frac{1}{2}\left(\frac{3}{4}k_h\right)\gamma_{dry}H^2 \tag{30}$$

or

$$\Delta P_{AE} = \frac{3}{8}\left(k_h\frac{\gamma_{dry}}{\gamma_{sat}\text{-}\gamma_w}\right)(\gamma_{sat} - \gamma_w)H^2 \tag{31}$$

In other approach, by representing the excess pore water pressure in the backfill using the pore pressure ratio, r_u, the active earth pressure acting on wall with cohesionless backfill can be computed using

$$p_{AE} = K_{AE}\gamma_{sub}(1 - r_u)(1 - k_v)$$

$$\varphi = \tan^{-1}\left[\frac{\gamma_{sat}k_h}{\gamma_{sub}(1 - r_u)(1 - k_v)}\right] \tag{32}$$

Steedman-Zeng Method

The dynamic nature of earthquake loading in M-O method is considered in a very approximate way without taking any effect of time. To reach the dynamic response characteristics of rigid walls during an earthquake taking into account the phase difference due to finite shear wave propagation within the backfill soil, Steedman and Zeng (1990) proposed a simple pseudo-dynamic approach to determine the seismic response of fixed-base cantilever walls subjected to a harmonic horizontal acceleration considering finite shear wave velocity within backfill material. Choudhury and Nimbalkar (2006) extended the Steedman-Zeng approach to take into account the wall friction angle, soil

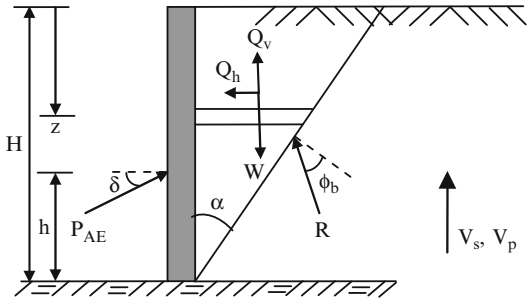

Analysis and Design Issues of Geotechnical Systems: Rigid Walls, Fig. 17 Retaining wall considered for computation of pseudo-dynamic active earth pressure

friction angle, shear wave velocity (Vs), primary wave velocity (Vp), and both the horizontal and vertical seismic accelerations ($k_h g$ and $k_v g$) on the seismic active earth pressure behind the wall (Fig. 17).

If the retaining wall is subjected to both the horizontal and vertical seismic accelerations ($k_h g$ and $k_v g$), the accelerations at any depth z and time t, below the top of the wall, can be expressed as

$$\ddot{u}(z,t) = k_h g \sin\left[\omega\left(t - \frac{H-z}{V_s}\right)\right]$$

$$\ddot{v}(z,t) = k_v g \sin\left[\omega\left(t - \frac{H-z}{V_p}\right)\right] \quad (33)$$

The mass of a thin element of wedge at depth z is

$$m(z) = \gamma_b \frac{H-z}{g \tan\alpha} dz \quad (34)$$

The total horizontal and vertical inertial forces acting within the failure zone can be expressed as

$$F_h(t) = \int_0^H m(z)\ddot{u}(z,t)dz = \frac{\lambda\gamma_b k_h}{4\pi^2 \tan\alpha}[2\pi H\cos\omega\zeta + \lambda(\sin\omega\zeta - \sin\omega t)]$$

$$F_v(t) = \int_0^H m(z)\ddot{v}(z,t)dz = \frac{\eta\gamma_b k_v}{4\pi^2 \tan\alpha}[2\pi H\cos\omega\psi + \eta(\sin\omega\psi - \sin\omega t)] \quad (35)$$

where $\lambda = 2\pi V_s/\omega$ is the wavelength of the vertically propagating shear wave, $\zeta = t - H/V_s$, $\eta = 2\pi V_p/\omega$ is the wavelength of the vertically propagating primary wave, and $\psi = t - H/V_p$. For rigid wedge, the shear wave velocity and the primary wave velocity tend to infinite, and total horizontal and vertical inertial forces will be equivalent to the pseudo-static force assumed in the Mononobe-Okabe method. The total (static + seismic) active thrust, $P_{AE}(t)$, can be obtained by resolving the forces on the wedge and considering the equilibrium of the forces, and hence $P_{AE}(t)$ can be expressed as follows:

$$P_{AE}(t) = \frac{F_h(t)\cos(\alpha-\varphi_b) + W\sin(\alpha-\varphi_b) - F_v(t)\sin(\alpha-\varphi_b)}{\cos(\delta+\varphi_b-\alpha)} \quad (36)$$

The seismic active earth pressure coefficient, K_{AE}, is defined as

$$K_{AE} = \frac{2P_{AE}}{\gamma_b H^2} \quad (37)$$

Substituting for F_h and F_v, K_{AE} is derived as

$$K_{AE} = \frac{1}{\tan\alpha}\frac{\sin(\alpha-\varphi_b)}{\cos(\delta+\varphi_b-\alpha)} + \frac{k_h}{2\pi^2\tan\alpha}\left(\frac{2\pi V_s}{\omega H}\right)\frac{\cos(\alpha-\varphi_b)}{\cos(\delta+\varphi_b-\alpha)}m_1 - \frac{k_v}{2\pi^2\tan\alpha}\left(\frac{2\pi V_p}{\omega H}\right)\frac{\sin(\alpha-\varphi_b)}{\cos(\delta+\varphi_b-\alpha)}m_2 \quad (38)$$

where

$$m_1 = \left[2\pi os2\pi\left(\frac{t\omega}{2\pi} - \frac{H\omega}{2\pi V_s}\right) + \left(\frac{2\pi V_s}{H\omega}\right)\left(\sin 2\pi\left(\frac{t\omega}{2\pi} - \frac{H\omega}{2\pi V_s}\right) - \sin 2\pi\left(\frac{t\omega}{2\pi}\right)\right)\right]$$

$$m_2 = \left[2\pi os2\pi\left(\frac{t\omega}{2\pi} - \frac{H\omega}{2\pi V_p}\right) + \left(\frac{2\pi V_p}{H\omega}\right)\left(\sin 2\pi\left(\frac{t\omega}{2\pi} - \frac{H\omega}{2\pi V_p}\right) - \sin 2\pi\left(\frac{t\omega}{2\pi}\right)\right)\right] \quad (39)$$

From the above equation, it can be noted that K_{AE} is function of the dimensionless parameters $\frac{H\omega}{2\pi V_s}$, $\frac{H\omega}{2\pi V_p}$, $\frac{t\omega}{2\pi}$, and the wedge angle, α. The maximum value of K_{AE} is obtained by optimizing K_{AE} with respect to $\frac{t\omega}{2\pi}$ and α. This parameter would be a function of $\frac{H\omega}{2\pi V_s}$ and $\frac{H\omega}{2\pi V_p}$ which is the ratio of time for shear wave and primary wave to travel the full height of the wall to the period of lateral shaking.

The seismic active earth pressure distribution can be obtained by differentiating the total active thrust as

$$p_{AE}(t) = \frac{\partial P_{AE}(t)}{\partial z} = \frac{\gamma z}{\tan\alpha}\frac{\sin(\alpha - \varphi_b)}{\cos(\delta + \varphi_b - \alpha)} + \frac{k_h \gamma z}{\tan\alpha}\frac{\cos(\alpha - \varphi_b)}{\cos(\delta + \varphi_b - \alpha)}\sin\left[\omega\left(t - \frac{z}{V_s}\right)\right] - \frac{k_v \gamma z}{\tan\alpha}\frac{\sin(\alpha - \varphi_b)}{\cos(\delta + \varphi_b - \alpha)}\sin\left[\omega\left(t - \frac{z}{V_p}\right)\right] \quad (40)$$

Design earth pressures determined by the Steedman-Zeng method or in general by Choudhury-Nimbalkar that account for backfill amplification should be considered for design of unusually displacement-sensitive walls such as tall retaining gravity walls.

Performance-Based Design

The observations after severe earthquakes have shown that retaining walls could fail during earthquakes by sliding away from the backfill or due to combined action of sliding and rocking displacements, while the post-event serviceability of such structures is also related to the wall displacements induced by the earthquake. Accordingly, any approaches that predict post-earthquake wall displacements should provide a more indication of retaining walls performances. Therefore, an alternative design approach, so-called performance-based design, could be used on the basis of permanent displacements for the wall when selecting an allowable displacement for design.

Performance-based design of retaining walls must account for the likely displacements the retaining wall may experience during an earthquake in addition to calculating the usual factors of safety against failure in bearing capacity, sliding, and overturning. There are several procedures available such as Richard and Elms (1979), Whitman and Liao (1985), and Wu and Prakash (2001) to estimate the permanent displacements of rigid walls.

In the Richards-Elms method, only the displacements of the sliding modes are taken into account. Considering the gravity rigid wall shown in Fig. 18, when the active backfill edge is subjected to ground acceleration toward the backfill, the resulting inertial forces will act away from the backfill. Therefore, in the limit state of sliding motion where the level of ground acceleration, so-called yield acceleration, is large enough to cause the wall to slide on its base, the horizontal and vertical equilibrium equations are

$$T = F_h + (P_{AE})_h$$

$$N = W + (P_{AE})_v \quad (41)$$

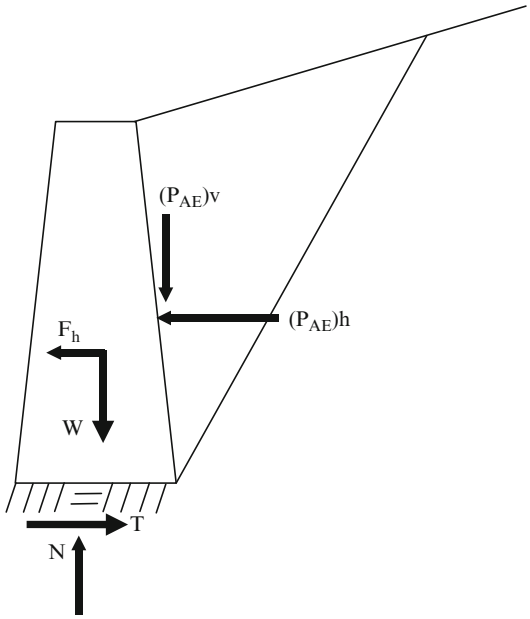

Analysis and Design Issues of Geotechnical Systems: Rigid Walls, Fig. 18 Gravity retaining wall considered in Richard-Elms method

Substituting $T = N \tan\varphi_b, F_h = a_y W/g, (P_{AE})_h = P_{AE}\cos(\delta+\beta)$, and $(P_{AE})_v = P_{AE}\sin(\delta+\beta)$, the yield acceleration can be computed by

$$a_y = \left[\tan\varphi_b - \frac{P_{AE}\cos(\delta+\beta) - P_{AE}\sin(\delta+\beta)}{W}\right] g \tag{42}$$

In calculating $P_{AE,}$ since the M-O method requires that a_y be known, the solution of the above equation must be obtained iteratively. In the Richard-Elms, based on the sliding block analysis, the permanent block displacement is determined as

$$\delta = 0.087\frac{V_{max}^2}{\alpha_{max}}\left(\frac{a_y}{a_{max}}\right)^{-4} \tag{43}$$

where V_{max} is the peak ground velocity and $a_{max} = k_h g$ is the horizontal peak ground acceleration.

A realistic model for estimating the dynamic displacement must account for the combined action of possible displacement modes including sliding and rocking vibrations and considering (1) soil stiffness in sliding and rocking, (2) geometrical and material damping in sliding and rocking, and (3) nonlinear coupling effects for stiffness and damping. Wu and Prakash (2001) proposed a model for simulating the response of rigid retaining walls subjected to seismic loading. This model (Fig. 19) consisted of a rigid wall resting on the foundation soil and subjected to a horizontal ground motion and analyzed the problem as a case of combined sliding and rocking vibrations including the effect of various important parameters such as soil stiffness in sliding, soil stiffness in rocking, geometrical damping in sliding, geometrical damping in rocking, material damping in sliding, and material damping in rocking.

An important step in the performance design procedure is the selection of the permissible displacement. There are some guidelines given available based on experience or judgment (Huang 2005). Eurocode (1994) gives the permissible horizontal displacement equal to 300 amax (mm) where amax is the maximum horizontal design acceleration, while AASHTO (2006) suggests this parameter to be limited to 250 amax (mm). Wu and Prakash (1996) proposed that the permissible horizontal displacement should be 2 % of the height of the retaining wall, H, while the failure horizontal displacement is equal to 0.1H. According to the Japanese Railway Technical Research Institute (JRTRI 1999), permissible differential settlement = 0.1–0.2 m (damage needing minor retrofit measures).

Severe differential settlement = >0.2 m (damage needing long-term retrofit measures).

It may be noted that Eurocode 8 (1994) and Wu and Prakash (1996) recommend using specified horizontal displacements of the retaining wall for evaluating its seismic performance, while JRTRI suggests the use of vertical differential settlement as the performance criterion which seems reasonable for traffic accessibility and retrofit purposes after the earthquake.

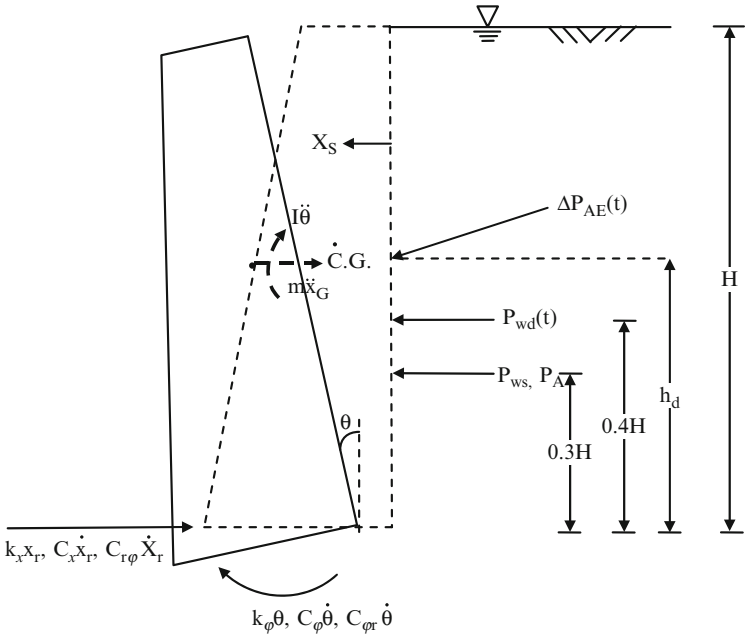

Analysis and Design Issues of Geotechnical Systems: Rigid Walls, Fig. 19 Free body diagram of forced vibration of a gravity retaining wall retaining saturated backfill soil

Any procedure in the performance-based design of retaining walls should follow these steps:

- Assume a permissible displacement, δ_{perl}
- Determine the yield acceleration that corresponds the permissible displacement as

$$a_y = \left(0.087 \frac{V_{max}^2 \alpha^3_{max}}{\delta_{per}}\right)^{1/4} \tag{44}$$

- Having the yield acceleration determined in the previous step, calculate P_{AE} using the M-O method.
- Calculate the wall weight required to limit the wall displacement to the permissible displacement taken in the first step as

$$W = \left[\frac{P_{AE} \cos(\delta + \beta) - P_{AE} \sin(\delta + \beta) \tan \varphi_b}{\tan \varphi_b - a_y/g}\right] \tag{45}$$

A factor of safety 1.2–1.5 should be applied to the weight of the wall to take into account the probability of exceedance in permissible displacements of the wall, the importance of the wall, the effects of failure, and the cost of repair.

Cross-References

- Bridge Foundations
- Seismic Analysis of Masonry Buildings: Numerical Modeling
- Seismic Design of Earth-Retaining Structures

References

AASHTO (2006) Recommended LRFD guidelines for the seismic design of highway bridges. American Association of State Highway and Transportation Officials (AASHTO), National Cooperative Highway Research Program (NCHRP), Transportation Research Board

ASCE 4–98 (2000) Seismic analysis of safety related nuclear structures and commentary. American Society of Civil Engineers

CHBDC (1998) Canadian highway bridge design code. Canadian Standards Association, Rexdale, Ontario

Choudhury D, Nimbalkar SS (2006) Pseudo-dynamic approach of seismic active earth pressure behind retaining wall. J Geotechnic Geol Eng 24:1103–1113

Choudhury D, Singh S (2006) New approach for estimation of static and seismic active earth pressure. Geotech Geol Eng 24(1):117–127

Choukeir M, Juran I, Hanna S (1997) Seismic design of reinforced-earth and soil-nailed structures. Ground Improv 1:223–238

Chwang AT (1978) Hydrodynamic pressures on sloping dams during earthquakes. Part 2. Exact theory. J Fluid Mech 87:343–348

Dakoulas P, Gazetas G (2008) Insight into seismic earth and water pressures against caisson quay walls. Geophys J Roy Astron Soc 58(2):95–111

EAK (2002) Empfehlungen des Arbeitsasschusses Kustenschutzwerke. Die Kuste, H. 65

EAU (1996) Recommendations of the committee for waterfront structures, harbours, and waterways, 7th edn. Ernst & Sohn, Berlin

Ebeling RM, Morrison EE, Whitman RV, Liam Finn WD (1992) A manual for seismic design of waterfront retaining structures. US Army Corps of Engineers, Technical report ITL-92-11

EN 1997 (2002) Eurocode 7 geotechnical design – Part 1: General rules. CEN European committee for standardization, Bruxelles

EUROCODE 8 (EUROPEAN PRE-STANDARD) (1994) Design provisions for earthquake resistance of structures-Part 5: Foundations, retaining structures and geotechnical aspects. The Commission of the European Communities

FEMA 369 (2000) The 2000 NEHRP recommended provisions for new buildings and other structures. Part 2: Commentary. Federal Emergency Management Agency

FHWA (1997) Geotechnical engineering ciruclar #3. Design guidance: geotechnical earthquake engineering for highways, design principles. FHWA-SA-97-076, Federal Highway Administration, vol I, U.S. Department of Transportation

Ghosh P (2008) Seismic active earth pressure behind a non-vertical retaining wall using pseudo-dynamic analysis. Can Geotech J 45(1):117–123

Horvath JS (2005) Integral-abutment bridges: geotechnical problems and solutions using geosynthetics and ground improvement. In: Proceeding IAJB 2005: the 2005 FHWA conference on integral abutment and jointless bridges, Baltimore, pp 281–291

Huang C (2005) Seismic displacement of soil retaining walls situated on slope. J Geotech Geoenviron Eng 131(9):1108–1117

International Code Council (2006) IBC (International Building Code). International Code Council, Country Club Hills, 664 pp

Japan Railway Technical Research Institute (JRTRI) (1999) Design guidelines for railway structures-aseismic design. Maruzen Co. Ltd

Kramer S (1996) Geotechnical earthquake engineering. Prentice-Hall, Upper Saddle River

Matsuo H, Ohara S (1965) Dynamic pore water pressure acting on quay walls during earthquakes. In: Proceedings of the third world conference on earthquake engineering, New Zealand, vol 1, pp 130–140

Matsuzawa H, Ishibashi I, Kawamura M (1985) Dynamic soil and water pressures of submerged soils. J Geotech Eng ASCE 111(10):1161–1176

Mononobe N, Matsuo H (1929) On the determination of earth pressures during earthquakes. In: Proceedings of world engineering congress

Mylonakis G, Kloukinas P, Papantonopoulos C (2007) An alternative to the Mononobe-Okabe equations for seismic earth pressures. Soil Dyn Earthq Eng 27:957–969

Okabe S (1926) General theory of earth pressure. Journal Japan Society of Civil Engineering, 12(1)

PIANC (2001) Seismic design guidelines for port structures. A. A. Balkema, Tokyo (International Navigation Institute)

Richard R, Elms DG (1979) Seismic behavior of gravity retaining walls. J Geotech Eng, ASCE 105:449–464

Richards R, Huang C, Fishman KL (1999) Seismic earth pressure on retaining structures. J Geotech Geoenviron Eng, ASCE 125(9):771–778

Seed HB, Whitman RV (1970) Design of earth retaining structures for dynamic loads. In Proceedings, ASCE Specialty Conference on Lateral Stresses in the Ground and Design of Earth Retaining Structures, pp 103–147

Steedman RS, Zeng X (1990) The influence of phase on the calculation of pseudo-static earth pressure on a retaining wall. Geotechnique 40:103–112

Tomlinson MJ (1995) Foundation design and construction. Wiley, New York

Veletsos AS, Younan AH (1994) Dynamic soil pressures on rigid retaining walls. Earthq Eng Struct Dyn 23:275–301

Werner PW, Sundquist KJ (1943) On hydrodynamic earthquake effects. Trans Am Geophys Union 30(5):636–657

Westergaard H (1931) Water pressure on dams during earthquakes. In: Transportations of ASCE, Paper no. 1835, pp 418–433

Whitman RV (1990) Seismic design and behavior of gravity retaining walls. In: Proceedings conference on design and performance of earth retaining structures, ASCE geotechnical special publication, vol 25. pp 817–842

Whitman RV, Liao S (1985) Seismic design of retaining walls, paper GL-85-1, U.S. Army engineer waterways experiment station, Vicksburg

Wood J (1973) Earthquake-induced soil pressures on structures. Report EERL 73–05, California Institute of Technology, Pasadena

Wu Y, Prakash S (1996) On Seismic Displacement of Rigid retaining Walls. In: Prakash S (ed) ASCE Geotechnical special publication: Analysis and Design of Retaining Structures Against Earthquakes, SP editor, pp 21–37

Wu Y, Prakash S (2001) Seismic displacements of rigid retaining walls. In: State-of-the-art paper number 705, proceedings fourth international conference on recent advances in geotechnical earthquake engineering and soil dynamics, San Diego

Zangar CN (1953) Hydrodynamic pressures on dams due to horizontal earthquakes. Proc Soc Exp Stress Anal 10:93–102

Analytic Fragility and Limit States [P(EDP|IM)]: Nonlinear Dynamic Procedures

Dimitrios Vamvatsikos
School of Civil Engineering, National Technical University of Athens (N.T.U.A.), Athens, Greece

Introduction

The determination of structural response given the seismic loading is of paramount importance in earthquake engineering. Due to the random nature of earthquakes, it is widely accepted that this is best done in probabilistic rather than deterministic terms. Thus, modern frameworks for performance-based earthquake engineering are based on the evaluation of the distribution of structural response, characterized by one or more engineering demand parameters (EDPs, e.g., peak interstory drift ratio or peak floor acceleration), given the level of a (typically scalar) intensity measure (IM, e.g., peak ground acceleration or first-mode spectral acceleration), used to characterize the earthquake loading (Cornell and Krawinkler 2000). This distribution is symbolized by the corresponding probability distribution function (PDF) of EDP given the IM: P(EDP|IM).

Such results are often employed in tandem with one or more distinct limit or damage states that characterize the performance (or state) of the structure, such as immediate occupancy, life safety, or near collapse. Then, the results of structural analysis can be distilled into the so-called building-level fragility functions associated with the violation of each limit state. Formally, a (building-level) fragility function is the cumulative distribution function of the seismic intensity, in terms of the IM, needed to violate the limit state. A limit state is usually tied to specific threshold capacity (EDP_c) values of one or more EDPs that can be either deterministic (i.e., assumed to be perfectly known) or probabilistic, the latter obviously being the more realistic option. When such values are exceeded, the limit state is deemed to have been violated. In the case where a limit state is defined via a *single* EDP, e.g., exceedance of 3 % peak interstory drift to define life safety (or worse), the fragility function is essentially the same as the probability function of the seismic demand EDP exceeding the capacity EDP_c given the IM, symbolized as P(EDPc < EDP|IM).

Fragility can be determined in a variety of ways, using, for example, empirical data from post-earthquake surveys or even expert opinion. For the vast majority of cases, though, computer-intensive analytical options are the most suitable choice. In this direction, recent advances in computer technology have allowed the consideration of nonlinear dynamic analysis as a realistic option. In the following, a number of approaches will be discussed on how to assess the distribution of EDP given IM and determine fragility functions using nonlinear dynamic analysis.

Intensity Measure and Ground Motions

The importance of selecting an efficient and sufficient IM (Luco and Cornell 2007) cannot be understated. An efficient IM will generally be well correlated with the EDPs of choice, thus showing low dispersion of demand given the IM, and subsequently allow the determination of EDP demand or IM capacity statistics using a relatively low number of ground motion records. Sufficiency is defined as the independence of the distribution of EDP given the IM from any other seismological parameters that may characterize the ground motion, e.g., duration, magnitude, spectral shape, or the presence of a pulse indicative of near-source forward directivity. A sufficient IM essentially captures all seismological information needed to determine the effect of a ground motion record on the structure being investigated (see also Jalayer et al. 2012). In other words, it frees the analyst from having to be careful regarding the selection (sampling) of ground motion records, as one only needs to match the required level of IM and no other seismological parameter.

A sufficient IM is essentially the premise of scaling, where the acceleration values of a ground motion time history are uniformly multiplied by a constant to reach the intensity needed. Still, it can be safely assumed that no IM for which a seismic hazard curve can be practically estimated (i.e., those for which ground motion prediction equations currently exist) will ever be 100 % sufficient for all sites and structures. Thus, excessive scaling may introduce biased estimates of response (Luco and Bazzurro 2007). Still, given the limitations of the catalogue of recorded ground motion records, scaling is often the only method to be used to reach truly high IM values that can force a modern well-designed structure to experience global collapse.

A standard IM choice is the 5 % damped first-mode (pseudo) spectral acceleration $S_a(T_1)$ (Shome et al. 1998; Shome and Cornell 1999). This is generally adequate for first-mode-dominated structures that do not displace far into the nonlinear region, as is the case of most existing brittle or moderately ductile low-/mid-rise buildings. For structures where higher modes become important or modern buildings that exhibit significant ductility, improved IM alternatives should be sought. One particularly attractive option is using $S_{agm}(T_i)$ geometric mean of spectral acceleration values at several periods T_i (Cordova et al. 2000; Vamvatsikos and Cornell 2005; Bianchini et al. 2009) that can largely alleviate the effect of spectral shape, being able to capture both the period elongation characterizing ductile structures and the effect of higher modes. Another option that can offer similar, if not better, sufficiency is the compound IM proposed by Luco and Cornell (2007) based on the combination of inelastic spectral displacement at the first mode and the elastic spectral displacement at the second mode of the structure. Its only disadvantage is the need for using specialized ground motion prediction equations to run seismic hazard analysis, developed according to Tothong and Cornell (2006).

Whenever an IM is not sufficient enough to remove the influence of other seismological parameters, their distribution at each IM level should be properly accounted for by appropriately selecting ground motion records. Thus, for example, if spectral shape, duration, or any other feature that cannot be accounted for by the IM is deemed to be important, the ground motion records used at different intensities should be chosen to reflect the anticipated distribution of those features given the IM. A prime example of a selection method is the conditional spectrum (CS) by Lin et al. (2013a, b), whereby the distribution of spectral shape, characterized by the parameter epsilon (Baker and Cornell 2006), is taken into account. Furthermore, Bradley (2010) has proposed the generalized conditional intensity measure (GCIM) approach to also incorporate other significant characteristics such as the duration and number of significant cycles of the ground motion. For additional information, see also Iervolino and Cornell (2005) and the comprehensive review of record selection provided by Katsanos et al. (2010).

While undoubtedly useful, ground motion selection is not a panacea. It is a method that is site and structure dependent, thus heavily encumbering or even precluding its use whenever a building portfolio or an entire building class (e.g., mid-rise steel frames of the Western USA) is to be assessed to extract fragility or vulnerability functions. Additionally, the boundaries of the recorded ground motions' catalogue put a limit on what can be actually represented by natural records. Thus, it is often the case that a combination of selection and scaling needs to be employed. Alternatively, one could also employ the results of CS or GCIM methods to create artificial ground motions that display the required characteristics. Still, this is an option that is presently available only for highly proficient analysts, as appropriate algorithms have not appeared in the literature so far.

Alternatively, a good rule for a general use is to utilize strong records that when unscaled can still damage the investigated structure, together with a relatively sufficient IM to allow scaling within reason. For most existing low-/mid-rise structures having low-to-moderate ductility that are not subject to near-field motions, this generally means employing $S_a(T_1)$ together with records having naturally high $S_a(T_1)$ values.

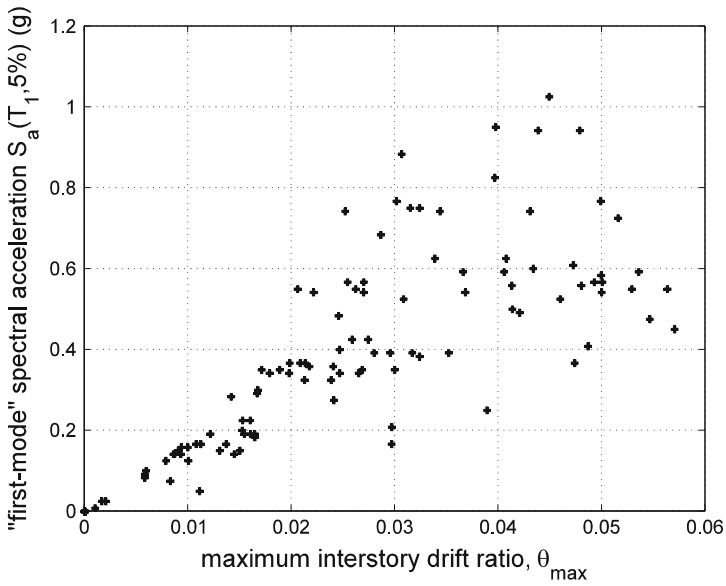

Analytic Fragility and Limit States [P(EDP|IM)]: Nonlinear Dynamic Procedures, Fig. 1 The resulting points of a cloud approach for a 9-story steel frame using $S_a(T_1)$ as the IM and the maximum over all stories peak interstory drift θ_{max} as the EDP

For modern ductile structures or non-ductile buildings that are not first-mode dominated (e.g., plan-asymmetric or tall structures) or whenever the site of interest is subject to near-field motions, a strong set of records together with an improved IM (see earlier discussion) should be preferred.

Analysis Strategies

Determination of fragility necessitates a wide-range assessment of structural response at multiple levels of intensity. There are several ways to organize the execution of nonlinear dynamic analyses, mainly differing in the manner of postprocessing and in how they can employ ground motion selection and scaling. The main candidates are three (Jalayer and Cornell 2009): cloud analysis, stripe analysis, and incremental dynamic analysis (IDA).

Of the three, cloud analysis is the least restrictive. Its name is derived from the characteristic cloud of results that appears in the IM versus EDP plane, where each point corresponds to one analysis (see Fig. 1). One can employ any combination of scaling and record set selection. At one end, one can employ only scaling, using a fixed record set that is scaled to several levels of intensity (typically by multiplying all natural accelerograms by the same scale factor). At the other end, scaling can be completely avoided (if possible, considering catalogue limitations) by using a separate set of natural records for each level of IM (within some tolerance of course). Extracting the P(EDP|IM) information can be done in several ways. One approach is to employ parametric regression, taking care to separately fit the non-collapsing IM-EDP points via a linear regression in logarithmic space. "Infinite EDP" points indicative of collapse should be accounted for using logistic regression (see Shome and Cornell 1999; Jalayer and Cornell 2009). Alternatively, a nonparametric approach can be used, employing, e.g., "running" 16/50/84 percentiles to estimate the median and dispersion of the EDP response at each level of the IM.

Stripe analysis is named after the characteristic stripes of points aligned in distinct rows at different IM levels (Fig. 2). Like cloud analysis, it may involve any number of sets of records, and it also needs to employ at least some scaling to make sure that all runs at a given IM level actually perfectly correspond to the IM level requested, without any tolerance. The importance of this detail is that the distribution of EDP given

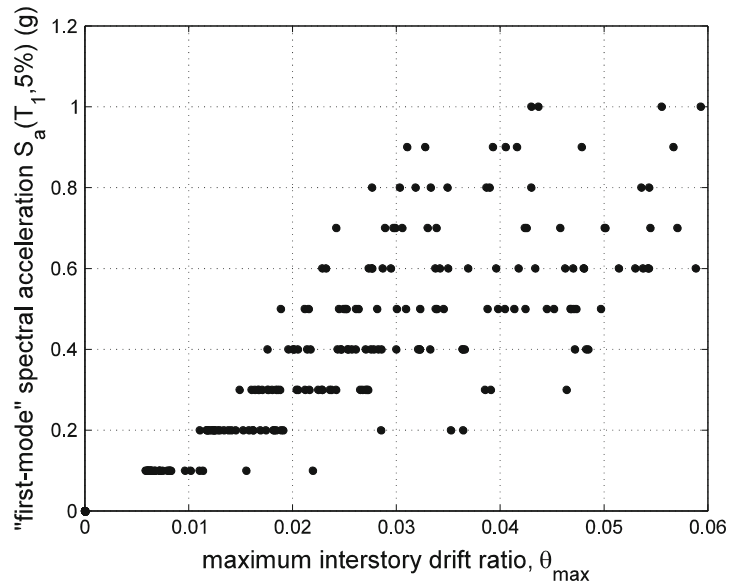

Analytic Fragility and Limit States [P(EDP|IM)]: Nonlinear Dynamic Procedures, Fig. 2 The resulting points of a stripe approach for a 9-story steel frame using $S_a(T_1)$ as the IM and the maximum over all stories peak interstory drift θ_{max} as the EDP

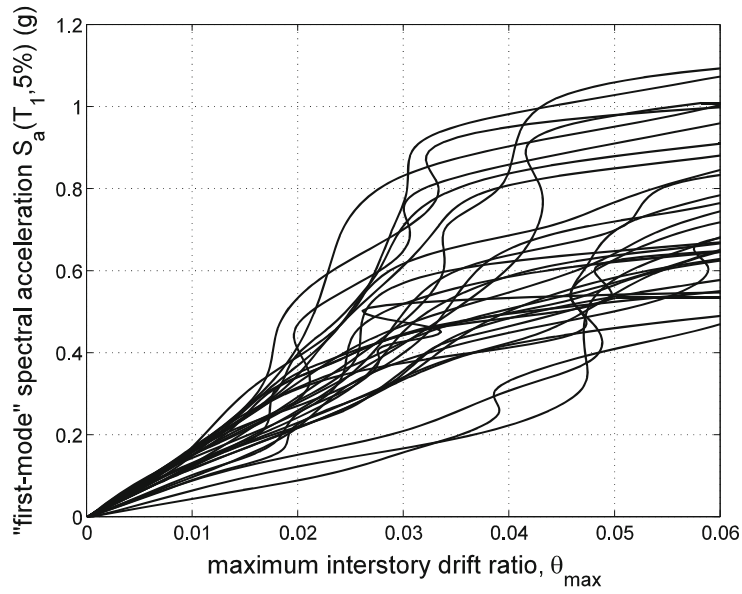

Analytic Fragility and Limit States [P(EDP|IM)]: Nonlinear Dynamic Procedures, Fig. 3 The resulting IDA curves for a 9-story steel frame using $S_a(T_1)$ as the IM and the maximum over all stories peak interstory drift θ_{max} as the EDP

IM is directly represented at each IM level by the empirical distribution of the EDP results extracted from the pertinent analyses. In other words, any statistical quantity of EDP given the IM (mean, 16/50/84 percentile, standard deviation, etc.) can be estimated directly from the corresponding EDP values without any need for parametric or nonparametric regression, thus considerably simplifying postprocessing.

Incremental dynamic analysis (IDA) is based on scaling and scaling only (Vamvatsikos and Cornell 2002). Its focus is on individual records, each of which is scaled to several levels of intensity, typically until collapse is reached. Although closely related to stripe analysis, its main advantage is that the IM levels of the different records do not need to match. Instead, a fixed number of nonlinear dynamic analyses can be utilized for

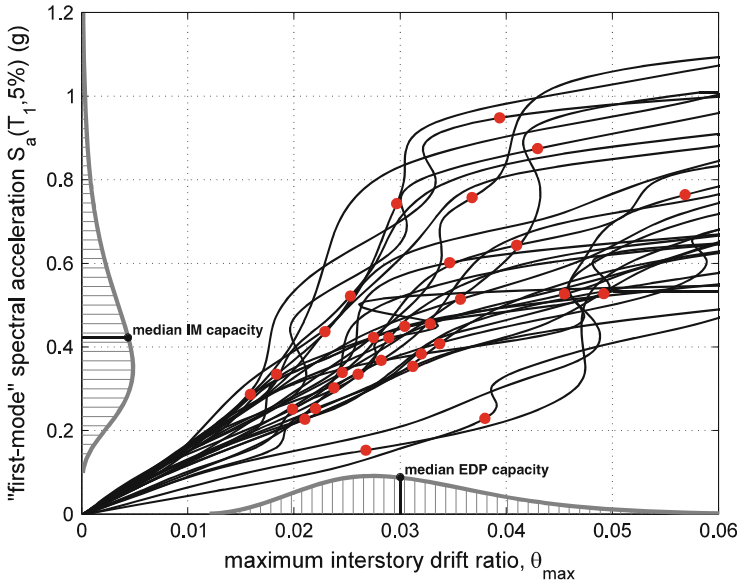

Analytic Fragility and Limit States [P(EDP|IM)]: Nonlinear Dynamic Procedures,
Fig. 4 Thirty IDA curves, thirty limit-state capacity points, and the corresponding EDP_c, IM_c PDFs for a 9-story steel frame (From Vamvatsikos 2013)

each record to achieve an accurate yet economical representation of response from elasticity to global dynamic instability. Then, interpolation of the results pertaining to each record is employed to generate continuous IDA curves (Fig. 3), as well as stripes, and subsequently derive the needed EDP|IM statistics (Vamvatsikos and Cornell 2004).

In practice, any of the above approaches can be used to derive equivalent results. The distinction may become important only in the sense of scaling versus selecting ground motion records that puts IDA at a potential disadvantage: It has to use the same set of ground motions for all intensity levels, needing a sufficient IM to provide unbiased results. On the other hand, the representation of the EDP|IM statistics via continuous IDA curves offers a powerful visual tool for understanding structural performance that can often tip the scales in its favor. In the end, the choice lies with the analyst and his/her understanding of the problem at hand.

As a final remark, it is important to remember that the aforementioned methods can only take into account the record-to-record variability. If other sources of uncertainty need to be incorporated, for example, model parameter variability, then more refined (and complex) approaches should be adopted instead (Liel et al. 2009; Dolsek 2009; Vamvatsikos and Fragiadakis 2010; Jalayer et al. 2011).

Determination of Fragility

A building-level fragility function is defined as a probability-valued function of the IM that represents the probability of violating a limit state given the IM level. Formally, it may be represented as $P(C < D|IM)$, i.e., as the probability of the seismic demand D exceeding the seismic capacity C given the IM. Two alternative yet equivalent formats exist to define the C and D terms, namely, the IM basis and the EDP basis. When a single EDP is used to define the limit state, this dichotomy is best understood by visualizing the first exceedance of the limit state as a single point on each IDA curve, having unique IM and EDP coordinates (Fig. 4).

If we choose to characterize demand and capacity by their IM counterparts, then $P(C < D|IM)$ simply becomes the cumulative distribution function (CDF) of the IM-valued capacity, IM_c. Simply plotting the empirical CDF of the IM_c values, as, for example, in Fig. 5, provides us with a ready estimate of the fragility function. By estimating the appropriate statistics (median, IM_{c50}, and standard deviation of the log

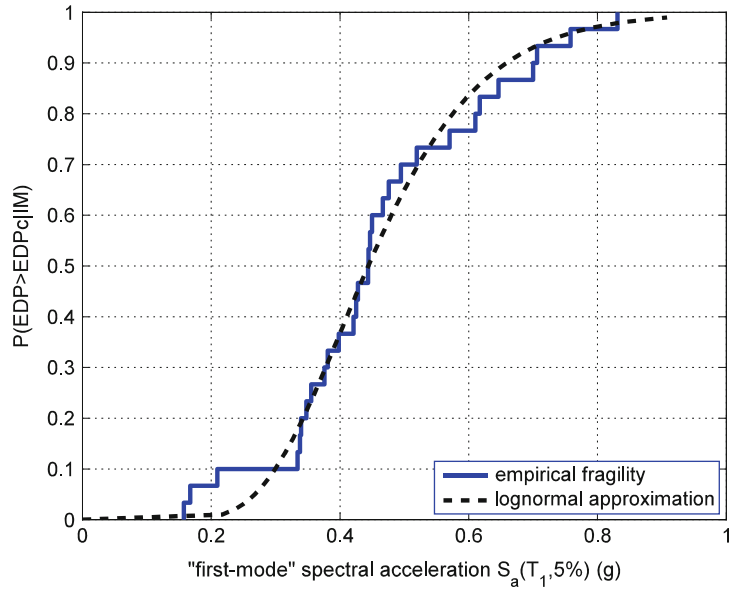

Analytic Fragility and Limit States [P(EDP|IM)]: Nonlinear Dynamic Procedures, Fig. 5 The empirical fragility function for exceeding a (deterministic) peak interstory drift of 3 % for the 9-story steel frame versus its lognormal approximation

values, β_{IMc}), one may also represent the results via an analytic lognormal approximation, as shown in Fig. 5, and formally represented by the following expression:

$$P(EDP_c < EDP|IM) = \Phi\left(\frac{\ln IM - \ln IM_{c50}}{\beta_{IMc}}\right). \quad (1)$$

If instead D and C are represented in EDP terms, then they are both potentially random quantities and integration is needed:

$$P(EDP_c < EDP|IM) = \int_0^{+\infty} P(EDP_c < EDP)\, P(EDP|IM)\ dIM. \quad (2)$$

The first term of the integrant is essentially the complementary cumulative distribution function (CCDF) of EDP_c, and the second is the probability distribution function (PDF) of EDP given the IM. Despite the apparent complexity of this approach, it is often the preferred method for estimating fragility (although not necessarily for representing it). This is best understood by considering the simpler case where the EDP capacity is deterministic, i.e., we presume to perfectly know the value of EDP that causes violation of the limit state. Then, the capacity points of Fig. 4 align themselves into a single vertical line that intersects all IDA curves at the limiting (single) EDP_c value, meaning that all the dispersion in the fragility function (or the IM_c values, equivalently) originates from the records themselves. Inversely, if one wants to introduce the (typically considerable) uncertainty in EDP_c, he/she had best go through the EDP route; otherwise, it is not possible to obtain the inflated β_{IMc} dispersion of Eq. 1. Regardless of the route taken, though, the end result can always be represented in terms of the lognormal function parameters IM_{c50} and β_{IMc} of Eq. 1.

Summary

A key ingredient of modern frameworks for performance-based earthquake engineering is the assessment of the distribution of structural demand given the seismic intensity. Expressed as the probability of exceeding specific levels of the structural response indicative of defined limit states, this is also known as fragility. Recent advances in computer technology have allowed

the use of resource-intensive nonlinear dynamic analysis as the tool of choice for analytically estimating such fragility functions. For practically implementing such an assessment, several strategies exist on how to select and/or modify ground motion records and apply them to a structural model at several levels of intensity. Clouds, stripes, and incremental dynamic analysis curves, each characterized by the appearance of the corresponding results in the response versus intensity space, are among the most prominent techniques. Despite their superficial differences, they may all achieve the same fidelity in their results, practically differing only in the ease of postprocessing and interpretation. In all cases, parameterization by the (typically scalar) intensity measure means that considerable attention should be paid to its selection, as well as the selection of the ground motions, to ensure the unbiasedness of the estimates.

Cross-References

- ▶ Analytic Fragility and Limit States [P(EDP|IM)]: Nonlinear Static Procedures
- ▶ Assessment of Existing Structures Using Response History Analysis
- ▶ Incremental Dynamic Analysis
- ▶ Nonlinear Dynamic Seismic Analysis
- ▶ Seismic Collapse Assessment
- ▶ Seismic Fragility Analysis
- ▶ Seismic Loss Assessment
- ▶ Time History Seismic Analysis

References

Baker JW, Cornell CA (2006) Spectral shape, epsilon and record selection. Earthq Eng Struct Dyn 35(9):1077–1095

Bianchini M, Diotallevi PP, Baker JW (2009) Predictions of inelastic structural response using an average of spectral accelerations. In: Proceedings of the 10th international conference on structural safety & reliability (ICOSSAR), Osaka

Bradley BA (2010) A generalized conditional intensity measure approach and holistic ground motion selection. Earthq Eng Struct Dyn 39(12):1321–1342

Cordova PP, Deierlein GG, Mehanny SS, Cornell CA (2000) Development of a two-parameter seismic intensity measure and probabilistic assessment procedure. Proceedings of the 2nd US-Japan Workshop on Performance-based Earthquake Engineering Methodology for RC Building Structures, Sapporo, Hokkaido

Cornell CA, Krawinkler H (2000) Progress and challenges in seismic performance assessment. PEER Center News, http://peer.berkeley.edu/news/2000spring/index.html. Accessed May 2014

Dolsek M (2009) Incremental dynamic analysis with consideration of modelling uncertainties. Earthq Eng Struct Dyn 38(6):805–825

Iervolino I, Cornell CA (2005) Record selection for non-linear seismic analysis of structures. Earthq Spectra 21(3):685–713

Jalayer F, Cornell CA (2009) Alternative non-linear demand estimation methods for probability-based seismic assessments. Earthq Eng Struct Dyn 38:951–972

Jalayer F, Elefante L, Iervolino I, Manfredi G (2011) Knowledge-based performance assessment of existing RC buildings. J Earthq Eng 15(3):362–389

Jalayer F, Beck JL, Zareian F (2012) Analyzing the sufficiency of alternative scalar and vector intensity measures of ground shaking based on information theory. J Eng Mech ASCE 138(3):307–316

Katsanos EI, Sextos AG, Manolis GD (2010) Selection of earthquake ground motion records: a state-of-the-art review from a structural engineering perspective. Soil Dyn Earthq Eng 30:157–169

Liel AB, Haselton CB, Deierlein GG, Baker JW (2009) Incorporating modeling uncertainties in the assessment of seismic collapse risk of buildings. Struct Saf 31(2):197–211

Lin T, Haselton CB, Baker JW (2013a) Conditional-spectrum-based ground motion selection. Part I: Hazard consistency for risk-based assessments. Earthq Eng Struct Dyn 42(12):1847–1865

Lin T, Haselton CB, Baker JW (2013b) Conditional-spectrum-based ground motion selection. Part II: Intensity-based assessments and evaluation of alternative target spectra. Earthq Eng Struct Dyn 42(12):1867–1884

Luco N, Bazzurro P (2007) Does amplitude scaling of ground motion records result in biased nonlinear structural drift responses? Earthq Eng Struct Dyn 36:1813–1835

Luco N, Cornell CA (2007) Structure-specific scalar intensity measures for near-source and ordinary earthquake ground motions. Earthq Spectra 23(2):357–392

Shome N, Cornell CA (1999) Probabilistic seismic demand analysis of nonlinear structures. RMS program, report no. RMS35, PhD thesis, Stanford University, CA

Shome N, Cornell CA, Bazzurro P, Carballo JE (1998) Earthquakes, records and nonlinear responses. Earthq Spectra 14(3):469–500

Tothong P, Cornell CA (2006) An empirical ground-motion attenuation relation for inelastic spectral displacement. Bull Seismol Soc Am 96(6):2146–2164

Vamvatsikos D (2013) Derivation of new SAC/FEMA performance evaluation solutions with second-order hazard approximation. Earthq Eng Struct Dyn 42:1171–1188
Vamvatsikos D, Cornell CA (2002) Incremental dynamic analysis. Earthq Eng Struct Dyn 31(3):491–514
Vamvatsikos D, Cornell CA (2004) Applied incremental dynamic analysis. Earthq Spectra 20(2):523–553
Vamvatsikos D, Cornell CA (2005) Developing efficient scalar and vector intensity measures for IDA capacity estimation by incorporating elastic spectral shape information. Earthquake Engineering and Structural Dynamics 34(13):1573–1600
Vamvatsikos D, Fragiadakis M (2010) Incremental dynamic analysis for estimating seismic performance sensitivity and uncertainty. Earthq Eng Struct Dyn 39(2):141–163

Analytic Fragility and Limit States [P(EDP|IM)]: Nonlinear Static Procedures

Matjaž Dolšek
Faculty of Civil and Geodetic Engineering, University of Ljubljana, Ljubljana, Slovenia

Synonyms

Fragility analysis; Fragility curve; Limit state; Nonlinear static procedure; Pushover analysis; SDOF model; Seismic demand; Target displacement; Uncertainty

Introduction

Nonlinear static (pushover-based) procedures were initially developed for the seismic performance assessment of structures (e.g., Saiidi and Sozen 1981; Fajfar and Fischinger 1988; Paret et al. 1996; Chopra and Goel 2002) and later on used also for the fragility analysis (e.g., Fragiadakis and Vamvatsikos 2010; Barbato et al. 2010; Dolšek 2012; Jalayer et al. 2011; Rota et al. 2014; Kosič et al. 2014). For example, Jalayer et. al (2011) proposed the use of Bayesian method for calculating fragility curve of the reinforced concrete frame. Rota et al. (2014) adopted logic tree approach for evaluating the effects of modelling uncertainties on the fragility curves of masonry buildings. Alternatively, the impact of the modelling uncertainties on the fragility curve can be simulated by utilizing the so-called probabilistic SDOF model (Kosič et al. 2014). The advantage of pushover analyses in comparison with nonlinear response history analysis lies in the former's simplicity, since the results of pushover analysis are very intuitive. This makes pushover-based methods attractive for practical applications. On the other hand, they are based on several assumptions. Thus, the analyst should have good background knowledge in order to be able to adequately interpret results obtained by using pushover-based methods. However, many studies have shown that, in the case of simple bridges and buildings up to around eight stories high, the mean/median response can be sufficiently accurately predicted by means of conventional pushover analysis. In the case of more complicated structures, the analyst should think about taking into account, at least approximately, torsional effects and the so-called higher mode effects (e.g., Reyes and Chopra 2011; Kreslin and Fajfar 2012). Reyes and Chopra (2011) and Kreslin and Fajfar (2012) used linear elastic analysis in estimating higher mode contributions seismic demands. If the target displacement is obtained by nonlinear response history analysis utilizing the single-degree-of-freedom (SDOF) model, then it is possible to consider the different system failure modes obtained from the pushover analyses (Brozovič and Dolšek 2014). In this case, the failure-based SDOF models are used in addition to the modal-based SDOF model associated with the first model.

It should be noted that the main objective of this entry is to introduce the use of conventional pushover-based method for fragility analysis, taking into account the randomness of ground motion and the epistemic (modeling) uncertainty. Thus, not all issues associated with pushover-based methods are precisely addressed.

The entry has been organized into three subentries. The theoretical background for the prediction of the parameters of SDOF models is first described. This subentry is subdivided into two

parts. The transformation of the equations of motion to a conventional equation of motion of a SDOF model is presented in the first part, while in the second part, the procedure to determine the parameters of the SDOF model using pushover analysis is described. The first subentry provides an insight into the SDOF model, which represents a key link between the pushover analysis and seismic demand. Quite precise instructions are given on how to determine a SDOF model which can be used to assess the seismic demand by nonlinear dynamic analysis. The first subentry is followed by an overview of the different types of pushover analysis and the limit states. Some variants of pushover analyses are only mentioned, since it is not the aim of this entry to provide an insight into different types of pushover analysis. In the final subentry, pushover-based fragility analysis is explained with emphasis on the step-by-step procedure, which is also demonstrated by means of an example of fragility analysis for a four-story reinforced concrete frame building. The EDP-based and IM-based formulations of the fragility function are introduced. This is followed by explaining three procedures for the estimation of the fragility parameters using pushover-based methods. Finally, the most comprehensive procedure, which takes into account the ground-motion randomness and modeling uncertainty, is demonstrated by explaining each step of the pushover-based fragility analysis.

The Theoretical Background for Predicting Parameters of the SDOF Model

The main objective of this derivation is to introduce the theoretical background for the determination of the parameters of the SDOF model, which is one of the key components of the pushover-based methods. The advantage of the SDOF model is its simplicity. Thus, it can be used to determine the seismic demand based on nonlinear response history analyses. However, it is important to understand the theoretical limitations of such approach.

Transformation of Equations of Motion to a Conventional Equation of a Single-Degree-of-Freedom Model

The seismic response of structures can, in general, be described by the equation of motion

$$\mathbf{M}\ddot{\mathbf{U}} + \mathbf{C}\dot{\mathbf{U}} + \mathbf{K}\mathbf{U} = -\mathbf{M}\ddot{\mathbf{U}}_{\mathbf{g}} \tag{1}$$

where the first, second, and third parts of the equation on the left-hand side represent, respectively, the vectors of the inertial, damping, and resisting forces. The sum of these forces should be in equilibrium with external load, which, in the case of an earthquake, is expressed by the product of the mass matrix $\mathbf{M}$ and the vector of the ground acceleration $\ddot{\mathbf{U}}_{\mathbf{g}}$. Equation 1 is derived for the simulation of the seismic response of a structure relative to the ground. Thus, the displacements $\mathbf{U}$, velocities $\dot{\mathbf{U}}$, and accelerations $\ddot{\mathbf{U}}$ are vectors which are expressed relative to the ground. The kinematic quantities are, in general, simulated at all joints of the finite elements which form the structure. The matrix $\mathbf{C}$ is a damping matrix, which is often modeled in proportion to the mass matrix and/or the stiffness matrix $\mathbf{K}$. It should be noted that all kinematic quantities are functions of time. In the case of the nonlinear response of a structure, the stiffness matrix and, in some cases, also the damping matrix depend on the history of the structure's deformations.

In order to achieve brevity of the derivation, it is assumed that the building structure is symmetric in plan. The problem therefore simplifies to the planar case. It is further assumed that the seismic response of the building can be described just by the horizontal displacements at each story level. The external load of Eq. 1 simplifies as follows:

$$\mathbf{M}\ddot{\mathbf{U}} + \mathbf{C}\dot{\mathbf{U}} + \mathbf{K}\mathbf{U} = -\mathbf{M}\mathbf{1}\ddot{u}_g \tag{2}$$

where $\mathbf{1}$ is a vector with ones, and $\ddot{u}_g$ is the ground acceleration. It should be noted that the vector of the resisting forces,

$$\mathbf{F}=\mathbf{K}\mathbf{U} \tag{3}$$

which are function of time, can now be understood as the external, equivalent, static forces

which produce a vector $\mathbf{U}$ of displacements at any individual floor level, at any instant in time. Despite simplifications, Eq. 2 is a system of n-dependent nonhomogenous second-order differential equations with nonlinear coefficients, where n stands for the number of stories of the building structure. Several methods exist for the solution of this equation at any instant in time, but there are also several reasons to further simplification of the problem.

For example, all nonlinear structural models are just an approximation of the realistic seismic response of a structure. The majority of current structural models are capable of simulating several of the failure modes that can be observed in realistic structures. From this point of view, the question arises as to whether it is justified to treat the whole system as dynamic, if the model used to represent a building structure is already a proxy of reality. Furthermore, although the solution of the equation of motion will provide exact results from the theoretical point of view, the seismic loading is not known in advance. Thus, the selection of inappropriate ground motions could have a greater impact on the results than the selected method of analysis. Finally, solving system of equations of motion is extremely time demanding and, in the case of complex systems, also related to poor convergence of the numerical results obtained. These are just some reasons that it is often not practical to use response history analysis in order to simulate the seismic response of a structure. Therefore, Eq. 2 is often further simplified.

The solution of Eq. 2 would be significantly easier if the motion of the structure could be described with sufficient accuracy by reducing the number of differential equations to just one, e.g., in the case of building structures, by simulating just the top (roof) displacement. From the theoretical point of view, such a simplification can be achieved by assuming a displacement vector $\mathbf{U}$ in the following form:

$$\mathbf{U} = \boldsymbol{\Psi}\, u_t \tag{4}$$

where $\boldsymbol{\Psi}$ is a displacement vector that is independent of time and is normalized to a top displacement equal to 1, and u_t is the top displacement, which is a function of time. Based on such an assumption, it becomes clear that a multi-degree-of-freedom (MDOF) model of a structure can be transformed into a single-degree-of-freedom (SDOF) model. This is achieved by substituting all the kinematic quantities in the form of Eq. 4 and pre-multiplying Eq. 2 by the vector $\boldsymbol{\Psi}^T$:

$$\boldsymbol{\Psi}^T\mathbf{M}\boldsymbol{\Psi}\,\ddot{u}_t + \boldsymbol{\Psi}^T\mathbf{C}\boldsymbol{\Psi}\,\dot{u}_t + \boldsymbol{\Psi}^T\mathbf{K}\boldsymbol{\Psi}\,u_t = -\boldsymbol{\Psi}^T\mathbf{M}\,\mathbf{1}\,\ddot{u}_g \tag{5}$$

Equation 5 can be rearranged into the following form:

$$m_\psi\,\ddot{u}_t + c_\psi\,\dot{u}_t + k_\psi u_t = -m_*\,\ddot{u}_g \tag{6}$$

by realizing that the results of the multiplication of the matrices (Eq. 5) are scalars:

$$\begin{aligned} m_\psi &= \boldsymbol{\Psi}^T\mathbf{M}\boldsymbol{\Psi} \\ c_\psi &= \boldsymbol{\Psi}^T\mathbf{C}\boldsymbol{\Psi} \\ k_\psi &= \boldsymbol{\Psi}^T\mathbf{K}\boldsymbol{\Psi} \end{aligned} \tag{7}$$

$$m_* = \boldsymbol{\Psi}^T\mathbf{M}\,\mathbf{1} \tag{7a}$$

By introducing Eq. 6, it is clear that the system of n-dependent differential equation has been simplified to just one equation of motion, where the unknown quantities are the displacement, velocity, and acceleration at the top of the building. However, it still does not have the form of the conventional equation of motion, since $m_* \neq m_\psi$. In order to make Eq. 6 equivalent to the conventional equation of motion, a so-called transformation factor, which relates the top displacement of the structure to the displacement of the SDOF model, needs to be defined as follows:

$$\Gamma = \frac{m_*}{m_\psi} = \frac{\boldsymbol{\Psi}^T\mathbf{M}\,\mathbf{1}}{\boldsymbol{\Psi}^T\mathbf{M}\boldsymbol{\Psi}} \tag{8}$$

and the kinematic quantities of the SDOF model as

$$u_* = \frac{u_t}{\Gamma}, \quad \dot{u}_* = \frac{\dot{u}_t}{\Gamma}, \quad \ddot{u}_* = \frac{\ddot{u}_t}{\Gamma} \tag{9}$$

Equation 6 can now be transformed into the conventional equation of motion of the SDOF model by taking into account Eqs. 8 and 9:

$$m_* \ddot{u}_* + c_* \dot{u}_* + k_* u_* = -m_* \ddot{u}_g \tag{10}$$

where

$$c_* = \Gamma c_\psi \tag{11}$$

and

$$k_* = \Gamma k_\psi \tag{11a}$$

Determination of the Parameters of the SDOF Model Using Pushover Analysis

There are no exact instructions as to how to determine the parameters of the SDOF model since the mass m_*, the damping c_*, and the stiffness k_* all depend on the assumed displacement shape. In order to obtain a practical solution to Eq. 10, the analyst has to determine the force-displacement relationship of the SDOF model taking into account certain hysteretic rules, which are often assumed to be similar to those used for the structural components. However, the displacement of the SDOF model can be simply determined according to Eq. 9. Some further explanation is needed in order to be able to better understand the background for the determination of the forces of the SDOF model from the pushover curve. In general, the product of the stiffness k_* and u_* represents a force in the spring of the SDOF model:

$$F_* = k_* u_* \tag{12}$$

which should be expressed in a different form by taking into account Eqs. 11a and 9:

$$F_* = k_\psi u_t \tag{13}$$

Equation 13 can be further transformed by substituting k_ψ using Eq. 7 and with consideration of Eqs. 3 and 4:

$$F_* = \boldsymbol{\Psi}^T \mathbf{F} \tag{14}$$

It should be noted that the force-displacement relationship of the SDOF model is, in general, nonlinear due to the nonlinear response of the structure. Thus, there is no exact answer as to which is the most appropriate shape of the normalized displacement vector $\boldsymbol{\Psi}$ or which are the most appropriate lateral forces $\mathbf{F}$. If it is assumed that the structure oscillates just in one given mode shape, then $\boldsymbol{\Psi}=\boldsymbol{\Phi}$. If it is further assumed that the mode shape $\boldsymbol{\Phi}$ does not change significantly with increasing damage to the structure and that the damping does not affect the shape of the buildings' oscillation, then it can be shown, by analogy to the modal analysis, that the shape of the equivalent static forces which causes lateral displacements that are equivalent to the mode shape can be expressed as follows:

$$\mathbf{F} = \mathbf{M}\boldsymbol{\Phi} \tag{15}$$

Substituting Eq. 15 into Eq. 14 and realizing that in such a case $\boldsymbol{\Psi}=\boldsymbol{\Phi}$, it can be shown that

$$F_* = \boldsymbol{\Phi}^T \mathbf{M} \boldsymbol{\Phi} \tag{16}$$

Multiplying and dividing Eq. 16 by $m_* = \boldsymbol{\Psi}^T \mathbf{M}\,\mathbf{1}$ and taking into account Eq. 8 produces the following result:

$$F_* = \frac{\boldsymbol{\Phi}^T \mathbf{M} \mathbf{1}}{\Gamma} \tag{17}$$

Eq. 18 can be further simplified by realizing that $\mathbf{F}^T = \boldsymbol{\Phi}^T \mathbf{M}$:

$$F_* = \frac{\mathbf{F}^T \mathbf{1}}{\Gamma} = \frac{F_b}{\Gamma} \tag{18}$$

where F_b is the so-called base shear, i.e., the sum of the lateral forces $\mathbf{F}$. The force-displacement relationship of the SDOF model is thus obtained simply by dividing the quantities at the structural level by the so-called transformation factor. However, it should be emphasized that Eq. 18 may not be sufficiently accurate in the case when the pushover curve is based on a higher mode shape. Equation 9 can be used, together with Eqs. 14 or 18, to determine the

force-displacement $F_* - u_*$ relationship of the SDOF on the basis of the pushover curve.

It is often useful to know the period of the SDOF model, which can be obtained by analyzing Eq. 10. It is well known that the radial frequency of an oscillating body is

$$\omega_* = \sqrt{\frac{k_*}{m_*}} = \frac{2\pi}{T_*} \tag{19}$$

whence it follows that

$$T_* = 2\pi\sqrt{\frac{m_*}{k_*}} \tag{20}$$

The stiffness of the SDOF model can be expressed by means of Eq. 12. The period of the SDOF model thus equals

$$T_* = 2\pi\sqrt{\frac{m_* u_*}{F_*}} \tag{21}$$

In order to solve Eq. 10, it is necessary to define the damping model c_*. The so-called Rayleigh damping model is often assumed at the level of the structure. In this case, the damping matrix is expressed as a linear combination of the mass and stiffness matrices:

$$\mathbf{C} = \alpha\mathbf{M} + \beta\mathbf{K} \tag{22}$$

where α and β are constant values. The question arises as to how to relate the damping model at the structural level to the damping model for the SDOF model. Starting from Eq. 11 and taking into account Eq. 7 for c_ψ as well as Eq. 22, it can be shown that

$$\begin{aligned} c_* = \Gamma c_\psi = \Gamma \boldsymbol{\Psi}^T \mathbf{C} \boldsymbol{\Psi} = \Gamma \boldsymbol{\Psi}^T (\alpha\mathbf{M} + \beta\mathbf{K})\boldsymbol{\Psi} = \\ = \Gamma \left(\alpha \boldsymbol{\Psi}^T \mathbf{M} \boldsymbol{\Psi} + \beta \boldsymbol{\Psi}^T \mathbf{K} \boldsymbol{\Psi}\right) = \\ = \alpha\Gamma m_\psi + \beta\Gamma k_\psi \end{aligned} \tag{23}$$

Substituting Eqs. 8 and 11 into Eq. 23, the following equation is obtained:

$$c_* = \alpha m_* + \beta k_* \tag{24}$$

whence it can be shown that the same damping constants α and β of the SDOF model are equal to that assumed for the response history analysis of the entire structure. The damping constants α and β, or only one of these constants, if damping is proportional to the mass or stiffness matrix only, are often determined by assuming a certain ratio of critical damping. Describing the relationship between the damping constants and the ratio of critical damping is, however, outside the scope of this derivation.

Equation 10 can be solved by numerical integration which is implemented in conventional software for response history analysis. However, the solution depends, in general, on the ground motion and assumptions adopted for the determination of the parameters of the SDOF model, i.e., the mass m_*, the damping model, the force-displacement relationship $F_* - u_*$, and the hysteretic rules.

In the simplest and the most commonly used approach, the parameters of the SDOF model are determined by performing pushover analysis taking into account invariant distribution of the lateral forces. In this case, the procedure for the determination of the parameters of the SDOF model can be decomposed into the following steps:

1. Define the distribution of the lateral forces **F** for the pushover analysis.
2. Perform the pushover analysis. This results in the relationship between the force vector **F** and the displacement vector **D** from elastic range to the collapse of the structure. The corresponding base shear F_b and the top displacement u_t form the so-called pushover curve.
3. Assume the shape of the normalized displacement vector $\boldsymbol{\Psi}$.
4. Idealize the pushover curve $F_b - u_t$ using a bilinear or multi-linear shape or the shape of any other curve which can be used to simulate the $F_* - u_*$ force-displacement relationship of the SDOF model.
5. Compute the $F_* - u_*$ force-displacement relationship of the SDOF model. The force F_* at the characteristic points of the idealized

pushover curve can be obtained, in the case of the SDOF model, according to Eq. 14. In the case when the distribution of displacement vector **D** is more or less constant for all levels of damage, then the forces F_* can be determined by Eq. 18.

6. Assume hysteretic behavior of the SDOF model.
7. Compute the mass m_* of the SDOF model according to Eq. 7.
8. Compute the damping constants α and/or β based on the assumed damping model and the ratio of critical damping.

Pushover Analysis and Limit States

Pushover analysis is a kind of nonlinear static analysis which aims at determining the relationship between the lateral forces and the engineering demand parameters (EDPs) for all performance levels of a structure. The results of pushover analysis are very intuitive, which makes it attractive for practical applications. It is clear that the relationship between the forces and the deformations are linearly elastic until damage occurs to the first element. Beyond this level, an increment of lateral forces causes a greater increment in the deformations in comparison with that observed in the case of linear elastic analysis, since the stiffness of the structure is reduced due to the damage which has occurred to some of the elements. When the deformations reach a certain level, the maximum strength of the structure is reached. From here on, the strength of the structure decreases due to the softening of the material (e.g., see Fig. 2) or due to second-order effects, if they are considered in the analysis. In less general case, when the softening of material and second-order effects is not taken into account, the pushover curve becomes a straight line once a plastic mechanism forms.

The strength and deformation capacity, the available ductility, and the system failure mode represent the global results of the pushover analysis, which should always be checked in the case when seismic performance assessment of structure is based on a nonlinear analysis method. The results of a pushover analysis are usually presented in the form of a pushover curve, which represents a relationship between the base shear and top (roof) displacement of the investigated structure (e.g., see Fig. 2). The pushover curve is, in fact, a characteristic of the structure. However, it depends on the type of pushover analysis used.

The pushover analysis becomes an approximate analysis method if it is used for the prediction of expected seismic performance of a structure (e.g., Saiidi and Sozen 1981; Fajfar and Fischinger 1988; Fajfar 2000). In this case, it is important that the structural model implicitly accounts for the cyclic deterioration. However, the results of pushover analysis are used for the definition of the SDOF model, which represents a link between the seismic action and the seismic demand.

The seismic demand at the level of the SDOF model can be obtained by means of numerous procedures. Once the displacement at the level of the SDOF model has been obtained, it can be transformed to the selected EDP at the structural level. Since several phenomena associated with the response of a structure during an earthquake are neglected in pushover-based methods, it is clear that the results of such simplified procedure are approximate also from the theoretical point of view. Due to the approximate nature of pushover-based procedures, many types of pushover analysis have been developed in recent decades. Some of them are briefly described below.

Types of Pushover Analysis

Conventional pushover analysis (e.g., Saiidi and Sozen 1981; Fajfar and Fischinger 1988) is based on an invariant distribution of the lateral forces. The shape of the lateral forces is therefore independent of deformations, whereas the shape of the deformations is dependent on the level of structural damage. This is the most common type of pushover analysis, which is recommended by some guidelines and building codes (e.g., FEMA 356, Eurocode 8). It is usually prescribed that pushover analysis should be performed for at least two vertical distributions of the lateral loads

in order to assess the range of EDPs that might occur during actual dynamic response. Eurocode 8 suggests the use of the so-called uniform and modal load patterns, which are, respectively, proportional to the story masses and the lateral forces from the elastic analysis. According to FEMA 356, two patterns have to be selected from two groups. The first load pattern should be consistent with the modal pattern, whereas a second pattern can be based on a uniform load pattern or on an adaptive load distribution which accounts for the redistribution of the lateral loads, taking into account the properties of the yielded structure. Due to the simplicity of conventional pushover analysis, even more than two pushover analyses can be easily performed. For example, an iterative pushover-based procedure (IPP) (Celarec and Dolšek 2013) involving model adaptation was recently introduced, which aims at improving the capability of simulations based on simplified nonlinear models. It was shown that the IPP can be used to approximately simulate the shear failure of columns (Celarec and Dolšek 2013; Kosič et al. 2014), although simplified nonlinear models are not capable of direct simulation of such effects.

Adaptive pushover analysis is an alternative to conventional pushover analysis. In force-based adaptive pushover analysis, the load vectors are gradually updated due to the damage occurring to the structure, which affects the mode shapes. One of the first procedures for the adaptive lateral load for pushover analysis was proposed by Bracci et al. (1997). Many different procedures for force-based adaptive pushover analysis followed. Most approaches involve response spectrum analysis which is performed for the different modal characters of the structure which are associated with selected stages of the pushover analysis. However, Aydinoğlu (2003) has argued that the load patterns should be based on an inelastic rather than an elastic response spectrum. It was soon realized that force-based adaptive pushover analysis offers only a relatively minor advantage in comparison with conventional pushover analysis. As a result of such an observation, a displacement-based adaptive pushover procedure was proposed (Antoniou and Pinho 2004), which, however, did not provide significantly improved prediction in comparison to the force-based algorithms that are used for adaptive pushover analysis.

Conventional or adaptive pushover analysis provides a single pushover curve, which can be used in conjunction with the SDOF model to obtain the expected values of EDPs. For some types of buildings and EDPs, such a simulation of the seismic response of a structure provides sufficiently accurate results. However, the analyst has to be careful when interpreting the results of the seismic performance assessment of a structure on the basis of one pushover curve, since it is not possible to assess all types of EDPs on the basis of single pushover analysis. In general, the dynamic response of a structure is far more complex, especially if it suffers significant damage. In general, several system failure modes can be observed due to the randomness of ground motions. Additionally, in the case of taller buildings, several modes can significantly contribute to the results. On the other hand, mode shapes depend on the scale of inflicted damage, which gradually increases during a strong earthquake. Thus, the maximum values of EDPs do not appear at the same instant in time. Furthermore, the impact of mode shapes varies with respect to the EDPs. For example, the higher mode effects can be significant for the prediction of story drifts and for the internal forces in the upper parts of taller buildings. Much effort has been expended in order to try to approximately account for the so-called effect of higher modes. One of the first attempts in this direction has been made by Paret et al. (1996), who performed several pushover analyses using a lateral load pattern based on different elastic mode shapes. A theoretical basis for the modal pushover analysis procedure for estimating the seismic demand for buildings was introduced by Chopra and Goel (2002). The method involves several pushover analysis and corresponding modal-based SDOF models, whereas the overall response is obtained by combining the results of all considered modes. Recently, a general pushover analysis was introduced (Sucuoğlu and Günay 2011). It is based on several pushover analyses, which are performed

on the basis of the lateral forces obtained as a combination of the modal forces. It was also shown that the so-called higher system failure modes can significantly contribute to the response of taller buildings. Brozovič and Dolšek (2014) have shown that system failure modes observed due to the randomness of ground motion can be sufficiently accounted for by the envelope-based pushover analysis procedure, which is based on several pushover analyses and the use of failure-based SDOF models. The failure-based SDOF models utilize the displacement vectors corresponding to the system failure modes that are observed from pushover analyses in the case of second or higher modes. This significantly improves the prediction of the intensity causing a designated limit state, if the structure is sensitive to the effects of higher modes.

Definition of Limit States

As already mentioned above, pushover analysis is the simplest nonlinear analysis method, which has been included in several guidelines and standards for seismic performance assessment and the retrofitting of buildings. The results of pushover analysis can be used, in conjunction with the target displacement for a given seismic action, to check whether the structural performance satisfies the defined performance objectives. For this purpose, building codes provide limit states at the component or structural level. Eurocode 8-3 (CEN 2005) utilizes the following limit states: damage limitation (DL), significant damage (SD), and near collapse (NC). These limit states are explicitly defined at the component level, whereas definitions at the structural level are only descriptive. For example, it is prescribed that the near-collapse limit state at the structural level is attained when a structure is heavily damaged, with some residual lateral strength and stiffness, but is still capable of sustaining vertical loads and aftershocks of moderate intensity. However, moderate permanent drifts are present, and it is not likely, from the economic point of view, that repair of the building could be justified. Note that the NC limit state is often defined at the global level, i.e., when the strength in the post-capping range of pushover curve decreases for 20 %. Each country can prescribe return periods of the design seismic action associated with these limit states. By default, it is assumed that appropriate levels of protection are achieved when the structural performance for the DL, SD, and NC limit states is checked for seismic actions corresponding to return periods of 225, 475, and 2475 years, respectively. The prestandard for the seismic rehabilitation of buildings FEMA 356 (2000), which was issued a few years before the Eurocode 8-3, is based on similar metrics for checking the target building performance. The basic structural performance levels of a building are immediate occupancy (IO), life safety (LS), and collapse prevention (CP). FEMA 356 states that building performance is a combination of the performance of both the structural and the nonstructural components. The description of performance levels (i.e., limit states), which are discrete damage states selected from among the infinite spectrum of possible damage states that buildings could experience during an earthquake, consists of estimates rather than precise predictions (FEMA 2000).

According to the brief overview of limit states provided in some standards, it is clear that there are many different definitions of them. In general, each limit state is associated with a certain degree of damage. However, there are some restrictions regarding the definition of limit states on the basis of pushover analysis. For example, the pushover analysis is not able to explicitly simulate cycling deterioration. Thus, in the case of pushover analysis, limit states cannot be dependent on the level of cyclic deterioration. Since damage models are often defined by story drifts or the rotations in plastic hinges, such a limitation of pushover analysis, associated with an inability to simulate cycling deterioration, is not critical, provided that the nonlinear model used for pushover analysis implicitly accounts for cyclic deterioration of the structural components. In the case of nonstructural components, it is common to define a limit state by the level of story acceleration, which is not explicitly simulated by pushover analysis. A simplified model for story acceleration is therefore also required.

Although there are no critical restrictions for the definition of limit states in the case when seismic demand is obtained by the pushover-based method, it should be realized that the accuracy of pushover-based methods is limited. The analyst should therefore be careful when checking the limit states, especially in the case when target performance is defined at the component level. It is thus recommended that the limit states should be defined at the global and structural levels, taking into account the global parameters obtained from the pushover curve. Even in this case, it is recommended that the structural damage associated with such defined limit states should be checked, since it is possible that a flexible structure has not suffered significant damage even though the corresponding point on the pushover curve is beyond the post-capping point. Such performance can be observed in the case of flexible frames, where the P-Δ effect has a quite significant impact on structural performance.

Pushover-Based Seismic Fragility Analysis

The result of fragility analysis is the fragility function, which represents the probability that an engineering demand parameter (*EDP*) will exceed a certain limit-state value *edp* given an intensity $IM = im$. In the simplest case, it is assumed that the seismic fragility function is based on a lognormal distribution function:

$$P(EDP > edp|IM = im) = 1 - \Phi\left(\frac{\ln edp - \ln \mu_{edp}}{\sigma_{\ln edp}}\right) \quad (25)$$

where $\Phi\left(\frac{\ln edp - \ln \mu_{edp}}{\sigma_{\ln edp}}\right)$ represents the standard normal distribution function, μ_{edp} is the median value of the EDP given the intensity *im*, and $\sigma_{\ln\ edp}$ is the standard deviation of the natural logarithms of the EDP given that $IM = im$. The above definition is suitable when the limit state is based on a threshold value of an engineering demand parameter. In the case of an IM-based definition of a limit state, which is common for the collapse limit state, the fragility function can be defined as follows:

$$P(LS|IM = im) = \Phi\left(\frac{\ln im - \ln \mu_{imLS}}{\sigma_{\ln imLS}}\right) \quad (26)$$

where $P(LS|IM = im)$ is the probability of exceeding the limit state *LS* if the intensity measure assumes a value equal to *im*, μ_{imLS} is the median limit-state intensity, and $\sigma_{\ln\ imLS}$ is the corresponding standard deviation of the natural logarithms. The fragility function is therefore defined by two parameters, the median value μ_{edp} or μ_{imLS} and the corresponding standard deviation $\sigma_{\ln\ edp}$ or $\sigma_{\ln\ imLS}$. Many different procedures for the estimation of these parameters based on pushover analysis have been developed. It should also be noted that many different procedures for fragility analysis exist. Some of them can also be used on the basis of seismic performance assessment utilizing pushover analysis (e.g., Jalayer et al. 2011; Rota et al. 2014).

The accuracy of determination of the fragility parameters (μ, $\sigma_{\ln}$) depends on the method for seismic performance assessment of a structure and the level of the simulations, which accounts for the effect of uncertainty.

Deterministic Approach for Assessing the Parameters of the Fragility Function

In the simplest case, the effects of uncertainty can be assumed by the default values of $\sigma_{\ln}$. Consequently, the deterministic seismic performance of a structure can be used. This enables the use of analytical models for the determination of the target displacement. Parametric studies have shown that the $\sigma_{\ln\ imLS}$ depends on the limit state and the type of seismic intensity measure. If the intensities causing collapse are assessed by the spectral acceleration corresponding to the first vibration period, the $\sigma_{\ln\ imLS}$ is in the interval between 0.3 and 0.5 (Lazar and Dolšek 2014). The $\sigma_{\ln\ imLS}$ increases with respect to the period of structure if it is assessed on the basis of peak ground acceleration. It varies between 0.5 and

0.75. The value of $\sigma_{\ln\ imLS}$ can additionally increase if epistemic uncertainties are considered in addition to the record-to-record randomness.

In Europe, the most commonly used approach for the determination of expected seismic response based on pushover analysis is the N2 method (e.g., Fajfar 2000), which has been implemented in Eurocode 8 (CEN 2004), whereas the so-called coefficient method is used in the United States (e.g., FEMA 356 (2000)). According to Eurocode 8 and FEMA 356, the target displacement (d_t and δ_t), respectively, can be determined as follows:

$$d_t = \Gamma \cdot \frac{\mu(q_u, T^*, T_C)}{q_u} \cdot S_e(T^*) \frac{T^{*2}}{4\pi^2}, \quad (27)$$

$$\delta_t = C_0 \cdot C_1(R, T_S, T_e) C_2 C_3 \cdot S_a(T_e) \frac{T_e^2}{4\pi^2}, \quad (28)$$

where the parameters Γ and C_0 have the same meaning, i.e., they are the so-called transformation or modification factors which relate the spectral displacement of an equivalent SDOF model to the roof displacement of the MDOF model. For the experienced reader, it is also trivial that the last parts of Eqs. 27 and 28 represent the elastic spectral displacement S_{de}, whereas the middle part of Eqs. 27 and 28 corresponds to the so-called inelastic displacement ratio C (e.g., Miranda 2000), which depends on many parameters, such as the ground motion type, the hysteretic behavior, the force-displacement relationship, the masses, damping, and others. For reasons of simplicity, formulas for the determination of the inelastic displacement ratio have been introduced based on the results of parametric studies. For example, in Eurocode 8, the simplified $R - \mu - T$ relationship proposed by Fajfar (2000) is used to define the inelastic displacement ratio, whereas in FEMA 356 (2000), two additional parameters are used to define the inelastic displacement ratio, i.e., the parameter C_2, which represents the effect of a pinched hysteretic shape, stiffness degradation, and strength deterioration on maximum displacement, and the parameter C_3, which represents the increased displacement due to dynamic P-Δ effects. Note that the meaning of all the variables in Eqs. 27 and 28 is described in the corresponding references (CEN 2004; FEMA 2000).

Consideration of Ground-Motion Randomness in Estimation of Parameters of Fragility Function

The first level of simulations involves consideration of the effect of ground-motion randomness. In general, the target displacement according to this approach is based on nonlinear dynamic analysis of the SDOF model. The analyst should therefore select an appropriate set of ground motions and define the SDOF model, which could be used for nonlinear dynamic analysis as previously described in this entry. The results of such analyses are samples of EDP values given the different values of the intensities or the sample of limit-state intensities, which could be used to estimate the parameters of the fragility function. Some alternatives exist which can be used in order to avoid the use of nonlinear dynamic analysis at the level of the SDOF model. Vamvatsikos and Cornell (2006) developed the SPO2IDA software tool, which is capable of recreating the seismic behavior of a single-degree-of-freedom (SDOF) model with a quadri-linear force-displacement relationship. They performed a parametric study by suitably varying the five parameters of the force-displacement relationship, which are negative and nonnegative hardening, the residual plateau, ductility at the beginning of strength degradation, and ductility at collapse. Based on the results of the parametric study, regression analysis was used to define each segment of the approximate 16th, 50th, and 84th fractile IDA curves. Although SPO2IDA is a useful software tool, it is not easy to extend its applicability, since a new regression analysis is required if the seismic response parameters are to be computed for additional ground motion records. More recently, Peruš et al. (2013) introduced a web-based methodology for the prediction of approximate IDA curves, which consists of two independent processes. The result of the first process is a response database of the single-degree-of-freedom model, whereas the second process involves the prediction of approximate

IDA curves from the response database by using n-dimensional linear interpolation. Such an approach makes possible user-friendly prediction of the seismic response parameters with high accuracy. In order to demonstrate the capabilities of the proposed methodology, a web application for the prediction of the approximate 16th, 50th, and 84th fractile response of a reinforced concrete structure was developed (http://ice4risk.slo-projekt.info/WIDA/). Note that web-based methodology for the prediction of the approximate IDA curves estimates an error of the predicted IDA curves of a SDOF model.

Consideration of Ground-Motion Randomness and Epistemic Uncertainty in Estimation of Parameters of Fragility Function

In a general case, fragility parameters should be based on simulations which take into account the effects of ground-motion randomness and the other knowledge-based sources of uncertainty, such as physical uncertainties, modeling uncertainties, human errors, uncertainties associated with the knowledge level about the structure, and others. In order to account for knowledge-based uncertainties, the simulations can be performed at the level of a MDOF model (e.g., Fragiadakis and Vamvatsikos 2010; Dolšek 2012) or a SDOF model (Kosič et al. 2014). Many different simulation methods can be used to perform pushover analysis with consideration of knowledge-based uncertainties (e.g., Barbato et al. 2010; Jalayer et al. 2011). It is convenient and straightforward to utilize Monte Carlo simulation with Latin hypercube sampling (e.g., Fragiadakis and Vamvatsikos 2010; Dolšek 2012). The LHS technique uses stratification of the probability distribution function of the random variables X_i and consequently requires significantly fewer simulations in comparison with the ordinary type of Monte Carlo simulation. In general, two steps are needed to determine the sample of random variables, which are directly applied in the structural model. First, each random variable is sampled by inverse method using equidistant points between sample probabilities. If the random variables are correlated, the sample should be generated in such a way that the correlation structure between the random variables is simulated in the best possible manner. This represents the second step in the process of the determination of the sample of random variables. The problem can be successfully solved by the stochastic optimization method called simulated annealing. More details are available elsewhere (e.g., Dolšek 2012).

However, all the referenced procedures are based on simulations which are performed at the level of a MDOF model. Recently, an approximate procedure utilizing a deterministic MDOF model and uncertainty analysis at the level of a SDOF model was proposed (Kosič et al. 2014). It can be classified as being somewhere in between the aforementioned procedures for the determination of fragility parameters on the basis of pushover methods, both in terms of computational time and in terms of accuracy. Such an approach is computationally less demanding, since all the simulations are performed at the level of the so-called probabilistic SDOF model. It can therefore be attractive for the fragility analysis of more extensive building stock.

Example: Pushover-Based Seismic Fragility Analysis of the RC Frame Building With Consideration of Ground-Motion Randomness and Modeling Uncertainty

A simple variant of a pushover-based fragility analysis is demonstrated by means of an illustrative example. The procedure involves conventional pushover analyses and the nonlinear dynamic analyses of corresponding SDOF models. The effects of ground-motion and modeling uncertainties are accounted for, respectively, by the set of ground motions and the set of structural models which are generated by Monte Carlo with LHS. The step-by-step procedure for the determination of the fragility curve is as follows:

1. *Preparation of data regarding the structure and the seismic hazard at the location of the structure*. It is important to obtain as accurate as possible data regarding the seismic hazard in order to reduce the effect of uncertainties.

Information regarding the seismic hazard and the soil type are important for the selection of appropriate ground motions.

2. *Definition of limit states*. In general, limit states can be defined at the component or structural level. As briefly discussed above, there is no critical restriction regarding the definition of limit states if the seismic demand is based on a pushover analysis procedure.
3. *Identification of epistemic uncertainties*. Uncertainties are often divided into aleatoric and epistemic, although there is no need to make such a distinction. In this example, the aleatoric uncertainties are accounted for by the set of ground motions (step 5), whereas the effects of the epistemic uncertainties are incorporated by the set of structural models. The most important sources of epistemic uncertainty should be modeled by appropriate random variables.
4. *Determination of the set of structural models utilizing Monte Carlo with LHS*. The LHS technique uses stratification of the probability distribution function of the random variables and consequently requires fewer simulations in comparison with a crude Monte Carlo simulation. However, any appropriate LHS technique can be used in order to generate the sample of the uncertain input parameters. It has been previously shown (e.g., Dolšek 2012) that the effect of epistemic uncertainties can be simulated with sufficient accuracy by a number of structural models, which is at least twice the number of random variables. It is worth emphasizing that the nonlinear structural model should implicitly account for cyclic deterioration.
5. *Selection of an appropriate set of ground motions*. Many different procedures exist for the selection of an appropriate set of ground motions. Ground motions are usually selected to match the target spectrum, which is, in the simplest case, the elastic acceleration spectrum prescribed by a building code.
6. *Calculation of pushover curves for all the structural models simulated in step 4*. Different types of pushover analysis can be performed. Conventional pushover analysis, which is based on the invariant lateral load, is the simplest and is the most often applied. The results of the pushover analysis are pushover curves and the seismic demand on the structure given the top displacement. In general, more than one pushover analysis per structural model is required.
7. *Determination of the SDOF models*. This step requires the transformation of top displacement and base shear to the displacement (Eq. 9) and force (Eq. 14 or Eq. 18) of the SDOF model. The force-displacement relationship of the SDOF model should be multilinear. Negative post-capping stiffness can also be applied in order to estimate the collapse capacity. It is usually assumed that the hysteretic behavior is the same as that prescribed for the components of the structural models. The mass of the SDOF model should be determined according to Eq. 7a, whereas the damping can be proportional to mass and/or stiffness (Eq. 24).
8. *Response history analyses for all SDOF models and ground motions*. Since, in the case of SDOF models, the response history analysis is not computationally demanding, it is recommended that the records should be scaled and that the relationship between the ground-motion intensity and the displacement of the SDOF model should be computed for several levels of damage, e.g., from elastic behavior to collapse.
9. *Assessment of seismic demand at the level of structural model*. The displacement obtained from the response history analysis of the SDOF model should be transformed to the top displacement using Eqs. 8 and 9. Any other engineering demand parameter at the level of structure can be obtained from the results of the pushover analysis on the basis of the known top displacement. However, if more than one pushover analysis is performed per structural model, in order to account for the effect of higher failure modes, then the total demand can be obtained by enveloping the results of all pushover

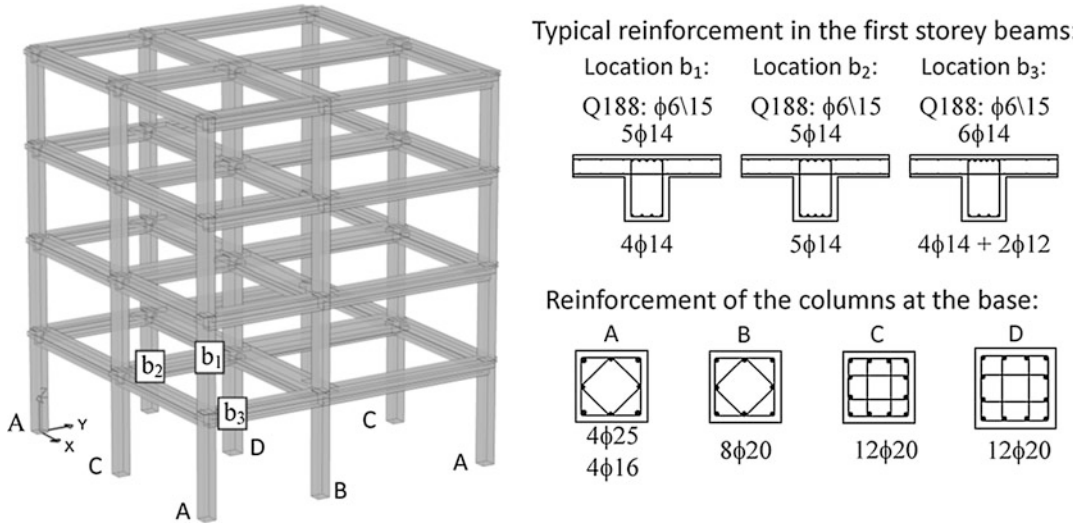

Analytic Fragility and Limit States [P(EDP|IM)]: Nonlinear Static Procedures, Fig. 1 A view of the investigated four-story building and the reinforcement in selected columns and beams

analyses (e.g., Brozovič and Dolšek 2014) or by combining the results together according to an appropriate combinational rule (Chopra and Goel 2002). The results of this step are samples of the engineering demand parameters given the intensities or samples of limit-state intensities.

10. *Calculation of the fragility parameters and the fragility curve*. Fragility curves can be directly estimated on the basis of the sample values. In the case when the fragility curves are based on an assumed lognormal distribution, the method of moments, the maximum likelihood method, the method of counted percentiles, or any other suitable method can be used to calculate the median engineering demand parameters or the limit-state intensities and the corresponding dispersions.

The application of the above-described step-by-step procedure for the determination of the fragility curves is demonstrated by means of a four-story reinforced concrete frame building (Fig. 1), which was previously analyzed (Dolšek 2012). Just a brief overview of the procedure is presented.

Step 1. The structure was designed for a peak ground acceleration of 0.3 g, soil type B, and ductility class high (behavior factor = 5). Concrete of quality C25/30 and B500 Tempcore reinforcing steel were used to construct the building. Minimum and maximum mean concrete strengths of 32 MPa and 56 MPa were measured. The modulus of elasticity of the concrete varied from 28.5 to 35.3 GPa. The mean yield strength exceeded the characteristic yield strength by between 10 % and 20 %, depending on the diameter of the reinforcing bars. However, the average value of the yield strength of the reinforcing steel amounted to about 580 MPa.

Step 2. Fragility analysis was performed for the limit states of damage limitation (DL), significant damage (SD), and near collapse (NC), as defined in Eurocode (CEN 2005). It was assumed that the DL limit state is attained at the structural level if the longitudinal reinforcement in all the columns in any story starts to yield. It was further assumed that the SD and NC limit states are reached, at the structural level, when the moment exceeds the maximum moment in the case of the first column or the rotation exceeds the ultimate rotation in the case of first column, respectively. However, additional criteria for the occurrence of the SD and NC limit states were

defined. It was assumed that the top displacement corresponding to the NC limit state should not be less than that associated with 80 % of the maximum base shear measured in the post-capping range of the pushover curve. Similarly, it was assumed that the top displacement corresponding to the SD limit state should be not less than the 75 % of the NC limit-state top displacement.

Step 3. Since full knowledge about the building structure was available, only the following modeling uncertainties were considered in the fragility analysis: mass, strength of the concrete and the reinforcing steel, effective slab width, damping, and the model for determining the initial stiffness and ultimate rotation in the plastic hinges of the beams and columns. A normal or lognormal distribution was assumed for the majority of the nine random variables ($N_{\text{var}} = 9$). The statistical characteristics of the input random variables were taken from literature as reported elsewhere (Dolšek 2012). All the considered input random variables were assumed to be uncorrelated with respect to the story masses, which were assumed to be perfectly correlated and modeled by one random variable. The highest value of the coefficient of variation was adopted for the prediction of the ultimate rotations in the beams (0.6) and columns (0.4).

Step 4. Realization of the random variables was based on the LHS technique. The size of the sample was assumed to be equal to 20, which is slightly larger than twice the number of all the random variables considered in the fragility analysis. The correlation matrix of the sample was almost identical to the target correlation matrix. Note that this is only a necessary condition for the prediction of the seismic response parameters with the required accuracy, whereas the sufficient condition is related to the number of simulations, which is, in the case of the example, relatively low ($N_{\text{sim}} = 20$). However, the results of performed studies have shown that, in the case when N_{sim} is larger than twice the number of random variables (N_{var}), an increase in the number of simulations does not significantly affect the estimated median seismic response parameters and the corresponding dispersion. The results of this step were 20 structural models based on the sample of random variables. For comparison, an additional "deterministic" structural model was also created by assuming median values of the random variables.

Step 5. A set of 14 ground motions ($N_{gm} = 14$) were selected from European Strong Motion Database to match the Eurocode-based acceleration spectrum. All the selected records were recorded on stiff soil and had peak ground acceleration greater than 0.1g. The mean acceleration spectrum of the selected ground motions matched reasonably well with the target Eurocode-based spectrum. It should be noted that ground motions selected in this way often overestimate the seismic response with respect to that based on hazard-consistent ground motions.

Step 6. The lateral load pattern for conventional pushover analyses was based on the first vibration mode (Eq. 15). For simplicity, the structure was analyzed in the Y direction only (see Fig. 1). The pushover curves for all structural models from *Step 4* are presented in Fig. 2. An extensive scatter can be observed in the case of the deformation capacity of the realized structural models, whereas the difference in the strength is less. However, no significant differences can be observed between the deterministic model and the so-called median pushover curve. The limit-state top displacement and the corresponding base share are highlighted for the DL, SD, and NC limit states. The high coefficient of variation of the limit-state top displacement, which increases gradually with respect to the severity of the limit state, is partly the consequence of the high coefficient of variation of the input parameters and partly the consequence of the formation of different system failure modes, which were observed from pushover analyses.

Step 7. The pushover curves were idealized by means of a trilinear force-displacement relationship, also taking into account negative post-capping stiffness. Transformation of the

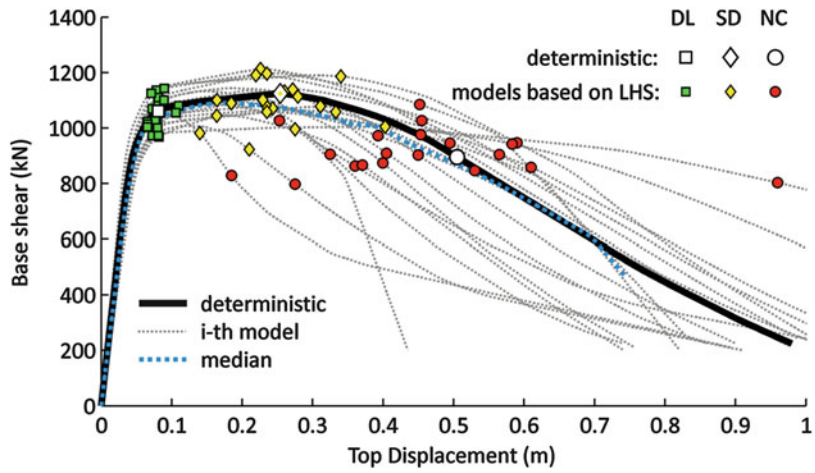

Analytic Fragility and Limit States [P(EDP|IM)]: Nonlinear Static Procedures, Fig. 2 The pushover curves corresponding to the structural models based on the LHS technique, the pushover curve corresponding to the deterministic model, and the median pushover curve. The points on the pushover curve represent the limit-state top displacements

idealized pushover curve to the parameters of an equivalent SDOF model was performed by dividing the base shear and top displacement of the idealized pushover curve by a transformation factor Γ (Eq. 8). The mass of the SDOF model and the force-displacement relationships of the SDOF model were obtained according to Eq. 7a and Eqs. 9 and 18, respectively. Note that the number of the SDOF models was the same as the number of pushover curves. All the parameters of the SDOF models differed from one another due to the epistemic uncertainties. However, the peak-oriented hysteretic model and damping proportional to the tangent stiffness were assumed to be invariant.

Step 8. The response history analyses were performed for each SDOF model by scaling the ground-motion intensity in order to obtain the complete relationship between the peak ground acceleration and the displacement of the SDOF model. The results are presented in Fig. 3, where the highlighted points indicate the limit-state intensities which were used for the calculation of the fragility parameters.

Steps 9 and 10. The limit-state top displacements highlighted in Fig. 2 were transformed into the displacement of the corresponding SDOF model, which was then used to determine the limit-state intensities. The limit-state displacements and the limit-state intensities shown in Fig. 3a are presented for the deterministic SDOF model, taking into account just ground-motion randomness. The variability can be observed only for the limit-state intensities, while in the adjacent figure (Fig. 3b), variability can be observed also for the limit-state displacements. The latter variability is the consequence of the effect of epistemic uncertainty. The sample of limit-state intensities presented in Fig. 3b was used to estimate the parameters of the fragility curves. The median values and the corresponding dispersion of natural logarithms were estimated according to maximum likelihood method. The fragility curves were then obtained using Eq. 26. The results are presented in Fig. 4.

A flatter fragility curve can be observed in the case of the DL limit state if the effects of epistemic uncertainty are considered in the fragility analysis. This is in agreement with expectations and can be modeled by using the mean estimate approach, in which it is assumed that the effects of epistemic uncertainties on the fragility curve can be modeled by simply inflating the dispersion. However, in the case of the NC limit state, it is clear that incorporating the epistemic uncertainties in the determination of the fragility curve causes a shift of the fragility curve to the left, which means that the effects of epistemic

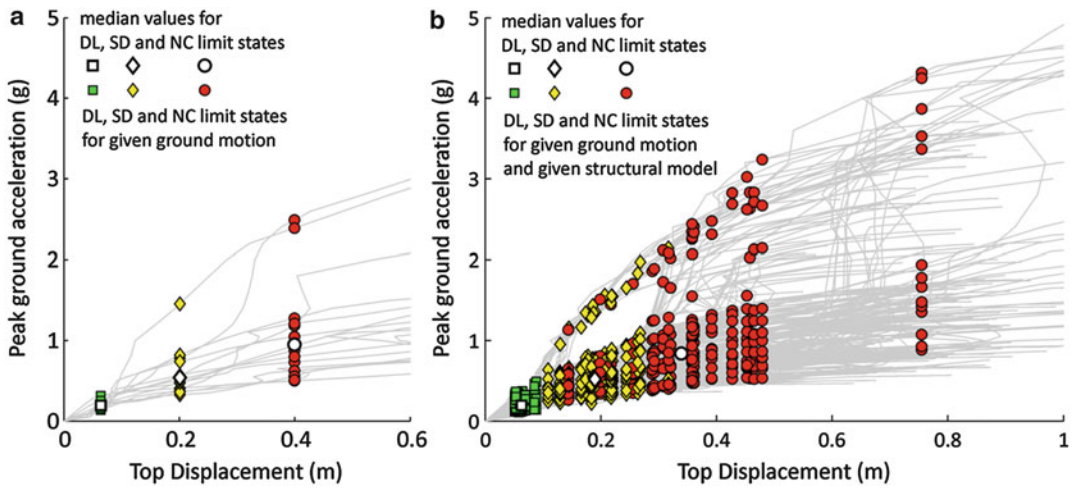

Analytic Fragility and Limit States [P(EDP|IM)]: Nonlinear Static Procedures, Fig. 3 The limit-state peak ground accelerations and displacements associated with the set of structural models and (**a**) the deterministic SDOF model and (**b**) the SDOF models based on the LHS technique. The median limit-state points for the DL, SD, and NC limit states are also presented

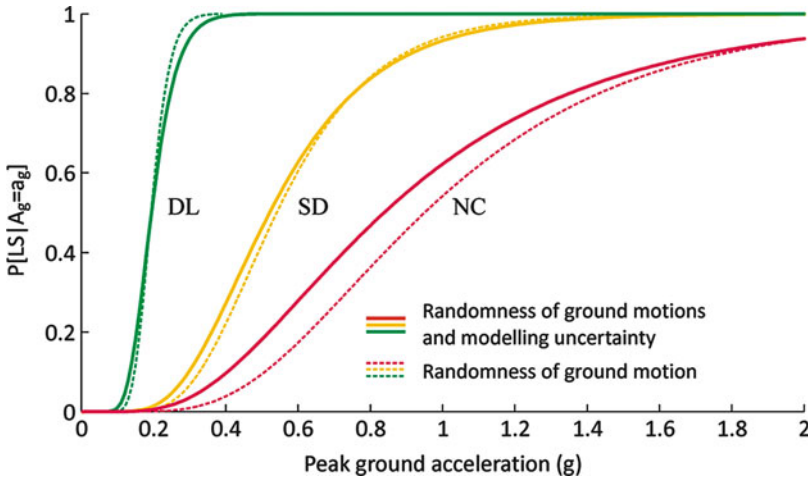

Analytic Fragility and Limit States [P(EDP|IM)]: Nonlinear Static Procedures, Fig. 4 The fragility curves for the DL, SD, and NC limit states taking into account only the randomness of ground motions and both, i.e., randomness of the ground motions and modeling uncertainty

uncertainty reduced the median limit-state intensity. This effect was frequently observed, especially in the case of reinforced concrete frames.

Summary

Pushover-based methods are used around the world as a tool for the approximate seismic performance assessment of structures. Due to their computational efficiency, pushover-based methods are attractive also for fragility analysis, which incorporates the effects of ground motions and other sources of uncertainty. In this entry, emphasis was placed on explaining the theoretical background for predicting seismic demand using a SDOF model, since it is important to understand the basic assumptions of the approximate methods. A variant of the pushover-based fragility analysis is then explained through a

step-by-step procedure and demonstrated by means of an example of a four-story building. It has been shown that pushover-based methods can be successfully used for fragility analysis. However, the analyst should always be aware of the approximate nature of pushover-based methods. Such an awareness will allow him to decide to which type of structures and for what purpose individual pushover-based methods can be applied.

Cross-References

- ▶ Reinforced Concrete Structures in Earthquake-Resistant Construction
- ▶ Seismic Fragility Analysis
- ▶ Seismic Reliability Assessment, Alternative Methods for
- ▶ Uncertainty Theories: Overview

References

Antoniou S, Pinho R (2004) Development and verification of a displacement-based adaptive pushover procedure. J Earthq Eng 8(5):643–661

Aydinoğlu MN (2003) An incremental response spectrum analysis procedure based on inelastic spectral displacements for multi-mode seismic performance evaluation. Bull Earthq Eng 1(1):3–36

Barbato M, Gu Q, Conte JP (2010) Probabilistic push-over analysis of structural and soil-structure system. J Struct Eng 136(11):1330–1341

Bracci JM, Kunnath SK, Reinhorn AM (1997) Seismic performance and retrofit evaluation of reinforced concrete structures. J Struct Eng 123(1):3–10

Brozovič M, Dolšek M (2014) Envelope-based pushover analysis procedure for the approximate seismic response analysis of buildings. Earthq Eng Struct Dyn 43(1):77–96

Celarec D, Dolšek M (2013) Practice-oriented probabilistic seismic performance assessment of infilled frames with consideration of shear failure of columns. Earthq Eng Struct Dyn 42(9):1339–1360

CEN (2004) Eurocode 8: design of structures for earthquake resistance – part 1: general rules, seismic actions and rules for buildings, EN 1998–1. European Committee for Standardisation, Brussels

CEN (2005) Eurocode 8: design of structures for earthquake resistance – part 3: assessment and retrofitting of buildings, EN 1998–3. European Committee for Standardisation, Brussels

Chopra AK, Goel RK (2002) A modal pushover analysis procedure for estimating seismic demands for buildings. Earthq Eng Struct Dyn 31(3):561–582

Dolšek M (2012) Simplified method for seismic risk assessment of buildings with consideration of aleatory and epistemic uncertainty. Struct Infrastruct Eng 8(10):939–953

Fajfar P (2000) A nonlinear analysis method for performance-based seismic design. Earthq Spectra 16(3):573–592

Fajfar P, Fischinger M (1988) N2 – a method for non-linear seismic analysis of regular buildings. Proceedings of ninth world conference on earthquake engineering, vol V, Tokyo-Kyoto

FEMA (2000) Prestandard and commentary for the seismic rehabilitation of buildings, vol 356, FEMA. Federal Emergency Management Agency, Washington, DC

Fragiadakis M, Vamvatsikos D (2010) Fast performance uncertainty estimation via pushover and approximate IDA. Earthq Eng Struct Dyn 39(6):683–703

Jalayer F, Elefante L, Iervolino I, Manfredi G (2011) Knowledge-based performance assessment of existing RC buildings. J Earthq Eng 15(3):362–389

Kosič M, Fajfar P, Dolšek M (2014) Approximate seismic risk assessment of building structures with explicit consideration of uncertainties. Earthq Eng Struct Dyn 43(10):1483–1502

Kreslin M, Fajfar P (2012) The extended N2 method considering higher mode effects in both plan and elevation. Bull Earthq Eng 10(2):695–715

Lazar N, Dolšek M (2014) Incorporating intensity bounds for assessing the seismic safety of structures: does it matter? Earthq Eng Struct Dyn 43(5):717–738

Miranda E (2000) Inelastic displacement ratios for structures on firm sites. J Struct Eng 126(10):1150–1159

Paret TF, Sasaki KK, Eilbeck DH, Freeman SA (1996) Approximate inelastic procedures to identify failure mechanisms from higher mode effects. In: Proceedings of 11th world conference on earthquake engineering (P.No. 966), Acapulco

Peruš I, Klinc R, Dolenc M, Dolšek M (2013) A web-based methodology for the prediction of approximate IDA curves. Earthq Eng Struct Dyn 42(1):43–60

Reyes JC, Chopra AK (2011) Three-dimensional modal pushover analysis of buildings subjected to two components of ground motions, including its evaluation for tall buildings. Earthq Eng Struct Dyn 40:789–806

Rota M, Penna A, Magenes G (2014) A framework for the seismic assessment of existing masonry buildings accounting for different sources of uncertainty. Earthq Eng Struct Dyn 43(7):1045–1066

Saiidi M, Sozen MA (1981) Simple nonlinear seismic analysis of R/C structures. J Struct Div ASCE 107(5):937–953

Sucuoğlu H, Günay MS (2011) Generalized force vectors for multi-mode pushover analysis. Earthq Eng Struct Dyn 40(1):55–74

Vamvatsikos D, Cornell CA (2006) Direct estimation of the seismic demand and capacity of oscillators with multi-linear static pushovers through IDA. Earthq Eng Struct Dyn 35(9):1097–1117

Ancient Monuments Under Seismic Actions: Modeling and Analysis

Ioannis N. Psycharis
School of Civil Engineering, Department of Structural Engineering, National Technical University of Athens (N.T.U.A.), Athens, Greece

Synonyms

Classical monuments

Introduction

Classical monuments are made of structural elements (called drums in case of columns), which lie one on top of the other without mortar. Columns are connected to each other with architraves (epistyles) consisting of stone beams, usually made of marble. A characteristic example is shown in Fig. 1 from the Olympieion of Athens, Greece.

Architrave beams are usually connected to each other with iron clamps and dowels. However, in most cases no structural connections are provided between the drums of the columns. Only in few cases, iron shear connectors (dowels) are provided at the joints, which restrict, up to their yielding, sliding but do not affect rocking. The wooden dowels that were usually placed at the joints among the drum of the columns were aiming at centering the stones during construction and, practically, do not have any effect on their seismic response.

Due to their spinal construction, columns of ancient monuments respond to strong earthquakes with intense rocking and sliding of the drums. Therefore, the dynamic analysis of ancient monuments is a difficult problem to treat, since it does not follow the behavior rules of continuum systems.

Several investigators have examined the seismic response of classical monuments and, in general, of stacks of rigid bodies analytically, numerically, or experimentally, mostly using two-dimensional models (e.g., Allen et al. 1986; Sinopoli 1989; Psycharis 1990; Winkler et al. 1995; Psycharis et al. 2000; Konstantinidis and Makris 2005; Papaloizou and Komodromos 2009 among others) and lesser three-dimensional ones (e.g., Papantonopoulos et al. 2002; Mouzakis et al. 2002; Psycharis et al. 2003, 2013; Dasiou et al. 2009a, b). These studies have shown that, due to the domination of rocking, the characteristics of the response are similar to the ones of the simplest case, the rocking of a rigid block. They have also shown that these structures, despite their apparent instability to horizontal loads, are, in general, earthquake resistant (Psycharis et al. 2000), which is also proven from the fact that many classical monuments built in seismic prone areas have survived for almost 2,500 years.

In general, the dynamic behavior of ancient monuments is highly nonlinear and complicated. The abovementioned extensive numerical and experimental investigations have shown that such structures do not possess natural modes in the classical sense and the period of free vibrations is amplitude dependent. During a strong earthquake the response alternates between different "modes" of vibration, each one being governed by a different set of equations of motion. As a result, the response is highly nonlinear. An example of this nonlinearity is that a column may collapse under a certain earthquake motion and be stable under the same excitation magnified by a value greater than one.

In addition, the response is very sensitive to even trivial changes of the parameters of the system or the excitation. This was verified during experiments, since "identical" experiments produced significantly different results in some cases. The sensitivity of the dynamic behavior was also evident in the numerical analyses, in which trivial changes in the excitation or the system parameters changed the response significantly. Another effect of the response sensitivity is the significant out-of-plane displacements observed for purely planar excitations: in some experiments, the deformation in the direction normal to the plane of the excitation was of the same order of magnitude with the principal deformation.

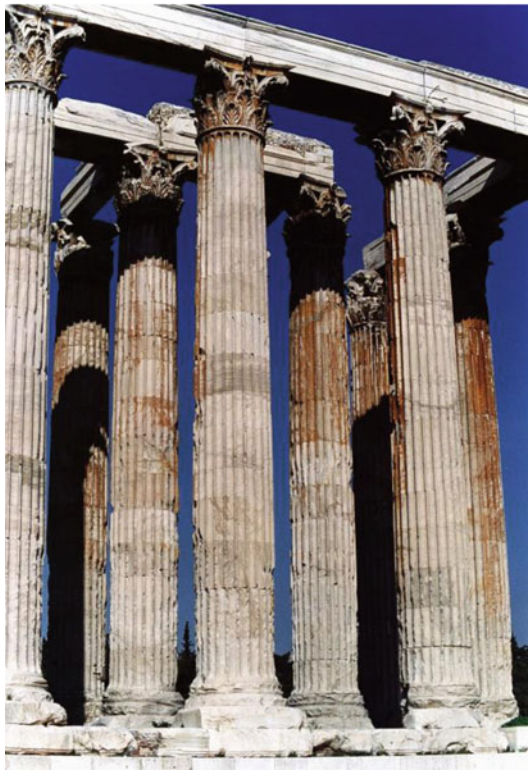

Ancient Monuments Under Seismic Actions: Modeling and Analysis, Fig. 1 SE corner of the Olympieion of Athens, Greece

The vulnerability of classical monuments to earthquakes depends on two main parameters: (i) the predominant period of the ground motion and (ii) the size of the structure. The period of the excitation affects significantly the response and the risk of collapse, with low-frequency earthquakes being much more dangerous than high-frequency ones. In the first case, the response is characterized by intensive rocking, while in the latter rocking is usually restricted to small values, but significant sliding of the drums occurs, especially at the upper part of the structure. In this sense, near field ground motions, which contain long-period directivity pulses, might bring these structures to collapse. The size of the structure is another important parameter, with bulkier structures being much more stable than smaller ones with the same aspect ratio of dimensions.

Despite their apparent instability, classical monuments without significant damages are not vulnerable to usual earthquake motions. However, collapse can occur much easier if imperfections are present, as cutoff of drums, displaced drums, inclined columns due to foundation failure, etc. Such imperfections are common in ancient monuments and may endanger the safety of the structure in future earthquakes.

It is evident that the dynamic analysis of classical monuments for earthquake loads is a very important part of the restoration/preservation process. However, it is not an easy task. Due to the complicated response, such analyses can only be performed using powerful computational codes that can account for rocking, sliding, and even complete separation of the individual stones. Additionally, all such analyses are inevitably based on assumptions concerning the material and joint properties, some of which are difficult to evaluate. Therefore, and taking under consideration the sensitivity of the response, one must have in mind that any dynamic analysis of an ancient monument contains a certain amount of doubt. In any case, the earthquake response of ancient monuments does not follow general rules, and each monument deserves a case-by-case investigation that focuses on the specific monument, recognizing its current condition and local seismic hazard.

In this article, the basic features of the dynamic response of multi-drum columns and colonnades are presented, and critical points regarding their modeling and analysis for seismic loads are discussed. First, the important features of the simplest case, the rocking block, are presented. Then, the dynamics of multi-drum columns and groups of columns (colonnades) are discussed, while emphasis is given to the sensitivity of the response to several parameters of the numerical model. Finally, guidelines regarding the proper selection of base motion acceleration time histories to be used in the analyses are presented.

Rocking Response of a Rigid Block

Despite its apparent simplicity, the rocking response of a rigid block sitting on a rigid base

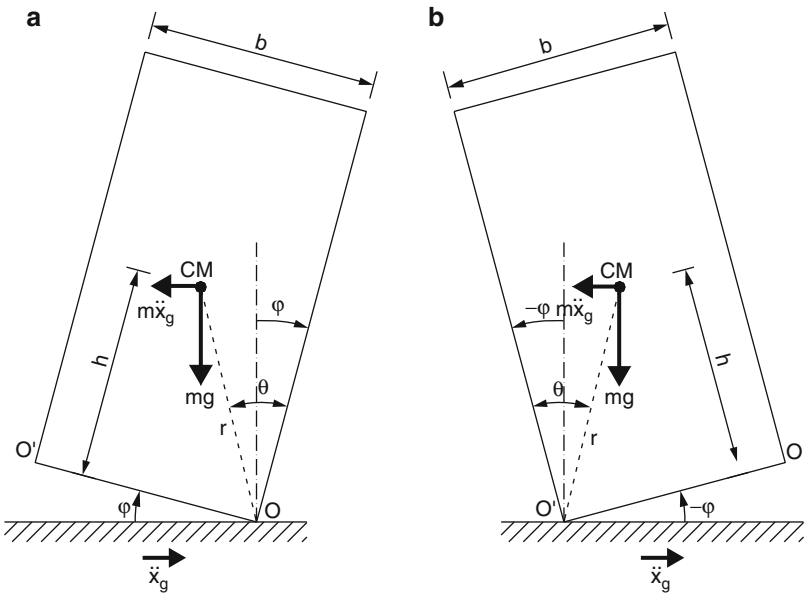

Ancient Monuments Under Seismic Actions: Modeling and Analysis, Fig. 2 Rocking of a rigid block on a rigid base without sliding: (**a**) positive angle of rotation; (**b**) negative angle of rotation

is a complicated problem that has attracted the interest of many researchers in the last century. The basic scope of these investigations has been the estimation of the required intensity of the ground motion to overturn slender bodies during strong earthquakes. The first attempts towards this aim were made by Milne (1885), Milne and Omori (1893) and Kirkpatrick (1927). However, it was Housner (1963) who first tackled the problem systematically, deriving the equations of motion that govern the rocking response of a rigid, freestanding block and examining the overturning risk under simple ground pulses.

Equation of Motion

Let us consider the rocking block shown in Fig. 2. The block and the base are considered rigid, and the coefficient of friction is assumed to be large enough to prevent sliding of the block. In Fig. 2, a rectangular block is shown, with dimensions: width of the base $= b$ and height of the center of mass (CM) from the base $= h$. However, the equations of motion and the basic features of the response that are presented in the following are also valid for any symmetric block in the vertical direction with such dimensions and arbitrary shape.

Assuming that the block has been set into rocking motion, the rotation can either happen about corner O of the base (Fig. 2a), which corresponds to positive angles of rotation (clockwise), or about corner O′ of the base (Fig. 2b), which corresponds to negative angles of rotation (counterclockwise). The distinction between positive and negative angles of rotation is essential, because a different equation governs the motion in each case.

Under a horizontal base excitation $\ddot{x}_g(t)$, the equation of motion can easily be derived by applying Newton's second law for the moments about the pole of rotation (point O for positive rotations, point O′ for negative rotations) and taking under consideration that, apart from the weight, a horizontal inertial force (d' Alembert force) acts at CM, equal to $-m\ddot{x}_g(t)$. Then, the equation of motion can be written in the form:

$$I_O\ddot{\varphi} \pm mgr\,\sin(\theta \mp \varphi) = -m\ddot{x}_g r\,\cos(\theta \mp \varphi) \tag{1}$$

where φ is the rocking angle, m is the mass of the block, r is the distance of CM from the pole of rotation (point O or O′), θ is the slenderness angle defined by $\theta = \tan^{-1} b/(2h)$, I_O is the mass moment of inertia about O or O′, and g is the acceleration of gravity. In this equation, whenever a double sign appears, the upper one

corresponds to $\varphi > 0$ (clockwise rotation) and the lower one to $\varphi < 0$ (counterclockwise rotation).

Introducing the parameter p defined by

$$p^2 = \frac{mgr}{I_O} \tag{2}$$

and using the sgn() function, Eq. 1 can be written in the following general form:

$$I\ddot{\varphi} + p^2 \sin\left[\theta \mathrm{sgn}(\varphi) - \varphi\right] = -p^2 \cos\left[\theta \mathrm{sgn}(\varphi) - \varphi\right] \tag{3}$$

The parameter p is a characteristic frequency of the system. Actually it is equal to the pendulum frequency of the block when hung about the corner of the base.

As mentioned above, Eqs. 1 and 3 are valid for any rigid block with an axis of symmetry about the vertical axis through CM, with I_O being the mass moment of inertia about the corner of the base. In the special case of a homogeneous rectangular block, I_O is given by the following relation:

$$I_O = \frac{m\left[b^2 + (2h)^2\right]}{3} = \frac{4mr^2}{3}, \tag{4}$$

and the characteristic frequency p becomes

$$p = \sqrt{\frac{3g}{4r}} \tag{5}$$

For small angles of rotation ($\varphi << 1$), Eq. 1 can be linearized about the equilibrium position assuming that $\cos\ \varphi \approx 1$ and $\sin\ \varphi \approx \varphi$ and neglecting the second order term containing the product $\varphi \cdot \ddot{x}_g(t)$. Taking under consideration that $r\sin\ \theta = b/2$ and $r\cos\ \theta = h$, the following linearized equation can be derived:

$$I_O\ddot{\varphi} - mgh\varphi = \mp mg\frac{b}{2} - mh\ddot{x}_g \tag{6}$$

For large angles of rotation, when the block is close to the verge of overturning, the linearization should be performed about the point of unstable equilibrium assuming that $|\theta \mp \varphi| << 1$, thus $\cos(\theta \mp \varphi) \approx 1$ and $\sin(\theta \mp \varphi) \approx (\theta \mp \varphi)$. Then, Eq. 1 becomes

$$I_O\ddot{\varphi} - mgr\varphi = \mp mgr\theta - mr\ddot{x}_g \tag{7}$$

It is noted that, as evident from Eqs. 6 and 7, the rocking block corresponds to a system with negative stiffness. Also, for slender blocks with slenderness angle θ less than about 20°, the linearized Eqs. 6 and 7 do not differ significantly, since $\tan\theta \approx \sin\theta \approx \theta$. Analyses of such blocks showed that the linearized equations can predict with acceptable accuracy for engineering purposes the response and the overturning risk of the block.

Impact with the Ground

During rocking, the pole of rotation alternates from point O to O′, or vice versa. The alteration of the pole of rotation takes place when the block hits the ground and is accompanied by energy dissipation due to the change in the velocity of the center of mass which is schematically shown in Fig. 3. Let us assume that the angular velocity before impact is $\dot{\varphi}_1$ and after impact is $\dot{\varphi}_2$. Then, one can write

$$\dot{\varphi}_2 = \varepsilon \cdot \dot{\varphi}_1 \tag{8}$$

where ε is a coefficient of restitution. If we assume that the impact is fully plastic, i.e., that there is no rebound of the block on the base, the value of ε can be calculated applying the principle of conservation of the angular momentum about point O′ before and after impact (Housner 1963), which gives

$$\varepsilon = 1 - \frac{mb^2}{2I_O} \tag{9}$$

Equation 9 implies that the coefficient of restitution ε and the dissipated energy depend solely on the geometry of the block. However, experimental investigation (e.g., Priestley et al. 1978; Aslam et al. 1980) showed that the actual value of ε might be significantly different than the theoretical value of Housner, depending on the

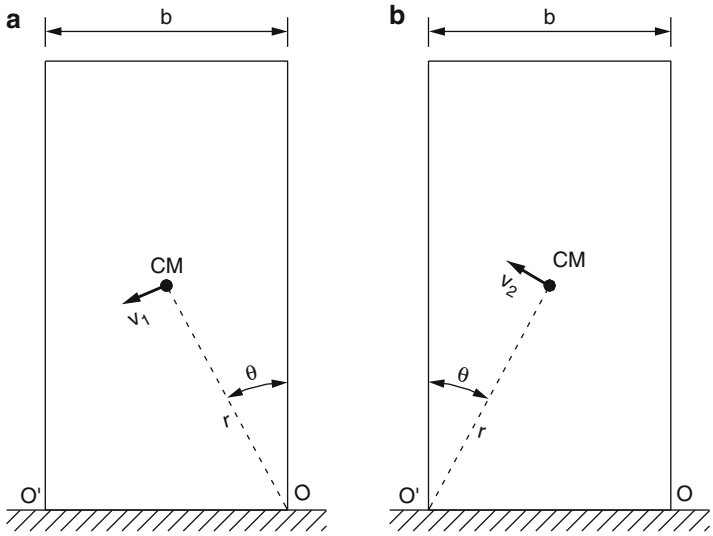

Ancient Monuments Under Seismic Actions: Modeling and Analysis, Fig. 3 Change in the velocity of the CM during impact from positive to negative angles of rotation: (**a**) immediately before impact, when the pole of rotation is point O; (**b**) immediately after impact, when the pole of rotation is point O′

materials of the block and the base. For this reason, in many analyses ε is considered an independent parameter of the problem rather than been calculated from Eq. 9.

Free Vibrations

In case that the block is rocking freely ($\ddot{x}_g(t) = 0$), the linearized equation of motion (7) becomes

$$\ddot{\varphi} - p^2\varphi = \mp p^2\theta \tag{10}$$

where p is given by Eq. 2. Note that p is not the eigenfrequency of the system, since, due to the negative stiffness, rocking blocks do not possess eigenfrequencies in the classical sense. The solution of Eq. 10 is

$$\varphi(t) = A\cosh(pt) + B\sinh(pt) \pm \theta \tag{11}$$

where the coefficients A and B are determined from the initial conditions. For example, for an initial tilt of the block, $\varphi_0 < \theta$, the initial conditions are $\varphi(t = 0) = \varphi_0$ and $\dot{\varphi}\ (t = 0) = 0$, and Eq. 11 becomes

$$\varphi(t) = \theta - (\theta - \varphi_0)\cosh(pt) \tag{12}$$

Equation 12 describes the motion of the block around point O as it comes back to the equilibrium position with positive angles of rotation. When φ becomes zero, the block hits the base and the rotation continues around point O′ with the motion been described by the equation describing negative rotations. According to Eq. 8, the initial angular velocity of this motion is reduced compared with the velocity of the block when it hits the base. Due to the different equations of motion describing each regime of the response, the overall behavior is nonlinear.

If there was not any dissipation of energy during impact, the time elapsed from the angle of maximum tilt (initially equal to φ_0) up to the point when the block reaches the equilibrium position ($\varphi = 0$) would correspond to one fourth of the period T of free vibrations. Therefore, setting $\varphi = 0$ for $t = T/4$ in Eq. 12, the period of free vibrations can be calculated:

$$T = \frac{4}{p}\cosh^{-1}\left(\frac{1}{1 - \varphi_0/\theta}\right) \tag{13}$$

However, in real structures dissipation of energy does occur at each impact. For this reason, the block will attain a reduced maximum tilt after each impact, and the period of free vibrations will continuously decrease. Using Eq. 8,

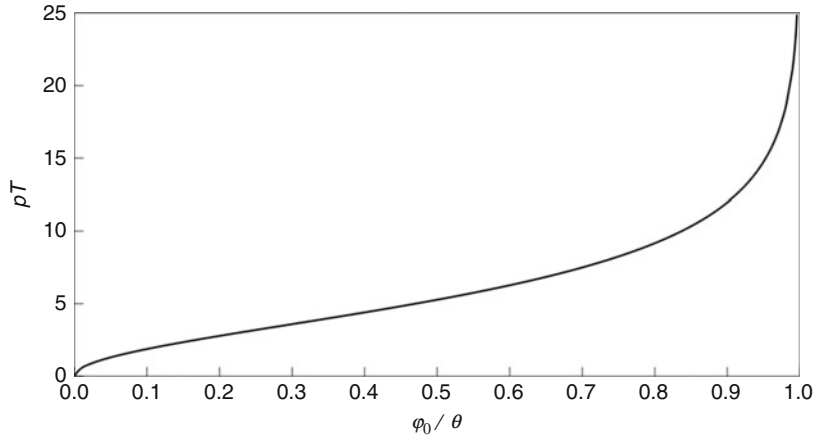

Ancient Monuments Under Seismic Actions: Modeling and Analysis, Fig. 4 Dependence of the period of free vibrations on the normalized initial tilt, φ_0/θ

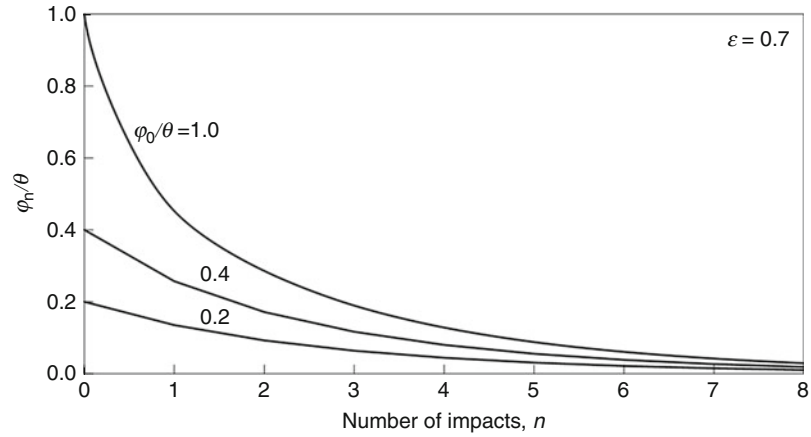

Ancient Monuments Under Seismic Actions: Modeling and Analysis, Fig. 5 Variation of the amplitude of free vibrations with the number of impacts for $\varepsilon = 0.7$

Housner (1963) calculated that the amplitude φ_n of the free vibrations after the n^{th} impact is

$$\frac{\varphi_n}{\theta} = 1 - \sqrt{1 - \varepsilon^n \left[1 - \left(1 - \frac{\varphi_0}{\theta}\right)^2\right]} \qquad (14)$$

The plot of the dimensionless product pT versus the normalized initial tilt angle, φ_0/θ (Eq. 13), is given in Fig. 4, while in Fig. 5 the decrease of the amplitude with the number of impacts is plotted for $\varepsilon = 0.7$ and various values of the normalized initial tilt, φ_0/θ.

Initiation of Rocking Under Earthquake Excitation

Under a seismic ground excitation $\ddot{x}_g$, rocking starts when the base acceleration reaches a critical value, $\left(\ddot{x}_g\right)_{cr}$. At that time, the overturning moment about O or O′ due to the d' Alembert inertial force, $M_A = m\left(\ddot{x}_g\right)_{cr} h$, becomes equal with the restoring moment due to the weight of the block, $M_E = mgb/2$; therefore

$$\left(\ddot{x}_g\right)_{cr} = (\tan\theta) g \qquad (15)$$

For slender blocks ($\theta < 20^\circ$), the critical base acceleration can be approximated by

$$\left(\ddot{x}_g\right)_{cr} = \theta g \qquad (16)$$

If the peak acceleration of the base motion, pga, is smaller than $\left(\ddot{x}_g\right)_{cr}$, the earthquake is not strong enough to initiate rocking of the block.

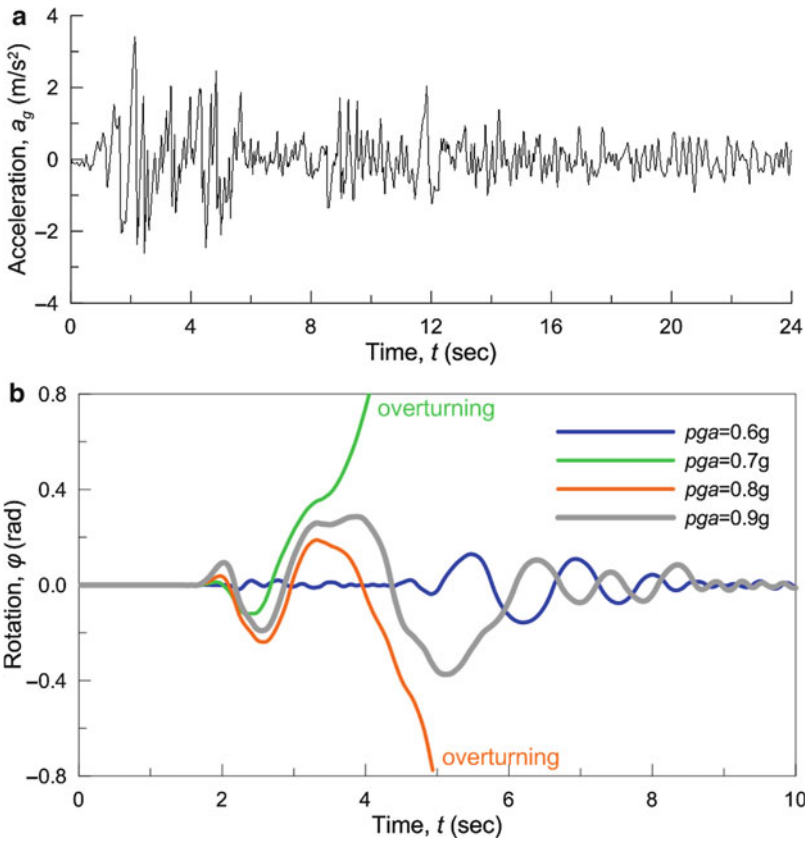

Ancient Monuments Under Seismic Actions: Modeling and Analysis, Fig. 6 (**a**) El Centro (1940) earthquake. (**b**) Rocking response of an orthogonal block of dimensions $b = 0.50$ m, $2\ h = 1.5$ m for the El Centro earthquake amplified to several values of pga (for $\varepsilon = 0.85$)

As evident from Eq. 15, the slenderer the block, the smaller is the required base acceleration to set it into rocking motion.

Nonlinearity and Sensitivity of the Response

As mentioned above, the rocking response is highly nonlinear. This is illustrated in Fig. 6b, in which the time history of the angle of rotation of an orthogonal block with dimensions $b = 0.50$ m, $2\ h = 1.50$ m is shown for the El Centro (1940) earthquake (Fig. 6a) amplified to four different values of the peak ground acceleration: $pga = 0.60$ g, 0.70 g, 0.80 g, and 0.90 g. In all cases, the coefficient of restitution was set to $\varepsilon = 0.85$, which corresponds to Housner's theoretical value according to Eq. 9. It is seen that the response of the block is stable for $pga = 0.60$ g (blue line), while the block overturns in the direction of positive rotations for $pga = 0.70$ g (green line). Increasing the base excitation to $pga = 0.80$ g the block overturns in the opposite direction (negative rotations). However, if the base motion is amplified even more to $pga = 0.90$ g, the response is stable again and overturning does not occur (gray line).

Apart from the nonlinearity, another characteristic of the response is its sensitivity to even trivial changes of the parameters. This sensitivity has been proven by the non-repeatability of the same experiment (Yim and Chopra 1984). In Fig. 7, the sensitivity of the response of the abovementioned block to the value of the coefficient of restitution ε is shown. In this plot, the response of the block is shown for the El Centro record amplified to $pga = 0.50$ g and for three values of the coefficient of restitution: $\varepsilon = 0.85$ (Housner's value), $\varepsilon = 0.87$, and $\varepsilon = 0.88$.

It is seen that the response for $\varepsilon = 0.87$ (green line) is very similar with the one for $\varepsilon = 0.85$

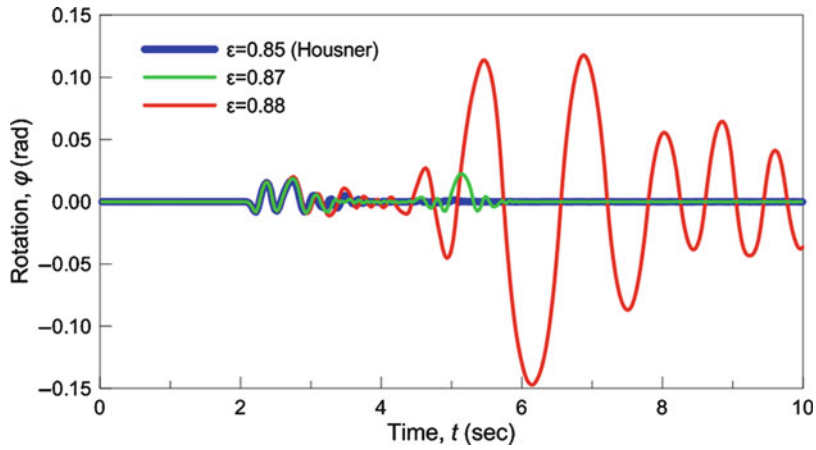

Ancient Monuments Under Seismic Actions: Modeling and Analysis, Fig. 7 Rocking response of an orthogonal block of dimensions $b = 0.50$ m, $2h = 1.5$ m for the El Centro earthquake amplified to $pga = 0.50$ g for various values of the coefficient of restitution ε

(blue line), except for an additional small rocking response of the block around $t = 5$ s, which does not occur for $\varepsilon = 0.85$. However, if we slightly increase the coefficient of restitution to $\varepsilon = 0.88$, intense rocking occurs after $t = 4$ s with significantly larger amplitude than the amplitude in the time interval $2.0 < t < 3.5$ s when all the rocking response takes place for $\varepsilon = 0.85$. It is interesting to notice that this intense rocking for $\varepsilon = 0.88$ occurs after the strong motion of the ground excitation (see Fig. 6a).

It must also be noted that although, in general, a decrease in the value of ε leads to smaller rocking amplitude, due to the larger dissipation of energy during impact, it is also possible that a smaller coefficient of restitution produces larger rocking response (Aslam et al. 1980). This counterintuitive phenomenon is attributed to the nonlinearity of the response.

Main Features of the Rocking Response

Except for the abovementioned nonlinearity and the sensitivity of the response, an important feature of the dynamic behavior is its dependence on the dimensionless quantity pT_p with T_p being the predominant period of the ground motion. Actually, for harmonic excitation (which can be extrapolated to pulse-like ground motions) the normalized response can be expressed solely as a function of four dimensionless terms (Zhang and Makris 2001; Dimitrakopoulos and DeJong 2012):

$$\frac{g \cdot \varphi_{\max}}{pga} = f\left(pT_p, \frac{g \tan\theta}{pga}, \tan\theta, \varepsilon\right) \tag{17}$$

Assuming that ε is known, Eq. 17 implies that:

- For a given base excitation (given pga and T_p), the response depends on the slenderness θ and the characteristic frequency p. The latter is a function of the size of the block. The value of p decreases inversely with the size of the block (e.g., see Eq. 5 for an orthogonal block), measured with the distance r. Therefore, for the same slenderness there is an important size effect on the response. Actually, among two blocks with the same slenderness θ but different size, the smaller one will experience more intense rocking than the larger one. This is shown in Fig. 8, in which the response of two blocks with $\tan\theta = 0.5$ but different size ($b = 0.50$ m for the left block and $b = 1.5$ m for the right) is shown for the same impulse base excitation. It is seen that the small block overturns, while the large one does not.
- For a given block (given θ and p), the rocking response and the overturning risk greatly depend on the predominant period of the base excitation. In general (for details see Zhang and Makris 2001; Dimitrakopoulos and DeJong 2012), the required normalized amplitude of the base acceleration, $pga/(g\tan\theta)$, to cause overturning decreases as the

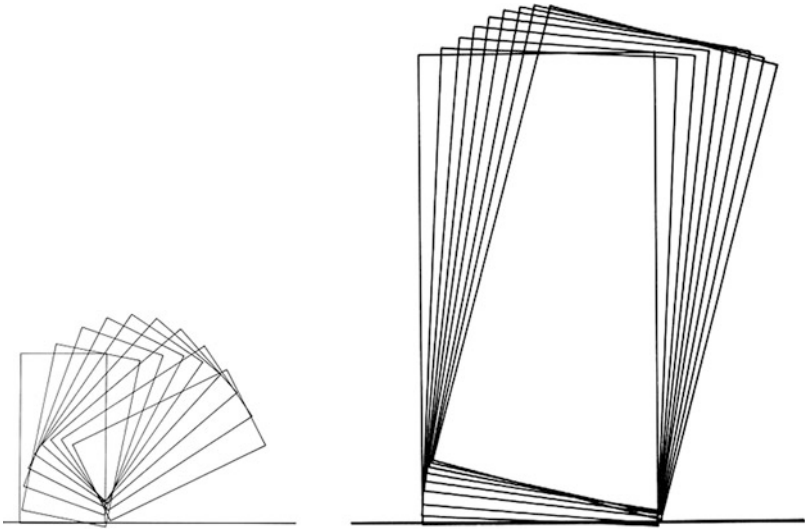

Ancient Monuments Under Seismic Actions: Modeling and Analysis, Fig. 8 Rocking response of two similar orthogonal blocks of the same slenderness ($\tan\theta = 0.5$) and different size (base width $b = 0.50$ m in the *left* block and $b = 1.50$ m in the *right*) for the same impulse base excitation

period T_p increases. In other words, the block is more vulnerable to long-period earthquakes than to high-frequency ones.

It should be noted that the inequality $\varphi > \theta$ is a necessary but not a sufficient condition for overturning to occur, since it is possible that the rocking angle attains temporarily values larger than θ (i.e., $\varphi_{\max} > \theta$) without overturning. Of course such cases are exceptional, since for $\varphi > \theta$ the weight of the block produces an overturning moment instead of a restoring one; thus, the block will not topple only if at the same time a quite large restoring inertial force develops due to the ground motion, capable to reverse this situation and bring the block back to stable state.

Dynamics of Multi-drum Columns and Colonnades

Difficulties and Uncertainties of the Dynamic Analysis

As mentioned in the Introduction, columns of ancient monuments are made of individual structural elements, called drums, which are put one on top of the other without mortar or any other connecting material (Fig. 9). The wooden dowels that were usually placed at the joints between the drums of the columns were aiming at centering the stones during construction and, practically, do not have any effect on the seismic response. In few cases steel connections (dowels) are

Ancient Monuments Under Seismic Actions: Modeling and Analysis, Fig. 9 Photo of a single standing and a fallen column of the Olympieion of Athens, Greece, showing the multi-drum construction of ancient columns

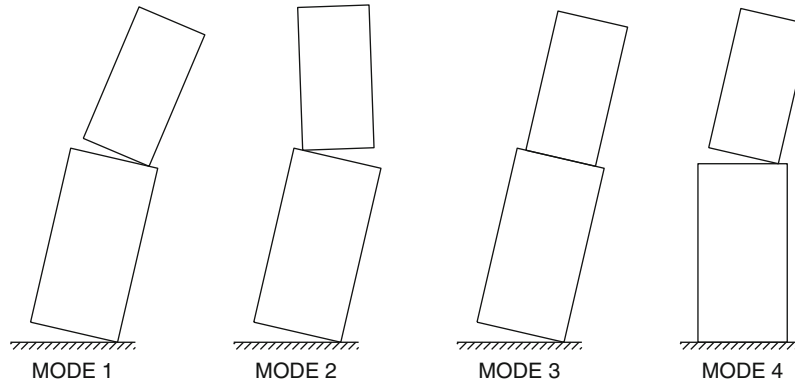

Ancient Monuments Under Seismic Actions: Modeling and Analysis, Fig. 10 The four rocking "modes" of vibration of a two-block assembly (Psycharis 1990)

provided at the joints, which restrict, up to their yielding, sliding but do not affect, in general, rocking.

Due to their spinal construction, ancient columns respond to strong earthquakes with intense rocking and sliding of the drums. In addition, due to the cylindrical shape of the drums, wobbling also occurs during rocking. Usually, rocking dominates the response of multi-drum columns, which, for this reason, is characterized by the strong nonlinearity and the sensitivity discussed in the previous section. In addition, the analysis is extremely difficult and complicated due to the many "modes" of response in which multi-block systems can respond, as it will be discussed in the ensuing.

Furthermore, there is a number of other uncertainties associated with the seismic analysis of ancient monuments: the existing damage, which might be crucial to the stability of the monument to future earthquakes but is difficult to implement in the numerical models; the difficulties in representing accurately the real geometry; and the "vague" properties that must be assigned to the joints in the numerical models. All these issues will be discussed in the following; however, taking into consideration the sensitivity of the rocking response to even small changes in the parameters, one must have in mind that, no matter how accurate an analysis is, there is always an inherent uncertainty in the results.

Analysis of the Dynamic Response

The dynamic response of multi-drum columns, and, in general, of stacks of rigid blocks, is governed by the motion of the stones, which can rock and slide individually or in groups. In case of cylindrical drums, wobbling also occurs during rocking. The dynamic analysis of such systems is a difficult task that can only be treated numerically, since there are many different "*modes*" in which the structure can vibrate. For example, for a system of two blocks, there are four "modes" of rocking vibrations, shown in Fig. 10 (Psycharis 1990). In case of multi-drum columns, the corresponding modes increase exponentially with the number of the drums and, for typical columns with many drums, can be tens of thousands.

It is noted that the term "modes" of vibration is used here to denote the different patterns of the response. These "modes" of response must not be confused with the "eigenmodes" of continuous systems. Rocking structures do not possess natural modes in the classical sense.

Under an earthquake excitation, the response of the column continuously alternates from one "mode" to another (Fig. 11). Each "mode" is governed by a different set of equations of motion, while criteria must be defined for the transition between "modes." It is evident, therefore, that sophisticated numerical codes are needed for the dynamic analysis of ancient monuments, able to take under consideration the sliding of the drums, the opening of the joints (rocking), and even complete separation and recontact of the drums.

In general, numerical models for the analysis of masonry structures may be classified into two major conceptual classes: (i) equivalent

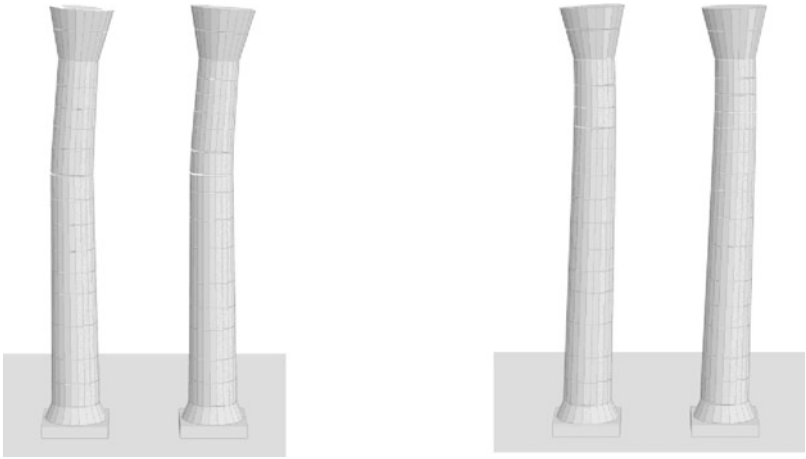

Ancient Monuments Under Seismic Actions: Modeling and Analysis, Fig. 11 Response of two columns of Olympieion of Athens at two different time instances during intense ground shaking. The geometry of the two columns is slightly different (the *left* has 14 drums and the *right* 15) leading to different "modes" of vibration (numerical results obtained with 3DEC software)

continuum models, in which the influence of the joints between blocks is introduced by means of special constitutive relations, and (ii) discontinuous models, in which the joints are represented explicitly, leading to an idealization of the structure model as a block assemblage. The finite element method is the preferred numerical tool for models of the first type, while either finite element implementations with joint elements or discrete element methods are capable of handling the second type.

For stone masonry structures, particularly those composed of multi-drum columns and architraves as ancient monuments, block models are an obvious option. Deformation and failure of these structures is mainly governed by the relative movements between blocks. The blocks can be assumed rigid without significant loss of precision.

One method that has been proven to be very efficient in dealing with such systems is the distinct (or discrete) element method (DEM) introduced by Cundall in the 1970s in the context of rock mechanics and later extended to three-dimensional problems (Cundall 1988). The code 3DEC (Itasca 1998), which was used for most of the analyses presented herein, is based on DEM.

This method provides the means to apply the conceptual model of a masonry structure as a system of blocks. The system deformation is concentrated at the joints, where frictional sliding or complete separation may take place. The method calculates the displacements and the forces in the individual blocks and applies compatibility laws to detect new contacts between the bodies. DEM employs an explicit algorithm for the solution of the equations of motion of the blocks, taking into account large displacements and rotations (Itasca 1998; Papantonopoulos et al. 2002).

Comparison of experimental (shaking table) data concerning the seismic response of a marble drummed replica of a column of the Parthenon in 1:3 scale with the numerical results produced by 3DEC (Papantonopoulos et al. 2002) showed satisfactory agreement in the maximum displacements during the seismic motion and in the residual deformation of the column (Fig. 12). Exact agreement could not be obtained, due to the sensitivity of the dynamic response to even trivial changes in the parameters (Mouzakis et al. 2002; Dasiou et al. 2009a). For example, repetition of the same experiment led to different results in many cases. An example is shown in Fig. 13, in which the recorded response during two similar experiments (EQ14 and EQ15) is depicted, showing significantly different residual deformation. The differences between these "similar" experiments were (i) trivial differences in the initial geometry of the column due to slightly different (not visible) relocation of the drums at their initial position and (ii) small difference (less than 2 %) in the shaking table motion. It is interesting to note that the numerical analyses also

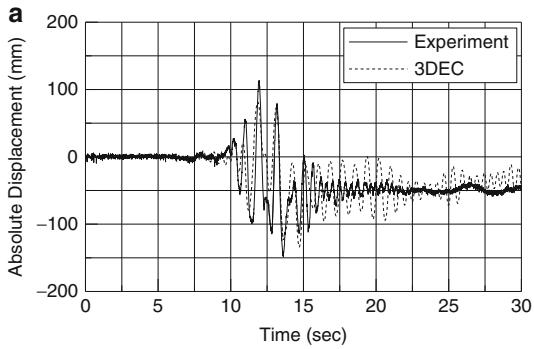

Ancient Monuments Under Seismic Actions: Modeling and Analysis, Fig. 12 Comparison of experimental (shaking table) and numerical (3DEC) results concerning the horizontal displacement at the top of the capital of a 1:3 replica of a column of the Parthenon under seismic excitation: (**a**) x-direction; (**b**) y-direction (Papantonopoulos et al. 2002)

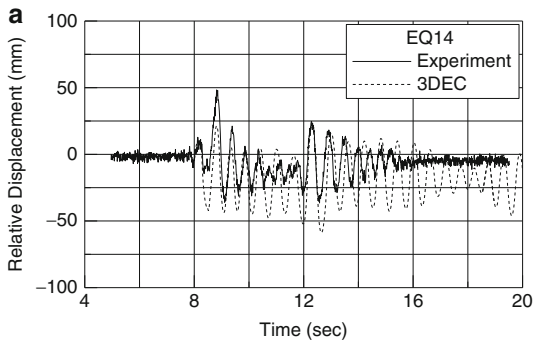

Ancient Monuments Under Seismic Actions: Modeling and Analysis, Fig. 13 Horizontal displacement at the top of the capital of a 1:3 replica of a column of the Parthenon under seismic excitation for the same experiment repeated twice (Papantonopoulos et al. 2002)

showed different response, caused by the abovementioned small difference in the base excitation (the geometry was exactly the same in the numerical models). These comparisons, and additional ones concerning more complicated structural systems comprising of three columns connected with architraves (Dasiou et al. 2009b), showed that DEM, and specifically 3DEC, can reliably predict the seismic response of classical monuments.

It must be emphasized that the application of sophisticated numerical models for the prediction of the seismic response of ancient columns and colonnades requires the knowledge of the value of several parameters which, in general, are not known a priori (this issue is discussed in detail in the following). In this sense, experimental data of the seismic response of multi-drum columns are extremely valuable since they can be used for the calibration of the numerical models.

Modeling Aspects

Regardless of the numerical method that will be used for the analysis of the seismic response, assigning values to the parameters of the numerical model is not a straightforward procedure. Due to the sensitivity of the response, the parameters of the numerical model and the more or less accurate geometrical representation of the structure can affect the results significantly. For this reason, experimental data are generally needed in order to calibrate these parameters, especially the

ones concerning the properties at the joints. In the following, several critical aspects related to the sensitivity of the response to several parameters are discussed.

Joint Parameters

In the distinct element method, the interaction forces between two blocks are applied at a set of contact points located at the vertex-to-face and the edge-to-edge intersections. These forces depend on the relative displacement between the blocks according to the constitutive model adopted for the joints. In the normal direction, the joint behavior is governed by the normal stiffness coefficient, k_n, which relates the contact stress with the normal contact displacement. No tensile strength is considered, so this spring element is only active in compression. In the shear direction, an elastoplastic stress-displacement law is usually assumed. The elastic range is characterized by the shear stiffness, k_s, while the shear strength is governed by the Coulomb friction coefficient, μ, with no cohesive strength component.

The appropriate values to be assigned to the stiffness coefficients k_n and k_s depend on the material of the drums. Since typical values for various materials are not provided in the literature, the assignment of these values is not easy. If experimental data are available, the coefficients can be calibrated against these data. However, such data are very few and concern specific materials only (usually marble). It is noted that loose contacts at the joints due to deteriorations of the contact surfaces might also affect the results.

One way to overcome this difficulty is to calibrate k_n and k_s so that the natural period of the column for small amplitude oscillations matches the one determined by ambient vibration measurements. It is noted that for low-amplitude vibrations multi-drum columns behave like continuous systems and do possess natural modes. This approach has the advantage that the effect of existing imperfections at the joints can be included in the joint stiffness.

Concerning the coefficient of friction, it varies from a static value μ_s at the initiation of sliding to a lower value, which degrades to the kinetic value μ_k, where $\mu_k \leq \mu_s$. This change in friction depends not only on the normal stresses on the drum interface during sliding but also on the number of reversals and the amount of cumulative slip. A considerable number of laboratory test results on surfaces of limestone and marble specimens of different roughness can be found in literature. Although the test procedures differ, the evidence is that, with increasing normal stress σ_n, the static friction coefficient increases, while the difference $(\mu_s - \mu_k)$ decreases. This means that, other things being equal, it is easier for drums to slide in the upper parts of a multi-drum column than near its pedestal and also that, once sliding begins, the drop of the static coefficient μ_s to the residual value of μ_k may lead to larger and more rapid displacement in the upper parts than at lower levels of the shaft.

The proper assessment of the joint parameters is essential for the analysis, since they affect the response significantly. An example of the effect of the value of k_n and k_s on the response of a six-drum column with a two-piece capital is illustrated in Fig. 14 for three different combinations of the normal and shear coefficients (Toumbakari and Psycharis 2010). It is evident that the values of k_n and k_s affect both the amplitude of the response and the residual deformation of the column.

Significant might also be the effect of the coefficient of friction. An example is shown in Fig. 15 for the column of Olympieion of Athens (the existing dowels at the joints were not considered in this analysis) under a strong earthquake motion. Three values of the coefficient of friction were examined: $\mu = 0.55$, 0.75, and 1.05. It is noted that the typical value of μ for marble is about 0.70–0.75; thus, the value $\mu = 0.55$ is considered rather low, while the value $\mu = 1.05$ is unrealistically high. It is seen that the value of the coefficient of friction affected mainly the response and the residual dislocation of the drums at the upper part of the column, where the developed accelerations were large enough to initiate sliding.

Damping

The dissipation of energy due to sliding is automatically taken under consideration with the

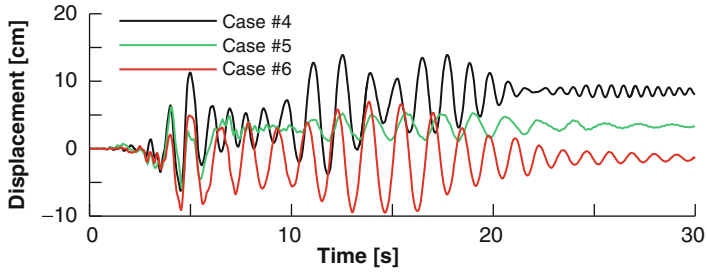

Case	k_n [Pa/m]	k_s [Pa/m]
4	$5x10^9$	$1x10^9$
5	$0.5x10^9$	$0.1x10^9$
6	$1x10^9$	$0.2x10^9$

Ancient Monuments Under Seismic Actions: Modeling and Analysis, Fig. 14 Time histories of the displacement at the top of the capital of a freestanding column for three different sets of the joint stiffness (Toumbakari and Psycharis 2010)

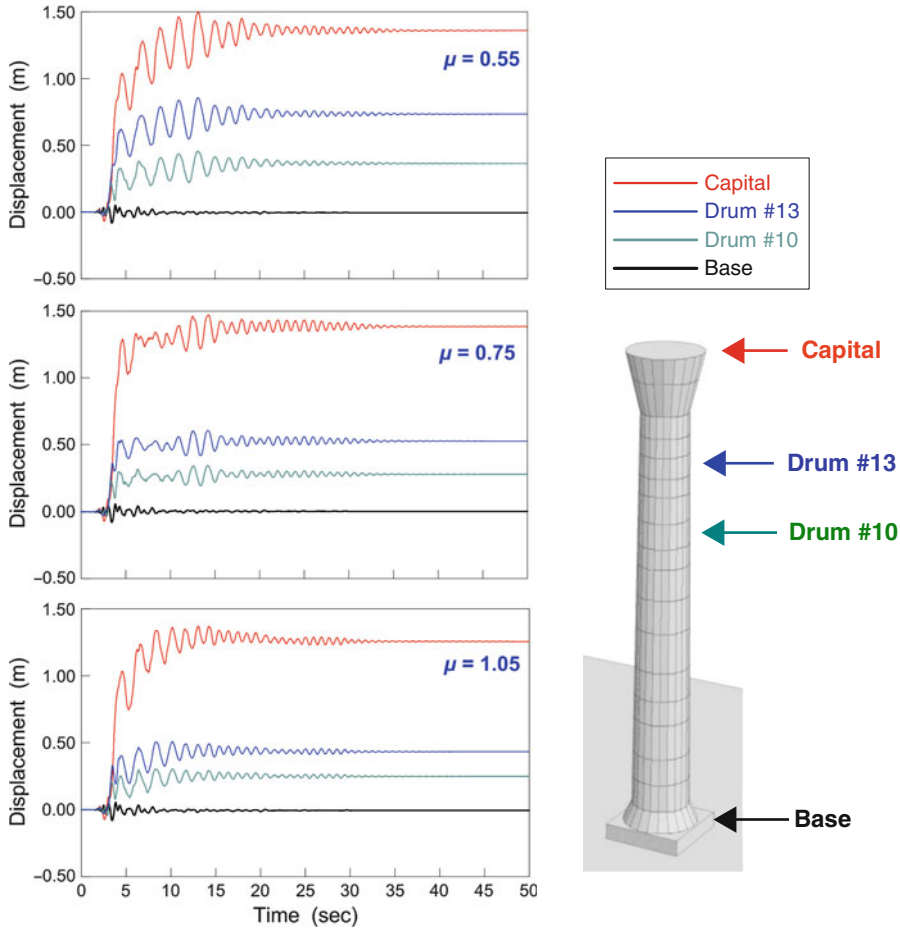

Ancient Monuments Under Seismic Actions: Modeling and Analysis, Fig. 15 Time histories of the displacement at various positions along the height of a freestanding column for three different values of the coefficient of friction

elastoplastic model of the shear stiffness. However, since elastic properties are assumed at the joints, extra damping must be introduced to the numerical model to account for the dissipation of energy due to the impacts between drums during rocking.

Shaking table experiments on multi-drum columns showed very low attenuation. These results

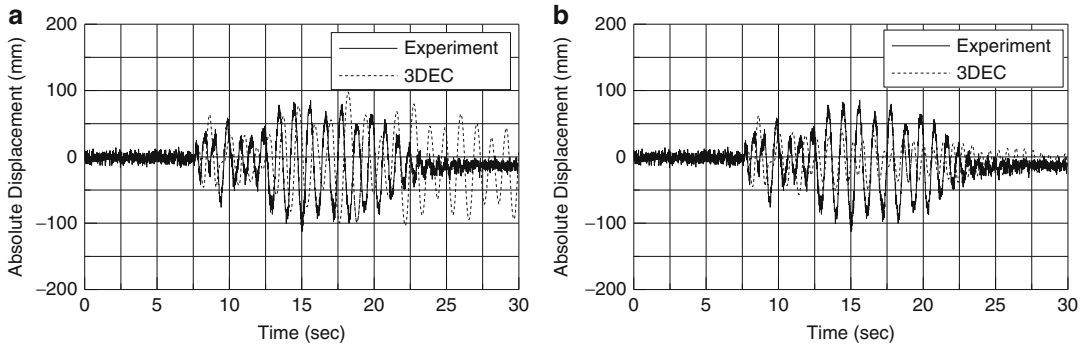

Ancient Monuments Under Seismic Actions: Modeling and Analysis, Fig. 16 Comparison of numerical results with experimental data for (**a**) zero damping and (**b**) 0.5 % stiffness-proportional damping (Papantonopoulos et al. 2002)

lead to the conclusion that, to be conservative, the numerical simulations should be performed with very low or even zero damping, at least during the strong shaking. This is illustrated in Fig. 16, in which the numerical results for zero damping and 0.5 % stiffness-proportional damping are compared with experimental data (Papantonopoulos et al. 2002). It is seen that the introduction of even a small value of damping decreased unrealistically the amplitude during the strong shaking. However, it is necessary to introduce some damping towards the tail of the response in order to attenuate the free vibrations and be able to calculate the residual deformation of the column.

In general, whenever damping is used it is preferable to use the stiffness-proportional component of Rayleigh damping. However, explicit time-stepping algorithms, such as the one in 3DEC, require rather small time steps if stiffness-proportional damping is used. Thus, in order to avoid the increase in the computational effort, only the mass proportional component of Rayleigh damping can be adopted, with a low value though.

Required Accuracy of the Geometric Representation

One question that arises in conducting numerical analyses of ancient monuments is how accurately the model must represent the actual geometry. As a general rule, the geometry should be implemented as accurately as possible, due to the sensitivity of the response. However, exact modeling is practically impossible, due to the complicated geometry of the architectural details of the columns and the random shape of existing damage. In some cases, even the gross geometry (number and dimensions of drums) might not be easy to implement due to lack of information, since, in most monuments, the height of each drum and sometimes even the number of the drums of the columns are not constant (see Fig. 9). This happens because drums were made of marble of superior quality and the height of each drum depended on the available marble pieces, as ancient builders were trying to avoid any unnecessary loss of material.

In addition, numerical models containing large number of blocks might require extremely high computational time; thus, it might be desirable to simplify the model as much as possible.

An example of the effect of the number of drums considered in the analysis on the response of a column with a statue on top is given in Fig. 17 (Ambraseys and Psycharis 2011). In this case, the investigation concerned the risk of toppling of the statue. The column consisted of 15 drums, but analyses were also performed for columns of 5 drums, 30 drums, and 60 drums (see top of Fig. 17). In Fig. 17, the uplift of one corner of the statue is shown. It is seen that the response varied in each case while the statue overturned only in the case of the column with 15 drums.

It is evident therefore that the geometry must be implemented as accurately as possible in order to reach correct conclusions. However, if only gross results are sought, it might be adequate to

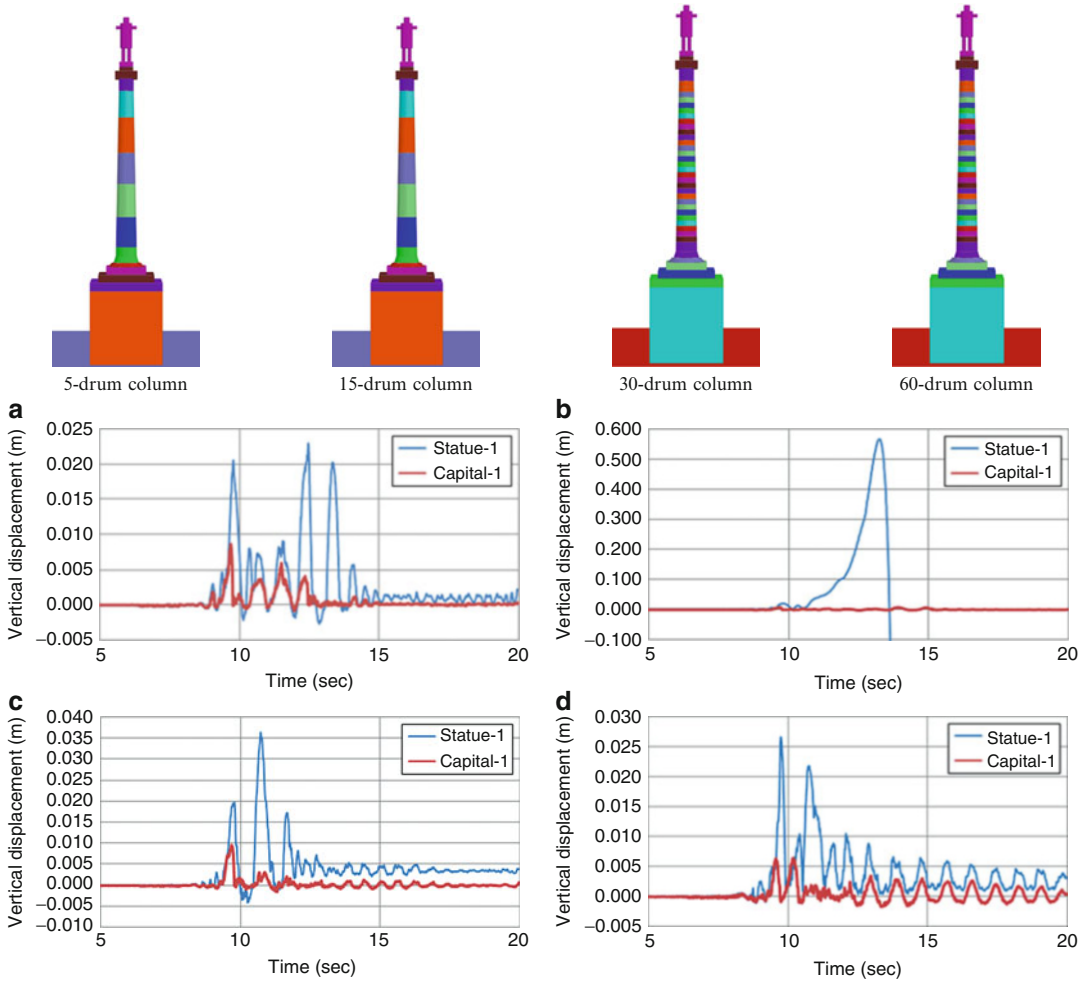

Ancient Monuments Under Seismic Actions: Modeling and Analysis, Fig. 17 Time histories of the vertical displacement of corner 1 of the base of the statue (*blue line*) and the capital (*red line*): (**a**) 5-drum column, (**b**) 15-drum column, (**c**) 30-drum column, and (**d**) 60-drum column. Overturning of the statue occurs only in case (**b**) (Ambraseys and Psycharis 2011)

apply very simple geometries, which can be analyzed much easier. An example is given in Fig. 18, in which the required amplitude of a harmonic excitation to cause overturning versus the period of the excitation (stability threshold) is shown for (a) the column of the temple of Zeus at Nemea, Greece, and (b) the column of the temple of Apollo at Bassae, Greece (Psycharis et al. 2000). The results obtained for the actual geometry of the multi-block columns are compared with the ones for the equivalent single-block columns, i.e., the monolithic columns with the same overall dimensions with the original columns. It is seen that the very simple single-block representation could predict with acceptable accuracy the overturning risk of the columns and thus it could be used as a first-order approximation within a decision making procedure.

Representation of Existing Damage

In their current condition, ruins of ancient structures present many different types of damage. Most common are missing pieces (cutoffs) that reduce the horizontal sections in contact, foundation problems resulting in tilting of the columns,

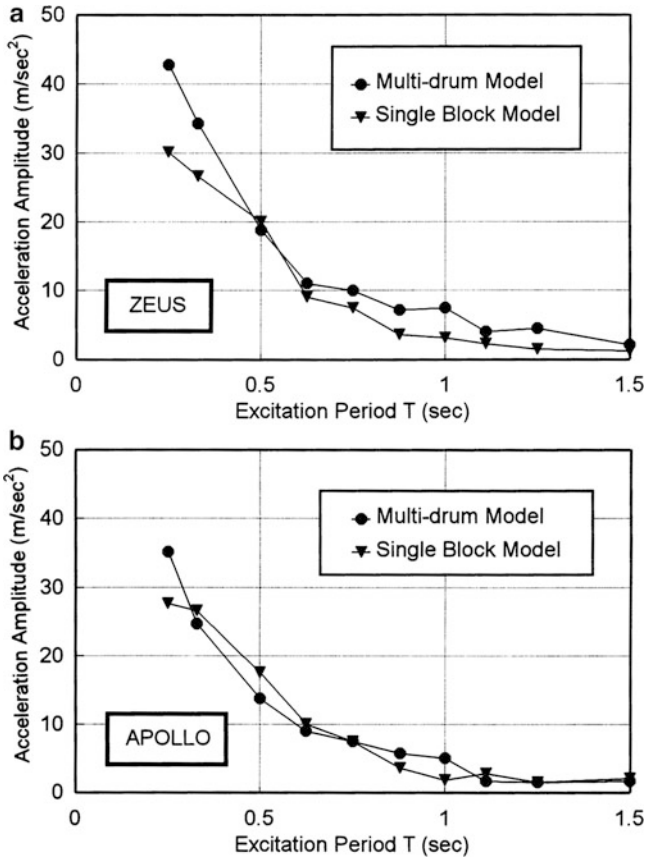

Ancient Monuments Under Seismic Actions: Modeling and Analysis, Fig. 18 Comparison of the stability threshold for the overturning of the multi-drum column and the equivalent single-block column: (**a**) column of the temple of Zeus; (**b**) column the temple of Apollo (Psycharis et al. 2000)

dislocated drums from previous earthquakes, and cracks in the structural elements that in some cases split the block in two. Such imperfections affect significantly the stability of the columns which, thus, are much more vulnerable to earthquake excitations compared with the original intact structures. Therefore, the abovementioned impressive stability of ancient monuments against earthquakes might not be a valid assumption any more, if significant damage is present.

An example of the effect of existing imperfections on the stability of ancient columns is shown in Fig. 19 for the column of the Parthenon in Athens (Psycharis et al. 2003). The maximum permanent displacement of the column is plotted versus the *pga* of the ground motion, and it is seen that the presence of the imperfections shown in the left drawing of Fig. 19 leads to larger displacements and significantly earlier collapse.

It is evident therefore that the damage that can be observed today in the monuments must be implemented in the numerical models. It should be mentioned, however, that this is not an easy task for several reasons: (i) because the existing damage has not always been mapped in the required detail, (ii) because the shape of missing pieces is irregular and very difficult to be modeled accurately, and (iii) because certain types of damage, as cracks in the stone blocks, are either unknown or impossible to take under consideration.

Modeling of Clamps and Dowels

In ancient monuments, iron clamps and dowels exist between the beams of architraves and the stones of walls. In columns, iron dowels were rarely put at the joints, connecting adjacent drums. In such cases, these connectors must be included in the numerical models because they

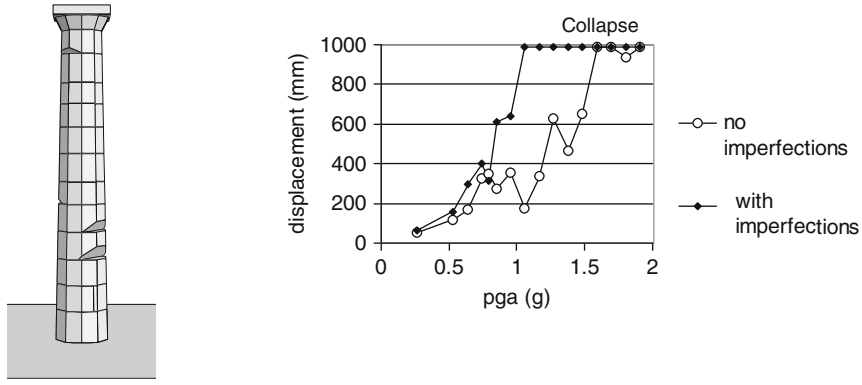

Ancient Monuments Under Seismic Actions: Modeling and Analysis, Fig. 19 Maximum permanent displacements of a column of the Parthenon under the Aigion, Greece (1995), earthquake amplified to several values of *pga* without and with the imperfections shown in the *left* diagram (Psycharis et al. 2003)

Ancient Monuments Under Seismic Actions: Modeling and Analysis, Fig. 20 Displacement at the top of a column of the Olympieion of Athens when the iron dowels at the joints are considered in the analysis (*red line*) and when they are neglected (*blue line*)

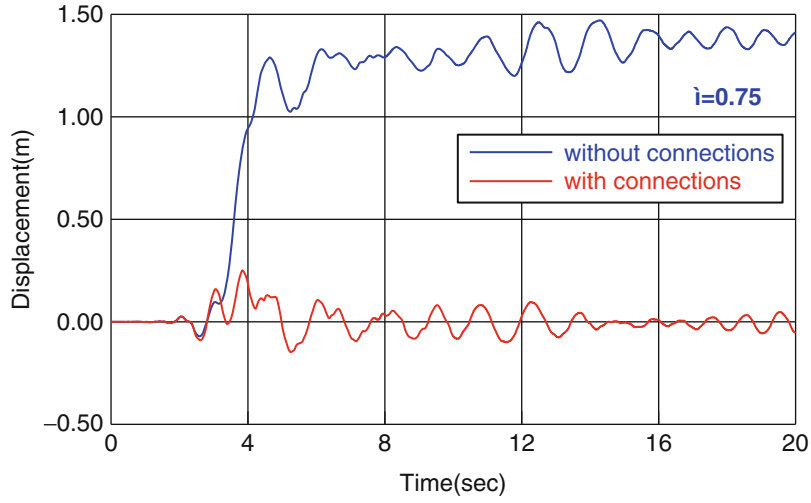

affect the response significantly. An example is shown in Fig. 20, in which the displacement of the capital of the column of the Olympieion of Athens is shown: (a) when the two iron dowels of 10 cm^2 cross section that exist at each joint are considered in the analysis and (b) when they are neglected. The difference in the response of the column, and especially in the amount of permanent deformation, is very large, showing the generally beneficial effect of the dowels on the seismic response. It must be noted, however, that there might be cases in which the prevention of sliding of the upper drums provided by the dowels could be unfavorable to the overall behavior of the column.

In general, dowels should be modeled as nonlinear shear connectors without tensile strength. However, one must have in mind that clamps and dowels were put in inserts carved in the stone blocks and the gap was usually filled with lead. For the dowels placed between the drums of columns, filling the gap with lead was not easy, and, frequently, parts were left without filling. For this reason, it is not usually known whether the dowels are tightly fixed to the drums or small displacements are allowed. This situation introduces an uncertainty in the numerical results, since, if the dowels were loose, the response of the columns would be different.

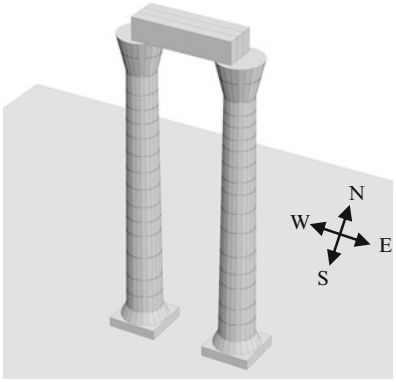

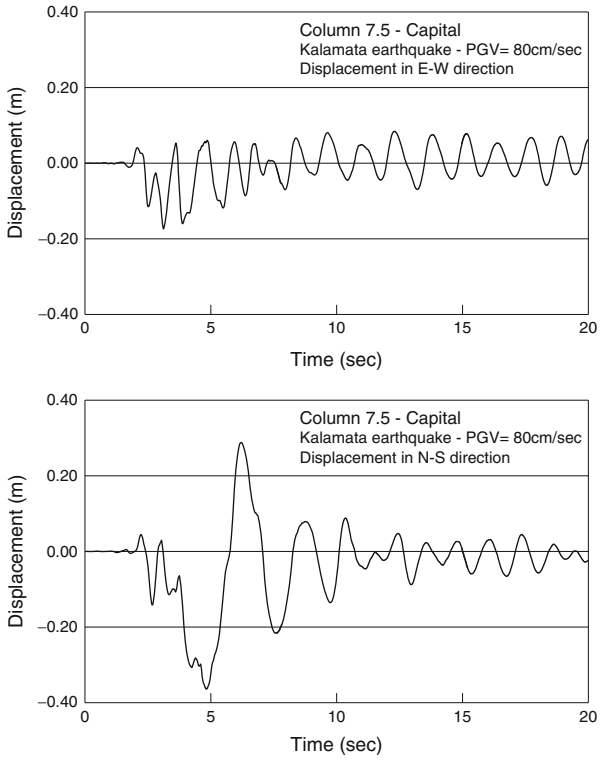

Ancient Monuments Under Seismic Actions: Modeling and Analysis, Fig. 21 Olympieion of Athens: displacement at the top of the E column in the in plane (E–W direction – *top* diagram) and the out of plane (N–S direction – *bottom* diagram)

It must also be noted that, for large rocking angles, it is possible that a dowel disengages from the upper drum. In that case, the dowel might not be able to reinsert in the mortise during the reversed motion due to the wobbling and the sliding of the drums, blocking thus the proper sitting of the upper drum. In most cases, however, shear dowels are inserted several centimeters in the drums, and, thus, it is not probable that rocking can cause their disengagement, even for strong ground motions.

2D Versus 3D Analysis

For freestanding columns, and despite the symmetry of the column about the vertical axis, there is a significant difference in the response between two-dimensional and three-dimensional analysis. Two-dimensional analysis is unable to capture all the aspects of the real response, mainly the rotation of the drums around the vertical axis due to the simultaneous rocking in two normal directions. For cylindrical blocks, the pole of rotation continuously changes its position, moving along the perimeter of the base of the drum (wobbling). It is interesting to note that it was observed during shaking table experiments for purely plane excitation that even small disturbances in the direction normal to the plane of rocking could cause significant amplification of the response in that direction (Papantonopoulos et al. 2002).

In general, comparisons between 2D and 3D analyses show that the 2D approach underestimates the response, predicting greater stability.

For systems involving many columns in line or in corner (colonnades), 3D analyses are evidently necessary. In such cases, it has been observed that the end column of each row suffers significant out-of-plane deformation which, for strong earthquake motions, might be significantly larger than the in-plane one. An example is shown in Fig. 21 for a set of two columns of the

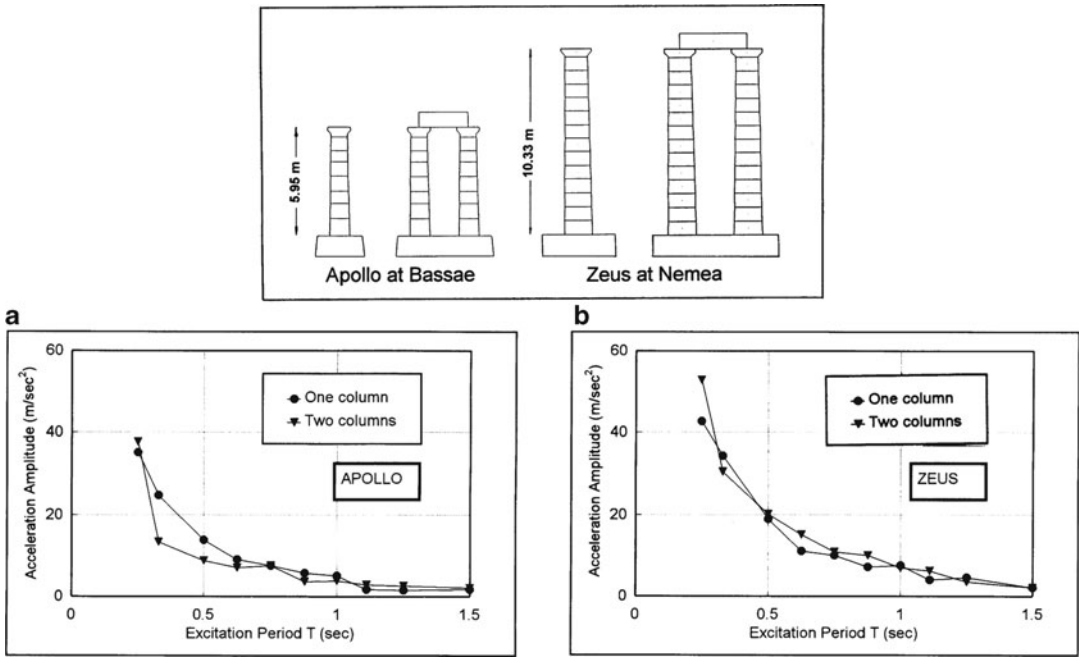

Ancient Monuments Under Seismic Actions: Modeling and Analysis, Fig. 22 Stability threshold for the collapse of the freestanding column and the set of two columns under harmonic excitations: (**a**) columns of the temple of Apollo; (**b**) columns of the temple of Zeus (Psycharis et al. 2000)

Olympieion of Athens connected with an architrave. Under a three-dimensional earthquake excitation, the displacement at the top of the east column was much larger in the out-of-plane direction (bottom diagram) than in the in-plane one (top diagram).

Size Effect

Similarly to the single rocking block (see section "Main Features of the Rocking Response"), the size of ancient monuments affects their dynamic response and their vulnerability to earthquakes, with larger structures being more stable than smaller ones. This is shown in Fig. 22, in which the minimum required acceleration amplitude of a harmonic excitation of varying period to cause collapse (stability threshold) is shown for two cases: (a) the columns of the temple of Apollo at Bassae, Greece, of height 5.95 m and (b) the columns of the temple of Zeus at Nemea, Greece, of height 10.33 m (Psycharis et al. 2000). Results are given for the freestanding column and the set of two columns. It is seen that, for the same period of excitation, significantly larger acceleration is needed to overturn the larger columns of Zeus compared with the smaller columns of Apollo.

Another interesting observation is that the stability threshold of each monument was similar for the freestanding column and the set of two columns. This means that restoration of fallen architraves does not necessarily lead to enhanced stability of the monument against future earthquakes. Figure 22 shows that such restoration of the architraves might be favorable or unfavorable depending on the characteristics of the structure: in the case of Apollo, it was generally unfavorable; in the case of Zeus, it was generally favorable.

It should be mentioned that the above observation concerns the in-plane collapse of the columns (2D analyses). However, shaking table tests on sets of columns connected with architraves in line or in corner have shown that the architrave beams are the most vulnerable parts of monuments, as they are the first pieces that fall down

(in the out-of-plane direction). The collapse of the architraves endangers the stability of the whole monument, since it is possible that they hit the columns during their fall.

Selection of Ground Motions

The earthquake response of ancient monuments is dominated by the rocking of the drums of the columns. As mentioned in section "Main Features of the Rocking Response," rocking is greatly affected by the predominant period of the excitation. It is evident, therefore, that the vulnerability of a monument depends on the frequency content of the ground motion, with long-period earthquakes being much more dangerous than high-frequency ones. This is shown in Fig. 22, in which the stability threshold decreased exponentially as the period of excitation increased in all cases. Previous analyses (Psycharis et al. 2000) have shown that low-frequency earthquakes force the structure to respond with intensive rocking, whereas high-frequency ones produce significant sliding of the drums, especially at the upper part of the structure.

It is evident that the choice of the earthquakes that will be used in the analyses is very important, as the dynamic response of multi-drum columns and colonnades and the danger of collapse are sensitive to the energy and frequency content of the time history of the input ground motion. Apart from the abovementioned strong effect of the predominant period of the ground motion, the time sequence of the various phases in the record might also be significant. In this sense, it is essential to constrain the selection of the base excitations to what one may call suitable surrogate ground acceleration time histories that could replicate as closely as possible the time histories of past and anticipated earthquakes.

Records must be chosen from past earthquakes which are associated specifically with the tectonics and the seismicity of each region or with earthquakes from other regions of similar tectonics. They may not be always available or in sufficient numbers, but they should not be selected arbitrarily. The identification of active or potentially active faults, including blind faults, the long-term seismic history of the region and reliable magnitudes as well as regionally representative data on strong ground motions are important parameters that must be considered in this choice. Among the important characteristics of ground motion, time histories to be used in 3D numerical analyses are their maximum velocity and associated period as well as the directivity effects which will be present depending on the proximity of the monuments to a potentially active fault.

From the geological point of view, three independent source parameters are required to describe an earthquake: the fault dimension, the static moment M_0, and either the mean stress or energy released by faulting or strain energy change. For sites close to the causative fault, the ground motions will show pronounced directivity effects in their ground velocity and displacements. These will appear as long-period amplitude pulses linearly related to the seismic moment. Additionally, the effect of the source mechanism on directivity will be that ground accelerations due to strike-slip faulting will be larger than those due to normal faulting, while ground velocities and displacements will be larger for thrust faulting compared with normal earthquakes.

It is evident, therefore, that the choice of which time histories to include and which to exclude in order to constrain ground motions is an important decision. There is a balance to be struck between being not restrictive enough in the time histories used, leading to unreliable results and hence predictions due to errors and uncertainties, and being too restrictive, which leads to a too small set of time histories and hence nonconclusive results.

Summary

In this chapter the main characteristics of the response of ancient monuments to earthquakes and the difficulties and uncertainties encountered in the analysis, mainly in what regards the values assigned to the parameters of the numerical

model and the selection of surrogate earthquake motions, are presented and discussed. Based on the results of previous studies, the main features of the response can be summarized as follows:

- Owing to rocking and sliding, the response is nonlinear. The nonlinear nature of the response is pronounced even for the simplest case of a rocking single block. In addition, multi-drum columns can rock in various "modes," which alternate during the response increasing thus the complexity of the problem. The word "mode" denotes the pattern of rocking motion rather than a natural mode in the classical sense, since rocking structures do not possess such modes and periods of oscillation.
- The dynamic behavior is sensitive to even trivial changes in the geometry of the structure or the base-motion characteristics. The sensitivity of the response has been verified experimentally, since "identical" experiments produced significantly different results in some cases. The sensitivity of the response is responsible for the significant out-of-plane motion observed during shaking table experiments for purely planar excitations.
- The vulnerability of the structure greatly depends on the predominant period of the ground motion, with earthquakes containing low-frequency pulses being in general much more dangerous than high-frequency ones. The former force the structure to respond with intensive rocking, whereas the latter produce significant sliding of the drums, especially at the upper part of the structure.
- The size of the structure affects significantly the stability, with bulkier structures being much more stable than smaller ones of the same slenderness.
- Classical monuments are not, in general, vulnerable to earthquakes. However, their stability might have been significantly reduced in the damaged condition that they are found today. Types of damage that might increase their vulnerability to earthquakes include cutoff of drums, displaced drums, inclined columns due to foundation failure, cracks in the stones, etc.

Cross-References

- ▶ Ambient Vibration Testing of Cultural Heritage Structures
- ▶ Archeoseismology
- ▶ Damage to Ancient Buildings from Earthquakes
- ▶ Nonlinear Dynamic Seismic Analysis
- ▶ Seismic Actions due to Near-Fault Ground Motion
- ▶ Seismic Behavior of Ancient Monuments: From Collapse Observation to Permanent Monitoring
- ▶ Seismic Strengthening Strategies for Heritage Structures
- ▶ Seismic Vulnerability Assessment: Masonry Structures
- ▶ Selection of Ground Motions for Response History Analysis
- ▶ Sustained Earthquake Preparedness: Functional, Social, and Cultural Issues

References

Allen RH, Oppenheim IJ, Parker AP, Bielak J (1986) On the dynamic response of rigid body assemblies. Earthquake Eng Struct Dyn 14:861–876

Ambraseys N, Psycharis IN (2011) Earthquake stability of columns and statues. J Earthquake Eng 15:685–710

Aslam M, Godden WG, Scalise DT (1980) Earthquake rocking response of rigid bodies. J Struct Div ASCE 106(ST2):377–392

Cundall PA (1988) Formulation of a three-dimensional distinct element model – part I: a scheme to detect and represent contacts in a system composed of many polyhedral blocks. Int J Rock Mech Min Sci 25:107–116

Dasiou ME, Mouzakis HP, Psycharis IN, Papantonopoulos C, Vayas I (2009a) Experimental investigation of the seismic response of parts of ancient temples. In: Prohitech conference, Rome, 21–24 June 2009

Dasiou ME, Psycharis IN, Vayias I (2009b) Verification of numerical models used for the analysis of ancient temples. In: Prohitech conference, Rome, 21–24 June 2009

Dimitrakopoulos EG, DeJong MJ (2012) Revisiting the rocking block: closed form solutions and similarity laws. Proc R Soc A 468(2144):2294–2318

Housner GW (1963) The behaviour of inverted pendulum structures during earthquakes. Bull Seismol Soc Am 53:403–417

Itasca Consulting Group (1998) 3DEC – universal distinct element code, Minneapolis

Kirkpatrick P (1927) Seismic measurements by the overthrow of columns. Bull Seismol Soc Am 17(2):95–109
Konstantinidis D, Makris N (2005) Seismic response analysis of multidrum classical columns. Earthquake Eng Struct Dyn 34:1243–1270
Milne J (1885) Seismic experiments. Trans Seismol Soc Jpn 8:1–82
Milne J, Omori F (1893) On the overturning and fracturing of brick and columns by horizontally applied motion. Seismol J Jpn 17:59–86
Mouzakis H, Psycharis IN, Papastamatiou DY, Carydis PG, Papantonopoulos C, Zambas C (2002) Experimental investigation of the earthquake response of a model of a marble classical column. Earthquake Eng Struct Dyn 31:1681–1698
Papaloizou L, Komodromos P (2009) Planar investigation of the seismic response of ancient columns and colonnades with epistyles using a custom-made software. Soil Dyn Earthquake Eng 29:1437–1454
Papantonopoulos C, Psycharis IN, Papastamatiou DY, Lemos JV, Mouzakis H (2002) Numerical prediction of the earthquake response of classical columns using the distinct element method. Earthquake Eng Struct Dyn 31:1699–1717
Priestley MJN, Evison RJ, Carr AJ (1978) Seismic response of structures free to rock on their foundation. Bull N Z Natl Soc Earthquake Eng 11(3):141–150
Psycharis IN (1990) Dynamic behaviour of rocking two-block assemblies. Earthquake Eng Struct Dyn 19:555–575
Psycharis IN, Papastamatiou DY, Alexandris AP (2000) Parametric investigation of the stability of classical columns under harmonic and earthquake excitations. Earthquake Eng Struct Dyn 29:1093–1109
Psycharis IN, Lemos JV, Papastamatiou DY, Zambas C, Papantonopoulos C (2003) Numerical study of the seismic behaviour of a part of the Parthenon Pronaos. Earthquake Eng Struct Dyn 32:2063–2084
Psycharis I, Fragiadakis M, Stefanou I (2013) Seismic reliability assessment of classical columns subjected to near-fault ground motions. Earthquake Eng Struct Dyn 42:2061–2079
Sinopoli A (1989) Dynamic analysis of a stone column excited by a sine wave ground motion. Appl Mech Rev Part 2 44:246–255
Toumbakari EE, Psycharis IN (2010) Parametric investigation of the seismic response of a column of the Aphrodite Temple in Amathus, Cyprus. In: 14th European conference on earthquake engineering, Ohrid, 30 Aug 2010–3 Sept 2010
Winkler T, Meguro K, Yamazaki F (1995) Response of rigid body assemblies to dynamic excitation. Earthquake Eng Struct Dyn 24:1389–1408
Yim CS, Chopra AK (1984) Dynamics of structures on two-spring foundation allowed to uplift. J Eng Mech ASCE 110(7):1124–1146
Zhang J, Makris N (2001) Rocking response of free-standing blocks under cycloidal pulses. J Eng Mech ASCE 127:473–483

Archeoseismology

Manuel Sintubin
Department of Earth and Environmental Sciences, Geodynamics and Geofluids Research Group, KU Leuven, Leuven, Belgium

Synonyms

Archeological seismicity; Earthquake archeology; Seismic archeology

Introduction

In 1991 an international conference was held in Athens (Greece), marking the beginning of the modern research field of **archeoseismology**, described as *"the study of ancient earthquakes from the complementary standpoints of their social, cultural, historical and physical effect"* (Stiros and Jones 1996). Besides the term archeoseismology, also the term **seismic archeology** was introduced to emphasize the use of archeological methods in the quest to better understand the effects of earthquakes on historical buildings and archeological remains. Moreover, in analogy with historical seismicity, also the term **archeological seismicity** was suggested.

Archeoseismology can thus be defined as **the interdisciplinary study of ancient earthquakes through evidence in the archeological record, such as destruction layers, structural damage to man-made constructions, cultural piercing features, indications of repairs, abandonment, cultural changes, etc**. Archeoseismology is thus seen as a subdiscipline of paleoseismology with a particular focus on man-made constructions as a potential source of paleoseismological information covering the last few millennia. By doing so, archeoseismology serves objectives proper to seismology and earthquake geology, i.e., parameterizing of earthquakes in an effort to assess the seismic hazard in a region.

Earthquake archeology can be considered as a synonym for archeoseismology. But earthquake archeology can also be seen to serve objectives proper to archeology, i.e., reconstructing human history, in particular attempting to better understand the true impact of earthquakes on human history. The term earthquake archeology can be traced to the Japanese term *jishin kōkogaku*, referring to a research field developed in the mid-1980s in Japan primarily through the initiative of Sangawa Akira, a geomorphologist at the Geological Survey of Japan, focusing on sediment deformation features within archeological contexts (Barnes 2010).

Since the book *Archeoseismology* (Stiros and Jones 1996), a series of special issues of journals has reflected the evolution of the burgeoning discipline over the last two decades towards an ever increasing multidisciplinary discipline (McGuire et al. 2000; Galadini et al. 2006a; Caputo and Pavlides 2008; Sintubin et al. 2010; Silva et al. 2011).

In the current entry, **archeoseismology** is considered as a discipline belonging to the broad research realm of **earthquake sciences**, reflected by a continuum of overlapping and complementary research fields, each focusing a particular source of earthquake data, applying appropriate methods and techniques, and targeting a specific time window. In this respect, archeoseismology bridges the gap between **instrumental** and **historical seismology** on the one side and **paleoseismology** and **earthquake geology** on the other. Archeoseismology focuses on cultural material data spanning the last few millennia. It shares, however, a common goal with the other disciplines, i.e., a better understanding of the earthquake history within a region in an attempt to assess the seismic hazard and mitigate the seismic risk. Most valuable contribution of archeoseismology to seismic hazard assessment is situated in earthquake-prone regions with a long and lasting cultural heritage. Seismic-hazard practitioners are confronted with the problem that the instrumental record is too short (only spanning somewhat over a century) and the historical record too incomplete or even inexistent. By having the potential of determining earthquake activity over millennial time spans, archeoseismology can indeed extend the archive of earthquakes beyond written sources, thus becoming a legitimate and complementary source of seismic-hazard information.

After a short historical note, a summary of the different types of archeological evidence for ancient earthquakes, commonly used in archeoseismology, is given. Subsequently, the strengths, challenges, and pitfalls of archeoseismology are discussed. Some new developments in archeoseismology will be introduced. In conclusion, some issues and perspectives in archeoseismology are presented.

A Historical Note

In the first volume of the *Palace of Minos*, published in 1921 (Evans 1921), Sir Arthur Evans did not mention earthquakes as a possible cause for the destructions observed during excavation works at the Bronze Age, Minoan site of Knossos (Crete, Greece). In the second volume of the *Palace of Minos*, published in 1928 (Evans 1928), though, tectonic earthquakes became the primary destructive agent, not only leaving a clear marker horizons in the archeological stratigraphy but also causing cultural change as evidenced by discontinuities in ceramic style and architecture. So, what happened in those 7 years that completely changed Evans' thinking?

On 20 April 1922, during the excavation of the *"House of the Sacrificed Oxen"* and the *"House of the Fallen Blocks"* (Fig. 1) at Knossos, Evans experienced an earthquake, leading him to believe that earthquakes of tectonic nature (so not related to the volcanic activity of the Thera/Santorini volcano) may very well have caused damage to the Minoan buildings during the Bronze Age. But only after experiencing the dramatic earthquake that hit the Eastern Mediterranean on 26 June 1926 and caused severe damage in the region of Heraklion, Sir Arthur Evans got convinced that earthquakes are the primary destructive agent responsible for the main stages of destruction observed at Knossos. He developed a seismic archeological stratigraphy,

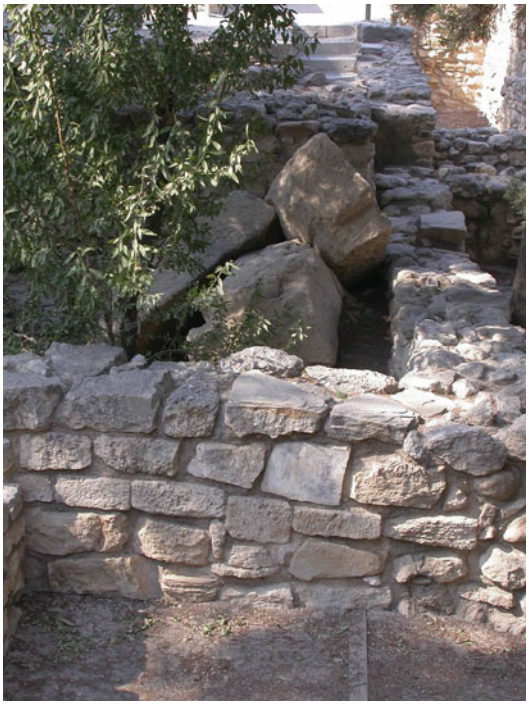

Archeoseismology, Fig. 1 The *"House of the Fallen Blocks"* at Knossos, of which the particular context of the massive blocks inspired Sir Arthur Evans that a major earthquake may have been responsible for this damage (cf. Sintubin 2011) © Sintubin

marked with a number of earthquake-related destruction horizons (cf. Jusseret and Sintubin 2013). This work of Sir Arthur Evans can thus indeed be seen as the earliest attempt to introduce earthquakes into archeological contexts.

Evans' ideas inspired a number of his colleagues around the Eastern Mediterranean, in particular Claude Schaeffer, excavator of the Bronze Age sites of Ugarit (Syria) and Enkomi (Cyprus). In his book *Stratigraphie Comparée et Chronologie de l'Asie Occidentale*, published in 1948 (Schaeffer 1948), Claude Schaeffer went even one step further by correlating archeological destruction layers attributed to earthquakes between Bronze Age archeological sites throughout the Asia Minor, the Caucasus, and the Middle East, setting the stage for the myths of regional earthquake catastrophes. Incorporating modern concepts of seismic storms, the myth of the Late Bronze Age seismic paroxysm around 1200 BC endured to date (e.g., Nur and Cline 2000).

Ever since, earthquakes became all too easy a "deus ex machina" to explain to otherwise inexplicable at archeological sites, eventually even to add drama to a site's history. While skeptical earthquake scientists portrayed this indiscriminate use of earthquakes as neocatastrophism, advocates see the earthquake hypothesis as the simplest solution, referring to Occam's razor. Therefore, many earthquake scientists still question the basic principles and practices of archeoseismology.

Ancient Earthquakes

Earthquakes that form the subject of archeoseismology are defined as **ancient earthquakes**, i.e., pre-instrumental earthquakes that can only be identified through indirect evidence in the archeological record (e.g., Sagalassos earthquake; cf. Similox-Tohon et al. 2005). Earthquakes that are documented in the historical record may be included if they left marks in the archeological record.

Earthquakes can basically be subdivided in **instrumental** and **pre-** or **noninstrumental**; the former are instrumentally recorded by seismometers, while the latter are indirectly recorded. The instrumental record covers a little more than a century since the first modern seismometers were designed in the 1890s.

Of **instrumentally recorded earthquakes**, all physical parameters (e.g., magnitude, seismic source, epicenter, duration, intensity distribution, sequence of aftershocks) can be derived. These earthquakes are the main subject of **seismology**. Recent earthquakes can have a major impact on cultural heritage (e.g., 2003 Bam M_W 6.6 earthquake), historical buildings (e.g., 2009 L'Aquila M_W 6.3 earthquake), and/or archeological remains. The latter earthquakes, affecting archeological remains, are though excluded from the field of archeoseismology.

Pre-or **noninstrumental earthquakes** are only indirectly recorded, in the historical, archeological, and/or geological record. Earthquake parameters that can be derived from these records concern macroseismological parameters, such as intensity, macroseismic epicenter, date, etc.

Historical earthquakes are pre-instrumental earthquakes of which information can be found in all types of historical – written – records (e.g., reports, epigraphy, epitaphs). All this historical information is compiled into earthquake catalogues. Archeoseismology can complement the knowledge with respect to historical earthquakes, when the evidence of specific, well-documented, historical earthquakes (e.g., 365 AD Crete earthquake) on archeological sites is searched for. Also, paleoseismology can add information to better constrain the macroseismological parameters of historical earthquakes.

Prehistorical earthquakes are earthquakes that have no historical record. They can both be ancient earthquakes or paleo-earthquakes.

Paleo-earthquakes, finally, can be interpreted widely, incorporating all prehistorical earthquakes, and even historical earthquakes. In this respect, it becomes synonymous to pre-instrumental earthquakes. One can opt to narrow down the definition of paleo-earthquakes to earthquakes of which evidence is only found in the geological and/or geomorphological record, being subject of **paleoseismology**. These earthquakes are also called **fossil earthquakes**.

Archeological Evidence for Ancient Earthquakes

Archeoseismology calls upon archeological material, ranging from a single occupation horizon within a Holocene stratigraphical context (e.g., Tuttle and Schweig 1995) to a widespread archeological site with monumental buildings (e.g., Similox-Tohon et al. 2006). Methodological developments in archeoseismology is indeed primarily grafted on archeological work in the Eastern Mediterranean and the Middle East, which depends strongly on identifying structural damage to monumental buildings and other cultural remains at archeological sites (e.g., Stiros 1996).

There are two limiting factors to archeoseismological investigations. The first is related to temporal aspects of the archeological record. On the one hand, the time span of occupancy of a site largely determines the archeoseismological potential of a site (cf. Sintubin and Stewart 2008). It is obvious that the longer the site's occupancy, the higher chances are that a major earthquake has affected the site and left its marks in the archeological record. On the other hand, the archeological record is not evenly distributed through time, to a large extent dependent on socioeconomic, political, and cultural conditions of an ancient society. Secondly, archeoseismological work is limited to archeological sites, which are commonly rather a rare occurrence. There is though a remarkable spatial bias advantageous to archeoseismology, due to a *"fatal attraction"* (Jackson 2006). On the one hand, there appears to be a close relationship between tectonically active environments – thus prone to earthquakes – and ancient civilizations along the southern boundary of the Eurasian Plate (Force and McFadgen 2010). On the other hand, many settlements are founded in seismic landscapes (Michetti and Hancock 1997), thus in the direct proximity of active earthquake faults, as convincingly illustrated by numerous archeological sites throughout the Mediterranean and the Middle East. **Seismic landscapes** are defined as the cumulative geomorphological and stratigraphical effect of signs left on the environment by its past earthquakes over a geologically recent time interval (Michetti and Hancock 1997).

The archeological record can be used in basically three ways to help confront the seismic-hazard threat. First, where archeological relics are displaced, they can be used to find active faults, show in which direction faults slipped during the earthquake(s), and establish comparative fault-slip rates. Second, archeological evidence can date episodes of faulting and shaking. Third, ancient signs of earthquake-related damage, commonly related to ground shaking or ground instabilities (e.g., liquefaction), can be searched for.

Structural Damage Due to Surface Rupturing or Ground Failure

The most obvious and straightforward archeological evidence of fault activity – and thus of earthquakes – are archeological remains that are

Archeoseismology, Fig. 2 The wall of the *Crusader Fortress of Vadum Iacob* (Ateret, Israel) (cf. Marco et al. 1997) is displaced *left* laterally over more than 2 m. The fortress has been built astride the Dead Sea transform plate boundary between the African and Arabian plates © Sintubin

partly displaced due to coseismic surface rupturing on an active fault. As already mentioned, it is definitively not a coincidence that archeological sites are astride active faults.

As cultural piercing features, these **faulted relics** not only serve to identify active faults, but they are also used to determine the type of faulting (normal, reverse, strike slip), the amount of coseismic slip related to a single earthquake, as well as the cumulative fault slip. All these data eventually allow to derive time-averaged fault-slip rates over time spans of centuries to millennia, very comparable to paleoseismological work. The fault-slip rates obtained from an archeological context can subsequently be compared to long-term slip rates from paleoseismological work, enabling the evaluation of potential slip deficits and thus increased seismic hazards.

The most spectacular cases of such faulted relics can be found astride strike-slip faults, in which case there can be no doubt of the tectonic nature of the displacement. Notorious examples are the Crusader Fortress of Vadum Iacob (Israel) (Fig. 2) (cf. Marco et al. 1997) and the Al Harif Roman aqueduct (Syria) (cf. Sbeinati et al. 2010), both located astride the Dead Sea fault, a left-lateral transform plate boundary between the African and Arabian plates. By the way, as long, linear structures, aqueducts are ideal cultural piercing features because chances are they cross more than one fault. Also in extensional settings, giving rise to the typical seismic landscapes of the Mediterranean (from Turkey to Spain), faulted relics are often encountered in archeological sites (Fig. 3) (e.g., Similox-Tohon et al. 2006). In these cases of dip-slip, normal-fault movements,

Archeoseismology, Fig. 3 The mosaic floor of the Roman *Neon Library at Sagalassos* (SW Turkey) has been cut by a normal fault, of which a post-363 AD activity (terminus post quem) can be inferred based on the archeological evidence (cf. Similox-Tohon et al. 2006) © Sintubin

particular caution should be paid to preclude gravitational mass movement that may or may not be seismically triggered (ground failure). Complementary and independent, usually paleoseismological and/or geophysical, evidence to support a tectonic nature of the normal displacement, observed in the faulted relics, is therefore imperative (e.g., Similox-Tohon et al. 2005).

Besides these on-fault effects, numerous off-fault, coseismic ground-failure features can find their way into the archeological record, such as landslides and rockfalls, subsidence and uplift, and liquefaction (see Rodríguez-Pascua et al. 2011 and references therein). The latter sediment-deformation features form the focus of earthquake archeology Japan style (Barnes 2010).

Archeological Destruction Horizons

An **archeological destruction horizon** (destruction layer/destruction deposit) designates a horizon in the archeological stratigraphy showing evidence of sudden destruction caused by human (e.g., war, vandalism) and/or natural agents (e.g., earthquake, storm, flood). These destruction horizons commonly occur on top of "living surfaces," evidenced by, e.g., in situ broken vases (Fig. 4), buried valuable objects, and/or skeletons of victims. Other criteria are, e.g., burned material, charcoal, collapsed architectural debris, and crushed, toppled objects.

The use of destruction horizons in archeoseismology goes back to the original work of Sir Arthur Evans in Minoan Knossos (Bronze Age Crete), inspiring several generations of archeologists who, often too easily

Archeoseismology, Fig. 4 In situ broken vessels, evidencing a collapse on a "living surface," as part of a destruction horizon at the Minoan site of *Sissi* (Crete) that has been attributed to an earthquake in the thirteenth century BC (cf. Jusseret and Sintubin 2012) © J. Driessen

("deus ex machina"), attributed destruction horizons to catastrophic earthquakes. Identifying the true agent, eventually responsible for the destruction horizon, is rarely clear and unambiguous and remains one of the major challenges of archeoseismology.

Destruction horizons, which can with a high degree of certainty be related to ground failure and/or ground shaking caused by an earthquake, are the most appropriate "proxies" for ancient earthquakes in archeological contexts dominated by rubble architecture and associated stratigraphy, such as the Bronze Age civilizations around the Mediterranean and the Harappan civilization in the Indus Valley. In these contexts, no appeal can indeed be made to structural damage evidence on monumental buildings and constructions.

Besides evidencing ancient earthquakes, material (e.g., charcoal) and artifacts (e.g., ceramics, coins) included in the destruction horizons can be used to date episodes of earthquake damage, by means of, e.g., radiocarbon dating, changes in ceramic styles, and numismatics. A major drawback is the temporal resolution of these dating methods with uncertainties ranging from decennia to centuries. On the one hand, this does not allow to pinpoint a destruction horizon to a specific historical earthquake. On the other hand, imprecise age control leads to discrete multiple earthquakes, among which the aftershock sequence of a major earthquake, being amalgamated to "oversized" earthquake catastrophes. Finally, weak time constraints on destruction horizons hamper any reliable territorial correlation of destruction horizons between

Archeoseismology, Fig. 5 Recycling of building material in repair works of a wall at *Susita* (Golan Heights) (cf. Sintubin 2011), possibly after a destructive earthquake © Sintubin

archeological sites, again giving rise to the danger of amalgamating regionally distinct earthquakes.

Other issues concerning destruction horizons are preservation and disturbance. Little is known about the way ancient societies coped with the aftermath of a major earthquake. Earthquake debris may have been cleared from streets and buildings and disposed at particular dumpsites, so that the earthquake destruction horizon is no longer preserved in the archeological record. Valuables and/or victims may have been recovered from the debris, while material may have been reused in rebuilding, leaving behind a highly disturbed earthquake destruction horizon. It is therefore fair to conclude that the visibility of earthquake destruction in the archeological stratigraphy is rather dependent on social factors than on physical parameters (cf. Jusseret and Sintubin 2012).

Finally, other archeological evidences, such as repairs, recycling of building materials (Fig. 5), complete or partial abandonment, and architectural and/or cultural changes, can further contribute to the identification of ancient earthquakes.

Structural Damage Due to Ground Shaking and Ground Motion

A third type of earthquake evidence in the archeological record are typical **strain structures in the building fabric** that are primarily caused by coseismic ground shaking and ground motion. These earthquake-related damage features are most conspicuous on monumental buildings and constructions, such as temples, fountains, theaters, basilicas, pavements, columns, statues, aqueducts, etc.

A first systematic inventory of possible earthquake-related damage typologies has been

introduced by Stiros (1996). Currently all these potential earthquake indicators are compiled in a comprehensive classification of **Earthquake Archeological Effects** (EAEs) (Rodríguez-Pascua et al. 2011), completely based on the guidelines of the Earthquake Environmental Effects (EEEs) that are used in the framework of the macroseismic Environmental Seismic Intensity scale (ESI2007, Michetti et al. 2007). These guidelines prescribe the difference between "primary (direct) effects" and "secondary (indirect) effects." In archeological contexts, the latter effects of which evidence can be found in the archeological record and in particular destruction horizons, reflect the way an ancient community copes with the consequences of an earthquake affecting their settlement. Besides the on-fault (e.g., surface rupturing) and off-fault (e.g., liquefaction) geological effects, the former effects are specifically recorded in strain structures in the building fabric.

Different types of strain structures can, on the one hand, be generated by coseismic ground motion: folded and fractured pavement; shock breakouts in flagstone pavement; tilted, rotated, displaced, and bent walls, etc. On the other hand, other types of strain structures in the building fabric can be generated by coseismic ground shaking: penetrative fractures in masonry walls and columns; rotated, displaced, and ejected masonry blocks in walls; rotated and displaced drums in columns (Fig. 6); dropped keystones in arches (Fig. 7); rotated steps in stairways; collapsed stairways; folded curbs; domino-type collapsed walls and columns; directional collapse of columns; collapsed vaults; impact markings on pavements; dipping broken corners and chipping marks; U-shaped gaps in walls, etc.

The obvious difficulty with these building fabric effects is that it remains very challenging to distinguish between damage caused by an earthquake and damage caused by other destructive physical or human agents, such as natural failure of the foundations, vandalism, or warfare. Moreover, standing or partially standing buildings and constructions at archeological sites in earthquake-prone regions most probably experienced ground shaking from numerous – minor to moderate to major – earthquakes over the life span of the structure, which makes it nearly impossible to attribute specific building fabric effects to a particular earthquake. Working with these damage typologies, possibly indicative of ground shaking, the investigator has to be very cautious not to "overinterpret" the potential earthquake archeological effects. Uncertainties, inherent to any archeologically based earthquake hypothesis, should moreover be assessed properly (cf. Sintubin and Stewart 2008).

Archeoseismology, Fig. 6 Displaced drums of a column in the *Temple of Aphrodite* in the Roman city of *Aphrodisias* (SW Turkey), as a potential earthquake archeological effect © Sintubin

Parameterization of Ancient Earthquakes

Besides the inherent ambiguities and uncertainties of archeological earthquake evidence, primarily resulting from the difficulty to

Archeoseismology, Fig. 7 A dropped keystone in the *Roman Baths at Sagalassos* (SW Turkey), interpreted as a potential earthquake archeological effect (cf. Similox-Tohon et al. 2006) © Sintubin

irrefutably distinguish between damage caused by earthquakes and that caused by other natural agents or human intervention, the main issue archeoseismology is confronted with is the question how earthquake evidence in destruction horizons and/or disturbed buildings can be meaningfully translated into physical earthquake parameters, such as intensity, magnitude, distance to epicenter, date of earthquake, ground acceleration, etc. Ultimately, because the limitations of the archeoseismological record are all too obvious when it comes to claiming its potential role in seismic-hazard studies, it all boils down to the question what the true added value is of archeoseismology.

In Search of a Shared Protocol and Standardized Methodology

Archeoseismology's greatest challenge – and its foremost attraction – remains to date the integration of principles and practices of a very wide range of sciences, from history, anthropology, archeology and sociology, over geology, geomorphology, geophysics, and seismology to architecture and structural engineering. Arguably the principle difficulty in archeoseismology is the lack of a shared protocol and of a rigorous and transparent standardized methodology (cf. Sintubin and Stewart 2008 and references therein).

Through the years, different, primarily qualitative, archeoseismological schemes have been proposed, consisting of points of interest (Karcz and Kafri 1978; Rapp 1986; Nikonov 1988; Stiros 1996), key research questions (Guidoboni 1996), or flow charts (Galadini et al. 2006b) that ought to be considered during excavation works at an archeological site by collaborative teams of seismologists, geologists, archeologists, etc. (see Sintubin and Stewart 2008 for synthetic

overview of archeoseismological schemes). More recently, the comprehensive classification of earthquake archeological effects (EAEs) (Rodríguez-Pascua et al. 2011) pursues the integration of archeoseismological evidence in the framework of the macroseismic Environmental Seismic Intensity scale (ESI2007, Michetti et al. 2007). These efforts to develop a shared protocol, however, are commonly designed from within a single scientific discipline.

Most of these schemes have been grafted onto the archeological work in the Mediterranean and the Middle East, strongly relying on strain structures in the building fabric (e.g., Stiros 1996). More quantitative approaches evaluate the probability of the occurrence of a proposed ancient earthquake by using a feasibility matrix for archeoseismological findings (Hinzen 2005) or assess the degree of certainty to which an archeological site has recorded an ancient earthquake by using a logic-tree formalism (Sintubin and Stewart 2008).

In recent years, a clear shift in perspective, from qualitative to more quantitative and multidisciplinary approaches, trying to integrate earthquake evidence from different perspectives (e.g., archeoseismology, geophysics, paleoseismology, geomorphology, geology), has definitively proven a major advancement in the discipline, supporting the reliability of the archeoseismological evidence (e.g., Similox-Tohon et al. 2006).

Because of the wide variety of disciplines involved, from the humanities and the social, natural, and engineering sciences, it seems, though, nearly inevitable that all practitioners who look at earthquake evidence in the archeological record will keep pursuing different objectives. The historian may want to know if an earthquake had any effect on the political, social, or military balance in a region. The engineer may be concerned about mitigating the seismic threat to our cultural and architectural heritage, while the seismologists are attempting to complete the historical catalogue of earthquakes and their physical parameters. Finding a balance between all these interests will also in the future remain archeoseismology's greatest challenge.

Ancient Seismoscopes

For assessing the seismic hazard of a region, an accurate catalogue of earthquakes and their physical parameters is imperative. Seismic-hazard practitioners need exact dates, magnitudes, source areas, etc. of past earthquakes. Taking into account the incompleteness of the archeological record, its limited spatial and temporal resolution, and the uncertainties inherent to archeological earthquake evidence, the skepticism with respect to the applicability of archeoseismology in **seismic-hazard studies** is indeed legitimate (cf. Sintubin 2011).

Some common pitfalls keep adding to the seismologist's skepticism. There is the **preservation problem**. The archeological record is not evenly distributed through time. Ancient history consists of long periods of cultural, social, and political stability and flourishing economies, during which any sign of earthquake is most probably expertly covered up. In contrast, during intervening, short periods of social and political upheaval, and economic crisis, signs of destructive earthquakes may be left extant, primarily because there is no impetus or funds to fully recover from the earthquake disaster. Only then, the earthquake leaves it marks in the archeological record, giving rise to an observational bias that focuses on periods of upheaval, destruction, abandonment, etc.

Another danger exists that "anomalous" earthquake catastrophes, supposedly proven by archeologists, are used uncritically in seismic-hazard assessments as "real" events (Ambraseys et al. 2002). Moreover, confronting the archeoseismological evidence, commonly poorly constrained in time and space, with the evenly incomplete and sometimes poorly constrained historical earthquake catalogues, may carry the risk of an arbitrary correlation, inevitably leading to **circular reasoning** (Rucker and Niemi 2010). When archeologists identify a destruction horizon as caused by an earthquake and consult existing earthquake catalogues to assign a date to the particular earthquake-related destruction horizon, the risk exists that historical seismologists add this particular archeological site to the catalogue as evidence

for that particular historical earthquake. This overreliance on historical catalogues clearly corrupts the usefulness of archeoseismology and should therefore be omitted from archeoseismological practices.

Given all these pitfalls, it becomes apparent that archeoseismological investigations should indeed not start from a seismological perspective but from the archeological earthquake evidence itself, with all its inherent limitations and uncertainties. Rather than simply complementing earthquake catalogues with potentially highly conjectural, ancient earthquakes, archeological sites may have the potential of becoming testing grounds to quantitatively assess site-specific ground effects. In this respect, archeological sites become **ancient seismoscopes** that can be used strategically to examine specific earthquake scenarios in a region (cf. Sintubin 2011). Archeological sites, especially those with a long and lasting history, do have the potential to have recorded the effects of a major earthquake. A quantitative assessment of the ground motions on archeological sites may indeed hold the eventuality to have narrowed down macroseismic parameters associated with the maximum credible earthquake in the region, irrespective of the time of occurrence, the magnitude, the seismic source, etc. With such an approach, archeoseismology enters in the logics of scenario-based, deterministic seismic risk assessment.

Archeoseismology, Fig. 8 Perfectly aligned *toppled columns* at *Susita* (Golan Heights), classically interpreted as indicative for the direction of strong ground motion caused by a major earthquake. Such earthquake hypothesis does not pass the test of scenario-based ground motion simulations (cf. Hinzen et al. 2011) © Sintubin

New Developments in Archeoseismology

This tendency towards a more standardized and quantitative approach of potential archeological earthquake evidence in archeological sites is fully exemplified in the rapid advances in **quantitative archeoseismology** (cf. Hinzen et al. 2011 and references therein). This recent development in archeoseismology primarily focuses on monumental architecture, the classical field of application of archeoseismology since its beginning (cf. Stiros 1996). Quantitative archeoseismology firstly applies modern techniques, such as 3D laser scanning (e.g., ground-based LIDAR), to obtain a three-dimensional structural model of the archeological damaged building or structure, allowing the construction of a very precise structural damage inventory. Using earthquake engineering models, the dynamic behavior of the ancient structure can be evaluated. Subsequently, scenario-based earthquake ground motion simulations enable testing a realistic earthquake hypothesis to explain the damage observed. This approach has already lead to the conclusion that in a number of cases, alternative, natural, or anthropogenic causes are more probable than the seismic cause that has originally been considered. Moreover, "classical" damage typologies attributed to earthquake-related ground motions, such as the perfectly aligned toppled columns (Fig. 8), could not be validated, even adding to the skepticism towards "classical" archeoseismological practices.

Besides this added value of quantitative archeoseismology with respect to monumental architecture, also the value of rubble architecture and associated destruction horizons get again particular interest in a more quantitative, **integrated territorial approach** that starts from the specific seismotectonic context and the empirical ground-motion relationships of potential earthquake sources and focuses on well-documented, high-visibility archeological contexts, characterized by very rapid ceramic change (~100-year time window) (cf. Jusseret and Sintubin 2012).

Issues and Perspectives in Archeoseismology

Archeoseismology will always be plagued by the ambiguities inherent to the archeological record of ancient earthquakes. In this respect, archeoseismology may very well never be able to deliver reliable and conclusive earthquake evidence that is needed to improve the **assessment of the seismic hazard** in a region. New developments towards more integrated, multidisciplinary approaches as well as quantitative archeoseismology will allow, though, that the potential of archeological sites as **ancient seismoscopes** is fully developed in the future.

The fact that the archeological visibility of earthquakes may be strongly biased towards the relatively short but commonly well-documented (e.g., rapid changes in ceramic styles) periods in a society's history of social, political, and/or economic turmoil opens unique perspectives for archeoseismological research. Preservation of archeological earthquake evidence may indeed rather be related to societal factors than to physical aspects of the ancient earthquakes. Ultimately, the relatively undisturbed, extant archeological record of earthquakes can tell us more about past societies and their attitude to physical disasters (cf. Jusseret and Sintubin 2012). A better appreciation of the complex way by which our ancestors responded to damaging earthquakes might indeed shed light on the societal factors defining the resilience or vulnerability of past societies. Eventually, by highlighting how our ancestors coped with earthquake disasters, archeoseismology could find new aspirations in establishing local **earthquake cultures** in earthquake-prone regions (cf. Sintubin et al. 2008), possibly providing a substantial contribution to the **mitigation of the earthquake risk**, by improving earthquake risk literacy and awareness.

Summary

Archeoseismology is the interdisciplinary study of pre-instrumental, **ancient earthquakes** through indirect evidence in the archeological record. As a burgeoning discipline within the broad research realm of **earthquake sciences**, archeoseismology bridges the gap between **instrumental** and **historical seismology** on the one side and **paleoseismology** and **earthquake geology** on the other.

The archeological record can be used in basically three ways in the identification and characterization of ancient earthquakes. The most obvious and straightforward archeological evidence of fault activity are archeological remains that are partly displaced due to coseismic surface rupturing on an active fault. As cultural piercing features, these **faulted relics** can be used to determine the type of faulting, the amount of coseismic slip, as well as the cumulative fault slip. Within the archeological stratigraphy, particular horizons can be designated to sudden destruction caused by human and/or natural agents. If the **archeological destruction horizons** can be attributed to an earthquake with a high degree of certainty, material included in the destruction horizons can be used to date episodes of earthquake damage. Destruction horizons are the most useful "proxy" for ancient earthquakes in archeological contexts dominated by rubble architecture and associated stratigraphy. A third type of earthquake evidence in the

archeological record are typical **strain structures in the building fabric** that are primarily caused by coseismic ground shaking and ground motion. These earthquake-related damage features are most conspicuous on monumental buildings and man-made constructions.

Archeoseismology will always be plagued by the ambiguities and uncertainties inherent to the archeological earthquake evidence, primarily resulting from the difficulty to irrefutably distinguish between damage caused by earthquakes and that caused by other natural or human agents. In this respect, archeoseismology may very well never be able to deliver reliable and conclusive earthquake evidence that is needed to improve the assessment of the seismic hazard in a region. Archeological sites have though the potential of becoming testing grounds to quantitatively assess site-specific ground effects. As **ancient seismoscopes**, archeological sites may hold the eventuality to have narrowed down macroseismic parameters associated with the maximum credible earthquake, irrespective of the time of occurrence and the physical parameters of the earthquake. Finally, preservation of archeological earthquake evidence may rather be related to societal factors than to physical parameters. In this respect, the relatively undisturbed archeological record of ancient earthquakes can tell us more about past societies and their attitude to physical disasters.

Cross-References

- ▶ Damage to Ancient Buildings from Earthquakes
- ▶ Damage to Buildings: Modeling
- ▶ Earthquake Location
- ▶ Earthquake Magnitude Estimation
- ▶ Earthquake Recurrence
- ▶ Earthquakes and Their Socio-economic Consequences
- ▶ Intensity Scale ESI 2007 for Assessing Earthquake Intensities
- ▶ Mechanisms of Earthquakes in Aegean
- ▶ Numerical Modeling of Masonry Infilled Reinforced Concrete Frame Buildings
- ▶ Paleoseismology
- ▶ Paleoseismology: Integration with Seismic Hazard
- ▶ Post-Earthquake Diagnosis of Partially Instrumented Building Structures
- ▶ Review and Implications of Inputs for Seismic Hazard Analysis
- ▶ Seismic Analysis of Masonry Buildings: Numerical Modeling
- ▶ Tsunamis as Paleoseismic Indicators

References

Ambraseys NN, Jackson JA, Melville CP (2002) Historical seismicity and tectonics: the case of the eastern Mediterranean and the middle East. In: Lee WHK, Kanamori H, Jennings PC, Kisslinger C (eds) International handbook of earthquake and engineering seismology, vol 81A, International geophysics series. Academic, Amsterdam, pp 747–763

Barnes GL (2010) Earthquake archaeology in Japan: an overview. In: Sintubin M, Stewart IS, Niemi TM, Altunel E (eds) Ancient earthquakes, Geological Society of America special paper, 471. Geological Society of America, Boulder, pp 81–96

Caputo R, Pavlides SB (2008) Earthquake geology: methods and applications. Tectonophysics 453:1–296

Evans A (1921) The palace of minos. A comparative account of the successive stages of the early cretan cvilization as illustrated by the discoveries at knossos. Volume I. The neolithic and early and middle minoan ages. MacMillan and Co., London

Evans A (1928) The palace of minos. A comparative account of the successive stages of the early cretan civilization as illustrated by the discoveries at knossos. Volume II: Part I. Fresh light son origins and external relations: The restoration in town and palace after seismic catastrophe towards close of M.M. III, and the beginning of the new era. MacMillan and Co., London

Force ER, McFadgen BG (2010) Tectonic environments of ancient civilizations: opportunities for archaeoseismological and anthropological studies. In: Sintubin M, Stewart IS, Niemi TM, Altunel E (eds) Ancient earthquakes, Geological Society of America special paper, 471. Geological Society of America, Boulder, pp 21–28

Galadini F, Hinzen K-G, Stiros SC (2006a) Archaeoseismology at the beginning of the 21st century. J Seismol 10:393–537

Galadini F, Hinzen K-G, Stiros SC (2006b) Archaeoseismology: methodological issues and procedure. J Seismol 10:395–414

Guidoboni E (1996) Archaeology and historical seismology: the need for collaboration in the Mediterranean area. In: Stiros S, Jones RE (eds) Archaeoseismology. Institute of Geology & Mineral Exploration and British School of Athens, Athens, pp 7–13

Hinzen K-G (2005) The use of engineering seismological models to interpret archaeoseismological findings in Tolbiacum, Germany: A case study. Bull Seismol Soc Am 95:521–539

Hinzen K-G, Fleischer C, Reamer SK, Schreiber S, Schütte S, Yerli B (2011) Quantitative methods in archaeoseismology. Quat Int 242:31–41

Jackson J (2006) Fatal attraction: living with earthquakes, the growth of villages into megacities, and earthquake vulnerability in the modern world. Philos Trans R Soc 364:1911–1925

Jusseret S, Sintubin M (2012) All that rubble leads to trouble: reassessing the seismological value of archaeological destruction layers in Minoan Crete and beyond. Seismol Res Lett 83(4):736–742

Jusseret S, Sintubin M (2013) The origins of an old myth: Sir Arthur Evans, Claude Schaeffer and the seismic destruction of Late Bronze Age Eastern Mediterranean civilizations. Seismol Res Lett 84(1):94–100

Karcz I, Kafr, U (1978) Evaluation of supposed archaeoseismic damage in Israel. J Archaeol Sci 5:237–253

Marco S, Agnon A, Ellenblum R, Eidelman A, Basson U, Boas A (1997) 817-year-old walls offset sinistrally 2.1 m by the Dead Sea transform, Israel. J Geodyn 24:11–20

McGuire WG, Griffiths DR, Hancock PL, Stewart IS (eds) (2000) The archaeology of geological catastrophes, Special publications, 171. Geological Society, London

Michetti AM, Hancock PL (1997) Paleoseismology: understanding past earthquakes using quaternary geology. J Geodyn 24(1–4):3–10

Michetti AM, Esposito E, Guerrieri L, Porfido S, Serva L, Tatevossian R, Vittori E, Audemard F, Azuma T, Clague J, Comerci V, Gürpinar A, McCalpin J, Mohammadioun B, Mörner NA, Ota Y, Roghozin E (2007) Intensity scale ESI 2007. Memorie descrittive della Carta Geologica d'Italia 74:41

Nikonov AA (1988) On the methodology of archeoseismic research into historical monuments. In: Marinos PG, Koukis GC (eds) Engineering Geology of Ancient Works, Balkema, Rotterdam, pp 1315–1320

Nur A, Cline EH (2000) Poseidon's horses: plate tectonics and earthquake storms in the late bronze age aegean and eastern mediterranean. J Archaeol Sci 27:43–63

Rapp GJ (1986) Assessing archaeological evidence for seismic catastrophies. Geoarchaeology 1:365–379

Rodríguez-Pascua MA, Pérez-López R, Giner-Robles JL, Silva PG, Garduño-Monroy VH, Reicherter K (2011) A comprehensive classification of Earthquake Archaeological Effects (EAE) in archaeoseismology: application to ancient remains of Roman and Mesoamerican cultures. Quat Int 242:20–30

Rucker JD, Niemi TN (2010) Historical earthquake catalogues and archaeological data: achieving synthesis without circular reasoning. In: Sintubin M, Stewart IS, Niemi TM, Altunel E (eds) Ancient earthquakes, Geological Society of America special paper, 471. Geological Society of America, Boulder, pp 97–106

Sbeinati MR, Meghraoui M, Suleyman G, Gomez F, Grootes P, Nadeau MJ, Al Najjar H, Al-Ghazzi R (2010) Timing of earthquake ruptures at the Al Harif Roman aqueduct (Dead Sea fault, Syria) from archaeoseismology and paleoseismology. In: Sintubin M, Stewart IS, Niemi TM, Altunel E (eds) Ancient earthquakes, Geological Society of America special paper, 471. Geological Society of America, Boulder, pp 243–267

Schaeffer CFA (1948) Stratigraphie Comparée et Chronologie de l'Asie Occidentale. Oxford University Press, London

Silva PG, Sintubin M, Reicherter K (2011) Earthquake archaeology and paleoseismology. Quat Int 242(1):1–253

Similox-Tohon D, Sintubin M, Muchez P, Vanhaverbeke H, Verhaert G, Waelkens M (2005) Identification of a historical morphogenic earthquake through trenching at ancient Sagalassos (SW Turkey). J Geodyn 40:279–293

Similox-Tohon D, Sintubin M, Muchez P, Verhaert G, Vanneste K, Fernandez M, Vandycke S, Vanhaverbeke H, Waelkens M (2006) The identification of an active fault by a multidisciplinary study at the archaeological site of Sagalassos (SW Turkey). Tectonophysics 420:371–387. [+Erratum in Tectonophysics, 435 (2007), 55–62]

Sintubin M (2011) Archaeoseismology: past, present and future. Quat Int 242:4–10

Sintubin M, Stewart IS (2008) A logical methodology for archaeoseismology: a proof of concept at the archaeological site of Sagalassos, southwest Turkey. Bull Seismol Soc Am 98(5):2209–2230

Sintubin M, Stewart IS, Niemi TM, Altunel E (2008) Earthquake archaeology – just a good story? Seismol Res Lett 79(6):767–768

Sintubin M, Stewart IS, Niemi TM, Altunel E (eds) (2010) Ancient earthquakes, Geological Society of America special paper, 471. Geological Society of America, Boulder

Stiros SC (1996) Identification of earthquakes from archaeological data: methodology, criteria and limitations. In: Stiros S, Jones RE (eds) Archaeoseismology. Institute of Geology & Mineral Exploration and British School of Athens, Athens, pp 129–152

Stiros SC, Jones RE (1996) Archaeoseismology. Institute of Geology & Mineral Exploration and British School of Athens, Athens

Tuttle MP, Schweig ES (1995) Archeological and pedological evidence for large prehistoric earthquakes in the New Madrid seismic zone, central United States. Geology 23(3):253–256

Artificial Offshore Seismic Sources

Wolfgang Rabbel and Dennis Wilken
Institute of Geosciences, University of Kiel, Kiel, Germany

Synonyms

Marine seismic sources; Seismic energy sources

Introduction

Artificial Offshore Seismic Sources are instruments that are used for generating short-duration pressure pulses in the marine water column, usually with constant repetition rate. They provide the acoustic energy for marine seismic surveys. Marine seismic surveys are performed in order to image geological structure (layers and faults) beneath the seafloor and to characterize rocks and rock strength in terms of seismic wave velocity or dynamic elastic constants. Therefore, short pressure pulses are applied to the water column that travel as acoustic waves down to the sea bottom where they are converted into seismic body and interface waves (elastic waves). These seismic waves penetrate deeper into the underground and are partially reflected at geological interfaces and/or refracted back to the surface (Fig. 1, right). This returning part of the wave field is recorded either at the seafloor with seismographs or in the water column with hydroacoustic receivers. In order to allow for profiling both seismic source and receivers are towed behind a vessel carrying out repeated measurements while moving forward. The technique of marine seismic has been developed and improved continuously since the late 1940s. This entry provides an overview of the purpose and principles marine seismic sources. More detailed information can be found, for example, in Jones (1999) and Meunier (2011).

General Considerations

The goal of marine seismic reflection surveys is to image geological structure down to a predefined target depth at highest possible resolution. Therefore, the pressure pulses generated by a marine seismic source are usually designed to have a sharp onset and short duration (some to some 10 ms; exception marine vibrator source) corresponding to a broadest possible frequency spectrum. The short duration, respective large bandwidth, is necessary to enable distinguishing of reflections (echoes) arriving at the receivers subsequently from interfaces at increasing depths. Seismic wave propagation is affected by absorption that leads to a notable continuous decrease of amplitudes starting from the high-frequency end of the spectrum. Therefore, penetration depth increases with decreasing signal frequency. While it propagates, the wave front widens and signal amplitudes decrease accordingly ("geometrical spreading"). This effect needs to be compensated for by increasing the initial strength of the pressure pulse in order to keep reflected signals of deep horizons detectable. Finally, in order to obtain a reliable depth section, the measured profiles have to be sampled spatially with a sufficiently high density realized by repeating the measurements while the vessel is moving. This implies that the marine seismic source needs to be reloadable within a certain time interval depending on the velocity of the ship. Typical repetition intervals are between 0.5 up to some 10 s. The target range relevant for seismic exploration – for example in earthquake engineering – may extend from near-seafloor layering down to several kilometers depth, for example, in order to detect and trace deep reaching fault systems. Correspondingly, different sorts of seismic sources are in use, each accounting for different target depth or infrastructure related situations (Table 1).

Types of Marine Seismic Sources and Their Key Principles

Airguns and GI-guns

Airguns or G-(Generator)-Guns generate an acoustic impulse by releasing a high pressure air

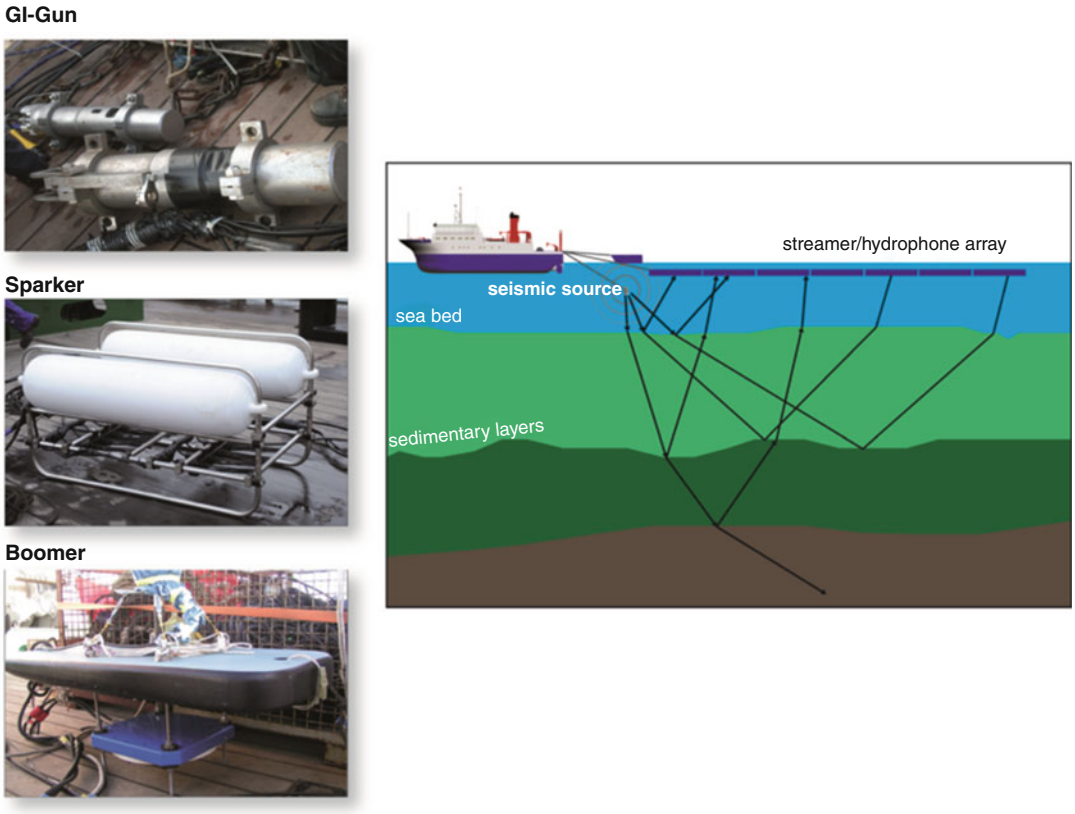

Artificial Offshore Seismic Sources, Fig. 1 *Right*: Principle of marine seismic data acquisition; pulse-like seismic waves travel through geological layers and are reflected back to the surface at interfaces where density or propagation velocity change; wave propagation paths indicated by rays (*black lines*). *Left*: examples of seismic sources for near-surface prospecting; from *top* to *bottom*: Airgun (GI-gun), Sparker, Boomer

bubble underwater. The radiation pattern of the airgun source corresponds to an acoustic dipole because an image-source mirrored at the water surface has to be considered in order to account for the free-surface condition. It causes a so-called ghost reflection following the primary pulse with negative polarity and a time delay depending on source depth. While moving to the sea surface, the generated bubble oscillates around the equilibrium of air- and hydrostatic water pressure with a natural period T. T depends on the energy of the injected air E, the confining hydrostatic pressure P of the water column, and the fluid density d according to the Rayleigh-Willis formula $T \approx 1.14 d^{1/2} P^{-5/6} E^{1/3}$. This oscillation generates an undesired lengthening of the seismic signal. In order to overcome the bubble oscillation, GI-(Generator Injector)-Guns are very common that inject a second air pulse to collapse the initial bubble before it starts to oscillate. G-Guns and GI-Guns can be mounted in arrays to enhance the signal amplitude and, when fired with time offsets, to modulate the shape of the signal.

The generated frequency content mainly depends on the volume of the airgun chamber, the assigned pressure, and the tow depth.

Water Guns

A water gun is a pneumatic seismic source operated by compressed air, too. The air is used to drive a piston pressing water from a chamber inside the gun into the water column. The seismic impulse is generated by the implosion of a cavity

Artificial Offshore Seismic Sources, Table 1 Technical data and properties of typical marine seismic sources. The given value of structural resolution corresponds to a quarter wavelength at 1,600 m/s wave speed

Source type	Chamber volume (l)	Energy per pulse (J) / pressure (dB reference 1 μPat 1 m)	Spectral width (Hz)	Main frequency (Hz)	Typical exploration depths	Resolution at main frequency (m)	Power supply unit
Airgun	0.2–32	~10 kJ/170–230 dB	–	10–200	Some 100 m to some km	2–40	Compressor
GI Gun	0.4–4	~10 kJ/170–230 dB	–	50–200	Some 100 m to some km	2–8	Compressor
Water Gun	0.2–2	~30 kJ	–	50–1,000	Some 100 m to some km	0.4–8	Compressor
Sparker	–	300–2,400 J	100–3 k	~1,500	Upto ~200 m	0.25	Capacitor bank
Boomer	–	300–700 J	500–4 k	~3,000	Upto ~100 m	0.15	Capacitor bank
Pinger	–	~100 J	2 k–150 k	–	Upto ~10 m	0.2–0.03	Electricalamplifier
Vibro source	–	Some 10 kW times sweep length (s)	6–100	–	Some 100 m to some km	4–100	Electrical current

created behind the expelled water. It is free of bubble oscillations and contains higher frequencies than typically generated by airguns.

Sparker

The sparker source generates an acoustic impulse by a high-voltage spark discharge between two electrodes in the water. The spark consists of a high-pressure plasma whose expansion and collapse generates the acoustic peak. The high voltage needed to generate such a plasma is stored in a bank of capacitors, which is reloaded for each shot. Sparkers can be used at different energy levels, depending on the capacitor bank. Commonly sparkers are used in arrays to enhance the signal amplitude and to maintain the signal shape which usually changes because the electrodes tend to tip-off during usage. Sparkers can be applied in brackish water and seawater.

Boomer

Boomers are also based on combining electromagnetic and mechanical principles. Similar to the sparker case, electric charges are assembled in a bank of capacitors releasing a high-voltage pulse to the source. The discharge is led through a flat coil inside the source body. From below an aluminum plate is pressed against the coil by springs. The magnetic field of the coil induces eddy currents inside this plate. These currents produce magnetic fields that repel the plate from the coil (Lenz's law). The spring then moves the plate back, leaving a collapsing cavitational volume that generates the acoustic impulse.

Pinger

Sediment echo sounders (SES) use piezoelectric "pingers" as electroacoustic converters.

Some materials (especially crystalline) tend to show electromechanical properties which means that the material is stretched when voltage is applied. Closely packed piezoelectric crystals are very effective electroacoustic converters and can be used as acoustic sources.

These pingers are applied as single point sources or – even more often – in arrays which enable, when used with time offsets, a modulation of the radiation pattern of the source. Alternative developments are based on the parametric nonlinearity effect to enhance the acoustic efficiency and the stability of the signal.

Marine Vibrator

Marine vibrator sources are basically volumetrically oscillating shells that transmit a chirp signal ("sweep") to the water column. The chirp is linearly modulated in frequency and lasts typically several seconds. Seismic reflections can only be recognized after the records were cross-correlated with the source signal. This concept was adopted from the onshore Vibroseis™ method (e.g., Sheriff and Geldart 1995). The shells are constructed flexible or otherwise expandable; the oscillations are driven by hydraulic, magnetostrictive, or electromagnetic devices placed inside (e.g., Tenghamn 2006; Meunier 2011). Like airguns and water guns, marine vibrators can be combined to form arrays in order to improve energy output and radiation characteristics. They work in a similar frequency range as airguns and release similar seismic energy in total. However, since they provide energy at lower rate over a much longer time interval they are causing less environmental impact than the impulsive source that release energy within some 10 ms. Since the vessel moves significantly while the source is active, Doppler effects occur in the records that need to be corrected in during data processing. For near-surface investigations, Vibroseis-type chirps can be generated through low-energy piezoelectric transducers. However, marine vibrators for deep (km-scale) sounding are still under development.

Summary

Artificial Offshore Seismic Sources are instruments emitting sound signals for marine seismic surveys that are performed for investigating offshore geological structure. Functional principles of marine seismic source depend on the required energy and frequency content of the signals, including piezoelectric and high-pressure air pulsers as low and high energy end members. The structural resolution of the seismic images of geological layering ranges from some 10 cm to some 10 m depending on the depth of the target horizons and the seismic sources applied.

References

Jones EJW (1999) Marine geophysics. Wiley, Chichester
Meunier J (2011) Seismic acquisition from yesterday to tomorrow. Society of Exploration Geophysicists, Tulsa
Sheriff LE, Geldart LP (1995) Exploration seismology, 2nd edn. Cambridge University Press, Cambridge
Tenghamn J (2006) An electrical marine vibrator with a flextensional shell. Explor Geophys 37:286–291

Assessment and Strengthening of Partitions in Buildings

Christis Z. Chrysostomou
Department of Civil Engineering and Geomatics, Cyprus University of Technology, Limassol, Cyprus

Synonyms

Infills; Infill walls; Masonry infills; Reinforced concrete infills

Introduction

Partitions in buildings are necessary architectural features that separate spaces in order to facilitate various functions that are required depending on the use of a building. These partitions in modern structures can be lightweight, for example, in case that they are used to subdivide office spaces, or can be heavy masonry partitions that are used mainly in reinforced concrete structures to subdivide the plan area of a building into various rooms. In the latter case, these are mostly built within the frame of the structure filling the gap, and they are therefore called infills or infill walls. Depending on the type of the material that is used to construct them, they can be called masonry infills or reinforced concrete (RC) infills.

Infill walls have attracted the attention of many researchers since the early 1950s, and much work has been undertaken to study their behavior and interaction with the surrounding

frames. In addition, efforts have been made to utilize infill walls as a means of producing economic designs by reducing the sizes of the members of the bounding frames.

A large number of researchers have studied the behavior of infilled frames. It is evident from their studies that infill walls can provide both an economic and practical means for the lateral stability of framed structures and a viable alternative for retrofitting existing structures to resist seismic, wind, and blast loads. Despite this, there is reluctance from the engineering community to use this structural system widely and treat infill walls as structural elements.

Therefore, although the subject of infilled frames has been studied for more than 60 years, there are still no definitive answers either about their behavior and interaction with the bounding frame or about the estimation of their stiffness and strength. Some problems that make it difficult for practicing engineers to use infill walls as structural elements are the inherent nonlinearity, the high degree of variability, and the inherent degradability of infill walls. The fact that infill walls exhibit completely different in-plane and out-of-plane behavior makes the problem even more difficult to tackle. This reveals the difficulties associated with this problem and the need for more research to answer these long-standing questions.

Nevertheless, the presence of infill walls has shown that in most cases they have beneficial effects on the behavior of structures during earthquakes and have contributed in the prevention of collapse of many structures. It is therefore for this reason that efforts have been made to use engineered infills to retrofit existing seismic-deficient buildings, since they present an economically viable solution.

In this entry, the in-plane behavior and in-plane failure modes of infilled frames are presented. Then, macro- and micromodels for infill walls are presented followed by the results of experimental investigations for the replacement of masonry infill walls with reinforced concrete infills, as an economically viable method for retrofitting existing structures. Finally, methods for strengthening existing partition walls are presented.

Behavior of Partitions

The modeling of the behavior of infilled frames under lateral loading (and mainly earthquake-induced loads) is a complex issue because these structures exhibit a highly nonlinear response due to the interaction between the masonry infill panel and the surrounding frame. This results to several modes of failure, each of which has a different failure load, and hence a different ultimate capacity and overall behavior.

At moderate loading levels, the infill of a non-integral infilled frame separates from the surrounding frame and the infill acts as a diagonal strut (Fig. 1). As the racking load is increased, failure occurs eventually in either the frame or the infill. The usual mode of frame failure results from tension in the windward column or from shearing in the column or beams or plastic hinging in columns or beams; however, if the frame strength is sufficient enough to prevent its failure by one of these modes, the increasing racking load eventually produces failure of the infill. In the most common situations, the in-plane lateral load applied at one of the top corners is resisted by a truss formed by the loaded column and the infill along the diagonal connecting the loaded corner and the opposite bottom corner. The state of stress in the infill gives rise to a principal compressive stress along the diagonal and a principal tensile stress in the perpendicular direction. If the infill is made of concrete, successive failures, initially by cracking along the compression diagonal and then by crushing near one of the loaded corners or by crushing alone, will lead to collapse; if the infill is made of brick masonry, an alternative possibility of shearing failure along the mortar planes may arise (Fig. 1).

Based on both experimental and analytical results during the last five decades, different failure modes of masonry-infilled frames were proposed that can be classified into five distinct modes given below:

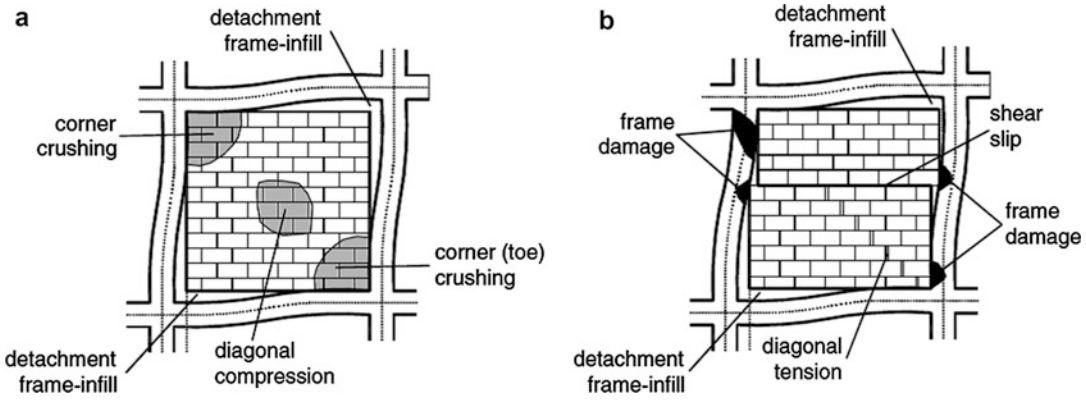

Assessment and Strengthening of Partitions in Buildings, Fig. 1 Failure modes of non-integral infilled frames: (**a**) Corner crushing (*CC*) and diagonal compression (*DK*) modes. (**b**) Sliding shear (*SS*), frame failure (*FF*), and diagonal cracking (*DK*) modes (Asteris et al. 2011 with permission from ASCE)

1. The corner crushing (CC) mode, which represents crushing of the infill in at least one of its loaded corners, as shown in Fig. 1a. This mode is usually associated with infilled frames consisting of a weak masonry infill panel surrounded by a frame with weak joints and strong members (Mehrabi and Shing 1997; El-Dakhakhni 2002; Ghosh and Amde 2002; El-Dakhakhni et al. 2003).
2. The diagonal compression (DC) mode, which represents crushing of the infill within its central region, as shown in Fig. 1a. This mode is associated with a relatively slender infill, where failure results from out-of-plane buckling of the infill.
3. The sliding shear (SS) mode, which represents horizontal sliding failure through bed joints of a masonry infill, as shown in Fig. 1b. This mode is associated with weak mortar joints in the infill and a strong frame.
4. The diagonal cracking (DK) mode, which is seen in the form of a crack across the compressed diagonal of the infill panel and often takes place with simultaneous initiation of the SS mode, as shown in Fig. 1b. This mode is associated with a weak frame or a frame with weak joints and strong members infilled with a rather strong infill (Mehrabi and Shing 1997; El-Dakhakhni 2002).
5. The frame failure (FF) mode, which is seen in the form of plastic hinges developing in the columns or the beam-column connections, as shown in Fig. 1b. This mode is associated with a weak frame or a frame with weak joints and strong members infilled with a rather strong infill.

Ghosh and Amde (2002), based on the finite element method and including interface elements at the frame-infill interface, confirmed the order of occurrence of the above five distinct failure modes. Of the five modes, only the CC and SS modes are of practical importance (Comité Euro-International du Béton CEB 1996), since most infills are not slender (El-Dakhakhni et al. 2003) and therefore the second mode (DC) is not favored. The fourth mode (DK) should not be considered as a failure mode, due to the post-cracking capacity of the infill to carry additional load. The fifth mode (FF) relates to the failure of the frame, and it is particularly important when examining existing structures, which in many cases exhibit frame weakness. It should be noted that these failure modes are only seen/applicable to the case of infill walls without openings on the diagonal of the infill panel.

Kappos and Ellul (2000), based on an analytical study of the seismic performance of masonry-infilled RC-framed structures, found that taking into account the infill in the analysis resulted in

an increase in stiffness as much as 440 %. It is clear that, depending on the spectral characteristics of the design earthquake, the dynamic behavior of the two systems dealt with by the author (bare vs. infilled frame) can be dramatically different. They also presented a very useful global picture of the seismic performance of the studied infill frames by referring to the energy dissipated by each component of the structural system. It is clear that at the serviceability level, over 95 % of the energy dissipation is taking place in the infill walls (subsequent to their cracking), whereas at higher levels, the RC members start making a significant contribution. This is a clear verification of the fact that masonry infill walls act as a first line of defense in a structure subjected to earthquake load, while the RC-frame system is crucial for the performance of the structure to stronger excitations (beyond the design earthquake).

The quantification of the in-plane properties of non-integral infilled frames and the prediction of the failure modes is a rather cumbersome task even when the load is applied monotonically. The problem becomes even more difficult when a dynamic load is applied, since the hysteretic behavior of the materials and their deterioration with the cyclic loading should be taken into consideration. Chrysostomou and Asteris (2012) discuss these issues and present methods for the determination of the in-plane stiffness, strength, and deformation capacity of infills along with the results of a parametric study that compares these methods and checks them against experimental results whenever possible. Based on the above material, recommendations are made for the in-plane material properties, failure modes, strength and stiffness, as well as deformation characteristics, of infilled frames.

Modeling of Partitions

In order for engineers to be able to use infills as an engineering element, a reliable mathematical model needs to be developed that simulates the combined behavior of the infill partition and the bounding frame. As explained in the previous section, the behavior of infilled frames is rather complex and it depends on a large number of parameters. Therefore, for the mathematical model to accurately simulate the behavior of infilled frames, it should take into consideration all these parameters.

The models for infills can be subdivided into macro- and micromodels. In the former, simple models are developed that are simulating the overall global behavior of infilled frames, while in the latter, surface or solid finite elements are used along with interface ones that simulate both the local and global behavior of both the infills and the bounding frames and their interaction. In the following two sections macro- and micromodels are presented.

Macromodeling

Since the first attempts to model the response of the composite infilled frame structures, experimental and conceptual observations have indicated that a diagonal strut with appropriate geometrical and mechanical characteristics could possibly provide a solution to the problem. Early research on the in-plane behavior of infilled frame structures undertaken at the Building Research Station, Watford (later renamed Building Research Establishment and now simply BRE), in the 1950s served as an early insight into this behavior and confirmed its highly indeterminate nature in terms solely of the normal parameters of design. On the basis of these few tests, a purely empirical interaction formula was later tentatively suggested for use in the design of tall framed buildings.

Diagonal Strut Model

In the early 1960s, Polyakov suggested the possibility of considering the effect of the infilling in each panel as equivalent to diagonal bracing, and this suggestion was later adopted by Holmes, who replaced the infill by an equivalent pin-jointed diagonal strut made of the same material and having the same thickness as the infill panel and a width defined by

$$\frac{w}{d} = \frac{1}{3} \tag{1}$$

where d is the diagonal length of the masonry panel. The "one-third" rule was suggested as

being applicable irrespective of the relative stiffness of the frame and the infill. One year later, Stafford Smith, based on experimental data from a large series of tests using masonry-infilled steel frames, found that the ratio w/d varied from 0.10 to 0.25. On the second half of the 1960s, Stafford Smith and his associates using additional experimental data related the width of the equivalent diagonal strut to the infill-frame contact lengths using an analytical equation, which has been adapted from the equation of the length of contact of a free beam on an elastic foundation subjected to a concentrated load. They proposed the evaluation of the equivalent width λ_h as a function of the relative panel-to-frame-stiffness parameter, in terms of

$$\lambda_h = h \sqrt[4]{\frac{E_w t_w \sin 2\theta}{4EIh_w}} \tag{2}$$

where E_w is the modulus of elasticity of the masonry panel, EI is the flexural rigidity of the columns, t_w is the thickness of the infill panel and equivalent strut, h is the column height between centerlines of beams, h_w is the height of infill panel, and θ is the angle, whose tangent is the infill height-to-length aspect ratio, being equal to

$$\theta = \tan^{-1}\left(\frac{h_w}{L_w}\right) \tag{3}$$

in which L_w is the length of infill panel (all the above parameters are explained in Fig. 2).

The use of this equation to seismic design is recommended for a lateral force level up to 50 % of the ultimate capacity.

Based on experimental and analytical data, Mainstone proposed an empirical equation for the calculation of the equivalent strut width, given by

$$\frac{w}{d} = 0.16\lambda_h^{-0.3} \tag{4}$$

Mainstone and Weeks and Mainstone, also based on experimental and analytical data, proposed a slightly modified empirical equation for the calculation of the equivalent strut width:

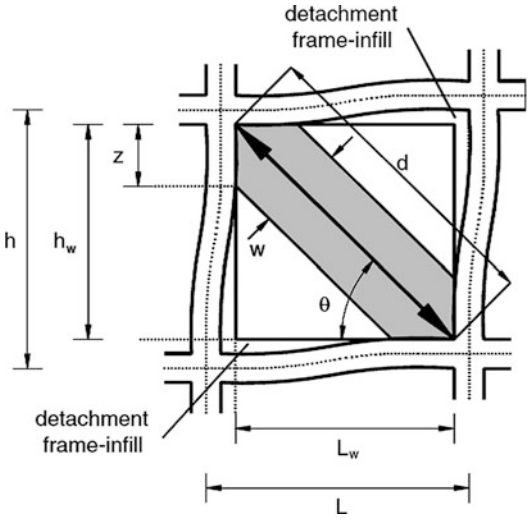

Assessment and Strengthening of Partitions in Buildings, Fig. 2 Definitions for the equivalent diagonal strut (Asteris et al. 2011 with permission from ASCE)

$$\frac{w}{d} = 0.175\lambda_h^{-0.4} \tag{5}$$

This formula was included in FEMA-274 for the analysis and rehabilitation of buildings as well as in FEMA-306, as it has been proven to be the most popular over the years. Although this equation is accepted by the majority of researchers dealing with the analysis of infilled frames, several variations were presented by various researchers trying to improve its applicability. A discussion and comparison of these proposals as well as references to the work of the various researchers mentioned above is given by Chrysostomou and Asteris (2012), and Asteris et al. (2011).

Multiple-Strut Models

In the last two decades, it became clear that one single-strut element is unable to model the complex behavior of the infilled frames. The bending moments and shear forces in the frame members cannot be adequately represented using a single diagonal strut connecting the two loaded corners.

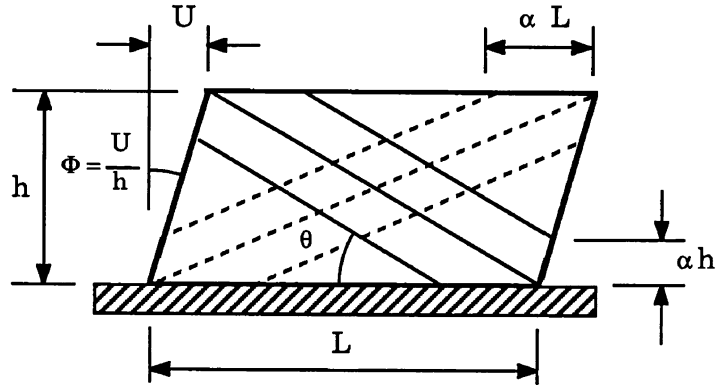

Assessment and Strengthening of Partitions in Buildings, Fig. 3 Six-strut model for masonry infill panel in frame structures (Chrysostomou 1991)

More complex macromodels were hence proposed, still typically based on a number of diagonal struts.

Thiruvengadam proposed the use of a multiple-strut model to simulate the effect of the infill panel. This particular model consists of a moment-resisting frame with a large number of pin-jointed diagonal and vertical struts. Initially, a perfect frame-infill bond condition is assumed, and the lateral stiffness of the infill, by its shear deformation, is modeled by a set of pin-ended diagonal struts running in both directions. These diagonals represent the shear and axial stiffness of the masonry infill. Similarly, the vertical stiffness contribution is accounted for by providing vertical struts. The objective of the aforementioned study was a realistic evaluation of the natural frequencies and modes of vibration, purposes for which the nonlinear phenomena do not play an important role. This model has been adopted by many researchers to investigate the effect of infill on the behavior of infilled frames and has been also included in FEMA-356, due to the great number of struts, as a method for modeling the special case of infilled frames with openings. Similarly, Hamburger and Chakradeo proposed a multiple-strut configuration that can account for the openings also, but the evaluation of the characteristics of the struts is rather complicated. They showed that for panels of typical configuration, the formation of these struts protects the beam-to-column connections, which have limited capacity in withstanding significant flexural demand, with plastic hinges forming instead within the mid-span region of the beam. They postulated that this resulted in a system of significant strength, stiffness, and ductility that behaves much like the modern eccentrically braced frame systems. Such behavior could, in part, be responsible for the observed good performance of these buildings in the 1906 San Francisco earthquake (Hamburger and Meyer 2006).

The main advantage of the multiple-strut models, in spite of the increase in complexity, is the ability to represent the actions in the frame more accurately. Syrmakezis and Vratsanou (1986) employed five parallel struts in each diagonal direction. It was stressed how different contact lengths play a significant effect on the bending moment distribution in the frame members.

Chrysostomou (1991, Chrysostomou et al. 2002) aimed at obtaining the response of infilled frames under earthquake loading by taking into account both stiffness and strength degradation of infills. Each infill panel was modeled by six compression-only inclined struts (Fig. 3). Three parallel struts were used in each diagonal direction and the off-diagonal ones were positioned at critical locations along the frame members. These locations are specified by a parameter α, which represents a fraction of the length or height of a panel and is associated with the position of the formation of a plastic hinge in a beam or a column. At any point during the analysis of the nonlinear response, only three of the six struts are active, and the struts are switched to the opposite direction whenever their compressive force reduced to zero.

In order to conduct nonlinear analysis, the force-displacement relationships corresponding to the equivalent strut model must be adequately defined. The modeling of hysteretic behavior increases not only the computational complexity but also the uncertainties of the problem.

In Chrysostomou's model, the hysteretic behavior of the six struts is defined by a hysteretic model, which consists of two equations. The first equation defines the strength envelope of a structural element and the second defines its hysteretic behavior. The shape of the envelope and the hysteretic loops is controlled by six parameters, all of which have physical meaning and can be obtained from experimental data. The advantage of this strut configuration over the single diagonal strut is that it allows the modeling of the interaction between the infill and the surrounding frame and it takes into account both strength and stiffness degradation of the infill, which is vital for determining the response of infilled frames subjected to earthquake load.

Saneinejad and Hobbs developed a method based on the equivalent diagonal strut approach for the analysis and design of steel or concrete frames with concrete or masonry infill walls subjected to in-plane forces. The proposed analytical model assumes that the contribution of the infill panel to the response of the infilled frame can be modeled by replacing the panel by a system of two diagonal masonry compression struts. The method takes into account the elastoplastic behavior of infilled frames considering the limited ductility of infill materials. Various governing factors such as the infill aspect ratio, the shear stresses at the infill-frame interface, and relative beam and column strengths are accounted for in this development. This model has been adopted by Madan et al. (1997) for static monotonic loading, as well as quasi-static cyclic loading. This model for masonry infill panels was implemented in IDARC 2D Version 4.0 (Vales et al. 1996), a computer-based analytical tool for the inelastic analysis and damage evaluation of buildings and their components under combined dynamic, static, and quasi-static loading.

El-Dakhakhni (2000, 2002) and El-Dakhakhni et al. (2001) suggested replacing the infill wall by one diagonal and two off-diagonal struts, on making use of the orthotropic behavior of the masonry wall as well as on some experimental observations and analytical simplifications, in order to simplify the nonlinear modeling of these structures.

Crisafulli investigated the influence of different multiple-strut models on the structural response of infilled reinforced concrete frames, focusing on the stiffness of the structure and the actions induced in the surrounding frame. Numerical results, obtained from the single-, two-, and three-strut models, were compared with those corresponding to a refined finite element. The lateral stiffness of the structure was similar in all the cases considered, with lower values for two- and three-strut models. It must be noted that, for the multiple-strut models, the stiffness may significantly change depending on the separation between struts. The single-strut model underestimates the bending moment because the lateral forces are primarily resisted by a truss mechanism. On the other hand, the two-strut model leads to higher values than those corresponding to the finite element model. A better approximation is obtained from the three-strut model, although some differences arise at the ends of both columns. Although the single-strut model constitutes a sufficient tool for the prediction of the overall response and the triple-strut model is superior in precision, Crisafulli adopted the double-strut model approach, accurate enough and less complicated compared to the other models.

More recently, Crisafulli and Carr (2007) proposed a new macromodel in order to represent, in a rational but simple way, the effect of masonry infill panels. The model is implemented as a four-node panel element which is connected to the frame at the beam-column joints. Internally, the panel element accounts separately for the compression and shear behavior of the masonry panel using two parallel struts and a shear spring in each direction. This configuration allows an adequate consideration of the lateral stiffness of the panel and of the strength of masonry panel, particularly when a shear failure along mortar joints or diagonal tension

failure is expected. Furthermore, the model is easy to apply in the analysis of large infilled frame structures. The main limitation of the model results from its simplicity, since the panel is connected to the beam-column joints of the frame, being thus not able to properly predict the bending moment and shear forces in the surrounding frame. A detailed presentation as well as references to the work on macromodels of the various researchers mentioned above is given by Asteris et al. (2011).

Micromodeling

The ability to model accurately the behavior of a structural system, including the infilled RC frame, depends on experimental work. A review of the available published experimental data describing the effect of infill walls on the overall structural response of RC frames finds significant scatter in the obtained results, due to the large number of uncertainties involved in the various investigations carried out to date. This data can describe qualitatively the effect of infill walls, but it is not yet possible to quantify this effect experimentally. Since the formulation and validation of mathematical (numerical or analytical) models is based on available experimental data, the validity of the yield predictions of current software packages is currently questionable.

Due to the difficulties, limitations, and high costs associated with the testing of infilled RC frames, resort is frequently made to the use of nonlinear finite element analysis (NLFEA). The use of the FE method can provide a more detailed description of the effect of infill walls on the response of infilled frames. At the same time, it allows the investigation to be extended to structural forms more complex than the simple structural elements that are usually studied experimentally (i.e., scaled models of one- or two-story infilled frames with column height to beam length equal to values from 0.75 to 1.25). To qualify for accurately capturing the behavior of a concrete structure, a FEA package must predict the structural response within an error of up to 20 %. Such a package should also employ appropriate constitutive models and adopt nonlinear numerical procedures capable of capturing the force redistribution and cracking processes of brittle materials.

To this end, constitutive relationships must be defined for the use of finite element models of infilled frames. The use of 3D solid, instead of linear, elements in constitutive models requires a considerably higher level of model sophistication. Models of concrete behavior are based either on regression analyses of experimental data (empirical models) or on continuum mechanics theories, which should also be verified against experimental data. Many such models have been proposed, but the application of FE packages in practical structural analysis has shown that the majority of constitutive relationships are case dependent, since the solutions obtained are realistic only for specific types of problems. The application of these packages to a different set of problems requires modification, sometimes significant, of the constitutive relationships. The situation is better for the reinforcement. However, complications arise with the introduction of bond-slip laws, which results in large discrepancies in predicted behavior.

Regarding the modeling of the infill panels, the great number of influencing factors, such as dimension and anisotropy of the bricks, joint width and arrangement of bed and head joints, material properties of both brick and mortar, and quality of workmanship, make the simulation of plain brick masonry extremely difficult. The level of complexity of the analytical model depends on whether masonry is considered as one-, two-, or three-phase material, where the three phases are comprised of the units, mortar, and unit-mortar interface.

Another level of complexity is added with the modeling of the infill-frame interface, which determines the boundary conditions of the infill and its interaction with the bounding frame. Springs and interface elements have been used by various researchers to represent the interaction between deformable structures such as these, where interfacial separation and sliding may arise.

Infill walls have also been represented by boundary elements. These are combined with FE, which can represent the bounding frame.

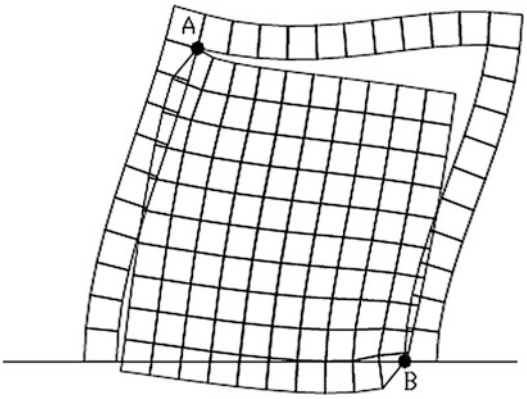

Assessment and Strengthening of Partitions in Buildings, Fig. 4 Finite element mesh for a non-integral infilled frame (Reprinted from Asteris et al. 2013 with permission from Elsevier)

This type of model reduces computational costs considerably, since the infill is represented by a single boundary element. However, the applicability of these models is limited to the elastic behavior of the infill; once cracks are initiated, boundary elements hold a disadvantage as they can be implemented only with extreme difficulty in nonlinear problems.

Mesh sensitivity poses a further challenge (Fig. 4). Very dense meshes are often thought to provide better results, but this is not always true when brittle materials are modeled. The size of the 3D brick FEs used for modeling concrete continua should be equivalent to the size of the cylinders used in testing. These are assumed to constitute a "material unit" for which average material properties are obtained. Hence, the volume of these specimens provides a general guideline for the size of the FE that should be used for the modeling of concrete structures. Furthermore, each Gauss point of a FE must correspond to a volume at least three times the size of the largest aggregate used in the concrete mix, in order to provide a realistic representation of concrete, rather than a description of its constituent materials.

Regarding the crack formation, the smeared-crack approach, rather than the discrete-crack approach, is usually adopted for the modeling of the cracking. With this approach, one may avoid the complexities linked to remeshing, which is required by the discrete-crack approach.

The discrete element method (DEM) originated from the studies of fractured rock masses and is also used for the modeling of infill walls. Due to its capability of representing explicitly the motion of multiple, intersecting discontinuities, the DEM is particularly suitable for the analysis of discontinuity, such as masonry structures, where significant deformation occurs as relative motion between the blocks. The disadvantage of this element arises in the case of complicated deformation problems (e.g., beam-column component behavior in an infilled frame), where the number of triangular elements into which the area has to be discretized may become very large. The main difference between DEM and other continuum-based methods (e.g., FEM) is that the contact points in DEM are automatically updated and changed based on the "contact overlap" concept, leading to the detection of new contacts and complete detachment of blocks as the calculation process allows.

For the solution of the nonlinear dynamics problem, FEA packages use an iterative scheme, such as the Newton-Raphson method, and an implicit or explicit integration scheme. Some of these procedures have been adapted to take into account the brittle nature of the constitutive model of concrete with satisfactory results.

A large number of procedures/techniques have been used to apply micromodeling to infill frames, while taking into account all of the above parameters. Each of these models has its own merits and limitations, as well as level of complexity, and has been used to study different sets of parameters affecting the behavior of infilled frames.

The knowledge acquired over the years has made possible the development of commercial packages that provide a wide selection of elements, constitutive relationships, and solution schemes that researchers may use as tools for the study of such complex problems as the ones described above. Nevertheless, only recently have such packages been used for the study of infilled frames. A thorough discussion of the above concepts and models is presented by Asteris et al. (2013).

Reinforced Concrete Infills in Reinforced Concrete Frames

The construction of new walls is the most effective and economic method for retrofitting multistory reinforced concrete (RC) buildings, especially those with pilotis (soft ground story). Their structural and economic effectiveness increases when selected bays of an existing RC frame are fully infilled with integral RC walls replacing masonry ones. Such a method is appealing since the intervention is concentrated in only certain bays of the frame and reduces the disturbance to the inhabitants as compared to the case of using concrete jackets on the columns.

Most of the experimental research work performed in the last decades has focused on other frequently used types of retrofitting, in particular on fiber-reinforced polymers (FRP) and concrete jackets. Research on the use of RC infill walls has mainly targeted what is feasible: testing of one- to two-story specimens. However, data is lacking for taller full-scale specimens that reflect real-life applications, due to the practical difficulties associated with the high forces needed for the tests. Regarding code provisions, Eurocode 8 – Part 3 fully covers retrofitting with FRP or concrete jackets, while it does not address the retrofitting of RC frames with the addition of new walls created by infilling selected bays.

Experimental research on reinforced concrete frames converted into walls by infilling with RC has been carried out almost exclusively in Japan and Turkey. The experiments in Japan (Chrysostomou et al. 2013, 2014) were performed on a total of 27 1:3–1:4 scale single-story one-bay RC-infilled frames with RC infill walls with a thickness of 26–60 % (on the average 43 %) of the width of the frame members. The test results were compared in most cases with monolithically cast specimens of the same geometric characteristics (in which the frame and the infill wall were cast at the same time and integrally connected). The connection of the RC infill to the bounding frame was done by means of epoxy-grouted dowels (17 specimens) or through mechanical devices, such as shear keys and dowels without epoxy (6 specimens). In four other test campaigns, the thickness of a preexisting thin wall was increased by 100–150 % without any direct connection of the new wall with the bounding frame. The failure mode of all specimens was in shear (including sliding at the interface). It is interesting to note that for epoxy-grouted dowels, the force resistance of the infilled frame was on average 87 % of the integral one, while for the mechanical connections it was 80 % on average. For the increased thickness of an existing thin infill wall, the force resistance was on average 92 % of the monolithic specimen, while the displacement at failure was on average 13 % smaller than for the integral specimen. For the epoxy-grouted dowels and for the mechanical connection, the ultimate deformation was on average 55 % and 115 % larger than in the integral specimen, respectively. The results show that although a deformable connection gives a somewhat reduced strength with respect to the monolithic case, the ultimate deformation of the retrofitted structure is considerably increased.

Among the specimens tested in Turkey (Chrysostomou et al. 2013, 2014), some were single-story one-bay 1:2 and 1:3 scale, with RC infill thickness 25 % and 33 % of the width of the frame members. Others were two-story one-bay scaled at 1:3, with infill wall thickness 33 % and 40 % of the width of the members of the bounding frame. The RC infill was in most cases fully connected on the perimeter with dowels, in some cases there was a gap between the infill and the columns, while in some other cases there was no connection other than simple bearing. In one case, the rebars of the infill were welded to those of the members of the frame, instead of using dowels, and monolithic specimens (not exactly similar to the infilled ones) were included for comparison purposes. Finally, there was a two-story three-bay specimen scaled at 1:3, with the middle bay infilled with a wall with 63 % thickness of the width of the frame members. The connection was made with epoxy-grouted dowels and the failure mode was predominantly flexural. In all other cases, the single-story walls failed in shear, while the two-story walls failed in a combination of flexure and shear sliding at the base.

The test specimens used in the experiments described in the previous paragraphs correspond to walls with failure modes dominated by shear, with low aspect ratios not representative of multistory slender walls. In fact, the failure mode of multistory slender walls is controlled by bending and the design is governed by the formation of a plastic hinge at the base. In such a case, shear will not have a detrimental effect on displacement and energy dissipation capacity. In addition, it has been shown numerically that higher modes may increase considerably the shear forces at the upper floors of a wall after the formation of a plastic hinge at the base. This aspect has never been studied experimentally because their height and number of stories has not been large enough to allow higher mode inelastic response. Another common element of past tests is the smaller thickness of the RC infill wall relative to the width of the frame members. As a result, the weak link of the structural system is either the infill wall in diagonal compression or its connection with the surrounding frame.

In order to start bridging the gap of knowledge regarding infilling of existing RC frames with RC walls, the effectiveness of seismic retrofitting of multistory multi-bay RC-frame buildings by converting selected bays into new walls through infilling with RC was studied experimentally at the European Laboratory for Structural Assessment (ELSA) of the Joint Research Centre in Ispra (Italy). Similar tests on scaled 0.75:1 specimens were performed at the Structures Laboratory of the University of Patras. Detailed description of the former results is presented by Chrysostomou et al. (2013, 2014) and for the latter by Fardis et al. (2013).

The test specimen in ELSA was designed based on a four-story prototype building structure consisting of four three-bay frames spaced at 6 m, with RC infilling of the exterior frames only. The specimen was designed at full scale to represent the two exterior frames of the prototype structure, spaced at 6 m and linked by a 0.15 m thick RC slab.

The dimension of the specimen in the direction of testing was 8.5 m (two exterior bays of 3.0 m and a central bay of 2.5 m), with an interstory height of 3.0 m and a total height, excluding the foundation, of approximately 12.0 m. The structure was designed for gravity loads only using the code provisions of the 1970s in Cyprus.

Assessment and Strengthening of Partitions in Buildings, Fig. 5 Elevation of the specimen in the lab with the south wall on the right of the picture (Chrysostomou et al. 2014 with kind permission from Springer Science and Business Media)

In order to facilitate the study of the effect of as many parameters as possible, the walls in the two frames, which had a thickness of 0.25 m equal to the width of the beams and columns of the bounding frame, were reinforced with different amounts of reinforcement, with the north frame being the stronger of the two. Figure 5 depicts the south and north frames, with the south one being on the right of the picture.

The design approached used by Fardis et al. (2013) was adopted and two parameters were examined: (a) the amount of web reinforcement in the walls and (b) the connection detail between the wall and the bounding frame. Regarding the connection with the bounding

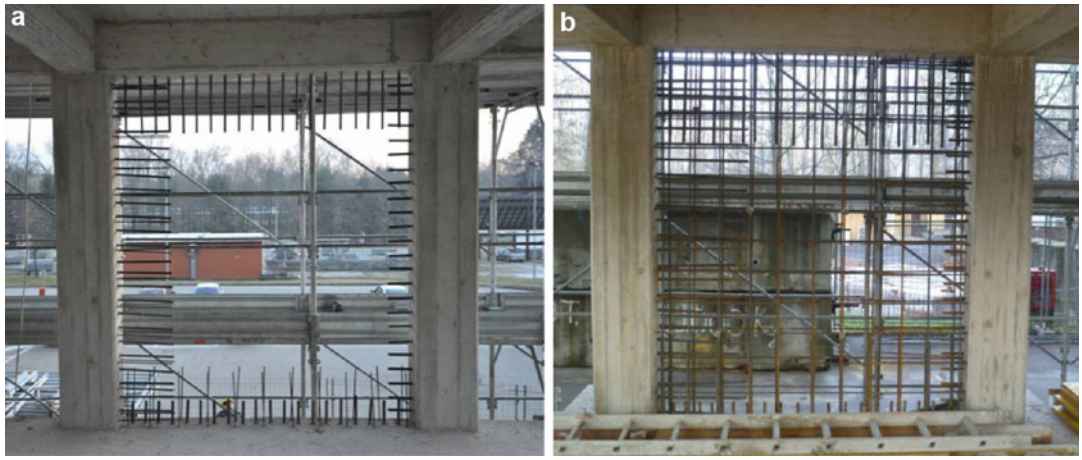

Assessment and Strengthening of Partitions in Buildings, Fig. 6 (**a**) Dowels and starter bars. (**b**) Dowels, starter bars, and web reinforcement (Chrysostomou et al. 2014 with kind permission from Springer Science and Business Media)

frame, two distinct connection details were used. In the first detail, the web bars are connected to the surrounding frame through lap splicing with same diameter starter bars epoxy grouted into the frame members. Short dowels are then used in order to transfer the shear at the interface between the wall and the frame members (see bottom beam of Fig. 6a).

In the second detail, longer dowels were used to act both as dowels and as anchorage of the web panel to the surrounding frame (see left column and top beam of Fig. 6a); to this end, the dowels are considered as lap spliced with the nearest – smaller diameter – web bars. The complete wall reinforcement (including web, starter bars, and dowels) is shown in Fig. 5b.

Since the lapping of the column reinforcement can only take compression forces, a lap-splice failure in tension would be highly detrimental to the whole experiment. Therefore, in order to safeguard against this type of failure and allow the experiment to be performed without any premature failure, it was decided to reinforce the bounding columns of the wall at the first floor with three-sided CFRP (carbon-fiber-reinforced polymer) for a height of 0.60 m from the base of the column (Fig. 7).

The testing campaign consisted of two pseudo-dynamic tests (one at 0.10 g and the other at 0.25 g) and a cyclic test. Some findings regarding the behavior of the structure are:

Assessment and Strengthening of Partitions in Buildings, Fig. 7 CFRP reinforcement of the column to safeguard against lap-splice failure (Chrysostomou et al. 2014 with kind permission from Springer Science and Business Media)

1. The structure managed to sustain an earthquake of 0.25 g without significant damage.
2. Some column lap splices failed with concrete spalling, but the structure continued to carry load.
3. The three-sided CFRPs protected the wall bounding columns at the firstt floor and prevented lap-splice failure.

4. The "weak" south frame behaved equally well as the "strong" north frame.
5. The slip displacements at the horizontal interfaces of the ground-floor walls were of the order of 0.8 mm, which is very close to the full engagement of the starter bars but not of the dowels.
6. The slip displacements between the wall and the bounding columns of the ground floor were of the order of 0.4 mm.
7. The behavior of the wall was mainly flexural; yielding took place at both the ground-floor and the first-floor walls.
8. The distribution of strains along the bounding columns of the walls shows that the ones for the ground floor are much larger than those of the first floor, while those of the second and third floors are negligible.
9. The two connection arrangements used behaved satisfactorily.
10. Higher mode effects appeared in the response of the structure.
11. Some vertical cracks appeared at the connection of the beams to both the exterior and the wall columns.
12. A horizontal crack appeared at the ground beam of the walls, which was the main cause for the loss of strength of the south frame.

It was demonstrated that this is a viable method for retrofitting and it can be used to strengthen existing ductility and strength-deficient structures. The recorded global and local behavior of the structure provides data for the development of numerical models, to facilitate the proposal of design guidelines for such a retrofitting method.

Strengthening of Partitions

In general, infill walls and in particular the masonry infill panels exhibit a small plastic region on the stress-strain curve due to significant decrease in stiffness, strength, and energy absorption capacity. In order to enhance the behavior of infill partitions and remove their inherent deficiencies, various researchers have proposed methods for improving the performance of these elements.

One of the methods is to use shotcreting on the faces of masonry infills which can increase the stiffness and the lateral load capacity of the infilled frame and reduce the lateral drift at the ultimate load. Calvi and Bolognini (2001) have performed full-scale tests in which they have placed a 10 mm plaster on both sides of a masonry infill wall covering either reinforcement (Ø5 mm or Ø6 mm) or wire meshes and have studied the behavior of the strengthened infilled frame. Based on their observations from the experiments, the introduction of some reinforcement in the mortar layers, with a geometrical percentage lower than 1 %, will almost double the acceleration levels for the occupational and damage limit states.

Another technique is the use of fiber-reinforced polymer (FRP) reinforcement to enhance the overall response of such systems. Several experimental studies have been performed which demonstrate that significant improvement of strength and energy absorption capacity can be achieved if adequate anchoring is provided.

Altin et al. (2008) investigated experimentally the behavior of strengthened masonry-infilled reinforced concrete (RC) frames using diagonal carbon fiber-reinforced polymer (CFRP) strips under cyclic loads. Test results indicated that, CFRP strips significantly increased the lateral strength and stiffness of perforated clay brick-infilled nonductile RC frames. Specimens receiving symmetrical strengthening showed higher lateral strength and stiffness, compared to the ones at which CFRP strips of the same width were applied to one of the interior or exterior surface of the infill wall. In the latter case, similar lateral strength and stiffness was obtained, irrespective of the side of placement of the strips.

Lunn and Rizkalla (2009) used glass fiber-reinforced polymer (GFRP) systems for increasing the out-of-plane resistance of infill masonry walls to loading. They have concluded that GFRP strengthening of infill masonry walls is effective in increasing the out-of-plane load-carrying capacity when proper anchorage of the FRP laminate is provided. They also note that the latter has a significant effect on the failure mode of the assemblage.

Papanicolaou et al. (2007) have used the textile-reinforced mortar (TRM), which is a new structural material, for testing its capability for increasing the load-carrying capacity and deformability of unreinforced masonry walls subjected to cyclic in-plane loading. TRMs comprise fabric meshes made of long woven, knitted, or even unwoven fiber rovings in at least two directions. The density of rovings in each direction can be controlled independently, thus affecting the mechanical characteristics of the textile and the degree of penetration of the mortar matrix through the mesh openings.

Based on the experimental results, the authors stated that, in terms of strength, TRM jackets are at least 65–70 % as effective as FRP jackets with identical fiber configurations. In terms of deformability, of crucial importance in seismic retrofitting of unreinforced masonry walls, TRM jacketing for shear walls is about 15–30 % more effective than FRP. They therefore conclude that TRM jacketing is an extremely promising solution for strengthening and seismic retrofitting of unreinforced masonry walls subjected to in-plane loading.

A more recent development is the use of engineered cementitious composites (ECC) which are a special class of fiber-reinforced cement-based composite materials, typically reinforced with polyvinyl alcohol fibers. Dehghani et al. (2013) have tested in diagonal compression a number of specimens with different ECC-strengthening configuration, and they evaluated their in-plane deformation and strength properties, including the post-peak softening behavior. They state that the proposed technique can effectively increase the shear capacity of masonry panels (1.5–2.8 times), improve their deformability, enhance their energy absorption capacity (35 times), and prevent the brittle failure mode.

Summary

The presence of infill walls has shown that in most cases they have beneficial effects on the behavior of structures during earthquakes and have contributed in the prevention of collapse of many structures. It is therefore for this reason that efforts have been made to use engineered infills to retrofit existing seismic-deficient buildings, since they present an economically viable solution. Several equations have been introduced to define the stiffness of infilled frames and their capacities, which are related to a number of failure modes. These were considered in macro- and micro mathematical models that have been proposed to simulate their behavior and their interaction with the bounding frame. The former are simpler (especially the single-strut models), while the latter require a higher level of modeling sophistication. The construction of new walls is the most effective and economic method for retrofitting multistory reinforced concrete (RC) buildings, especially those with pilotis (soft story). Their structural and economic effectiveness increases when selected bays of an existing RC frame are fully infilled with integral RC walls replacing masonry ones. Recent experimental investigations make possible the quantification of this methodology and the proposal of code equations for the design of such systems. Several methods exist for improving the properties of infilled panels avoiding brittle failure and increasing their load-carrying capacity as well as their energy absorption during an earthquake.

Cross-References

- ▶ Numerical Modeling of Masonry Infilled Reinforced Concrete Frame Buildings
- ▶ Retrofitting and Strengthening of Structures: Basic Principles of Structural Interventions
- ▶ Seismic Fragility Analysis
- ▶ Seismic Strengthening Strategies for Existing (Code-Deficient) Ordinary Structures
- ▶ Seismic Vulnerability Assessment: Reinforced Concrete Structures
- ▶ Strengthening Techniques: Code-Deficient R/C Buildings
- ▶ Strengthening Techniques: Code-Deficient Steel Buildings
- ▶ Time History Seismic Analysis

References

Altin S, Anil Ö, Kara ME, Kaya M (2008) An experimental study on strengthening of masonry infilled RC frames using diagonal CFRP strips. Compos Part B Eng 39(4):680–693

Asteris PG, Antoniou ST, Sophianopoulos DS, Chrysostomou CZ (2011) Mathematical macromodeling of infilled frames: state of the art. J Struct Eng ASCE 137(12):1509–1517

Asteris PG, Cotsovos DM, Chrysostomou CZ, Mohebkhah A, Al-Chaar GK (2013) Mathematical micromodeling of infilled frames: state of the art. Eng Struct 56:1905–1921

Calvi GM, Bolognini D (2001) Seismic response of reinforced concrete frames infilled with weakly reinforced masonry panels. J Earthq Eng 5(2):153–185

CEN (2004) Eurocode 2: design of concrete structures-part 1: general rules and rules for buildings (EN-1992-1-1), Comité Européen De Normalisation, Brussels

Chrysostomou CZ (1991) Effects of degrading infill walls on the nonlinear seismic response of two-dimensional steel frames. PhD thesis, Cornell University, Ithaca

Chrysostomou CZ, Asteris PG (2012) On the in-plane properties of infilled frames. Eng Struct 41:385–402

Chrysostomou CZ, Gergely P, Abel JF (2002) A six-strut model for nonlinear dynamic analysis of steel infilled frames. Int J Struct Stab Dyn 2(3):335–353

Chrysostomou CZ, Poljanšek M, Kyriakides N, Molina J, Taucer F (2013) Pseudo-dynamic tests on a full-scale 4-storey RC frame seismically retrofitted with RC infilling. Struct Eng Int J IABSE 23(2):159–166

Chrysostomou CZ, Kyriakides CN, Poljanšek M, Taucer F, Molina F (2014) Chapter 17: RC infilling of existing RC structures for seismic retrofitting. Seismic evaluation and rehabilitation of structures, geotechnical, geological and earthquake engineering, vol 26. doi:10.1007/978-3-319-00458-7_17

Comité Euro-International du Béton (CEB) (1996) RC frames under earthquake loading. State of the Art Rep., Tomas Telford Services, London

Crisafulli FJ, Carr AJ (2007) Proposed macro-model for the analysis of infilled frame structures. Bull N Z Soc Earthq Eng 40(2):69–77

Dehghani A, Fischer G, Alahi FN (2013) Strengthening masonry infill panels using engineered cementitious composites. Mater Struct. DOI 10.1617/s11527-013-0176-4

El-Dakhakhni WW (2000) Non-linear finite element modeling of concrete masonry-infilled steel frame, MSc thesis, Civil and Architectural Engineering Department, Drexel University, Philadelphia

El-Dakhakhni WW (2002) Experimental and analytical seismic evaluation of concrete masonry-infilled steel frames retrofitted using GFRP laminates. PhD thesis, Drexel University

El-Dakhakhni, WW, Elgaaly M, Hamid AA (2001) Finite element modeling of concrete masonry-infilled steel frame. In: 9th Canadian masonry symposium, The University of New Brunswick, Canada

El-Dakhakhni WW, Elgaaly M, Hamid AA (2003) Three-strut model for concrete masonry-infilled frames. J Struct Eng ASCE 129(2):177–185

Fardis MN, Schetakis A, Strepelias E (2013) RC buildings retrofitted by converting frame bays into RC walls. Bull Earthq Eng 11:1541–1561

Ghosh AK, Amde AM (2002) Finite element analysis of infilled frames. J Struct Eng ASCE 128(7):881–889

Hamburger RO, Meyer JD (2006) The performance of steel-frame buildings with infill masonry walls in the 1906 San Francisco earthquake. Earthq Spectra 22(S2):S43–S67

Kappos AJ, Ellul F (2000) Seismic design and performance assessment of masonry infilled R/C frames. In: Proceedings of the 12th world conference on earthquake engineering, paper no 989 on CD-ROM. Auckland, New Zealand

Lunn DS, Rizkalla SH (2009) Strengthening of infill masonry walls with FRP materials. J Compos Constr 15(2):206–214

Madan A, Reinhorn AM, Mander JB, Valles RE (1997) Modeling of masonry infill panels for structural analysis. J Struct Eng ASCE 123(10):1295–1302

Mehrabi AB, Shing PB (1997) Finite element modeling of masonry-infilled RC frames. J Struct Eng ASCE 123(5):604–613

Papanicolaou CG, Triantafillou TC, Karlos K, Papathanasiou M (2007) Textile-reinforced mortar (TRM) versus FRP as strengthening material of URM walls: in-plane cyclic loading. Mater Struct 40(10):1081–1097

Syrmakezis CA, Vratsanou VY (1986) Influence of infill walls to R.C. frames response. In: Proceedings of the eighth European conference on earthquake engineering, vol 3, Lisbon, pp 47–53

Vales RE, Reinhorn AM, Kunnath SK, Li C, Madan A (1996) IDARC2D version 4.0-a program for the inelastic damage analysis of buildings. Technical report NCEER-96-0010, National centre for earthquake engineering research, State University of New York, Buffalo

Assessment of Existing Structures Using Inelastic Static Analysis

Tatjana Isakovic
University of Ljubljana, Ljubljana, Slovenia

Synonyms

Nonlinear static analysis; Pushover-based analysis

Introduction

Over the last few decades, it has been found that the traditional procedures, which are based on elastic linear analysis, can only approximately estimate the typically nonlinear seismic response. Therefore, the inelastic methods of analysis have been gradually introduced into practice in order to estimate the seismic response more realistically. Contrary to the elastic linear methods which can only implicitly predict the performance, the objective of the inelastic seismic analysis procedures is to directly estimate the magnitude of inelastic deformations.

In general, the most refined and accurate inelastic method is the nonlinear response history analysis (NRHA). Nevertheless, it is only sporadically used in the design practice, since it is, for the time being, still too complex for regular use. It requires substantial experience and knowledge about the modeling of the dynamic response of structures and seismic loading. Specialized software is also needed. The results are typically quite extensive, and their interpretation is often time-consuming and too demanding for an engineer with an average knowledge about seismic engineering.

To keep the inelastic analysis relatively simple and make it more apparent for practicing engineers, different static inelastic methods have been developed. Mostly they are based on the pushover analysis. They are considered more user-friendly and relatively easy to understand. They have a great advantage in specifying the seismic input, i.e., they employ the familiar elastic response spectra instead of selecting and scaling ground motion histories (Kappos et al. 2012).

From the historical point of view, pushover analysis has been typically used as a convenient tool to estimate the nonlinear properties and capacity of individual structural components or the whole structure. It typically represents the first step of different static inelastic methods. More specifically, the static nonlinear analysis is performed using the multi-degree-of-freedom (MDOF) model of the analyzed structure. The main purpose of this analysis is to define the properties of the equivalent single-degree-of-freedom (SDOF) model, which is then further employed to estimate the maximum global displacement demand. This idea was first explored by Saiidi and Sozen (1981). Based on the estimated maximum global displacement demand, other response quantities of interest are then evaluated (see Fig. 1).

In the majority of pushover-based methods, the pushover analysis is performed in a similar manner (see section "Pushover Analysis: Numerical Models and the Lateral Load Pattern"). However, the techniques that are used to estimate the maximum displacement demand are quite different. The pushover-based methods can be classified with respect to different parameters, e.g., based on (a) the representation of the earthquake input, (b) the type of analysis performed on the SDOF model, and (c) the way how the stiffness of the equivalent SDOF model is defined.

The seismic input is represented by the acceleration response spectrum included in the codes and the displacement spectrum or with a set of accelerograms. The type of analysis is static, dynamic, or response history. The stiffness that is used to calculate the maximum displacement demand is the equivalent pre-yielding stiffness or the equivalent secant stiffness, usually obtained based on the pushover analysis. This variety of solutions can result in a different estimation of the response. In section "Different Applications of the Inelastic Pushover-Based Analysis, Adopted in the (Pre)Standards and Guidelines," those solutions (methods), which are adopted in Eurocode 8/3 (CEN 2005), ATC-40 (ATC 1996), and FEMA-356 (ASCE 2000), the recommended modifications in FEMA-440 (ATC FEMA 2005), and the displacement-based method, included in the NZSEE (2006), are presented. They were selected since they illustrate many of the basic concepts that are currently in use.

These methods are nowadays extensively and successfully used for the analyses of different types of buildings and bridges. Their popularity has increased since they are relatively simple to use but at the same time provide valuable information about the inelastic response, which is not possible to obtain with the elastic methods. They are a useful tool for understanding the general structural behavior corresponding to different

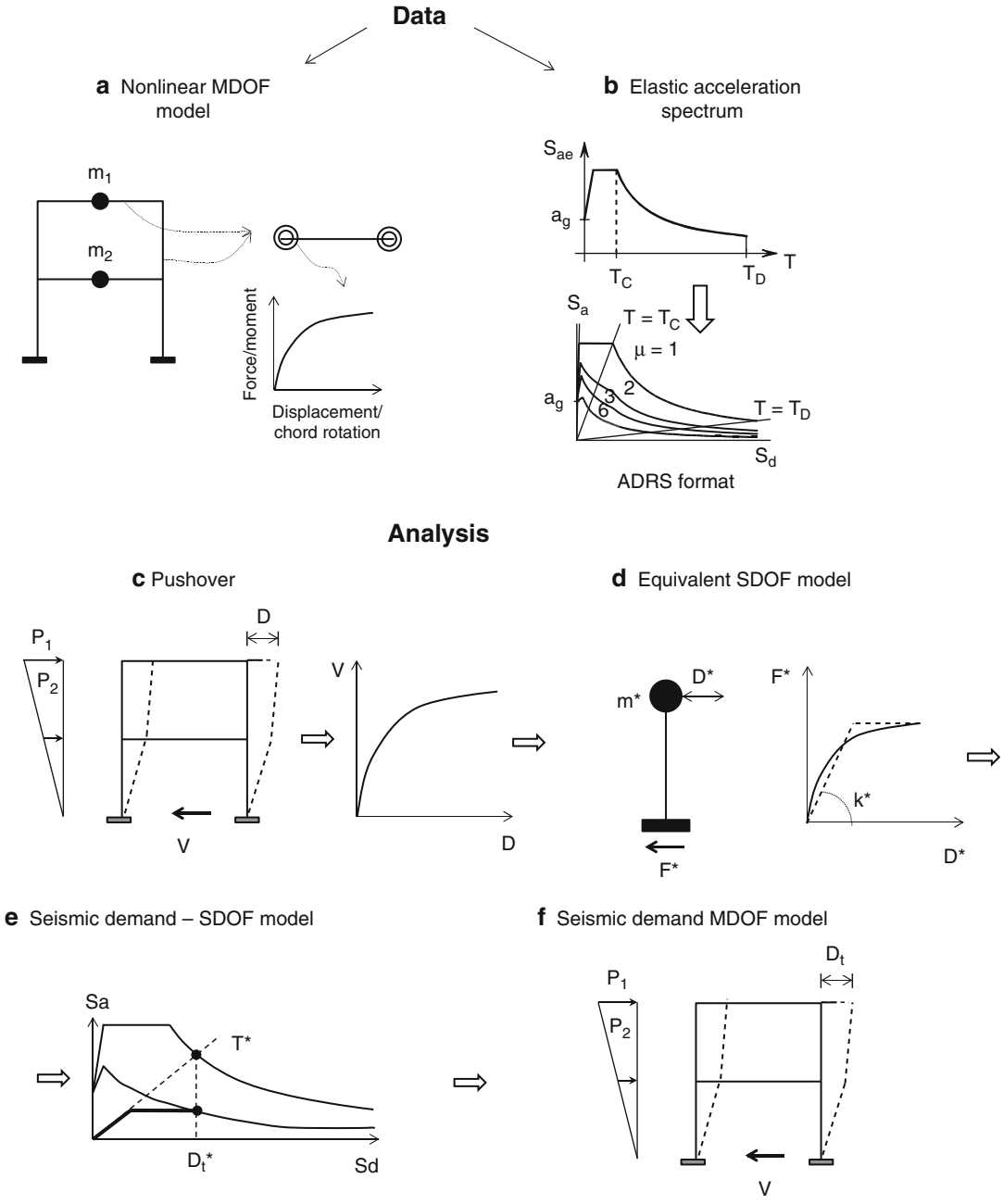

Assessment of Existing Structures Using Inelastic Static Analysis, Fig. 1 Version of the inelastic pushover-based analysis, included in EC8/3

seismic intensity levels. Besides other superior features, they can provide more realistic information about the force demand on brittle elements and the information on the influence of the strength degradation of individual components on the global behavior of the structure. They can identify the critical regions in the structure. This information is particularly useful when the existing structures have been evaluated and the strengthening techniques have been selected.

However, the pushover-based analysis includes certain assumptions which limit its capabilities. Basic variants of the above code methods can be characterized as single-mode nonadaptive methods, since they assume that the response is controlled by a single predominant mode, which remains unchanged after yielding occurs. This assumption limits their application, particularly when they are used for the assessment of those existing structures which are irregular in plan and/or in elevation. Consequently, the in-plan torsion and higher modes can significantly influence their response. In such cases the extended versions of the single-mode methods are needed. As an alternative, the other types of pushover methods, accounting for the influence of higher modes (multimode methods), can be used. Some issues that influence the applicability and the way of application of the single-mode methods are briefly discussed in section "Some Issues that Influence the Accuracy of the Inelastic (Single-Mode) Pushover-Based Methods." Some examples of the multimode pushover methods are briefly presented in section "Some Alternatives to Single-Mode Pushover-Based Methods."

The assumption that the fundamental mode shape is almost invariant can also limit and complicate the application of nonadaptive methods in existing structures, where the fundamental mode can change considerably depending on the seismic intensity. This can affect the choice of the lateral load pattern in the pushover analysis and make it more complex (see section "Different Applications of the Inelastic Pushover-Based Analysis, Adopted in the (Pre)Standards and Guidelines"). As an alternative, adaptive pushover methods can be used. An example of these methods is briefly presented in section "Some Alternatives to Single-Mode Pushover-Based Methods."

The methods presented in sections "Different Applications of the Inelastic Pushover-Based Analysis, Adopted in the (Pre)Standards and Guidelines" and "Some Alternatives to Single-Mode Pushover-Based Methods" were primarily developed for the analysis of buildings. The response of bridges, particularly in the transverse direction, can be significantly different and more complex. Therefore, some modifications of these procedures are needed. A short overview of the application of the inelastic static methods for the analysis of bridges is presented in section "Application of the Inelastic Static Methods to the Analysis of Bridges."

In this contribution, only those inelastic static methods that are included or referred to in the codes and national guidelines are presented. Quite a long list of other inelastic static procedures currently available in the literature can be created. Some of them are general, and some are specialized for certain types of structures. Many of them are presented in different state-of-the art reports (e.g., FEMA 440 2005; CEB-FIB 2003; Kappos et al. 2012, etc.) or other specialized literature (e.g., Bhatt 2011).

Pushover Analysis: Numerical Models and the Lateral Load Pattern

Pushover analysis is the static nonlinear analysis which is typically performed as the first step of the majority of the inelastic static methods for the seismic assessment of the (existing) structures. The structure is subjected to the lateral load (representing the inertial forces), the intensity of which is gradually increased. The corresponding lateral displacement at a certain location (the reference point or control point) in the structure is recorded. Then the pushover curve, representing the relationship between the base shear of the structure and the registered displacements, is constructed (see Fig. 1c).

The pushover analysis is usually performed employing the MDOF model of the structure which is similar to the linear elastic finite-element models (see Fig. 1a). The most important difference is that the properties of some or all of the components of the model include the post-elastic strength and deformation characteristics in addition to the initial elastic properties. They are usually defined approximating the response observed in the experiments or the response defined by the theoretical analysis of individual components. The envelopes or backbone curves

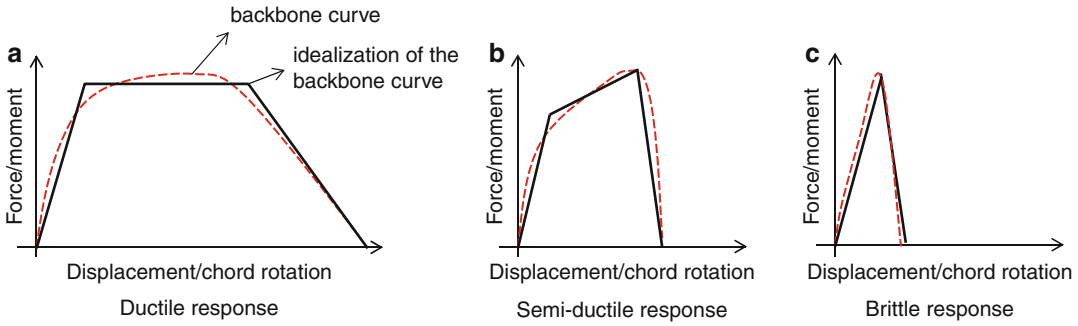

Assessment of Existing Structures Using Inelastic Static Analysis, Fig. 2 Idealized numerical models

are approximated based on the type of the response. Typical examples are presented in Fig. 2.

Contrary to the structures designed according to modern codes, where the brittle types of failure are in general avoided, in structures which were designed before the modern principles of seismic engineering were established, different types of brittle or semi-ductile failure of their structural components may be expected. Thus for the reliable estimation of their response, the appropriate numerical models should be employed. Their properties can be defined based on different procedures, defined in the (pre)standards, guidelines, and literature (e.g., CEN 2005, FEMA-356, ATC-40, CEB-FIP 2003). It is, however, worth noting that the available models which describe quite complicated mechanisms that reduce the ductility capacity of the structural components have been less frequently investigated and are often less reliable. The properties of these models are often defined using empirical or semiempirical procedures. The results of these procedures can be considerably different.

For example, the value of the shear strength of RC components can strongly depend on the method used to estimate it. The differences between different methods depend on many parameters, e.g., the amount of the flexural and shear reinforcement, the shear span ratio, the axial force, etc. Moreover, the numerical models that can take into account the complex interaction between shear and flexural response in the nonlinear range are still under investigation and evaluation (e.g., Mergos and Kappos 2008; Fischinger et al. 2012). Similar observations can be applied to other mechanisms, which reduce the ductility capacity of the structural components and the whole structure. Therefore, it is feasible to explore and compare different available options before the numerical model, and its properties are defined. All uncertainties related to the material properties should also be properly explored.

In the pushover analysis, the MDOF model of the structure is subjected to lateral forces that are intended to simulate the inertial forces expected in the building during an earthquake. They are usually distributed according to a selected (mostly invariant) pattern. It significantly influences the pushover curve and further determines the relative magnitudes of the shear forces, the moments, and deformations within the structure; therefore, it should be carefully selected, depending on the properties of the analyzed structure and the expected response. The distribution of the lateral inertial forces will in general vary continuously during the earthquake response, depending on the gradual formation of the plastic hinges in the structure. To take into account these changes, in many codes and guidelines, it is recommended to perform an analysis, taking into consideration at least two lateral force patterns. Typically the distribution of forces proportional to the fundamental mode of vibration in the elastic range and the uniform distribution are recommended. Then the most adverse results are taken into consideration. Other solutions

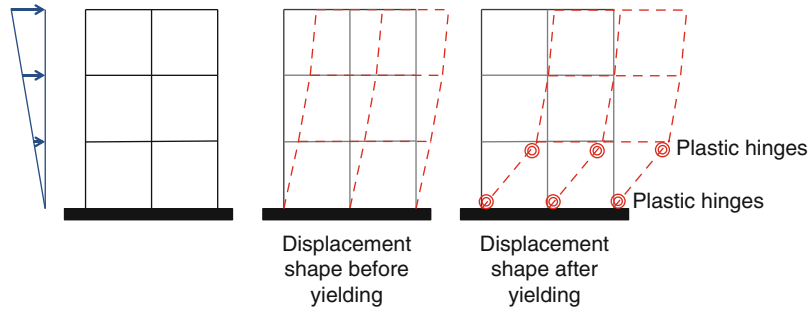

Assessment of Existing Structures Using Inelastic Static Analysis, Fig. 3 In some structures (e.g., with "soft" story), the deflection line can considerably change after yielding

recommended in the codes are presented in section "Different Applications of the Inelastic Pushover-Based Analysis, Adopted in the (Pre) Standards and Guidelines."

The approach described in the previous paragraph is in general appropriate for many structures, which are designed according to modern standards. However, in some older existing structures, this solution is not always suitable.

For example, in medium-rise frame buildings, which are designed according to capacity-design principles (where the columns' flexural strength exceeds the beam flexural strength), the triangular and uniform distribution are typically applied. In existing medium-rise buildings, this is also an appropriate solution, but only if the beam-sway mechanism is the most likely to be developed. In other words, the structure does not include a so-called soft. In opposite cases, the uniform distribution may not be able to frame the range of actions that may occur during the actual dynamic response. Thus a rather complex choice of the lateral force pattern may be needed. The response of such structures in the elastic range will be approximately linear (see Fig. 3). In the nonlinear range, the displacement pattern can considerably change after the formation of the plastic hinges, as is illustrated in Fig. 3. In such cases, some (pre) standards (e.g., FEMA-356, ATC-40) recommend the use of the adaptive load pattern, which can take into account changes of the displacement response shape corresponding to the seismic intensity applied. An alternative solution is the adaptive pushover-based methods (one of which is presented in section "Some Alternatives to Single-Mode Pushover-Based Methods"). Note, however, that if either the adaptive load pattern is used or the adaptive methods are applied, the analysis procedure is more complex and more demanding.

Similar observations to those presented above can be applied, e.g., to the RC dual and wall buildings, with the reinforcement that does not meet the requirements of current codes (e.g., where plastic hinges can form at the elevations above the foundations).

The accuracy of different lateral load patterns in structures where the higher modes have an important influence on the response is discussed in sections "Some Issues that Influence the Accuracy of the Inelastic (Single-Mode) Pushover-Based Methods" and "Application of the Inelastic Static Methods to the Analysis of Bridges".

Different Applications of the Inelastic Pushover-Based Analysis, Adopted in the (Pre)Standards and Guidelines

The static pushover analysis has no rigorous theoretical foundation. It is based on the assumption that the response of the structure (MDOF system) can be estimated using the results of the analysis of an equivalent SDOF oscillator (see Fig. 1). This means that it is assumed that the response is governed by one invariant mode of vibration. In general this is incorrect. However, the assumption is approximately fulfilled in many (regular) structures, where the influence of the higher modes is negligible and the deflection shape is almost invariable. Thus the seismic response of these MDOF systems is quite accurately estimated based on the analysis of an equivalent SDOF model. It is not the intention of this article

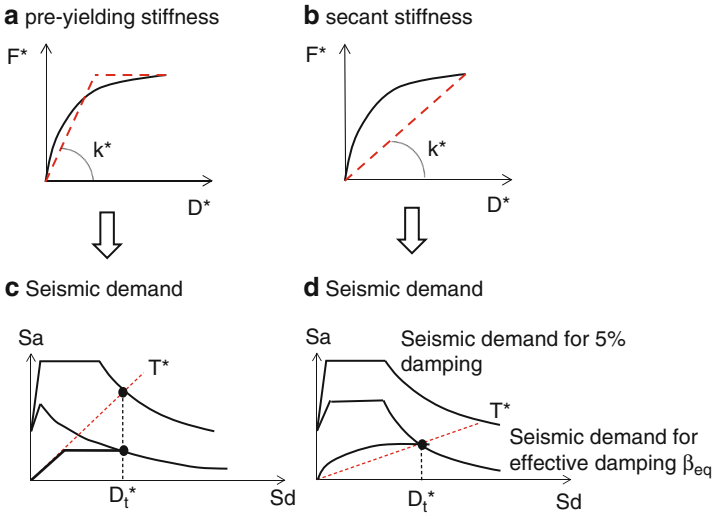

Assessment of Existing Structures Using Inelastic Static Analysis, Fig. 4 Two different concepts, which are used to define the properties of the equivalent SDOF model

to explain the theoretical background of the formulation of the equivalent SDOF system, since it can be found elsewhere (e.g., Krawinkler and Seneviratna 1998). Here, different applications of this basic concept, which are typically used for the assessment of the existing structures, are overviewed.

In most of the modern (pre)standards and guidelines for the assessment of existing structures, the simplest form of the pushover-based analysis is included. All methods that are included in these documents are based on the same basic concept presented above. However, these methods are not the same. The procedures which are used to define the properties of the equivalent SDOF model and those which are used to define the seismic demand of this model are different. In general two different approaches are used. The properties of the equivalent SDOF system are defined either based on the equivalent pre-yielding stiffness or based on the equivalent secant stiffness (see Fig. 4a, b).

If the first approach is employed, the maximum response of the SDOF oscillator is typically defined based on the 5 % damped acceleration spectra proposed in the codes. The target displacement of the equivalent SDOF system is obtained using the equal displacement rule approximation (see Fig. 4c). Since this approximation is only suitable for the medium- and long-period structures, the displacements are corrected for short-period structures. This approach is applied in, e.g., Eurocode 8/3 (EC8/3) and implicitly in FEMA-356 (see sections "Eurocode 8/3 (CEN 2005)" and "FEMA-356"). In FEMA-356, the maximum seismic displacements, estimated based on the analysis of SDOF system, are additionally corrected to take into account different issues which are not included in the pushover-based analysis such as strength degradation, P-Δ effect, etc.

If the secant stiffness is used to define the properties of the equivalent SDOF oscillator, typically the overdamped acceleration spectra are used (see Fig. 4d). Actually the capacity spectrum method approach is followed. It is explained later in section "ATC-40" where the method included into the ATC-40 is presented.

In the NZSEE 2006, different inelastic methods are included. The one which is conceptually different from those in other standards is described in this article (see section "FEMA-440"). Contrary to the previously mentioned procedures, the maximum seismic displacement at the reference point is assumed at the beginning of the analysis taking into account the estimated capacity of the structure. It is then used to estimate the properties of an equivalent SDOF model. The dynamic properties of the SDOF model are defined based on the secant stiffness corresponding to the assumed maximum

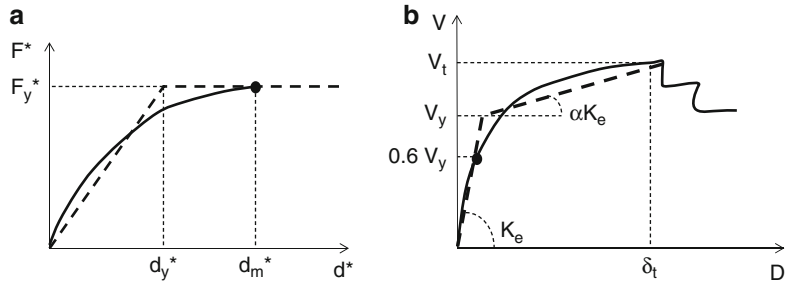

Assessment of Existing Structures Using Inelastic Static Analysis, Fig. 5 (**a**) Idealization of the capacity curve in EC8/2, (**b**) idealization of the pushover curve in FEMA 356

displacement. The seismic demand is estimated using the overdamped displacement spectra, derived from the 5 % damped acceleration spectra.

Since the methods included in different codes are conceptually different, they are presented in more detail in the next subsections. The FEMA-356 and ATC-40 methods were evaluated in the document FEMA-440, where their modifications are proposed. The main observations and the proposed modifications are presented in section "ATC-40." The matters of accuracy and different issues that can influence the pushover-based analysis of buildings are discussed in section "Some Issues that Influence the Accuracy of the Inelastic (Single-Mode) Pushover-Based Methods." The estimation of the response of bridges using the inelastic pushover-based analysis is presented in section "Application of the Inelastic Static Methods to the Analysis of Bridges."

Eurocode 8/3 (CEN 2005)

The method that is included in Eurocode 8/3 (EC8/3) was developed by Fajfar in the 1980s. Its description can be found in (Fajfar 1999). It is included in different parts of the Eurocode 8 standards. Actually the EC8/3 refers to Eurocode 8/1 (CEN 2004) – EC8/1 – and its informative annex B, where the suggested way of application of the method is presented. It is overviewed in Fig. 1.

In the first step, the pushover curve is constructed applying forces proportional to the assumed displacement shape. In EC8/3 it is required to consider at least two force patterns: (a) *modal pattern* – proportional to the lateral forces consistent with the lateral force distribution determined in an elastic analysis – and (b) *uniform load pattern*.

Based on the pushover analysis, the properties of the equivalent SDOF model are calculated. First, the pushover curve is converted to the capacity curve. Displacements and forces are divided by the transformation coefficient:

$$\Gamma = \frac{\Sigma m_i \phi_i}{\Sigma m_i \phi_i^2} \tag{1}$$

m_i is the mass at the location i in the structure (e.g., mass of ith floor of the building), and ϕ_i is a corresponding component of the assumed displacement shape.

Then the *equivalent pre-yielding stiffness* of the equivalent SDOF model k* is defined as is shown in Fig. 5a. The elastic-perfectly plastic idealization is proposed.

The mass of the SDOF oscillator is determined as

$$m^* = \sum m_i \phi_i \tag{2}$$

The period of vibration of the SDOF model is defined based on the m^* and k^*:

$$T^* = 2\pi \sqrt{\frac{m^*}{k^*}} \tag{3}$$

The target displacement d_t^* (inelastic displacement of the equivalent SDOF oscillator) is defined as

$$d_{et}^* = S_e(T^*) \cdot \left(\frac{T^*}{2\pi}\right)^2 \tag{4}$$

$$d_t^* = d_{et}^* \tag{5}$$

for medium- and long-period structures with $T^* \geq T_c$, where T_c is the corner period between the short- and medium-period range. $S_e(T^*)$ is the elastic acceleration in the response spectrum at the period T^*.

The same relationship is used for short-period structures if their response is elastic. If the response is nonlinear, then the target displacement is defined as

$$d_t^* = \frac{d_{et}^*}{q_u}\left(1 + (q_u - 1)\frac{T_C}{T^*}\right) \geq d_{et}^* \tag{6}$$

where q_u is the ratio between the acceleration in the structure with unlimited elastic behavior $S_e(T^*)$ and in the structure with limited strength F_y^*/m^*:

$$q_u = \frac{S_e(T^*)m^*}{F_y^*} \tag{7}$$

In the next step, the seismic displacement of the structure (MDOF model) is defined multiplying the target displacement by the transformation coefficient Γ.

The static nonlinear analysis of the MDOF system is repeated up to the estimated seismic displacement in order to be able to analyze different aspects of the response (e.g., story drifts, shear forces, bending moments). The same loading pattern as in the first pushover analysis is employed.

If the target displacement d_t^* is quite different from the displacement d_m^* used to determine the idealized elastic-perfectly plastic force-displacement relationship, an iterative procedure may be applied.

FEMA-356

In the first step, the pushover analysis is performed. As in the EC8/3, at least two lateral force patterns need to be applied. Three possibilities are defined for the *first load pattern*: (a) forces proportional to the fundamental mode; (b) forces proportional to the values of coefficient C_{vx}, defined in the standard; and (c) proportional to the story shear distribution calculated by combining the modal responses from a response spectrum analysis of the building. The use of patterns (a) and (b) is limited to structures where more than a 75 % mass participate in the fundamental mode. The pattern (c) can be used in structures where the period of the fundamental mode exceeds 1 s.

For the *second load pattern*, two options are defined: (a) uniform distributions and (b) an adaptive load distribution that changes when the new plastic hinges are formed (see the discussion in section "Pushover Analysis: Numerical Models and the Lateral Load Pattern"). Different options for the adaptive load distribution are referred to in Fajfar and Fischinger (1988), Eberhard and Sozen (1993), and Bracci et al. (1997).

The pushover curve is idealized as is shown in Fig. 5b. The idealization is bilinear. Note that only the case with a positive post-yield slope is presented in Fig. 5b. In the standard, the case with the negative post-yield slope is also considered. The effective period T_e is defined based on the pre-yielding stiffness, determined in the idealized pushover curve.

The seismic displacement (the term target displacement is used in FEMA-356, but it does not have the same meaning as in the EC8/3) is defined using the so-called coefficient method as

$$\delta_t = C_0 C_1 C_2 C_3 \cdot S_a \frac{T_e^2}{4\pi^2} g \tag{8}$$

where

T_e is the effective fundamental period

S_a response spectrum acceleration at the effective fundamental period

g gravitational acceleration

C_0 is the modification factor to relate the spectral displacement of an equivalent SDOF system to the roof displacement of the building's MDOF system. Actually it has a similar meaning as factor Γ in EC8/3

C_1 is the modification factor to relate the expected maximum inelastic displacements to the displacements calculated for the linear elastic response. The meaning is similar to the

relationship between d_t* and d_{et}*in EC8/3. For long- and medium-period structures, C_1 is 1, and for short-period structures, it is

$$C_1 = \frac{\left(1 + \frac{(R-1)\cdot T_s}{T_e}\right)}{R} \tag{9}$$

R is the ratio of elastic demand to the calculated strength capacity (a similar meaning to q_u in EC8/3).

The C_2 modification factor represents the effect of a pinched hysteretic shape, stiffness degradation, and strength deterioration on the maximum displacement response.

The C_3 modification factor represents increased displacements due to dynamic P-Δ effects.

ATC-40

While several similarities can be found between the EC8/3 and FEMA-356, the simplified nonlinear procedure in ATC-40 is rather different. It is based on the equivalent linearization. This is a version of the capacity spectrum method, which was first introduced by Freeman et al. (1975). The basic assumption is that the maximum displacement of the nonlinear SDOF system can be estimated from the maximum displacement of a linear elastic SDOF system that has the period and damping ratios that are larger than those of the initial values for the nonlinear system. The elastic SDOF system that is used to estimate the maximum inelastic displacements of the nonlinear system is usually referred to as the equivalent or the substitute system. The period and damping of the equivalent system are referred to as the equivalent period and equivalent damping ratio, respectively.

As in the previous two methods, the pushover analysis is performed first. In general, ATC-40 recommends the distribution of the lateral forces proportional to the fundamental mode pattern. In structures where the response considerably changes after yielding (e.g., in structures with soft stories – see the discussion in section "Pushover Analysis: Numerical Models and the Lateral Load Pattern"), the adaptive load pattern is required. In high-rise buildings or irregular buildings, the influence of the higher modes should be properly taken into account. The higher mode effects may be determined by doing higher mode pushover analyses.

The application of the capacity spectrum technique means that both the structural capacity curves and the demand response spectra are plotted in the spectral acceleration versus the spectral displacement domain and compared. Therefore in the next step, the pushover curve is converted to the capacity spectrum curve using the modal shape vectors, participation factors, and modal masses obtained from a modal analysis of the structure. The capacity spectrum curve represents the relationship between accelerations S_a and displacements S_d of the equivalent SDOF oscillator. Then the standard elastic acceleration spectrum (corresponding to 5 % damping) is converted to the ADRS format, where the spectral accelerations are presented as a function of the corresponding spectral displacements (see Fig 4d). In this way, the capacity curve and the seismic demand can be plotted on the same axes and compared.

The capacity spectrum method of equivalent linearization assumes that the equivalent damping of the system is proportional to the area enclosed by the capacity curve. The equivalent period, T_{eq}, is assumed to be the secant period at which the seismic ground motion demands, reduced by the equivalent damping, intersect the capacity curve (FEMA-440). Since the equivalent period and damping are both a function of the displacement, the solution to determine the maximum inelastic displacement (i.e., performance point) is iterative.

The equivalent period T_{eq} and effective viscous damping β_{eq} (which is used to reduce the seismic demand) are defined as

$$T_{eq} = T_0\sqrt{\frac{\mu}{1+\alpha\mu-\alpha}} \tag{10}$$

$$\beta_{eq} = 0,05 + \kappa\frac{2\cdot(\mu-1)\cdot(1-\alpha)}{\pi\cdot\mu\cdot(1+\alpha\mu-\alpha)} \tag{11}$$

where

T_0 is the initial period of vibration of the nonlinear system, α is the post-yield stiffness

ratio, and κ is an adjustment factor to approximately account for the changes in the hysteretic behavior in reinforced concrete structures.

The adjustment factor κ depends on the hysteretic behavior of the system. Three equivalent damping levels are defined. Type A corresponds to structures with reasonably full hysteretic loops, similar to the elastic-perfectly plastic oscillator. Type C corresponds to structures with severely degraded loops, and type B denotes the hysteretic behavior between types A and C. The value of κ and the corresponding equivalent damping is the largest for systems with a hysteretic behavior of type A. Their values decrease for degrading systems B and C. The existing buildings are in general categorized as structures of type C or B, depending on the shaking duration and hysteretic behavior of the structural components.

Based on the comparison of the capacity curve and seismic demand, the target displacement is defined. This displacement is then converted to roof displacement and other aspects of the response are defined.

The ATC-40 method is also well accepted due to the clear and useful visualization of the procedure. Note, however, that the procedure, defined in EC8/3, can also be presented in a similar manner; nevertheless, it is essentially different. The capacity curve as well as the seismic demand, defined in EC8/3, can also be converted to the ADRS format, plotted on the same axes and compared, as is presented in Fajfar (1999) and illustrated in Fig. 4c.

FEMA-440

FEMA-440 is the document where the previously described procedures (FEMA-356 and ATC-40) are evaluated. Improvements of both methods are recommended. Since the document is extended with many important observations, particularly for the existing structures, only some of the conclusions related to the methods included in FEMA-356 and ATC-40 are provided in this section. Some of them are also presented in section "Some Issues that Influence the Accuracy of the Inelastic (Single-Mode) Pushover-Based Methods."

Some Observations and Proposed Improvements of the Procedure, Included in FEMA-356

It was observed that the characteristic periods which are used to differentiate the response of short- versus medium- and long-period structures were found to be shorter than those observed from nonlinear response history analyses. This can result in an underestimation of the inelastic deformations for the periods between the characteristic period and the periods that are approximately 1.5 times the characteristic period.

The equal displacement rule approximation was found to lead to a relatively good approximation of the maximum inelastic deformations for systems with elastic-perfectly plastic behavior and periods longer than 1 s. This is not always applicable to soft soil sites and near-fault records.

The limiting values of coefficient C_1, which defines the ratio of elastic and inelastic deformations, can lead to a large underestimation of the displacements in short-period structures. Even if this limitation was not taken into account, the magnification of inelastic displacement demands with a decreasing lateral strength for short-period structures was found to be larger than that suggested by FEMA-356. The corrections of coefficient C_1 were proposed for short-period structures.

It was observed that in many cases the cyclic degradation does not increase the maximum displacements. Thus the use of the related coefficient C_2 is recommended only for structures with significant stiffness and/or strength degradation. Coefficient C_2 is corrected.

It was found that coefficient C_3, which is intended to represent an increase of displacements due to the dynamic P-Δ effects, cannot adequately take into account the possibility of dynamic instability. It was proposed that this coefficient be eliminated. Instead, it was proposed to use the NRHA for all structures where the strength is below the limit proposed in FEMA-440.

Some Observations and Proposed Improvements in the Procedure Included, in ATC-40

The accuracy of the estimated maximum displacement response in long-period structures depends on the hysteretic behavior type.

In structures with hysteretic behavior type A and periods longer than about 0.7 s, the ATC-40 procedure underestimates the maximum displacements. In structures with a hysteretic behavior type B and periods longer than about 0.6 s, small underestimations or overestimations of the maximum displacements were observed. This depends on the level of lateral strength and on the site class. For structures with hysteretic behavior type C, the ATC-40 procedure leads to an overestimation of the lateral displacements regardless of the period of the structure.

In short-period structures (with periods shorter than noted in the previous paragraph), a significant overestimation of the maximum displacements were observed. The overestimation increases with decreasing strength.

It was also found that the ATC-40 assumption, where it is supposed that the inelastic deformation demands of structures with hysteretic type B will be larger than those in structures with hysteretic type A, does not agree with the results of the NRHA. According to the NRHA, these deformations were approximately the same and in some cases even slightly larger in structures with hysteretic behavior type A. The provisions of ATC-40 do not address the potential dynamic instability that can arise in systems with in-cycle strength degradation and P-D effects.

The suggested improvements of the ATC-40 procedure are presented in chapter 6 of FEMA-440. They are focused on improved estimates of the equivalent period and equivalent damping. It is concluded that generally the optimal effective period is less than the secant period and the optimal effective damping is also less than that specified in ATC-40.

More details about the accuracy, advantages, and drawbacks of both methods can be found in Appendix A of FEMA-440.

NZSEE 2006

The NZSEE 2006 addresses different methods of analysis, referred to as (a) force-based method, (b) displacement-based method, (c) consolidated force-displacement-based method, and (d) method using a nonlinear pushover analysis (the pushover analysis is performed taking into consideration the same distribution of lateral load as in FEMA-356).

Since the displacement-based method (DBM) is different from those presented in the previous sections, it is described in more detail in the next paragraphs. The basis of the method was developed by Priestley (1995) and further evaluated in, e.g., Priestley et al. (2007). The method places a direct emphasis on establishing the ultimate displacement capacity of the lateral force-resisting elements. Contrary to the methods presented in the previous sections, where the seismic displacements were calculated using acceleration spectra, in the DBM, the displacement spectra are considered.

In the first step, the flexural and shear strengths of the critical sections of the structural components, assuming that no strength degradation occurs due to the cyclic lateral loading in the post-elastic range, are estimated. In the second step, the post-elastic deformation mechanism of the structure and the probable horizontal seismic base shear capacity (V_{prob}) are determined. It is recommended that the post-elastic mechanism is defined using the (a) simple lateral mechanism analysis (presented in the guidelines), (b) inelastic response history analysis, and (c) nonlinear pushover analysis. When the nonlinear pushover analysis is used to estimate the nonlinear response, it is performed in the same manner as in FEMA-356 (the same distribution of the lateral load is taken into account).

In the third step, the plastic rotation capacities of the structural members are determined. It is then eventually corrected if the shear failure occurs before the limits to the flexural plastic rotation capacity are reached. The story inelastic drift capacity is estimated from the plastic rotation capacities.

Considering the critical storey drift and the previously defined post-elastic deformation mechanisms, the overall displacement capacity U_{sc} and the ductility capacity μ are determined at the effective height h_{eff} of the substitute structure (an equivalent SDOF model of the structure). The effective secant stiffness k_{eff} at

the maximum displacement U_{sc} is determined as $k_{eff} = V_{prob}/U_{sc}$. Then the corresponding effective period of vibration T_{eff} is calculated as

$$T_{eff} = 2\pi\sqrt{\frac{M}{k_{eff}}} \tag{12}$$

where M is the effective mass of the substitute structure (an equivalent SDOF model of the structure). Alternatively T_{eff} can be estimated directly using the Rayleigh-Ritz equation.

Based on the evaluated ductility capacity, the equivalent viscous damping ξ_{eff} of the structure is defined. It is recommended to use the method suggested in Pekcan et al. (1999). In general the equivalent viscous damping is determined in a similar manner as in ATC-40, summing the viscous and hysteretic damping.

The structural performance factor S_p is calculated according to NZS 1170.5 (2004) and taking into consideration the detailing used in the structure. It is used to reduce the seismic design actions on a structure. The displacement demand is defined using the overdamped elastic displacement spectrum. It is defined reducing the displacement spectrum $\delta(T)$, derived from the 5 % damped elastic acceleration spectrum. The displacement spectrum $\delta(T)$ is reduced using the correction factor K_ξ:

$$K_\xi = \sqrt{\frac{7}{2+\xi}} \tag{13}$$

where $\xi = \xi_{eff}$.

Thus the spectral displacement demand of the analyzed structure at height h_{eff} is defined as

$$U_{sd} = S_p(\%NBS)_t \delta\left(T_{eff}\right) K_\xi \tag{14}$$

where $(\%\mathrm{NBS})_t$ is the target percentage of the new building standard. The %NBS is essentially the assessed structural performance of the building compared with the requirements for a new building.

Then the displacement capacity U_{sc} and the demand U_{sd} are compared. If $U_{sc}/U_{sd} \geq 1$, retrofit is unnecessary to achieve $(\%\mathrm{NBS})_t$ and vice versa.

Some Issues that Influence the Accuracy of the Inelastic (Single-Mode) Pushover-Based Methods

In this section, some issues that can influence the accuracy of the pushover-based methods are presented: the idealization of the capacity curve, the influence of the higher modes, and the influence of the in-plan torsion. In the last two subsections, the basic observations from FEMA-440 about the strength degradation and the soil structure interaction are cited.

Idealization of the Capacity Curve

In some methods presented in section "Different Applications of the Inelastic Pushover-Based Analysis, Adopted in the (Pre)Standards and Guidelines," the actual capacity curve is idealized either by elastic-perfectly plastic or by a bilinear relationship (see Figs. 4 and 5). This approximation is one of the key issues, since it defines the equivalent stiffness of the equivalent SDOF model. This stiffness further influences the period of the SDOF oscillator and the estimated value of the target displacement. Thus the approximation should be carefully performed.

The approximation of the capacity curve is usually performed equating the area bounded (energy) with the actual and idealized curve (see Fig. 5). At this stage, the target displacement should be assumed, because the compared areas depend on the maximum displacement. Thus if the assumed target displacement differs considerably from the value obtained at the end of the analysis of the SDOF system, iterations are strongly recommended. Otherwise the target displacement can be poorly estimated.

In structures that do not exhibit considerable strain hardening in the nonlinear range, the elastic-perfectly plastic idealization is accurate. When the strain hardening is considerable, e.g., in some types of bridges, bilinear idealization is more appropriate (see section "Application of the Inelastic Static Methods to the Analysis of Bridges" for more details).

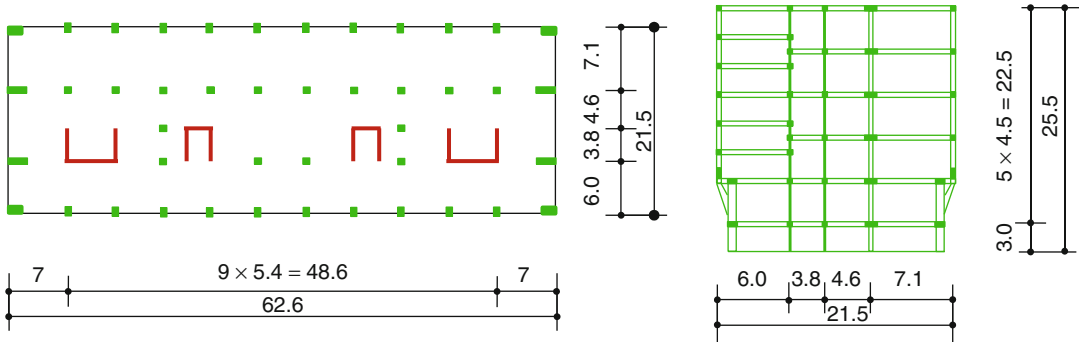

Assessment of Existing Structures Using Inelastic Static Analysis, Fig. 6 An example of the structure, irregular in plan and elevation

The Influence of Higher Modes

It was mentioned before that the basic variants of the methods described in section "Different Applications of the Inelastic Pushover-Based Analysis, Adopted in the (Pre)Standards and Guidelines" can be classified as single-mode nonadaptive methods since they assume that the response is controlled by a single predominant mode which remains unchanged after yielding occurs. This assumption limits their application. For example, when they are used for the analysis of existing structures which are irregular in elevation and/or in plan (see an example in Fig. 6), certain extensions are needed in order to take into account the important influence of higher modes and the in-plan torsion. In high-rise buildings, the influence of the higher modes can be important regardless of their irregularity. In such structures, multimode pushover methods (see section "Some Alternatives to Single-Mode Pushover-Based Methods" for more details) or NRHA can be used as an alternative to single-mode pushover-based methods.

The influence of the higher modes has been the subject of different studies. The one presented in FEMA-440 outlines the most important observations. Some of them are provided in the following paragraphs.

The nonlinear static pushover procedures appeared to be reliable for the design and evaluation of low-rise buildings. In relatively tall frame buildings, where the higher-mode response is significant, interstory drifts, story shears, and overturning moments can deviate significantly from the NRHA.

In buildings the importance of a higher-mode effect increases with the amount of inelasticity (note that in some bridges quite the opposite trend was observed – see section "Application of the Inelastic Static Methods to the Analysis of Bridges" for more details). Typical examples are, e.g., RC shear walls, where this phenomenon has been observed years ago. An explanation can be found elsewhere (e.g., Rejec et al. 2012).

Higher-mode contributions become more significant for structures with fundamental periods that fall into the constant-velocity part of the response spectrum. Forces which are developed due to the important influence of higher modes can considerably influence the failure mechanism. Thus the pushover analysis cannot always identify this mechanism.

In FEMA-440, a single first-mode distribution was found sufficient for the estimation of displacement and other quantities that were not significantly affected by higher modes. The adaptive load distribution was sometimes better and sometimes worse than the first-mode distribution. The uniform distribution is recommended in most of the codes as the second choice in order to frame the response quantities. However, in FEMA-440 it was found that it often did not fulfill this role. The uniform distribution was found to be the worst with regard to all the monitored response quantities. Thus it was not recommended as a stand-alone option.

All the codes addressed in this entry recognize that the single-mode pushover-based methods are less efficient when the higher modes are important. Thus they require these methods to be combined with the results of the linear dynamic procedures or the multimode pushover analysis is required. Specific solutions can be found in the particular standard.

The Influence of In-Plan Torsion, Two-Dimensional (2D) Versus Three-Dimensional (3D) Analysis

The in-plan torsion can importantly influence the response of the existing structures which are irregular in plan. In such structures, the 3D analysis is generally needed. The considerable influence of in-plan torsion can be expected in torsionally flexible structures, where the first mode of vibration is torsional. Substantial torsional effects can also be obtained in one direction of structures where the second mode of vibration is torsional.

It was observed that the inelastic static methods can significantly underestimate the displacements on the stiff/strong side of such buildings (see, e.g., Kreslin and Fajfar 2012). Thus the displacements on the stiff/strong side of the structure should be increased.

Most of the (pre)codes recognized this phenomenon. Thus they require an increase in the seismic displacements, defined by inelastic static methods, due to the torsional effects. All of them require a 3D analysis of the structures where the in-plan torsion is important. According to all codes, the accidental eccentricity should be taken into account in all analyses regardless of their torsional flexibility. The specific requirements related to an increase of displacements due to the torsional effects differ from standard to standard.

In general, the 3D pushover-based analysis and torsional effects are topics that require additional investigations. Thus, they are the subjects of numerous researches, reported in the literature. An overview of these researches is recently provided in Bhatt (2011).

The Strength and Stiffness Degradation

The strength degradation, including P-Δ effects, can lead to an apparent negative post-elastic stiffness in a force-deformation relationship for a structural model using nonlinear static procedures. The performance implications depend on the type of strength degradation (cyclic or in-cycle strength degradation). For structures that are affected by component strength losses, including P-Δ effects, occurring in the same cycle as yielding (in-cycle strength degradation), the negative post-elastic slope can lead to the dynamic instability of the structural model (FEMA-440 2005). For this reason, it is suggested that the pushover-based methods are only used if the strength of the structures is above a certain prescribed limit. Otherwise the use of the NRHA is recommended.

The Soil-Structure Interaction

There is a perception among many in the practicing engineering community that short, stiff buildings do not respond to seismic shaking as adversely as might be predicted analytically. There are several reasons why short-period structures may not respond as conventional analysis procedures predict. Among these are (a) radiation and material damping in supporting soils, (b) structures with basements that experience reduced levels of shaking, (c) incoherent input to buildings with relatively large plan dimensions, and (d) inaccuracies in modeling, including dumping of masses, neglecting the foundation's flexibility, and some elements that contribute to the strength (FEMA-440 2006). In FEMA-440 procedures, it is proposed that soil-structure interaction is incorporated into the nonlinear static analyses.

Some Alternatives to Single-Mode Pushover-Based Methods

Multimode procedures are considered as an alternative approach for the analysis of structures where the single-mode methods are less accurate. There are many multimode pushover methods described in the literature. In this section, two of them are briefly presented. The multimode pushover analysis (MPA) (Chopra et al. 2004) is selected as being representative of the

nonadaptive multimode pushover-based methods, and incremental response spectrum analysis (IRSA) (Aydinoğlu 2003) is selected as the representative of the adaptive multimode pushover-based methods. Both methods were addressed in FEMA-440. The MPA was evaluated as an alternative to the single-mode pushover-based methods, and the IRSA was recognized as the potential improvement of the inelastic analysis techniques that can be used to reliably address the MDOF effects.

The MPA Method

The MPA method was developed by Chopra and Goel (e.g., Chopra and Goel 2002). The analysis is performed in a similar manner as that presented in section "Eurocode 8/3 (CEN 2005)." However, the number of the analyses depends on the number of important modes, identified in the initial – elastic – state. The pushover analysis is performed separately for each important mode. The lateral load is proportional to the shape of the vibration mode. Based on each pushover analysis, the contribution of the related mode of vibration to the seismic displacements is defined. These contributions are then combined using the appropriate combination rule (e.g., SRSS). The method supposes that the modes of vibrations are invariant. Thus it can be classified as the nonadaptive method. This limits its applicability. When considerable changes of the mode shapes can be observed in the nonlinear range (an example is described in section "Pushover Analysis: Numerical Models and the Lateral Load Pattern"), the method is in general less reliable.

It was examined in FEMA-440 as an alternative to single-mode pushover-based methods. Taking into account a study of five buildings of very different properties, it was found to be more accurate than the single-mode pushover methods, but not completely reliable. Similar observations were obtained based on other studies, e.g., studies of bridges, presented in Kappos et al. (2012).

The IRSA Method

The IRSA method was developed by Aydinoğlu (2003). It is the multimode adaptive pushover method, which means that it can take into account the influence of the higher modes as well as their changes depending on the seismic intensity. The contributions of the different modes are considered in an incremental pushover analysis.

When the structure enters the nonlinear range, its dynamic properties are changed each time a new plastic hinge is developed. In regular structures, these changes are typically quite small. In irregular structures, the mode shapes as well as their contributions to the overall response can significantly change. IRSA can take into account these changes. More importantly, IRSA is also capable of taking into account the effect of modal coupling to the formation of the plastic hinges.

Different studies (e.g., Kappos et al. 2012) have confirmed that the method is quite reliable; however, it also has certain limitations, and thus it is not universal and cannot replace the NRHA in all cases, for example, in certain types of bridges.

Application of the Inelastic Static Methods to the Analysis of Bridges

With regard to their dimensions and structural systems, and in general with regard to their seismic response, bridges are quite different from buildings. Therefore the application of different pushover-based methods, which were originally developed for buildings, is not straightforward, particularly when the bridges are analyzed in the transverse direction. For the analysis of bridges in the transverse direction, the pushover methods in general should be applied in a slightly different manner. The analysis differs mainly regarding: (1) the choice of the reference point where the displacements are registered, (2) the distribution of the lateral load, and (3) the idealization of the capacity curve. These issues are briefly presented in the following subsections. In the last subsection, the applicability of the pushover methods for the analysis of bridges is discussed.

The Reference Point

In buildings, the center of mass of the roof is typically selected as the reference point.

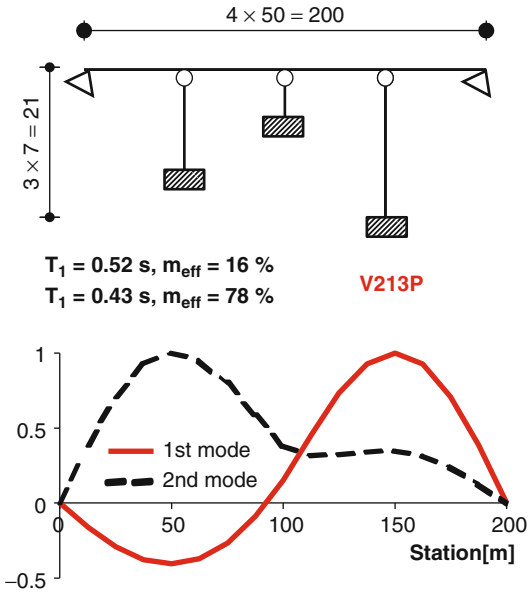

Assessment of Existing Structures Using Inelastic Static Analysis, Fig. 7 An example of a highly irregular bridge

In bridges, this choice is not straightforward. The specialized standards for the design of bridges often recommend the center of mass of the deformed deck as the reference point. An alternative solution could be the top of a certain column. However, in irregular bridges, both of these solutions could be inadequate.

In general, in highly irregular bridges, such as the one presented in Fig. 7, the position of the maximum displacement can considerably vary depending on the seismic intensity. In the bridge, presented in Fig. 7, the mode shapes, their importance, and the ratios are changing depending on the seismic intensity. When the response is in the elastic range, the maximum displacement is observed close to the top of the right pier. When the yielding of the central shortest pier is reached, the station of the maximum displacement is moved toward the center of the bridge (center of mass).

Three quite different pushover curves were obtained when each of the three columns was considered as the reference point (curves P1–P3 in Fig. 8a). Consequently, the dynamic properties of the equivalent SDOF model were also different. Since the importance of the different modes is changing considerably, depending on the seismic intensity, significantly different displacements of the structure (see curves P1–P3 in Fig. 8c) were estimated based on the pushover curves, presented in Fig. 8a. One can conclude that the pushover curve, corresponding to the column, where the maximum displacements were observed, should be used in the analysis. This is true, so far as this is the station of the maximum displacement of the superstructure, too.

The station of the maximum displacement of the superstructure in a viaduct, presented in Fig. 7, considerably changes depending on the seismic intensity. Thus, the corresponding pushover curve (see curve MD in Fig. 8b) does not coincide with any of the pushover curves constructed based on the displacements monitored at the top of a particular column. The corresponding displacements of the bridge are also significantly different from those calculated using the top of the columns as the reference points (see Fig. 8c).

Since the position of the maximum displacement is variable, it coincides with the center of mass only during stronger seismic intensities. Thus, the same conclusions as those presented in previous paragraphs can be applied for the center of mass, too.

One of the possible solutions is to consider the variable reference point when constructing the pushover curve. This means that the maximum displacement is monitored, wherever it is, in its variable position, which corresponds to a certain load level. In the case presented above, this further means that in the elastic range, the reference point is above the right pier, and after yielding of the central column, it is moved toward the center of mass. The resulting pushover curve is presented by a solid line in Fig. 8b, and the displacements of the superstructure with the bold solid line in Fig. 8c.

The Distribution of the Lateral Load

The lateral load pattern, in general, can be defined following the same basic recommendations as those for buildings: (a) distribution proportional

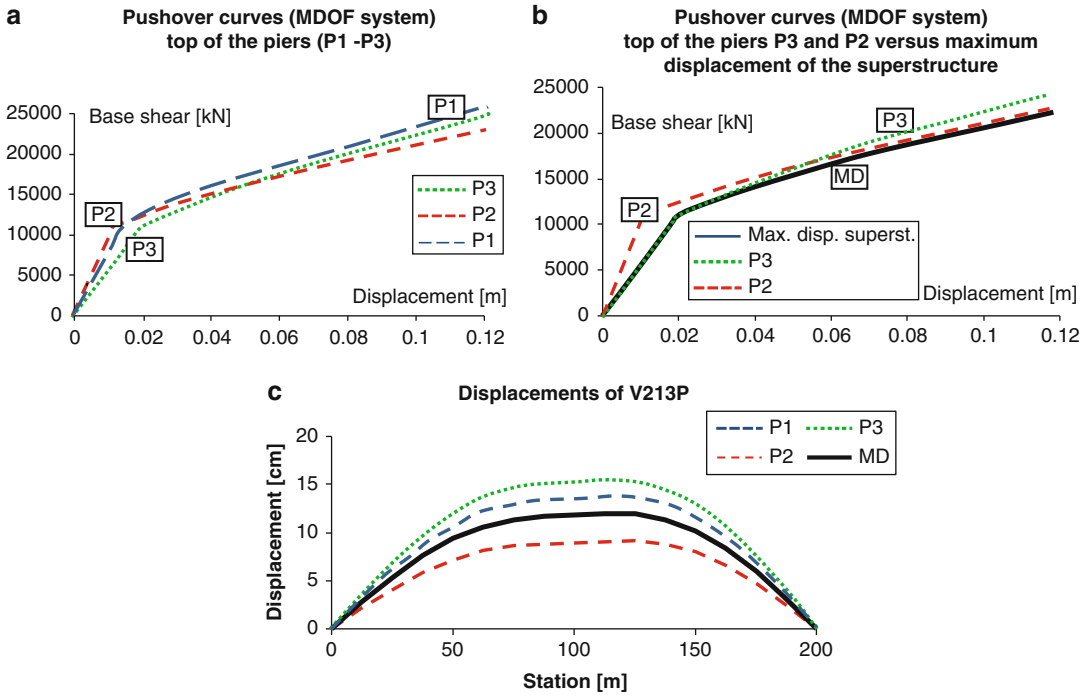

Assessment of Existing Structures Using Inelastic Static Analysis, Fig. 8 Pushover curves and displacement envelopes, obtained in a highly irregular viaduct, based on different reference points

to the fundamental mode of the bridge in the elastic range and (b) uniform distribution. Note however that the shape of the load pattern, proportional to the fundamental mode, depends on the type of the supports above the abutments as it is presented in Figs. 9 and 10. In regular bridges, pinned at the abutments, the parabolic distribution (see Fig. 9c) is also feasible.

The Idealization of the Capacity Curve

The idealization of the capacity curve can significantly influence the stiffness of the equivalent SDOF model and the estimated value of the maximum seismic displacement. When this stiffness is not adequately estimated, the actual and estimated maximum displacement can be significantly different. In some methods, such as that included in the EC8/3, the capacity curve is approximated using the elastic perfectly plastic idealization. However, in viaducts which are pinned at the abutments, this idealization can be inappropriate, since an underestimated equivalent stiffness of the SDOF system and an overestimated maximum displacement (see Fig. 11) can be obtained. Namely, in bridges with pinned abutments, the capacity curve can exhibit a considerable strain hardening slope, which should be properly taken into account. This is illustrated in Fig. 11.

Applicability of Pushover-Based Methods for the Analysis of Bridges

The single-mode methods can accurately predict the response of regular bridges where the influence of higher modes is not important. This is the case where the effective mass of the predominant mode exceeds 80 % of the total mass. When the methods are nonadaptive, they can be accurately used if the mode shapes do not significantly change based on the seismic intensity.

In bridges where the superstructure is considerably stiffer than the supporting elements (piers), the influence of the higher modes is in general negligible. Typical representatives are short- and medium-span bridges (e.g., the length of a bridge is less than 500 m), which are not

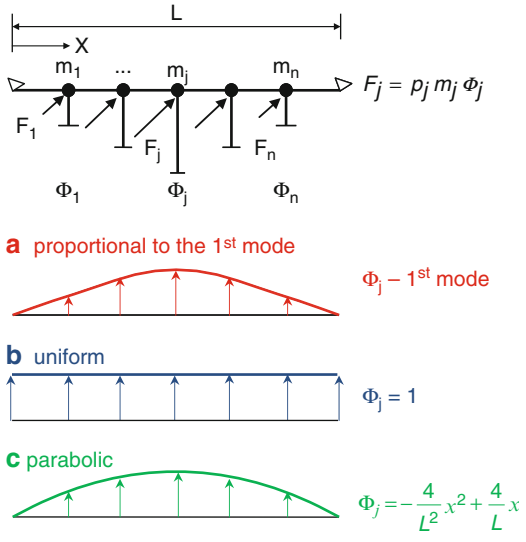

Assessment of Existing Structures Using Inelastic Static Analysis, Fig. 9 Distributions of the lateral load, appropriate for bridges that are pinned at the abutments

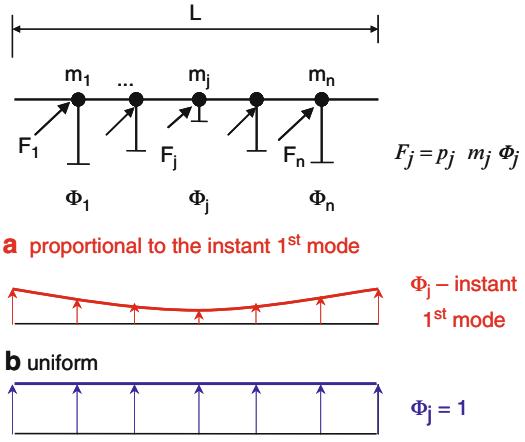

Assessment of Existing Structures Using Inelastic Static Analysis, Fig. 10 Distributions of the lateral load, appropriate for bridges with roller supports at the abutments

supported by very stiff (very short) piers (e.g., in single-column piers, the height of the columns exceeds 10 m).

Considerable changes of the mode shapes can be expected (and were observed) first of all in short bridges, where the displacements of the superstructure above the abutments are not restrained. In such bridges, the predominant mode usually changes considerably, when the damage of the side columns reduces their stiffness to such an extent that the torsional stiffness of the bridge becomes lower than its translational stiffness.

The accuracy of the single-mode pushover-based methods depends on: (a) the ratio of the superstructure stiffness and the stiffness of the bents (the length of the bridge and number and the location of the short columns along the bridge); (b) the relative strength of the columns, compared to the seismic intensity; and (c) the boundary conditions at the abutments (mostly in short bridges).

When the superstructure is stiff compared to the supporting columns (piers), it has a predominant role defining the response of the bridge. In such cases, the response is typically influenced by one predominant mode. However, if the bridge is supported by short stiff columns, they govern the response and cause the significant influence of the higher modes to the deflection line of the superstructure.

In many bridges, the accuracy of the single-mode methods increases with the seismic intensities (nonlinearity). Columns yield, their stiffness is reduced, and thus the superstructure has a more important role for the overall response. However, this is not the rule. In bridges where the torsional stiffness decreases when the columns yield, the single-mode methods cannot accurately predict the response at high intensity levels, due to the emphasized torsional rotations.

In bridges with roller supports above the abutments, considerable changes of mode shapes can occur, particularly when the side spans are relatively long. When they are supported by short stiff columns in the central part of the superstructure, considerable torsional effects can be obtained.

In long bridges, the influence of the higher modes in the majority of cases does not depend on the stiffness of the columns and their strength. In such bridges, the superstructure of the standard types becomes quite flexible, and consequently the higher modes become important, regardless of the stiffness and the strength of the columns.

When the response of the bridge is considerably influenced by the higher modes or the modes of vibration are changing considerably depending on the seismic intensity, the multimode pushover

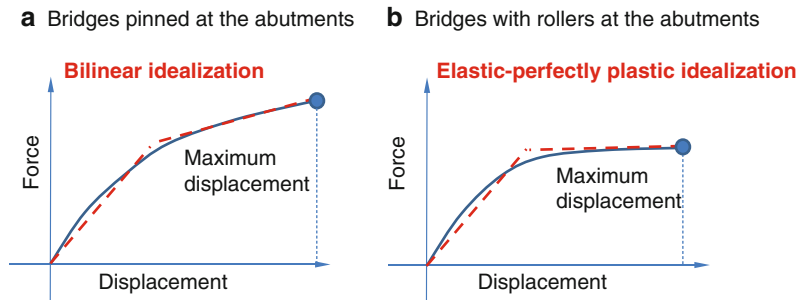

Assessment of Existing Structures Using Inelastic Static Analysis, Fig. 11 Idealization of the pushover curve

methods are needed. However, note that they also have certain limitations, which depend on their basic assumptions. For example, even quite accurate methods, such as IRSA (see section "Some Alternatives to Single-Mode Pushover Based Methods"), can fail to predict the response accurately when the bridge is supported by short stiff central columns. In such cases, the NRHA is needed.

More details and recommendations about the use of the pushover-based methods for the analysis of bridges can found in Kappos et al. (2012).

Summary

The inelastic static pushover-based methods, which are typically used for the assessment of the existing structures, are presented. Some of the basic concepts that are nowadays used are presented in the example of the four single-mode pushover-based methods included in the codes. Some parameters that influence the accuracy of these methods are presented: selection of the lateral load pattern, idealization of the capacity curve, numerical models, influence of the higher modes, and changes of the shapes of the vibration modes depending on the seismic intensity, in-plan torsion, strength degradation, and soil-structure interaction.

Two multimode pushover-based methods, which are typical examples of nonadaptive and adaptive multimode methods, are briefly overviewed. The application of the inelastic pushover-based methods to the analysis of bridges is discussed.

Cross-References

- ▶ Assessment and Strengthening of Partitions in Buildings
- ▶ Assessment of Existing Structures Using Response History Analysis
- ▶ Earthquake Response Spectra and Design Spectra
- ▶ Earthquake Return Period and Its Incorporation into Seismic Actions
- ▶ Equivalent Static Analysis of Structures Subjected to Seismic Actions
- ▶ European Structural Design Codes: Seismic Actions
- ▶ Incremental Dynamic Analysis
- ▶ Modal Analysis
- ▶ Nonlinear Dynamic Seismic Analysis
- ▶ Nonlinear Finite Element Analysis
- ▶ Numerical Modeling of Masonry Infilled Reinforced Concrete Frame Buildings
- ▶ Response Spectrum Analysis of Structures Subjected to Seismic Actions
- ▶ Retrofitting and Strengthening Masonries of Heritage Structures: Materials Used
- ▶ Retrofitting and Strengthening Measures: Liability and Quality Assurance
- ▶ Retrofitting and Strengthening of Contemporary Structures: Materials Used
- ▶ Retrofitting and Strengthening of Structures: Basic Principles of Structural Interventions
- ▶ Seismic Analysis of Concrete Bridges: Numerical Modeling
- ▶ Seismic Analysis of Masonry Buildings: Numerical Modeling
- ▶ Seismic Analysis of Steel and Composite Bridges: Numerical Modeling

- ▶ Seismic Analysis of Steel Buildings: Numerical Modeling
- ▶ Seismic Analysis of Steel–Concrete Composite Buildings: Numerical Modeling
- ▶ Strengthened Structural Members and Structures: Analytical Assessment
- ▶ Strengthening Techniques: Bridges
- ▶ Strengthening Techniques: Code-Deficient R/C Buildings
- ▶ Strengthening Techniques: Code-Deficient Steel Buildings
- ▶ Strengthening Techniques: Masonry and Heritage Structures

References

ATC 40, ATC (1996) Seismic evaluation and retrofit of concrete buildings, ATC-40 report, funded by the Seismic Safety Commission, published by the Applied Technology Council. Redwood City, California

Aydinoğlu NM (2003) An incremental response spectrum analysis procedure based on inelastic spectral displacements for multi-mode seismic performance evaluation. Bull Earthq Eng 1:3–36

Bhatt CAAF (2011) Seismic assessment of existing buildings using nonlinear static procedures (NSPs) –a new 3D pushover procedure, PhD thesis. Technical University of Lisbon, Instituto Superior Técnico, Lisbon

Bracci JM, Kunnath SK, Reinhorn AM (1997) Seismic performance and retrofit evaluation of reinforced concrete structures. J Struct Eng 123(1):3–10

CEB FIP (2003) Displacement–based seismic design of reinforced concrete buildings; state-of-the-art-report, fib Bulletin No 25, Laussane, Switzerland

CEN (2004) Eurocode 8: design of structures for earthquake resistance – part 1: general rules, seismic actions and rules for buildings. Comité Européen de Normalisation, Brussels

CEN (2005) Eurocode 8: design of structures for earthquake resistance. Part 3: strengthening and repair of buildings, EN 1998–3. European Committee for Standardization, Brussels

Chopra AK, Goel RK (2002) A modal pushover analysis procedure for estimating seismic demands for buildings. Earthq Eng Struct Dyn 31:561–582

Chopra AK, Goel RK, Chintanapakdee C (2004) Evaluation of a modified MPA procedure assuming higher modes as elastic to estimate seismic demands. Earthq Spectra 20(3):757–778

Eberhard MO, Sozen MA (1993) Behavior-based method to determine design shear in earthquake-resistant walls. J Struct Div Am Soc Civil Eng N Y 119(2):619–640

Fajfar P (1999) Capacity spectrum method based on inelastic demand spectra. Earthq Eng Struct Dyn 28(9):979–993

Fajfar P, Fischinger M (1988) N2 – a method for non-linear seismic analysis of regular structures. In: Proceedings of the ninth world conference on earthquake engineering, Tokyo-Kyoto

FEMA 356, ASCE (2000) Prestandard and commentary for the seismic rehabilitation of buildings, FEMA 356 report, prepared by the American Society of Civil Engineers for the Federal Emergency Management Agency, Washington, DC

FEMA 440, ATC, FEMA (2005) FEMA-440, improvement of nonlinear static seismic analysis procedures, applied technology council for department of Homeland Security, Federal Emergency Management Agency, Washington, DC

Fischinger M, Rejec K, Isakovic T (2012) Modelling Inelastic shear response of RC walls. In: Proceedings of 15th world conference on earthquake engineering, Sept 2012, Lisbon

Freeman A, Nicoletti JP, Tyrell JV (1975) Evaluations of existing buildings for seismic risk – a case study of Puget Sound Naval Shipyard, Bremerton, Washington, DC. In: Proceedings of the 1st U.S. national conference earthquake engineering, EERI, Berkeley, pp 113–122

Kappos AJ, Saiidi MS, Aydinoğlu MN, Isakovic T (2012) Seismic design and assessment of bridges: inelastic methods of analysis and case studies. Springer, Dordrecht/Heidelberg/New York/London

Krawinkler H, Seneviratna GDPK (1998) Pros and cons of a pushover analysis of seismic performance evaluation. Eng Struct 20(4–6):452–464

Kreslin M, Fajfar P (2012) The extended N2 method considering higher mode effects in both plan and elevation. Bull Earthq Eng 10(2):695–715

Mergos PE, Kappos AJ (2008) A distributed shear and flexural flexibility model with shear-flexure interaction for R/C members subjected to seismic loading. Earthq Eng Struct Dyn 37(12):1349–1370. doi:10.1002/eqe.812

NZS 1170.5 (2004) Structural design actions, part 5: earthquake actions – New Zealand. Standards New Zealand, Wellington

NZSEE (2006) Assessment and improvement of the structural performance of buildings in earthquake. New Zealand Society for Earthquake Engineering, Wellington

Pekcan G, Mander JB, Chen SS (1999) Fundamental considerations for the design of non-linear viscous dampers. Earthq Eng Struct Dyn 28:1405–1425

Priestley MJN (1995) Displacement-based seismic assessment of existing reinforced concrete buildings. Proc Pac Conf Earthq Eng 2:225–244. Melbourne

Priestley MJN, Calvi GM, Kowalsky MJ (2007) Displacement-based seismic design of structures. IUSS Press, Pavia

Rejec K, Isakovic T, Fischinger M (2012) Seismic shear force magnification in RC cantilever structural walls, designed according to Eurocode 8. Bull Earthq Eng 10(2):567–586

Saiidi M, Sozen M (1981) Simple nonlinear seismic analysis of R/C structures. J Struct Div ASCE 107(ST5):937–952

Assessment of Existing Structures Using Response History Analysis

Damian N. Grant
Arup Advanced Technology and Research, London, UK

Synonyms

Nonlinear dynamic analysis; Nonlinear response history analysis; Time history analysis

Introduction

Nonlinear response history analysis (NRHA) is used in both engineering industry and academia to assess the seismic performance of structures and to validate simpler analysis methods used in design or assessment. International building codes for the design of new buildings and assessment guidelines for existing buildings generally allow NRHA to be used, although the level of detail in published guidelines is mixed, and industry practice varies. In the past, NRHA was the domain of only a few specialists, but many structural analysis packages are now available to carry it out, and many engineering consultancies have the capability.

NRHA is the most general and most detailed analytic modeled approach in the earthquake engineer's toolkit, involving the numerical solution of the equation of the motion allowing for both material and geometric nonlinearity. The response of a structure to an earthquake ground motion is evaluated at small increments of time, tracking the development of plasticity in the structure as it deforms into the inelastic range. Different algorithms are available to numerically solve for forces and displacements at the current time step in terms of those at the previous time step and the applied ground acceleration over the time interval. Analysis programs commonly used in earthquake engineering use *implicit* solution algorithms, many of which are unconditionally stable (i.e., any analysis time step will lead to a stable evaluation of response, although small time steps are still needed for accuracy), but require iteration within each time step. Some packages used more for large-deformation analysis, such as those used in the automotive industry for crash simulation, use *explicit* solution algorithms which do not require iteration, but with the trade-off of requiring a very small time step for numerical stability (depends on application, but often of the order of 10 μs).

The most appropriate analysis methodology is very application-dependent and can evolve as a project progresses. If it is possible to demonstrate acceptable performance of a building on the basis of simple, conservative analyses, then a very detailed NRHA may require excessive engineering resource and time. On the other hand, for unusual structures or those for which initial findings are unclear, NRHA is often justified. This is especially true for the assessment of existing structures as the potential benefit of demonstrating compliance with target performance requirements (and therefore avoiding retrofit) often outweighs the engineering costs associated with advanced analysis. Existing structures are often deficient with respect to new design requirements – both qualitatively, in terms of code-required detailing, and quantitatively, in terms of seismic demand exceeding seismic resistance. This means that simplified code inputs and methods developed for code-compliant structures (such as allowable ductility levels) may not be appropriate for noncompliant structures, and more detailed analysis may be required to assess their performance.

There are many aspects of NRHA that can affect estimates of structural response, relating to appropriate numerical inputs, modeled methodologies for different materials and structural elements, and treatment of analysis outputs. On the input side, ground acceleration histories are required that are in some way consistent with the seismic hazard at the site (e.g., a code design spectrum). Different authors recommend the use of raw unscaled ground motions recorded in real earthquakes, scaled or otherwise modified real ground motions (including spectrally matched records, which are modified such that their

response spectrum matches a target spectrum), ground motions developed from physics-based simulations of fault rupture and seismic wave passage, and those generated artificially from the modification of white noise or some other mathematical approach. On the methodological side, structures can be modeled using a very detailed 3D finite element model, simplified with 2D shell elements (especially appropriate for structural walls and diaphragms) or simplified even further into 1D "stick" elements, routinely used for moment frame and braced frame structures. Nonlinear material behavior for the latter approach may be taken into account with distributed plasticity (numerical integration of the nonlinear stress–strain behavior over the length of the element) or lumped plasticity (assuming plasticity may be concentrated in a plastic hinge at the end of each member). Finally, on the output side, there are many different response quantities that can be monitored, including interstory drifts, base shear, and plastic deformations, and it is important to be able to link real descriptions of structural performance (from onset of cracking through to full structural failure) to the outputs of the analytic model. Each analyst will treat each of these aspects in different ways, potentially leading to very different estimates of seismic response of a given structure.

This entry outlines the application of NRHA to the assessment of seismic performance of existing structures, with an emphasis on those structures that do not meet prescriptive code requirements. Section "Performance Objectives and Assessment Methodology" discusses the setting of performance objectives and how these are affected by the assessment methodology adopted. Section "Modeling Considerations" covers general aspects of nonlinear dynamic analysis, including modeled considerations and interpretation of the outputs. Section "Published Codes, Standards and Guidelines" is a summary of international published guidelines on the topic, including ASCE/SEI 41-06, Eurocode 8 Part 3, the New Zealand Society for Earthquake Engineering Recommendations, and FEMA P-58. Finally, section "Summary" is a summary of the entry.

Performance Objectives and Assessment Methodology

Target seismic performance for assessment of existing structures depends on both the needs of building owners or occupants and on regulatory requirements. In many jurisdictions, seismic assessment and retrofit are carried out on a voluntary basis, and in this case, there is significant flexibility in setting performance objectives. This does not remove the responsibility of the engineer to educate the client on the seismic risk represented by different objectives. Many clients come into the assessment process with incomplete performance targets in mind, such as "to ensure life safety" or "functional performance after an earthquake," without a full appreciation of the uncertainties in seismic hazard definitions or the costs involved in achieving different levels of performance. Indeed, even engineers often misleadingly refer to performance objectives solely in terms of structural performance and do not refer to the fairly arbitrarily defined hazard levels with which these are associated.

Performance objectives will generally be expressed in terms of a target structural performance under one or more seismic hazard levels or a time period of exposure to the hazard. Performance objectives are expressed differently depending on the analysis to be carried out. Three potential analysis types are described in FEMA P-58 (section "FEMA P-58: Seismic Performance Assessment of Buildings"):

1. *Intensity-based assessment*, in which seismic performance and losses are evaluated for seismic input defined by a given response spectrum
2. *Scenario-based assessment*, in which the seismic input is a specific earthquake scenario, such as an historical event or potential rupture of a particular fault
3. *Time-based assessment*, in which losses are integrated over the occurrence of many potential earthquakes in a fully probabilistic way to allow estimates of, e.g., annualized seismic losses.

For intensity-based assessment (which is the default option in most codes and standards for seismic assessment, including ASCE 41, EC8-3, and the NZSEE Recommendations, reviewed in Section "Published Codes, Standards and Guidelines"), one or more performance objectives will be checked, each comprising a return period at which the probabilistic seismic hazard is evaluated and the desired structural and nonstructural performance at this hazard level. In ASCE 41, for example, the "basic safety objective" (BSO) is considered to be satisfying a life safety performance level under a 475-year return period ground motion and a collapse prevention performance level under a 2,475-year return period. Nonstructural performance objectives are also given, including a life safety objective to ensure that heavy equipment or façades do not fall and endanger life or impede egress.

Performance objectives both for assessment and (if required) retrofit design for existing structures are often allowed to be less onerous than in the design of new structures. This is justified primarily on the basis of pragmatism: incorporating seismic-resistant detailing into new buildings usually comes at a relatively small premium, whereas the cost of retrofit (including both direct and indirect costs) may be prohibitive. This is especially true of historical structures, where extensive strengthening measures may not be acceptable from a cultural heritage point of view (of course, this cultural heritage is exactly what seismic strengthening is trying to preserve in the long term). Less onerous performance objectives are also sometimes justified on the basis of a lower remaining design life than the nominal value adopted for existing structures (and therefore lower exposure period to seismic hazard). The BSO in ASCE 41, for example, is considered to represent a potentially higher risk than expected for properly designed and constructed new buildings. In jurisdictions where seismic assessment and retrofit are not obligatory, building owners may decide on performance objectives for themselves, based on a cost-benefit analysis of the cost of strengthening and the risk reduction in terms of future repair costs and potential loss of life following an earthquake.

The main goal of the latest generation of performance-based earthquake engineering guidelines (such as FEMA P-58) is to develop tools to convert engineering performance objectives into metrics that are more meaningful to other stakeholders, such as building owners, building tenants, and insurance companies. Performance may be quantified in terms of direct monetary costs (for repair or replacement), human impact (chance of casualties or fatalities), and indirect costs (time to repair, reoccupy, or return to function) – snappily summarized by the 3 Ds: "dollars, deaths, and downtime." Performance objectives expressed in this format of course place a higher burden on the analyst – particularly for areas outside the United States, where the default fragility functions given in *PACT* for various nonstructural components may not apply. The recently developed REDi^{TM} Rating System (Resilience-based Earthquake Design Initiative; Almufti and Willford 2013) bases its platinum, gold, and silver performance resilience objectives partly on numerical estimates of post-earthquake reoccupancy and functional recovery times and provides a useful framework for discussion of enhanced performance objectives with clients and other stakeholders.

Modeling Considerations

As with any engineering or scientific numerical modeled exercise, the outputs from NRHA are only as reliable as the specific modeled techniques used and the numerical inputs. Although NRHA is perceived as giving the most accurate estimates of building seismic performance, it has the disadvantage that model checking (of both inputs and outputs) may be hampered by complexity and potentially by computational power (e.g., the time taken to envelope results of large structural analysis models over multiple ground motions can discourage the analyst from checking all response quantities thoroughly). Analysts may be overconfident of the results of NRHA and feel that detailed modeled obviates the need to apply engineering principles to the assessment of structures.

The following subsections provide a summary of some modeled decisions and interpretations that face an analyst employing NRHA on an assessment project. Many of these aspects are covered in more detail in other chapters in this entry. The discussion is divided into aspects relating to the seismic input (ground acceleration histories), structural modeled, and treatment of outputs from the analysis.

Seismic Input

From the point of view of the structure, seismic action is felt through acceleration of the ground at the base – in both horizontal and vertical directions – and therefore NRHA requires appropriate ground acceleration histories to apply. In most cases, the seismic hazard is defined in the form of a response spectrum, and therefore compatibility with a target spectrum is one of the most important considerations in definition of ground acceleration histories, but nonstationary characteristics such as duration can also be important. Results can be very sensitive to the ground motions applied, and the ground motions to be used for a given application depend not only on the seismic hazard and expected seismic shaking at the site but also on the objectives of the analysis.

For the assessment of mean (expected) response only, current codes allow as few as three ground motions to be assessed, although if fewer than seven are used, the maximum of each response quantity across all the analyses should be used. These requirements date back to the level of computing power available in the 1980s and 1990s, and nowadays, seven is generally considered to be a sensible minimum, from which the arithmetic mean response can be taken (NEHRP Consultants Joint Venture 2011). For estimates of the statistical distribution of structural response quantities, many more ground motions will be required – NEHRP Consultants Joint Venture (2011) suggests 30 records, although this depends on the variability of structural response and the ground motions affecting the site.

There is a substantial body of literature on the development of ground motions appropriate for the NRHA of structures, and no consensus has yet been reached among researchers and codes of practice on the most appropriate methods. Categories of ground motions applied in seismic assessment are:

- Recorded by accelerometers in real earthquakes, applied to the structural model unmodified
- Recorded in real earthquakes multiplied by a linear scaling factor to achieve compatibility with the peak ground acceleration or other scalar measure of seismic intensity (e.g., spectral acceleration at the fundamental period of the structure)
- Recorded in real earthquakes modified to achieve spectrum compatibility across a range of structural periods (*spectral matching*)
- Generated from a purely mathematical algorithm, such as modified white noise
- Derived from a physics-based simulation of the seismic wave generation and propagation process.

NEHRP Consultants Joint Venture (2011) provides a discussion of the various considerations for development of ground motions for a project.

Most literature on ground motion development considers only a single component of horizontal input and does not discuss the proper treatment of horizontal variability and the application of multiple components of ground motion to a 3D analysis model. Ground motions recorded in real earthquakes are typically not axisymmetric – i.e., they do not shake each horizontal direction equally strongly. In fact, in some cases, structures with a certain period may be shaken strongly in one direction, whereas structures with a different period may be shaken more strongly in a different direction. Figure 1 shows an example of such a case, where the 1.3-s structural response is strongest at 79° from the x-axis and the 3.0-s structural response is strongest at 161°. Grant (2011) developed the software, *RspMatchBi*, to spectrally match recorded ground motions to retain the axes of strong shaking of the original motion while matching the

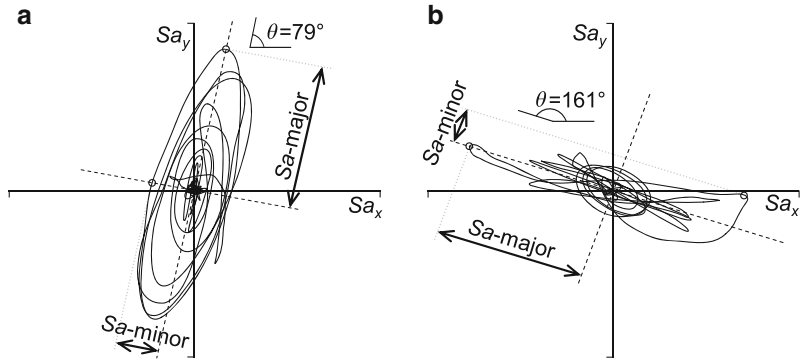

Assessment of Existing Structures Using Response History Analysis, Fig. 1 Response orbits (displacement of single degree of freedom oscillators) and definition of major and minor axes of response for PEER Record 184 from Imperial Valley event; (**a**) 1.3-s period response and (**b**) 3.0-s period response (From Grant et al. 2011)

spectra of the record to target spectra. NEHRP Consultants Joint Venture (2011) provides some discussion on the application of multicomponent ground motions to a structural model.

Structural Modeling

The most appropriate type of response history analysis model (or analysis model in general) is very application specific. If a simple and conservative model is adequate to demonstrate acceptable seismic performance, then there is little benefit in introducing extra detail and complexity. In practice, modeled requirements are different for every project, and it is not possible to give a recipe that can be followed for every application. The following are some aspects of structural analysis that are important for the use of NRHA in both the assessment of existing structures and in new design.

Linear Versus Nonlinear

Although the focus of this entry is on nonlinear analysis, the extra effort involved to introduce material and geometric nonlinearity is not always justified – particularly when target performance objectives restrict the response to the elastic or near-elastic range. This also applies at a component level – for example, force-controlled (brittle) elements are usually modeled linearly, given that their nonlinear response is generally unacceptable. Of course, even if heavily nonlinear response is acceptable, if input seismic demand is lower than the elastic response of the structure, nonlinear deformation is not expected, and a linear model would suffice. On the other hand, when a degree of nonlinearity is expected in the structure's seismic response, explicitly modeled this nonlinearity may be necessary, allowing a more accurate estimation of the overall structural response (e.g., peak displacements or storey drifts), but also a better understanding of how seismic demand is plastically redistributed among parallel load paths following first yield.

2D Versus 3D

Regular structures in plan, for which torsional response is expected to be minimal, are often analyzed with separate 2D models for each principal axis of the structure. In engineering practice (in contrast to academic research), projects on which NRHA is considered worthwhile are seldom particularly regular, although there are of course many exceptions. 3D analysis does not introduce significant complexity in pre- and post-processing when using modern analysis packages, with the exception that the ground motion input is more complicated.

Level of Detail

A given structure can be analyzed in different levels of detail: from an equivalent single degree of freedom representation through to a detailed finite element model. Often, several different

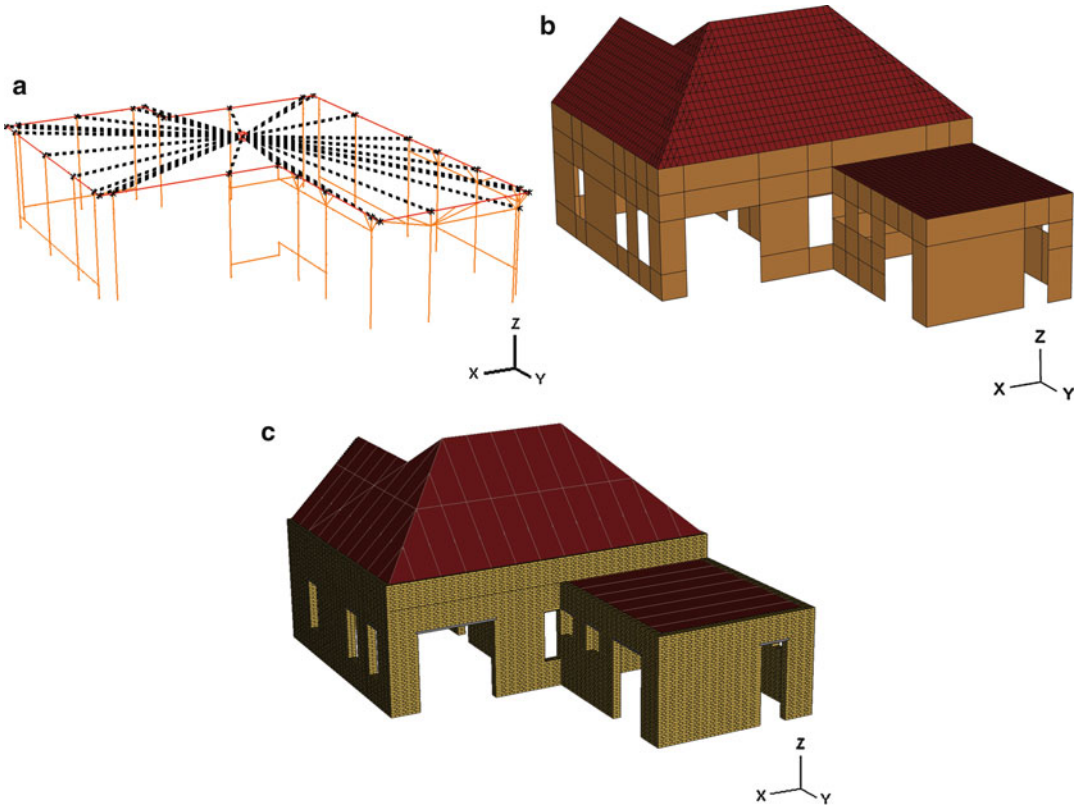

Assessment of Existing Structures Using Response History Analysis, Fig. 2 Different levels of analysis detail for modeling an unreinforced masonry house

levels of analysis will be considered for one project: for example, simplified models at an initial stage and for subsequent model checking, a main structural model (e.g., frame members modeled as 2D beam elements) for overall performance assessment, and detailed local models to calibrate aspects of the main model (e.g., modeled force transfer within a RC joint region using 3D solid elements for concrete, 2D beam elements for reinforcing bars, and bond and friction between them defined with a mathematical model).

Three different levels of detail are shown in Fig. 2, for the NRHA of an unreinforced masonry (URM) house. Figure 2a shows an equivalent frame model, in which masonry pier flexural and shear responses are modeled with nonlinear spring or link elements. For this model, the mass is lumped at an equivalent roof height, and a rigid diaphragm connects the mass to the tops of each of the wall piers. Figure 2b shows masonry walls modeled in 2D shell elements; masonry material models may be of a smeared crack type, in which the development of cracks in the walls is modeled explicitly, or a phenomenological hysteresis model in which backbone and cyclic hysteretic rules, based on experimental behavior, are used. Finally, Fig. 2c shows a model in which individual bricks are modeled with 3D solid elements. In this case, the interaction between bricks is described with a contact surface formulation, which allows for opening and closing of cracks between the bricks and the transfer of compression and traction across the interfaces. If calibrated correctly, this model can explicitly track the development of failure mechanisms in the URM wall up until the point of collapse.

Another example of a multilevel approach, as applied to the new design of an offshore platform, may be found in Gibson et al. (2012).

Boundary Conditions and Soil–Structure Interaction (SSI)

Although structural engineers are primarily interested in the seismic response of the building itself, in many cases, this cannot be accurately predicted without taking into account the interaction between the structure, its foundation, and the soil at the site. Soil behavior is generally nonlinear, at least for the range of strains of interest for earthquake engineering applications, but is often modeled with equivalent linear stiffness and damping properties. SSI literature (e.g., NEHRP Consultants Joint Venture 2012) refers to three main effects:

1. Inertial interaction – the forces and deformations on the structure–foundation–soil interface generated by inertial forces on the structure.
2. Kinematic interaction – the stiffening effect of the building's foundation on the soil around it and its effect on the soil vibrations.
3. Foundation deformations – foundation elements, such as piles embedded in the soil, are subjected to deformations from the building and soil and must be designed to accommodate these movements.

SSI can be taken into account in NRHA in different levels of detail: from ignoring it (simplest), adding springs at the base of the structure to represent soil and foundation flexibility, through to a direct nonlinear finite element analysis of the soil and its interaction with structural and foundation elements. The recent guide to SSI by the NEHRP Consultants Joint Venture (2012) summarizes the state of practice and requirements of design standards and codes.

Recognizing that soil properties are typically subject to more uncertainty than structural material properties, design and assessment guidelines sometimes require a bounding approach, wherein separate analyses are carried out with lower and upper bound soil properties, and the analysis results are enveloped. Due to the nature of site response and SSI, however, there is no guarantee that this will envelope the worst-case structural response. Several guidelines suggest a bounding approach for a serviceability level earthquake ground motion, but the use of the best-estimate soil properties for the evaluation of an ultimate level seismic response.

Material and Section Properties

Material and section properties depend on the type of modeled carried out and the hysteresis models available in the analysis software used. A common requirement of the international guidelines reviewed in section "Published Codes, Standards and Guidelines" is that member strengths should be taken based on "best-estimate" properties for deformation-controlled (ductile) responses and "lower-bound" properties for force-controlled (brittle) responses. Deformation-controlled actions include structural responses that exhibit a ductile nonlinear behavior and therefore may be permitted to deform into the plastic range without (necessarily) compromising the ability of the structure to support gravity loads and seismic forces. This includes flexure in steel and RC frame elements, axial deformation in steel braces, and rocking in masonry piers. Force-controlled actions include those responses that fail in a brittle manner when their capacity is exceeded and thus should usually be prevented to ensure structural integrity. This includes shear in frame elements and masonry piers.

Stiffnesses should be based on a best estimate, as otherwise the distribution of forces in the structure could be misevaluated. Structural modeled generally requires some degree of rationalization – e.g., plastic hinges are modeled with piecewise linear hysteretic backbones like those shown in Fig. 3 (from ASCE 41) – and the most appropriate simplifications will be application-dependent. In the backbone shown, AB is the nominal elastic range, BC the plastic range (shown with a small positive stiffness due to strain hardening and spread of plasticity), and DE the residual capacity, at which a small proportion of the peak capacity at point C is still carried, prior to final failure at point E. In ASCE 41, branch CD is modeled as very steep to account for sudden loss of strength, which may not be realistic for some component

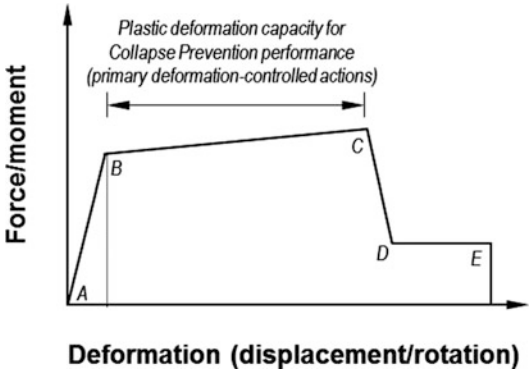

Assessment of Existing Structures Using Response History Analysis, Fig. 3 Component force–deformation backbone behavior to ASCE 41 (Adapted from ASCE 2007)

responses (ATC 2010). When modeled RC elements with the backbone shown in Fig. 3, the initial branch (AB) is taken to represent the cracked response, with the justification that the uncracked response is only attained on the first cycle (if at all). The stiffness of branch AB is then taken as an approximation of the stiffness up to a nominal first yield point. For elements expected to be pushed far into the inelastic range (beyond point B), the stiffness of AB will usually not have a large effect on the overall structural response, but for elements that are not expected to yield or maybe not even crack, using fully cracked stiffness for AB may lead to an underestimate of forces on these elements.

Assessment standards and guidelines have requirements for material testing (nondestructive or destructive) to establish material properties for NRHA. Generally, at least some destructive testing is required for NRHA to be appropriate, unless material properties are well-documented on design documentation. This follows from the "principle of consistent crudeness" (Elms 1985), according to which excessive detail is not appropriate in one aspect of a design process if significant uncertainties remain in other aspects.

Hysteretic Response of Components

As well as member strengths and backbone response, NRHA requires a model to describe response of members under cyclic loads. For example, if the backbone response in Fig. 3 is used to represent hysteretic response of a yielding member (such as a RC or steel beam in flexure), then unloading from the backbone may be at a stiffness close to the initial elastic stiffness of the member, and cyclic response may be close to elastoplastic. If, on the other hand, the backbone represents rocking of a structural wall, then unloading may retrace the backbone back through the origin, and the response is effectively nonlinear-elastic. A generic hysteretic response, generated using the Ibarra et al. (2005) hysteresis model, is shown in Fig. 4, under both monotonic and cyclic loading.

Most structural members' response degrades with nonlinear cyclic loading, meaning that the strength reduces for large deformations ("monotonic degradation") and that the stiffness and strength reduce over successive cycles out to a similar level of deformation ("cyclic degradation"). Monotonic degradation is illustrated in Fig. 4 by a decreasing monotonic backbone behavior when a certain displacement is exceeded. Cyclic degradation is shown by a reduction in the force carried under successive cycles to the same displacement level.

Degradation is especially important for those members that have not been designed with seismic-resistant detailing, but even well-detailed steel and RC plastic hinges degrade at higher levels of plastic deformation. As with other aspects of modeled, the relevance of modeled this degradation for seismic assessment depends on the type of elements in the structural system and the expected level of nonlinear demand on those elements. The plastic deformation limits tabulated in ASCE 41, for example, are artificially reduced to take into account the fact that most analysts will not include degradation in their analysis models. For more details of modeled aspects of structural degradation, see ATC (2010) and Deierlein et al. (2010). These references are more useful for modeled seismically detailed structural elements; the literature on modeled degradation in seismically deficient elements (poorly detailed RC or steel elements or URM) is not developed to the same level. The analyst should ensure that the structural model

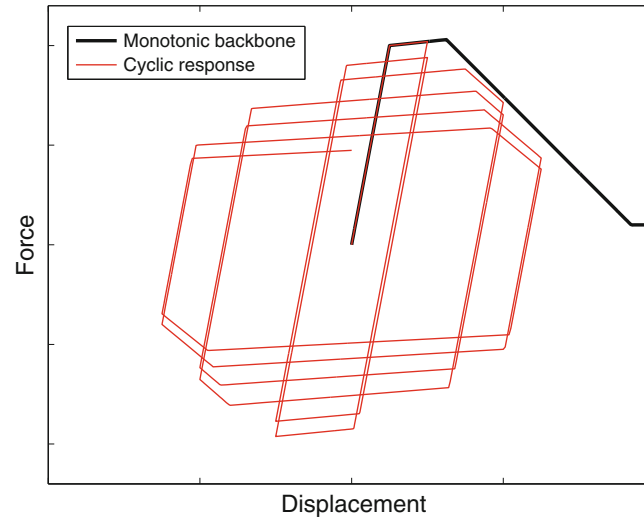

Assessment of Existing Structures Using Response History Analysis, Fig. 4 Component force–deformation hysteretic behavior, generated using the Ibarra et al. (2005) hysteresis model

adopted is able to accurately describe available experimental data for the level of strain expected in the analysis and the cyclic conditions expected.

Modeling Deficiencies in Structural Design

NRHA is most commonly adopted for the assessment of existing structures when the structural detailing is deficient with respect to modern code requirements, and therefore adequate seismic performance cannot be demonstrated by simpler analysis methods. Typical examples of detailing deficiencies are inadequate development lengths and splice lengths for reinforcing bars, transverse reinforcement in beam–column joints and plastic hinge regions, pre-Northridge steel beam–column connections, presence of unreinforced masonry infills in frame buildings, inadequate shear strength and/or failure to satisfy a capacity design hierarchy in beams and columns, and unreinforced masonry buildings in general. Although it may be desirable to address any of these deficiencies through retrofit when they are present, there are many cases when acceptable behavior can be demonstrated. Generally, detailing deficiencies such as splice lengths and beam–column joint details are addressed by limiting both the strength and plastic deformation capacity of the affected members. For example, when reinforcing bars are anchored with inadequate development length, ASCE 41 requires that the capacity of the bar in question is reduced by a linear ratio of the provided to required development length and also significantly reduces plastic rotation limits by up to a factor of 10.

Model Checking and Post-Processing

The amount of post-processing required for a given NRHA model is in some ways inversely related to the amount of rationalization and simplification that has gone into the modeled effort. For example, if URM walls are modeled with a discrete element approach (e.g., Fig. 2c) – wherein all bricks and their interaction are explicitly modeled – then crack widths can be evaluated explicitly, and the "no collapse" performance requirement can be checked by observation of the state of the model at the end of the analysis. In frame analyses – with 2D beam elements used for beams and columns – if monotonic and cyclic degradation are properly accounted for, collapse response can also be observed directly. More commonly, adequate performance of deformation-controlled elements is evaluated on the basis of observed peak plastic deformations (e.g., peak plastic hinge rotations in beams and columns, peak plastic axial deformation in braces, peak drifts in RC or URM walls) compared with allowable limits from published guidelines (e.g., those considered in section "Published Codes, Standards and Guidelines")

or experiments from the literature carried out specifically for the project. Performance of force-controlled elements is evaluated on the basis of observed forces from the analysis compared with capacities evaluated according to guidelines or engineering first principles.

As noted in section "Seismic Input", analyses are typically repeated for multiple earthquake ground motions, and potentially for multiple application orientations of each ground motion, to account for the fact that record-to-record uncertainty is relatively large compared to other sources of uncertainty. Appropriate processing of structural analysis results will depend on the considerations discussed in that section. When the peak response from multiple analyses is considered (say if fewer than seven ground motions are considered as input), this does not introduce significant difficulty – every analysis carried out must demonstrate acceptable response. Consideration of mean response, however, introduces several difficulties. For purely numerical quantities (e.g., plastic hinge rotation), typically codes are interpreted to refer to arithmetic mean, whereas the geometric mean would be more consistent with the common assumption of log-normally distributed structural response. For qualitative responses, such as "collapse" versus "no collapse," or "uplift at foundation" versus "no uplift," means cannot be evaluated. In these cases, the median is a more appropriate measure of central tendency of analysis results. Many engineers consider more than just statistics when interpreting analysis results – even if four out of seven analyses demonstrate no collapse, most engineers would be interested in assessing how collapse occurs in the other three and, if economically possible, prevent these modes of collapse from occurring. NEHRP Consultants Joint Venture (2011) provides further discussion of how analysis and performance objectives affect ground motion development and analyses carried out.

Residual deformations can be more important than peak transient deformations for evaluating performance criteria relating to post-earthquake operability or possibility of occupancy. For example, peak deformations during the earthquake may indicate some cracking that closes up following the earthquake and does not require structural repair. Residual deformations are sensitive to backbone characteristics (such as post-yield stiffness, line BC in Fig. 3), as well as cyclic hysteretic characteristics (such as unloading stiffness and pinching). Furthermore, estimating residual deformations in NRHA can require a significantly longer analysis, allowing time after the earthquake ground motion for the structure to settle. Residual deformations are not explicitly required to be checked in most published guidelines, although approximate limits are given in ASCE 41. FEMA P-58 discussed the estimation of residual interstory drifts in an appendix. On the basis that estimation of residual response is very sensitive to modeled and ground motion characteristics, it suggests using predefined relationships between residual and peak drifts and to not attempt to evaluate them in the main NRHA model.

Nonstructural components are seldom included in a NRHA model, and therefore their assessment is carried out in the post-processing phase. Some so-called nonstructural components, such as URM infill panels in frame buildings, should be included in the structural model, when their inclusion is expected to affect structural response. Nonstructural components are typically classified as either displacement/drift-sensitive (such as partitions or façade panels) or acceleration-sensitive (such as electrical equipment), and the performance of some equipment may be rated on the basis of a limiting peak drift or acceleration level. For more important equipment, response can be evaluated with a response history analysis using floor acceleration histories recorded in the main NRHA model or a response spectrum analysis using secondary response spectra, also from the main model. Finally, statistical performance of nonstructural components is often expressed in the form of a fragility function, which gives the probability of reaching different damage levels for a given level of acceleration or drift. Fragility functions for common types of equipment and other nonstructural components (at least for US practice) are given in FEMA P-58.

Published Codes, Standards, and Guidelines

This section provides a review of available international guidelines on the seismic assessment and retrofit design of existing structures. Regulatory requirements for demonstrating seismic performance vary, but in real projects, it is helpful to demonstrate compliance with documents such as the following to establish credibility – although this should establish a minimum duty of care and should not restrict the engineer from applying state-of-the-art methods and models when they contradict the published guidelines.

ASCE/SEI 41-06: Seismic Rehabilitation of Existing Buildings

ASCE/SEI 41-06 (ASCE 2007) – herein ASCE 41 – is perhaps the most complete published guideline available for assessment and retrofit design for existing buildings, including extensive provisions on NRHA. Acceptable nonlinear seismic performance is evaluated on a component-by-component basis (e.g., plastic rotations in beam and column plastic hinges), and all structural elements must satisfy these checks for compliance. Different limits are quantified for different performance objectives: Immediate Occupancy, Life Safety, and Collapse Prevention. Overall measures of structural performance such as interstory drifts are not explicitly checked, except to evaluate possibility of impact with adjacent buildings and in checking elements that span between stories such as reinforced concrete (RC) shear walls and nonstructural components.

ASCE 41 distinguishes between deformation-controlled and force-controlled actions, as discussed in section "Material and Section Properties". Deformation-controlled actions are modeled with their expected (mean) strength and nonlinear response quantities, while force-controlled actions are restricted to their lower-bound (mean minus one standard deviation) strength. The nonlinear response of force-controlled actions is not usually modeled, since exceeding their linear capacity would result in a sudden shedding of their load (although see note below about the updated version ASCE 41/SEI 41-13). Some deformation-controlled actions – such as flexure in columns of moment frames – may be inhibited for new structures using capacity design procedures, but for existing structures, it would be excessively conservative to condemn a noncompliant structure if adequate seismic performance can be demonstrated.

ASCE 41 tabulates nonlinear deformation acceptance criteria for all types of structural components; in fact, these criteria are routinely applied also for the performance-based seismic design of new structures and are referred to in guidelines for analysis and design of high-rise buildings (e.g., ATC 2010). Allowable plastic deformations are tabulated in terms of relevant characteristics such as performance objective, member slenderness (for steel braces), presence of high shear and axial load and compliance of transverse reinforcement with code requirements (for concrete beams and columns), and other noncompliances with respect to modern codes. A disadvantage of this tabular format is that sometimes small changes in assumptions (e.g., a change from "noncompliant" transverse reinforcement to "compliant" transverse reinforcement) can make a large step change to the allowable deformation, whereas the real effect modeled is likely to be continuous.

Nonlinear behavior of deformation-controlled actions is modeled following the generalized force–displacement or moment–rotation backbone illustrated in Fig. 3. Parameters (deformations and forces) to describe these curves are tabulated for every component in ASCE 41. Note that ASCE 41 does not provide guidance on modeled the cyclic response of components following the backbone in Fig. 3; therefore, modeled of hysteretic phenomena such as stiffness and strength degradation and pinching is not foreseen (see section "Hysteretic Response of Components"). ATC-72-1 (ATC 2010) notes that the force–displacement backbone represents a "cyclic envelope curve" (i.e., represents cyclically degraded response) rather than the force envelope that one would get from a monotonic test on the component. Furthermore, restricting deformations of primary structural components

to within point C on Fig. 3 ensures that the region in which cyclic degradation dominates is not reached.

The next edition of ASCE 41 – ASCE/SEI 41-13 (ASCE 2014) – has just been published and expands the remit of ASCE 41 to include the multitiered seismic assessment approach previously found in ASCE/SEI 31-03 (ASCE 2003). The nonlinear response history analysis procedures have been expanded somewhat, reflecting significantly increased application of this method and the availability of research efforts such as Deierlein et al. 2010; NEHRP Consultants Joint Venture 2010, since the publication of ASCE/SEI 41-06. Nonlinear behavior of force-controlled actions is now permitted to allow explicit modeled of post-failure redistribution following brittle failure. Finally, and importantly for this entry, the unreinforced masonry (URM) wall provisions have been updated; major changes are that bed-joint sliding is now considered a deformation-controlled action, while the pier rocking mechanism is now limited to lower axial load ratios and for piers at least 6″ in thickness.

Eurocode 8 Design of Structures for Earthquake Resistance Part 3: Assessment and Retrofitting of Buildings

Eurocode 8 Part 3 (CEN 2005) – herein EC8-3 – deals with both the seismic assessment and retrofitting of existing buildings. It is interesting to note that other Eurocodes do not cover non-seismic assessment of existing structures, but it was recognized by the code developers that many older structures in Europe did not take into account seismic resistance in their design (whereas presumably gravity and wind have been taken into account – at least by common design practice if not explicit calculation). In common with the other standards considered here, EC8-3 leaves the development and details of a national program for seismic risk mitigation to the member countries, including such critical aspects as what triggers the need for assessment of an existing building, timescales over which assessment and retrofitting must take place (if required), and the performance objectives (limit states and associated return periods of seismic action) that must be satisfied, either before or after strengthening. Performance objectives considered in the standard are defined as Near Collapse, Significant Damage and Damage Limitation – inconsistently with the performance objectives in EC8-1 for new structures – but the actual objective(s) to be checked is left to the National Annex.

Similarly to ASCE 41, EC8-3 distinguishes between ductile and brittle actions. For nonlinear analyses, capacities are evaluated on the basis of deformation for ductile actions and strength for brittle ones. Column flexure is considered a ductile action, although interestingly "strong column–weak beam" behavior is enforced for steel moment frames only (not reinforced concrete).

Acceptance criteria for nonlinear actions are contained in informative Annexes A, B, and C for RC, steel, and masonry, respectively. No guidance is given for the assessment of timber structures. Generally, for elements classified as primary components of the seismic force resisting system, allowable deformations are explicitly noted as mean minus one standard deviation estimates, and for secondary components, they are the mean values.

For RC beams and columns, allowable total or plastic rotations are expressed in terms of regression relationships on experimental data, including such aspects as section depth, shear and axial force ratios, longitudinal and transverse reinforcement ratio, and material properties. Modifications are also provided for lack of compliance with modern requirements, such as lap splices in plastic hinge zones and the use of smooth reinforcing bars. Alternative expressions are also provided for curvatures rather than rotations. Annex A is also notable for a ductility-dependent shear strength calculation and specific rules for concrete, steel, and fiber-reinforced polymer (FRP) jacketing of seismically deficient elements, including estimates of the strength and deformation capacities provided by these interventions that could be used in NRHA.

Acceptability criteria for steel elements, contained in Annex B, are more comparable to the equivalents in ASCE 41. They are expressed

as multiples of the yield displacement (for braces) or yield rotation (for flexural elements), with multipliers that are in most cases identical to those in ASCE 41, assuming Immediate Occupancy, Life Safety, and Collapse Prevention performance objectives (from ASCE 41) may be mapped directly on to Damage Limitation, Significant Damage, and Near-Collapse limit states (from EC 8-3). Rotation capacities for the three limit states are also provided for retrofitted components, using interventions such as haunched connections and reduced beam section connections.

Masonry acceptance criteria (in Annex C) are quantified in terms of wall drift – in common with ASCE 41 for flexure-controlled walls, but in contrast to ASCE 41 for shear-controlled walls for which strength criteria apply. For flexure-controlled walls, drift limits are given in terms of the slenderness ratio of width to the height of the point of contraflexure, which gives limits similar to those given in ASCE 41 for fix–fix boundary conditions of wall piers but doubles the limits for cantilever walls (mapping the limit states as discussed for steel).

Stress–strain relationships for different materials are contained in each of the other material-specific Eurocodes and may be used to develop force–displacement or moment–rotation relationships for use in nonlinear analysis. However, these typically do not consider the range of strains associated with near-collapse response of structures, and therefore in-cycle degradation of strength may not be considered (see section "Hysteretic Response of Components"). Furthermore, no guidance is provided for cyclic hysteresis models for a given structural element, except a generic statement that it "should realistically reflect the energy dissipation in the element over the range of displacement amplitudes expected in the seismic design situation."

New Zealand Society for Earthquake Engineering (NZSEE): Assessment and Improvement of the Structural Performance of Buildings in Earthquakes

The Building Act 2004 required territorial authorities (TAs) in New Zealand to adopt a policy on "earthquake-prone buildings" (EPBs) within 18 months of the passing of the Act. The corresponding Building Regulations defines an EPB as one that will have its ultimate capacity exceeded in earthquake ground motion one-third as strong as that required for new building design. The New Zealand Society for Earthquake Engineering developed its recommendations (NZSEE 2006) (herein "the NZSEE Recommendations") to assist TAs in developing their policies and engineers in carrying out assessments and design of seismic rehabilitation.

NRHA is allowed by the NZSEE Recommendations, although they note that NRHA should not be the sole adopted assessment procedure and should be supplemented by the results of a simplified approach. They cite such uncertainties as flexure–shear–axial force interaction, effect of axial force on column stiffness, degrading strength characteristics, and modeled of beam–column joints. Presumably, the restriction on the use of NRHA could be relaxed somewhat if more detailed analysis models are used that reduce these uncertainties. The focus of the NZSEE Recommendations is on linear analysis supplemented by an analysis of expected yielding mechanisms, and therefore the recommendations for NRHA are reasonably limited.

Nonlinear deformation limits for concrete members in the NZSEE Recommendations are evaluated in terms of yield and ultimate curvatures and an assumed nominal plastic hinge length. The yield curvature is given as a function of the yield strain in the reinforcement and the dimension of the section, and the ultimate curvature can be evaluated from a concrete strain limit, taking into account the effect of confinement and the neutral axis depth of the section at ultimate curvature. The plastic rotation capacity of steel sections is tabulated (in the New Zealand standard for design of steel structures) as a function of the section compactness and the axial load on the member. Allowable plastic hinge rotations for steel sections range from 0.5 % to 4 % for seismic load cases (higher values are given for links of eccentrically braced frames).

The NZSEE Recommendations contain useful discussion on the modeled of URM structures; they note the importance of including the distribution of mass in a masonry building and discuss the use of finite element modeled with 2D or 3D elements. However, the guidance is more targeted towards linear analysis; they recommend using a ductility factor of 1.0 and an equivalent viscous damping value of 15 % to account for energy dissipation due to cracking, sliding, and rocking, which do not seem to be appropriate for nonlinear analysis. Nevertheless, deformation limits are given as 1 % for elements failing in a rocking mode and 0.5 % for all other elements. Unique among the documents considered here, the Recommendations also give a rotation limit for spandrels of 0.5 % (based on the clear span).

FEMA P-58: Seismic Performance Assessment of Buildings

The ATC-58 and ATC-58-1 projects developed the so-called next-generation performance-based seismic design guidelines following on from "first-generation" projects such as ASCE 41. The outcome of these projects was FEMA P-58, published in 2012 (ATC 2012). This project takes one of the main original objectives of performance-based design – communicability of seismic performance to non-engineers – to the next level by providing guidance on converting results from analytic models into estimates of casualties, repair costs, and repair time. To achieve this in a meaningful way, the framework explicitly incorporates variability and uncertainty in both structural and nonstructural response. The probabilistic loss calculations are implemented in a computer program, *PACT* (Performance Assessment Calculation Tool).

FEMA P-58 considers the three basic assessment types discussed in section "Performance Objectives and Assessment Methodology." For each of these assessment types, a similar workflow is followed. Structural performance is assessed with NRHA (or other methods) and is quantified both in terms of collapse fragility (probability distribution of the ground motion level required to cause collapse) and probability distributions of other demand parameters associated with damage to structural and nonstructural components (e.g., peak floor acceleration and peak storey drift ratio). A building performance model is developed, which takes into account all the nonstructural components in the building and relates them to specific demand parameters (e.g., partitions in a floor are related to the storey drift in that floor). Fragility functions and consequence functions are provided for typical nonstructural components present in US buildings and incorporated in the software, *PACT*. A Monte Carlo analysis is carried out to sample each of these fragility functions to assess the expected damage and losses under the design earthquake ground motion.

FEMA P-58 evaluates economic and human losses as continuous variables, rather than checking for compliance with discrete limit states (such as "Life Safety" and "Collapse Prevention" used in ASCE 41). It is left to the building owner, engineer, or future code developer to define acceptable performance for a given project. Economic losses can be compared with the costs of seismic retrofit or with other insurance or investment costs.

Downtime calculations in FEMA P-58 are limited to estimates of repair time resulting from earthquake damage, which does not account for delays for required inspections, mobilization of engineering and contractors resources, financing, permitting, and utility disruption. It also only focuses on the time to achieve full recovery of the facility, but does not consider intermediate goals such as the time to reoccupy or return to functionality, which are of more direct concern to building owners. The downtime calculation was therefore improved as part of the development of the REDi^{TM} Rating System (Resilience-based Earthquake Design Initiative) guidelines (Almufti and Willford 2013), taking into account input from contractors, cost estimators, bankers, building department officials, and researchers. The REDi^{TM} Rating System uses this extended FEMA P-58 loss assessment approach to demonstrate that the REDi^{TM} resilience objectives are satisfied – primarily for new buildings, but also applicable for existing structures.

Summary

This entry has summarized the assessment of existing structures using nonlinear response history analysis. As noted in the introduction, NRHA is no longer the domain of specialist engineering consultancies, and many commonly used software packages are available to carry it out on projects.

It has been emphasized throughout this entry that the most appropriate modeled techniques and approximations to use are very application-dependent. Published guidance aimed at accurately estimating the collapse risk of well-detailed structures in highly seismic regions is not necessarily appropriate for assessing brittle URM buildings in low to moderate seismic regions. Furthermore, every client will have different requirements, and it is not always appropriate to use the most advanced analysis methods in cases where acceptable performance can be demonstrated by simpler methods or where the level of information available is limited (according to the principle of consistent crudeness). Nevertheless, this entry has attempted to summarize the different considerations that the analyst faces when setting up and interpreting his or her NRHA models for existing structures.

Several other entries in this volume consider different aspects of NRHA, and they should be consulted for more detailed guidance on each of the modeled decisions discussed in this entry.

Cross-References

- Analytic Fragility and Limit States [P(EDP| IM)]: Nonlinear Dynamic Procedures
- Assessment of Existing Structures Using Inelastic Static Analysis
- Damage to Buildings: Modeling
- Earthquake Response Spectra and Design Spectra
- Engineering Characterization of Earthquake Ground Motions
- Nonlinear Dynamic Seismic Analysis
- Nonlinear Finite Element Analysis
- Numerical Modeling of Masonry Infilled Reinforced Concrete Frame Buildings
- Performance-Based Design Procedure for Structures with Magneto-Rheological Dampers
- Response-Spectrum-Compatible Ground Motion Processes
- Retrofitting and Strengthening of Structures: Basic Principles of Structural Interventions
- Seismic Analysis of Masonry Buildings: Numerical Modeling
- Seismic Analysis of Steel Buildings: Numerical Modeling
- Seismic Analysis of Steel–Concrete Composite Buildings: Numerical Modeling
- Seismic Collapse Assessment
- Seismic Response Prediction of Degrading Structures
- Time History Seismic Analysis

References

Almufti I, Willford MR (2013) Resilience-based earthquake design (REDi) rating system, version 1.0. Arup. http://www.arup.com/Publications/REDi_Rating_System.aspx. Accessed Nov 2013

ASCE (2003) ASCE standard ASCE/SEI 31-03: seismic evaluation of existing buildings. American Society of Civil Engineers, Reston

ASCE (2007) ASCE standard ASCE/SEI 41-06: seismic rehabilitation of existing buildings. American Society of Civil Engineers, Reston

ASCE (2014) ASCE standard ASCE/SEI 41-13: seismic evaluation and retrofit of existing buildings. American Society of Civil Engineers, Reston

ATC (2010) PEER/ATC-72-1: modeling and acceptance criteria for seismic design and analysis of tall buildings. Applied Technology Council, Redwood City

ATC (2012) FEMA P-58: seismic performance assessment of buildings, vol 1–3. Applied Technology Council, Redwood City

CEN (2005) Eurocode 8: design of structures for earthquake resistance – part 3: assessment and retrofitting of buildings. European Committee for Standardization (Comité Européen de Normalisation), Brussels

Deierlein GG, Reinhorn AM, Willford MR (2010) Nonlinear structural analysis for seismic design. NEHRP seismic design technical brief no. 4, NIST GCR 10-917-5. National Institute of Standards and Technology, Gaithersburg

Elms DG (1985) Principle of consistent crudeness. Workshop on civil engineering application of fuzzy sets. Purdue University, West Lafayette

Gibson R, Wilcock TR, Grant DN, Gration DA (2012) Performance based seismic design of an offshore platform in the Caspian Sea. Struct Eng 90:14–22

Grant DN (2011) Response spectral matching of two horizontal ground motion components. Journal of Structural Engineering 137: 289–297

Grant DN, Padilla D, Greening PD (2011) Orientation dependence of earthquake ground motion and structural response. In: Dolšek M (ed) Protection of built environment against earthquakes. Springer, Dordrecht, 352 pp

Ibarra LF, Medina RA, Krawinkler H (2005) Hysteretic models that incorporate strength and stiffness deterioration. Earthq Eng Struct Dyn 34:1489–1511

NEHRP Consultants Joint Venture (2010) Applicability of nonlinear multiple-degree-of-freedom modeling for design. NIST GCR 10-917-9. National Institute of Standards and Technology, Gaithersburg

NEHRP Consultants Joint Venture (2011) Selecting and scaling earthquake ground motions for performing response-history analyses. NIST GCR 11-917-15. National Institute of Standards and Technology, Gaithersburg

NEHRP Consultants Joint Venture (2012) Soil-structure interaction for building structures. NIST GCR 12-917-21. National Institute of Standards and Technology, Gaithersburg

NZSEE (2006) Assessment and improvement of the structural performance of buildings in earthquakes. New Zealand Society for Earthquake Engineering, Wellington